DISSERTATION

KINETIC, MECHANISTIC, AND ACTIVE SITE STUDIES OF COPPER METAL-ORGANIC FRAMEWORK CATALYZED NITRIC OXIDE GENERATION FROM S-NITROSOGLUTATHIONE IN WATER AND BLOOD PLASMA

Submitted by

Robert Reeves Tuttle

Department of Chemistry

In partial fulfillment of the requirements

For the Degree of Doctor of Philosophy

Colorado State University

Fort Collins, Colorado

Fall 2021

Doctoral Committee:

Advisor: Melissa M. Reynolds

Richard Finke
Debbie Crans
Ketul Popat

ABSTRACT

KINETIC, MECHANSITIC, AND ACTIVE SITE STUDIES OF COPPER METAL-ORGANIC FRAMEWORK CATALYZED NITRIC OXIDE GENERATION FROM S-NITROSOGLUTATIHONE IN WATER AND BLOOD PLASMA

Catalytic generation of nitric oxide (NO) from endogenous sources by copper-based materials at the surfaces of implanted medical devices improves device performance by promoting vasodilation and inhibiting bacterial adhesion. Oxidation of the endogenous tripeptide *S*-Nitrosoglutathione (GSNO) to release NO is catalyzed by the copper-based metal-organic framework (MOF) $H_3[(Cu_4Cl)_3(BTTri)_8]$ (CuBTTri) in the presence of glutathione (GSH). MOFs are solid-state, crystalline, porous materials composed of metal cation nodes and organic linkers forming three-dimensional structures. MOFs have generated interest as catalysts because of their unparalleled tunability via synthesis (compared to other solids), well-defined structures, coordinatively unsaturated metal sites, and high surface areas. Mechanistic insight into MOF catalysts promises to allow for the directed design of next-generation catalysts via leveraging synthetic tunability. However, because necessary studies to propose reliable reaction mechanisms are rarely reported for MOF catalysts, mechanistic understanding is lacking in the field.

This Dissertation works toward a reaction mechanism of CuBTTri catalyzed GSNO to NO conversion in water in the presence of GSH. The strategies used to better understand this mechanism can also generate mechanistic knowledge in other MOF catalysis systems. Chapter I provides a discussion of NO release catalyzed by soluble and insoluble Cu-based species focusing on CuBTTri. Chapter I also introduces MOFs as catalysts and explains the requirements to propose a reliable reaction mechanism.

Chapters II and III focus on the development of monitoring methods to quantify [GSNO], [GSH], and [glutathione disulfide] (the other main reaction product, GSSG) in real time in H_2O and blood plasma. ^1H nuclear magnetic resonance (NMR) and ultraviolet-visible (UV-VIS) spectroscopies can together effectively monitor the NO release reaction. The observation of an inverse dependence on added GSH for CuBTTri versus solvated Cu ions for NO generation shows that the two catalysts operate via different reaction mechanisms. Chapter III shows how the monitoring method in H_2O reported in Chapter II can be extended to track the reaction in blood plasma. The observed GSNO to NO reaction stoichiometry is effectively identical in H_2O and blood plasma, which indicates that the mechanism does not change *in vivo* versus the model biological solvent H_2O. Hence, mechanistic findings in this dissertation for NO generation in water are likely biologically applicable.

Chapter IV establishes the catalytically active Cu sites in CuBTTri for GSNO to NO conversion. Studies comparing the reaction rate (-d[GSNO]/dt) to particle size revealed that ~100% of the observed catalysis is caused by Cu atoms on the external surfaces of CuBTTri particles. Kinetic poisoning studies of CuBTTri particles with potassium cyanide (KCN) and 3,3',3''-phosphanetriyltris (benzenesulfonic acid) trisodium salt (TPPTS) showed that the active sites are kinetically uniform. Fourier transform infrared spectroscopic analysis of CN-poisoned CuBTTri detected $Cu(CN)_3$ and Cu(CN) sites, which correspond to the idealized metal-terminated CuBTTri crystal structure. Size-selective kinetic poisoning studies of CuBTTri using TPPTS measured the active site density to be (1.3 ± 0.4)% of total Cu atoms in 600 ± 400 nm CuBTTri particles. Active site density was used to calculate a normalized turnover frequency for CuBTTri to make informed inter-catalyst comparisons.

Chapter V presents the rate law and proposed mechanism for CuBTTri catalyzed GSNO to NO conversion. Four other competing, minimalistic mechanistic hypotheses were considered and disproven. The mechanism proposed is a Cu^{II} to formally Cu^{III} redox mechanism with two proton-coupled electron transfer elementary steps. The proposed mechanism exhibits a derived rate law which matches the experimental rate law, has elementary steps which sum to the observed reaction stoichiometry, and provides a reasonable driving force for S-N bond homolysis in GSNO. Future computational and laboratory experiments suggested by the proposed mechanism promise to yield a level of mechanistic understanding for CuBTTri which has traditionally not been achievable for solid-state catalysts.

ACKNOWLEDGEMENTS

I would like to thank my research advisor, Melissa Reynolds, for her support and for giving me the freedom to take ownership of my degree. I would like to thank Rick Finke, his emphasis on disproof-based scientific research has forever changed how I look at the world. I would like to thank my committee members for their time and insightful questions. This work would not have been possible without the CIF/ARC scientists at CSU. Dr. Chris Rithner was invaluable in developing the necessary instrumental techniques in this dissertation and was a pleasure to work with. I am thankful for the CSU chemistry department faculty and staff who provided intellectual support. This work was supported financially by the National Science Foundation, National Institutes of Health, Department of Defense, and the Department of Energy. Heather Rubin mentored me early on with my lab technique and project development. To Scott Folkman, our discussions of catalysis, mechanism, and whatever else were a great way to spend a couple hours putting off real work. Carly Jewell and Chris Whitehead excellent editors and both challenged me intellectually every time I presented research result. Bella Neufeld, Chris Allison, and Jesus Tapia became my friends quickly after joining the Reynolds research group and made me feel welcome right away, I cannot stress enough how important that is for a starting graduate student. I need to thank Sarah Carroll for being my partner and best friend, going through graduate school together has made it better. My brother Andy, Mom, Dad, and friends; it would not have gotten done without you too. Lastly, to the molecules, thanks for keeping things interesting.

TABLE OF CONTENTS

I. INTRODUCTION

This dissertation is in a "journal's format." Each chapter was prepared as a manuscript for publication in a peer-reviewed chemistry journal. Therefore, the chapters follow the formatting guidelines for the journal the manuscript was submitted to. An overview begins each chapter, and the Supporting Information sections are included separately as appendices after each corresponding chapter. Below is an introduction to the field of copper-based, metal-organic framework catalyzed nitric oxide generation and a brief description of each chapter.

Implanted medical device failure because of bacterial adhesion and biofilm formation on device surfaces is harmful to patients, especially those who are immunocomprosmised.[1] One strategy to improve performance of medical devices is to generate nitric oxide (NO) at the surface of implanted devices.[2–8] NO is a vital biological signaling molecule responsible for the endothelium-derived relaxing factor and exhibits antibacterial activity.[8,9] Strategies for NO generation from medical devices which use endogenous sources of NO are desirable, as opposed to preloading NO donor molecules into medical device polymers (as the NO reservoir will ultimately run out).[10–14] Using an endogenous NO source ensures that as long as blood is flowing over the device surface, local NO flux can be achieved, extending the lifetime and improving the performance of the device.[11,13,15,16]

Since the 1990s, it has been known that solvated Cu^{2+} catalyzes the release of NO from a class of small molecules known as *S*-Nitrosothiols (RSNOs).[17–22] One RSNO known to be present in the human body at detectable levels is the nitrosated tripeptide *S*-Nitrosoglutathione (GSNO).[18,23–25] Therefore, it has been frequently proposed that Cu-based materials are a route towards NO generation from GSNO *in vivo*.[10,11] However, Cu ions are known to exhibit acute liver

toxicity and will leach out of many polymers in the presence of water and biological solvents.[12,26] The Cu-based catalyst for GSNO to NO conversion must therefore be a solid which does not leach Cu ions when exposed to *in vivo* conditions.[10]

In 2012 Harding et. al. reported that a solid-state material called a metal-organic framework (MOF) referred to as HKUST-1 composed of Cu^{2+} nodes and 1,3,5 benzenetricarboxylate linkers (CuBTC) catalyzes NO release from *S*-Nitrosocysteine (CysNO) in ethanol.[12] MOFs are a wide class of porous, crystalline, solid-state materials discussed in greater depth below (*vide infra*).[27,28] The 2012 study showed that NO release from an RSNO can be catalyzed by a solid-state, Cu-based material. However, CuBTC is not stable in water or biological solvents, meaning CuBTC is not a biologically applicable NO generation catalyst.[12,29,30] Achieving biologically applicable Cu-MOF catalyzed RSNO to NO conversion requires use of a Cu- MOF which is stable *in vivo* and catalyzes NO release from an endogenous RSNO (namely, GSNO).

In 2014, Harding et. al. reported a more biologically applicable NO generation system.[10] The 2014 study utilized a new Cu-based MOF, $H_3[(Cu_4Cl)_3(BTTri)_8]$ (CuBTTri, Figure 1.1). The 2014 study also employed a different RSNO, *S*-Nitrosocysteamine (CysamNO). CuBTTri was shown to be stable in biological media (whole blood) and phosphate buffered saline (PBS) based on powder X-ray diffraction (P-XRD) and Cu-ion leaching inductively-coupled plasma atomic emission spectroscopy (ICP-AES) data.[10] CuBTTri is unique in its stability under *in vivo* conditions among MOFs. In the 2014 study, the release of NO from CysamNO catalyzed by CuBTTri was measured in both whole blood and water. These NO generation measurements established that CuBTTri could be a biologically applicable NO generation catalyst. In 2016 and 2017, Lutzke and Neufeld et. al. reported a significant step forward for *in vivo* NO generation by showing that composite materials composed of polymers containing CuBTTri particles could

catalyze GSNO to NO conversion in water.[11,13,14] The 2016 report addressed Cu ion liver toxicity by showing that CuBTTri is compatible with human hepatocytes.[14] The previous work by Harding, Lutzke, and Neufeld et. al. set up CuBTTri up as the catalyst of interest for this dissertation.

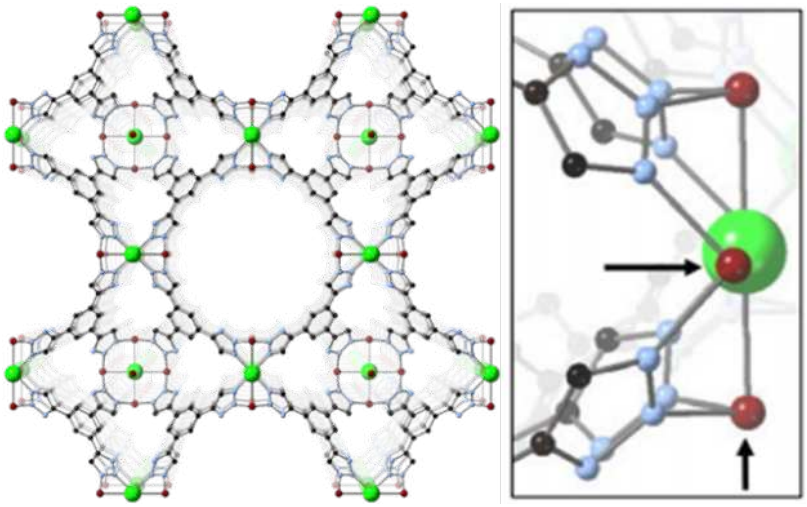

Figure 1.1. (Left) The CuBTTri unit cell showing carbon (black), nitrogen (blue), chlorine (green), and copper (red). (Right) Finer, more detailed view of nominally 3–coordinate $Cu_{surface}$ site (indicated with arrows) determined to be active for GSNO to NO conversion catalysis in Chapter IV of this Dissertation.

It is important to define exactly what a MOF is and why MOFs are interesting heterogeneous catalysts (for reasons beyond NO generation).[27,28,31,32] MOFs are porous, usually crystalline solids composed of metal cation or cluster nodes connected by organic linkers which form infinitely repeating 3-D structures.[27] Interest in MOFs is driven by, at least, the following four factors: i) MOFs exhibit unparalleled chemical and physical tunability compared to other solid-state materials (>10^5 different MOFs have been reported, versus ~10^2 zeolites[33]), ii) crystalline MOFs exhibit well-defined structural geometry, iii) MOFs are porous, allowing for diffusion of guest molecules into the channels of MOF structures, and iv) MOFs exhibit high surface areas, (MOFs bridge the gap in density between solids and liquids). MOFs have been investigated for several different applications,[34–39] but this dissertation will focus on understanding how to investigate and think about MOFs as solid-state catalysts.[28,32,40–42]

MOFs offer unique opportunities for study as heterogenous catalysts because the well-defined structures allow one to generate specific hypotheses up front about what catalytically active sites may look like and where they may be in the MOF structure (i.e., inside the MOF pores or on particle exterior surfaces).[43–45] MOFs also combine advantages traditionally associated with insoluble (recyclability, stability, ease of isolation) and soluble (tunability, defined structures) catalysts.[40] Through the mechanistic investigations in this dissertation, it will become clear that this line of thinking (i.e., MOFs can be approximated as solids composed of discreet homogeneous metal complexes) is useful, at least for CuBTTri and NO generation. However, we only arrive at that conclusion because of the disproof-based kinetic and mechanistic studies herein.[46] Mechanistic insight into MOF catalysts is often cited as one way to leverage tunability for directed design of future, improved MOF catalysts.[42,47–49] Surprisingly though, mechanistic investigations into MOF catalysis systems are lacking in the field.[28,50] Hence, MOF tunability currently cannot be fully taken advantage of in most systems.

Proposing a reliable reaction mechanism for CuBTTri catalyzed GSNO to NO conversion is the ultimate goal of this dissertation. The work described in each research chapter (II-V) and what specific questions we sought to answer, are informed by the following list, defining the five requirements necessary to propose a more reliable catalytic reaction mechanism:

1) *Determination of the kinetically dominant active site.*[43,45,51–54] Active site investigation in MOFs will ideally determine the location, number, and include some structural information of the active sites. Knowledge of the active site in MOF catalysts allows one to best design the studies necessary to address the four following requirements.

2) *The full catalytic reaction stoichiometry, including mass and charge balance.*[52,55] Often, the critical requirement of a balanced reaction is not reported in investigations of MOF catalysts. Without a balanced reaction in hand, one cannot write the correct series of elementary steps that sum to the observed stoichiometry. Without stoichiometry it is possible to propose a mechanism for a reaction other than the one of interest (i.e., the wrong reaction).

3) *Kinetics data must be obtained for all reactants present using direct physical handles if possible.* Comparing experimentally observed rate laws to rate laws derived for proposed mechanisms is essential to support or disprove competing mechanistic hypotheses.

4) *Elementary (or pseudo-elementary) steps which sum to the observed balanced reaction are required.* These elementary or pseudo-elementary steps define the rate constants for each step of the reaction. Elementary steps also define the concepts and associated language needed to describe the mechanism unequivocally.

5) *Consideration, and attempted disproof, of competing, deliberately minimalistic mechanistic hypotheses*. Mechanistic hypotheses should only contain the minimal elementary steps and assumptions necessary to explain all data (i.e., hypotheses must obey Ockham's razor.[46]

Prior to this dissertation, the above requirements had not been fulfilled for CuBTTri catalyzed GSNO to NO conversion in water.[45,55] In fact, *all five* requirements had not been fulfilled for any MOF catalysis system, demonstrating the need for this work in a more general sense. Each of the four research chapters in this dissertation addresses one or more of the requirements in the list above. Each chapter and the key results contained therein are summarized here.

Chapter II establishes a quantitative, direct method to monitor the NO release reaction from GSNO in water.[55] The monitoring method uses solvent-suppressed ^{1}H nuclear magnetic resonance (NMR) spectroscopy (Figure 1.2), which detects unique signals from GSNO, its corresponding thiol glutathione (GSH), and glutathione disulfide (GSSG) (the other reaction product in addition to NO).[56,57] Solvent-suppressed ^{1}H NMR spectroscopy can simultaneously quantify [GSNO], [GSH], and [GSSG] in real time in *protonated* solvent (H_2O as opposed to D_2O).[55] Running GSNO to NO conversion experiments in H_2O is necessary, as hydrogen bonding effects may account in part for the *in vivo* stability of GSNO and GSH.[58–61] Chapter V shows that proton transfer plays a

key role in the GSNO to NO conversion reaction mechanism (*vide infra*), confirming that studying the reaction in H_2O is necessary.

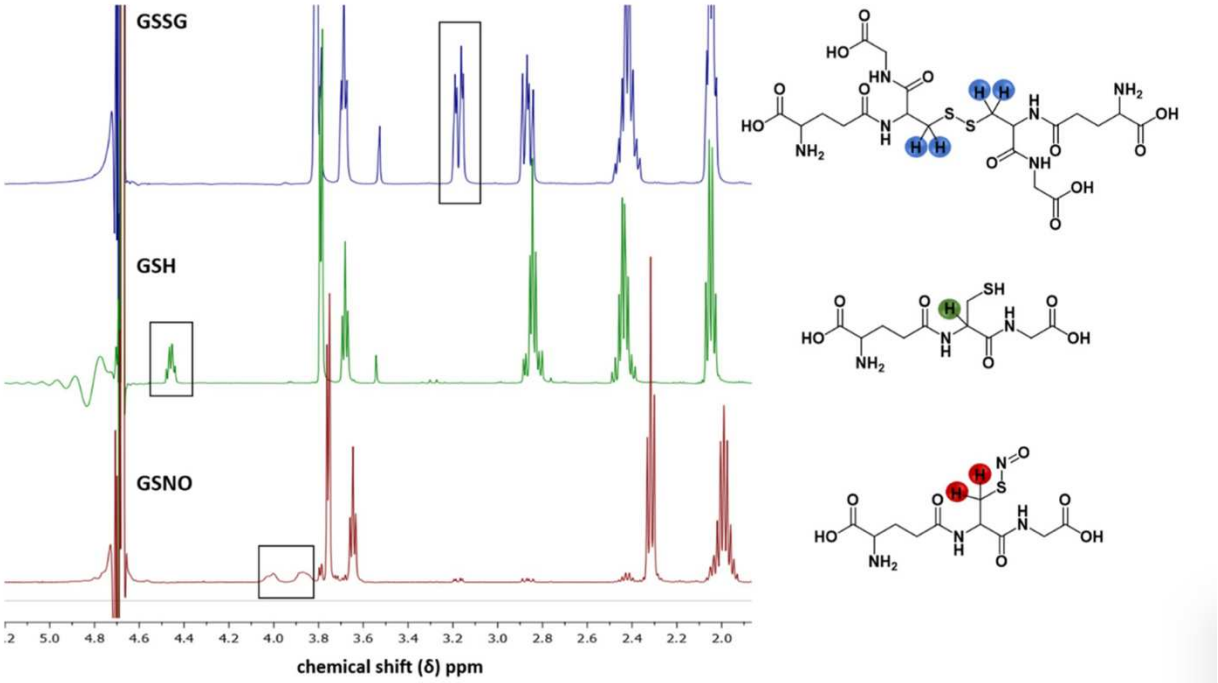

Figure 1.2. Structures and diagnostic peaks used for ^{1}H NMR spectroscopic analysis of GSSG (blue, top), GSH (middle, green), and GSNO (bottom, red). The diagnostic protons responsible for the boxed signal in each spectrum are highlighted in blue, green, or red.

Chapter II details how we determined the reaction stoichiometry and dependence on added GSH for both CuBTTri and solvated Cu^{2+} catalyzed GSNO to NO conversion. For CuBTTri catalyzed reactions, added stoichiometric GSH (relative to GSNO) was required to observe significant GSNO to NO conversion within 16 h. However, stoichiometric levels of GSH completely poisoned the Cu^{2+} ions for catalysis. These two results suggest that CuBTTri and solvated Cu^{2+} catalyze GSNO to NO conversion through different mechanistic pathways. Before more thoroughly investigating the mechanism of CuBTTri as an NO generation catalyst, we sought to confirm that the findings for the reactions in Chapter II were biologically relevant by investigating the same reaction in a biological solvent.

Chapter III details how CuBTTri catalyzed GSNO to NO conversion can be quantitatively, directly monitored in blood plasma.[62] Monitoring reactions in biological solvents, such as blood plasma, is difficult because the complex solvent matrix presents many potentially interfering signals.[63–69] Combining ^{1}H NMR and ultraviolet-visible (UV-VIS) spectroscopies with a nitric oxide analyzer (NOA)[12] allowed us to monitor the concentrations of GSNO, GSSG, and NO in blood plasma in real time. The only difference in the stoichiometry for the NO release reaction observed in blood plasma as opposed to water was minor NO scavenging by the blood plasma solvent.[70] The effectively identical stoichiometries indicate that the reaction mechanism for GSNO to NO conversion catalyzed by CuBTTri does not change when the reaction moves from water to blood plasma. Hence, mechanistic findings determined for the CuBTTri/GSNO/GSH/NO system in water are likely applicable to the mechanism *in vivo*.

Chapter IV addresses the questions of location, density, and structure of the catalytically active sites in CuBTTri for GSNO to NO conversion.[45] CuBTTri samples were ground and filtered to generate three sets of differently sized particles. Comparing the reaction rate (-d[GSNO]/dt) to the ratio of particle exterior surface area to interior volume revealed that ~100% of the NO release catalysis is caused by Cu sites on the exterior surfaces of CuBTTri particles (Figure 1.3). Intrapore Cu sites account for ~0% of the catalytic activity. The size of the largest pore window diameter in CuBTTri (2 nm when desolvated) supports the hypothesis that GSNO diffusion to intrapore metal sites followed by catalysis will either occur not at all, or at a much slower rate than reaction at the exterior surfaces of CuBTTri particles.[71–73] Evidence for catalysis confined to MOF particle exterior surfaces disproves, for the NO release reaction, the favored hypothesis in most MOF catalysis literature that intrapore metal sites are equally as active for catalysis as exterior surface metal sites.[49] CuBTTri catalyst poisoning by potassium cyanide (KCN) followed by Fourier

transform infrared (FT-IR) spectroscopy showed two distinct Cu to CN binding modes, $Cu(CN)_3$ and Cu(CN), suggesting that there are two distinct Cu sites present in CuBTTri.[74–78] Analysis of the idealized, metal-terminated CuBTTri crystal structure shows that bulk, intrapore sites in the solid have one vacant coordination site to accept one CN molecule and that exterior surface sites have three vacant coordination sites to accept three CN molecules.[79–81] Correspondence between the predicted and observed Cu to CN binding ratios led us to propose that Cu(CN) sites are *inactive* intrapore sites (Cu_{pore}), and that $Cu(CN)_3$ sites are catalytically *active* particle exterior surface Cu sites ($Cu_{surface}$). $Cu_{surface}$ sites can be described as naturally occurring, particle termination defect sites which form kinetically during the solvothermal CuBTTri synthesis. Size-selective catalyst poisoning experiments employing a poison which cannot diffuse into CuBTTri pores (3,3',3''-phosphanetriyltris benzenesulfonic acid trisodium salt (TPPTS)) determined the active site density in CuBTTri.[54] TPPTS poisoning showed that for 600 ± 400 nm octahedral particles (1.3 ± 0.4)% of the total Cu sites in CuBTTri are active for catalysis.[82]

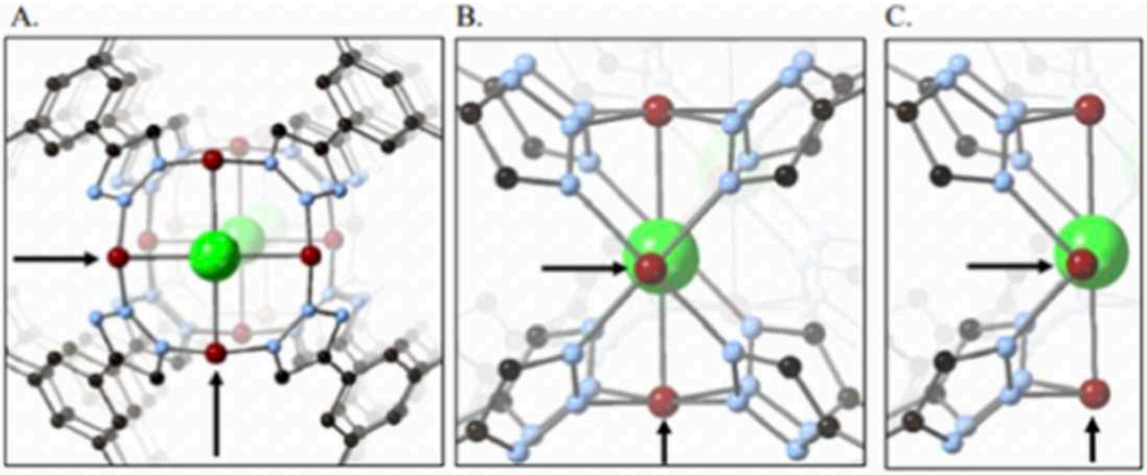

Figure 1.3. Finer, more detailed view than provided in Figure 1.1 of nominally 3-coordinate $Cu_{surface}$ (A, C) and nominally 5-coordinate Cu_{pore} (B) (red = copper, green = chlorine, blue = nitrogen, black = carbon) based on the X-ray structure of an isostructural MOF and assuming to start an idealized, metal-terminated surface of CuBTTri. Vacant coordination sites within CuBTTri would presumably be occupied by H_2O pre-reaction, while surface Cu sites could be coordinated by anything from H_3BTTri ligand to Cl^- to H_2O. Ligands that are expected to be displaced by GSNO or GSH in the catalytic reaction—an assumption supported quantitatively by the results in Chapters IV and V. Hydrogen atoms have been omitted for clarity.

Chapter V presents the experimentally determined rate law and currently favored Cu^{II} to Cu^{III} redox, proton-coupled electron transfer (PCET) mechanism for CuBTTri catalyzed GSNO to NO conversion. The NO release reaction is observed experimentally to be 1st order in [GSNO], 1st order with saturation in [GSH], 1st order in catalyst, and inverse 1st order with saturation in [OH^-]. The experimental rate law, reaction stoichiometry, and knowledge of the $Cu_{surface}$ active sites were used to construct competing mechanistic hypotheses, which were then systematically disproven until what remained was our currently favored Cu^{II} to Cu^{III} mechanism. The mechanism proposed in Chapter V illustrates the ubiquity of simultaneous transfer of protons and electrons in biological systems and illustrates the special nature of GSNO and GSH as NO release substrates. GSNO is a metastable NO shuttle designed by nature which will not release NO spontaneously in solution (as many other RSNOs do).[20,23,24,83] The PCET steps involving oxidation/reduction of $Cu^{II/III}$ provide the driving force for S-N bond homolysis and explain why GSH must be added to the reaction to observe catalysis by CuBTTri.[55] The currently favored mechanism is presented alongside four competing alternative hypotheses. Only the Cu^{II} to Cu^{III} mechanism satisfies all five requirements for proposing a reliable mechanism as outlined previously. The appendix to Chapter V presents future studies suggested by specific features of the currently favored mechanistic hypothesis and the predictive power of mechanism. Future work will provide molecular-level mechanistic insight for CuBTTri, which is rarely achieved for solid-state catalysts.

Chapter VI closes this dissertation with a summary of the key results in each chapter and an outlook on the CuBTTri/GSNO/GSH/NO reaction in broader context. The conclusions from this work are analyzed along with other MOF catalysis and NO release literature to provide a broader view of both fields.

REFERENCES

1. VanEpps, J. S. & Younger, J. G. Implantable Device-Related Infection. *Shock (Augusta, Ga.)* **46**, 597–608 (2016).

2. Mengel, A. & Lindermayer, C. *Nitric Oxide: Methods and Protocols*. (Springer, 2018).

3. Marletta, M. A. Nitric oxide: biosynthesis and biological significance. *Trends in Biochemical Sciences* **14**, 488–492 (1989).

4. Bogdan, C. Nitric oxide and the immune response. *Nature Immunology* **2**, 907–916 (2001).

5. Carpenter, A. W. & Schoenfisch, M. H. Nitric oxide release: Part II. Therapeutic applications. *Chemical Society Reviews* **41**, 3742–3752 (2012).

6. Knott, A. B. & Bossy-Wetzel, E. Nitric oxide in health and disease of the nervous system. *Antioxidants & redox signaling* **11**, 541–554 (2009).

7. Schairer, D. O., Chouake, J. S., Nosanchuk, J. D. & Friedman, A. J. The potential of nitric oxide releasing therapies as antimicrobial agents. *Virulence* **3**, 271–279 (2012).

8. Paricio, L., Neufeld, B. & Reynolds, M. Combined influence of nitric oxide and surface roughness in biofilm reduction across bacteria strains. *Biointerphases* **14**, 21004 (2019).

9. Palmer, R. M. J., Ferrige, A. G. & Moncada, S. Nitric oxide release accounts for the biological activity of endothelium-derived relaxing factor. *Nature* **327**, 524–526 (1987).

10. Harding, J. L., Metz, J. M. & Reynolds, M. M. A Tunable, Stable, and Bioactive MOF Catalyst for Generating a Localized Therapeutic from Endogenous Sources. *Advanced Functional Materials* **24**, 7503–7509 (2014).

11. Neufeld, M. J., Lutzke, A., Jones, W. M. & Reynolds, M. M. Nitric Oxide Generation from Endogenous Substrates Using Metal–Organic Frameworks: Inclusion within Poly(vinyl alcohol) Membranes To Investigate Reactivity and Therapeutic Potential. *ACS Applied Materials & Interfaces* **9**, 35628–35641 (2017).

12. Harding, J. L. & Reynolds, M. M. Metal Organic Frameworks as Nitric Oxide Catalysts. *Journal of the American Chemical Society* **134**, 3330–3333 (2012).

13. Neufeld, M. J., Lutzke, A., Tapia, J. B. & Reynolds, M. M. Metal–Organic Framework/Chitosan Hybrid Materials Promote Nitric Oxide Release from S-Nitrosoglutathione in Aqueous Solution. *ACS Applied Materials & Interfaces* **9**, 5139–5148 (2017).

14. Neufeld, M. J., Ware, B. R., Lutzke, A., Khetani, S. R. & Reynolds, M. M. Water-Stable Metal–Organic Framework/Polymer Composites Compatible with Human Hepatocytes. *ACS Applied Materials & Interfaces* **8**, 19343–19352 (2016).

15. Neufeld, B. H. & Reynolds, M. M. Critical nitric oxide concentration for Pseudomonas aeruginosa biofilm reduction on polyurethane substrates. *Biointerphases* **11**, 31012 (2016).

16. Roberts, T. R. *et al.* A metal organic framework reduces thrombus formation and platelet aggregation ex vivo. *The journal of trauma and acute care surgery* **85**, 572–579 (2018).

17. Gorren, A. C. F., Schrammel, A., Schmidt, K. & Mayer, B. Decomposition ofS-Nitrosoglutathione in the Presence of Copper Ions and Glutathione. *Archives of Biochemistry and Biophysics* **330**, 219–228 (1996).

18. Singh, S. P., Wishnok, J. S., Keshive, M., Deen, W. M. & Tannenbaum, S. R. The chemistry of the S-nitrosoglutathione/glutathione system. *Proceedings of the National Academy of Sciences of the United States of America* **93**, 14428–14433 (1996).

19. Singh, R. J., Hogg, N., Joseph, J. & Kalyanaraman, B. Mechanism of Nitric Oxide Release from S-Nitrosothiols. *Journal of Biological Chemistry* **271**, 18596–18603 (1996).

20. Dicks, A. P. *et al.* Identification of Cu+ as the effective reagent in nitric oxide formation from S-nitrosothiols (RSNO). *Journal of the Chemical Society, Perkin Transactions 2* 481–487 (1996) doi:10.1039/P29960000481.

21. P. Dicks, A., Herves Beloso, P. & Lyn H. Williams, D. Decomposition of S-nitrosothiols: the effects of added thiols. *Journal of the Chemical Society, Perkin Transactions 2* 1429–1434 (1997) doi:10.1039/A701594A.

22. Askew, S. C., Barnett, D. J., McAninly, J. & Williams, D. L. H. Catalysis by Cu2+ of nitric oxide release from S-nitrosothiols (RSNO). *Journal of the Chemical Society, Perkin Transactions 2* 741–745 (1995) doi:10.1039/P29950000741.

23. Broniowska, K. A., Diers, A. R. & Hogg, N. S-nitrosoglutathione. *Biochimica et biophysica acta* **1830**, 3173–3181 (2013).

24. R. Noble, D., R. Swift, H. & Lyn H. Williams, D. Nitric oxide release from S-nitrosoglutathione (GSNO). *Chemical Communications* 2317–2318 (1999) doi:10.1039/A907891F.

25. Tsikas, D. *et al.* UPLC-MS/MS measurement of S-nitrosoglutathione (GSNO) in human plasma solves the S-nitrosothiol concentration enigma. *Journal of chromatography. B, Analytical technologies in the biomedical and life sciences* **927**, 147–157 (2013).

26. Luza, S. C. & Speisky, H. C. Liver copper storage and transport during development: implications for cytotoxicity. *The American journal of clinical nutrition* **63**, 812S–20S (1996).

27. Furukawa, H., Cordova, K. E., O'Keeffe, M. & Yaghi, O. M. The Chemistry and Applications of Metal-Organic Frameworks. *Science* **341**, 1230444 (2013).

28. Yang, D. & Gates, B. C. Catalysis by Metal Organic Frameworks: Perspective and Suggestions for Future Research. *ACS Catalysis* **9**, 1779–1798 (2019).

29. Zhang, R. *et al.* Improving laccase activity and stability by HKUST-1 with cofactor via one-pot encapsulation and its application for degradation of bisphenol A. *Journal of Hazardous Materials* **383**, 121130 (2020).

30. Al-Janabi, N. *et al.* Mapping the Cu-BTC metal–organic framework (HKUST-1) stability envelope in the presence of water vapour for CO2 adsorption from flue gases. *Chemical Engineering Journal* **281**, 669–677 (2015).

31. Furukawa, H., Müller, U. & Yaghi, O. M. “Heterogeneity within Order” in Metal–Organic Frameworks. *Angewandte Chemie International Edition* **54**, 3417–3430 (2015).

32. Gascon, J., Corma, A., Kapteijn, F. & Llabrés i Xamena, F. X. Metal Organic Framework Catalysis: Quo vadis? *ACS Catalysis* **4**, 361–378 (2014).

33. How many MOFs are there in the CSD? *Cambridge Crystallographic Data Centre* (2016).

34. Tan, W. *et al.* Electrostatic Interaction-Induced Formation of Enzyme-on-MOF as Chemo-Biocatalyst for Cascade Reaction with Unexpectedly Acid-Stable Catalytic Performance. *ACS Applied Materials & Interfaces* **11**, 36782–36788 (2019).

35. Cao, S.-L. *et al.* Novel Nano-/Micro-Biocatalyst: Soybean Epoxide Hydrolase Immobilized on UiO-66-NH2 MOF for Efficient Biosynthesis of Enantiopure (R)-1, 2-Octanediol in Deep Eutectic Solvents. *ACS Sustainable Chemistry & Engineering* **4**, 3586–3595 (2016).

36. Otto, T. *et al.* Effects of multivariate linker substitution, metal binding, and reactor conditions on the catalytic activity of a Pd-functionalized MOF for olefin hydrogenation. *Applied Catalysis A: General* **488**, 248–255 (2014).

37. Feng, X. *et al.* Size, Shape, and Porosity Control of Medi-MOF-1 via Growth Modulation under Microwave Heating. *Crystal Growth & Design* **19**, 889–895 (2019).

38. Qi, Z., Wang, L., You, Q. & Chen, Y. PA-Tb-Cu MOF as luminescent nanoenzyme for catalytic assay of hydrogen peroxide. *Biosensors and Bioelectronics* **96**, 227–232 (2017).

39. Ahmad, N. *et al.* Synthesis of 2D MOF having potential for efficient dye adsorption and catalytic applications. *Catalysis Science & Technology* **8**, 4010–4017 (2018).

40. García-García, P., Müller, M. & Corma, A. MOF catalysis in relation to their homogeneous counterparts and conventional solid catalysts. *Chemical Science* **5**, 2979–3007 (2014).

41. Gu, X., Lu, Z.-H., Jiang, H.-L., Akita, T. & Xu, Q. Synergistic Catalysis of Metal–Organic Framework-Immobilized Au–Pd Nanoparticles in Dehydrogenation of Formic Acid for Chemical Hydrogen Storage. *Journal of the American Chemical Society* **133**, 11822–11825 (2011).

42. Chen, X. *et al.* Tuning Zr12O22 Node Defects as Catalytic Sites in the Metal–Organic Framework hcp UiO-66. *ACS Catalysis* **10**, 2906–2914 (2020).

43. Behrens, M. *et al.* The Active Site of Methanol Synthesis over Cu/ZnO/Al₂O₃ Industrial Catalysts. *Science* **336**, 893 LP – 897 (2012).

44. Danilina, N., Krumeich, F., Castelanelli, S. A. & van Bokhoven, J. A. Where Are the Active Sites in Zeolites? Origin of Aluminum Zoning in ZSM-5. *The Journal of Physical Chemistry C* **114**, 6640–6645 (2010).

45. R Tuttle, R., J Folkman, S., N Rubin, H., G. Finke, R. & M. Reynolds, M. Copper Metal–Organic Framework Surface Catalysis: Catalyst Poisoning, IR Spectroscopic, and Kinetic Evidence Addressing the Nature and Number of the Catalytically Active Sites En Route to Improved Applications. *ACS Applied Materials & Interfaces* **0**, (2020).

46. Hoffman, R., Minkin, V. I. & Carpenter, B. K. Ockham's Razor and Chemistry. *International Journal for Philosophy of Chemistry* **3**, 3–28 (1997).

47. Wu, H. *et al.* Unusual and Highly Tunable Missing-Linker Defects in Zirconium Metal–Organic Framework UiO-66 and Their Important Effects on Gas Adsorption. *Journal of the American Chemical Society* **135**, 10525–10532 (2013).

48. Kaur, G. *et al.* Controlling the Synthesis of Metal–Organic Framework UiO-67 by Tuning Its Kinetic Driving Force. *Crystal Growth & Design* **19**, 4246–4251 (2019).

49. Xiao, D. J., Oktawiec, J., Milner, P. J. & Long, J. R. Pore Environment Effects on Catalytic Cyclohexane Oxidation in Expanded Fe2(dobdc) Analogues. *Journal of the American Chemical Society* **138**, 14371–14379 (2016).

50. Metzger, E. D., Comito, R. J., Hendon, C. H. & Dincă, M. Mechanism of Single-Site Molecule-Like Catalytic Ethylene Dimerization in Ni-MFU-4l. *Journal of the American Chemical Society* **139**, 757–762 (2017).

51. Bayram, E. & Finke, R. G. Quantitative 1,10-Phenanthroline Catalyst-Poisoning Kinetic Studies of Rh(0) Nanoparticle and Rh4 Cluster Benzene Hydrogenation Catalysts: Estimates of the Poison Kassociation Binding Constants, of the Equivalents of Poison Bound and of the Number of Cata. *ACS Catalysis* **2**, 1967–1975 (2012).

52. Hornstein, B. J., Aiken, J. D. & Finke, R. G. Nanoclusters in Catalysis: A Comparison of CS2 Catalyst Poisoning of Polyoxoanion- and Tetrabutylammonium-Stabilized 40 ± 6 Å Rh(0) Nanoclusters to 5 Rh/Al2O3, Including an Analysis of the Literature Related to the CS2 to Metal Stoichiometry Issue. *Inorganic Chemistry* **41**, 1625–1638 (2002).

53. Bayram, E. *et al.* Is It Homogeneous or Heterogeneous Catalysis Derived from [RhCp*Cl2]2? In Operando XAFS, Kinetic, and Crucial Kinetic Poisoning Evidence for Subnanometer Rh4 Cluster-Based Benzene Hydrogenation Catalysis. *Journal of the American Chemical Society* **133**, 18889–18902 (2011).

54. Bayram, E. *et al.* Mononuclear Zeolite-Supported Iridium: Kinetic, Spectroscopic, Electron Microscopic, and Size-Selective Poisoning Evidence for an Atomically Dispersed True Catalyst at 22 °C. *ACS Catalysis* **2**, 1947–1957 (2012).

55. Tuttle, R. R., Rubin, H. N., Rithner, C. D., Finke, R. G. & Reynolds, M. M. Copper ion vs copper metal–organic framework catalyzed NO release from bioavailable S-Nitrosoglutathione en route to biomedical applications: Direct 1H NMR monitoring in water allowing identification of the distinct, true reaction stoichiometries and thio. *Journal of Inorganic Biochemistry* **199**, 110760 (2019).

56. Simpson, A. J. & Brown, S. A. Purge NMR: Effective and easy solvent suppression. *Journal of Magnetic Resonance* **175**, 340–346 (2005).

57. Choi, L.-S. & Bayley, H. S-Nitrosothiol Chemistry at the Single-Molecule Level. *Angewandte Chemie International Edition* **51**, 7972–7976 (2012).

58. Roy, B., du Moulinet d'Hardemare, A. & Fontecave, M. New Thionitrites: Synthesis, Stability, and Nitric Oxide Generation. *The Journal of Organic Chemistry* **59**, 7019–7026 (1994).

59. Broniowska, K. A., Diers, A. R. & Hogg, N. S-nitrosoglutathione. *Biochimica et biophysica acta* **1830**, 3173–3181 (2013).

60. Baciu, C., Cho, K.-B. & Gauld, J. W. Influence of Cu+ on the RS-NO bond dissociation energy of S-nitrosothiols. *The journal of physical chemistry. B* **109**, 1334–1336 (2005).

61. Williams, D. L. H. The Chemistry of S-Nitrosothiols. *Accounts of Chemical Research* **32**, 869–876 (1999).

62. Tuttle, R. R., Daly, R. E., Rithner, C. D. & Reynolds, M. M. Monitoring a MOF Catalyzed Reaction Directly in Blood Plasma. *ACS Applied Materials & Interfaces* (2021) doi:10.1021/acsami.1c08917.

63. Pocius, P. A., Clark, J. H. & Baumrucker, C. R. Glutathione in Bovine Blood: Possible Source of Amino Acids for Milk Protein Synthesis. *Journal of Dairy Science* **64**, 1151–1154 (1981).

64. Stone, W. H. The Relation of Human and Cattle Blood Groups. *Transfusion* **2**, 172–177 (1962).

65. de Graaf, R. A. & Behar, K. L. Quantitative 1H NMR Spectroscopy of Blood Plasma Metabolites. *Analytical Chemistry* **75**, 2100–2104 (2003).

66. Amin, T. M. & Sirs, J. A. The Blood Rheology of Man and Various Animal Species. *Quarterly Journal of Experimental Physiology* **70**, 37–49 (1985).

67. Nicholson, J. K., Foxall, P. J. D., Spraul, Manfred., Farrant, R. Duncan. & Lindon, J. C. 750 MHz 1H and 1H-13C NMR Spectroscopy of Human Blood Plasma. *Analytical Chemistry* **67**, 793–811 (1995).

68. Bligh, S. W. A., Boyle, H. A., Mcewen, A. B., Sadler, P. J. & Woodham, R. H. 1H NMR studies of reactions of copper complexes with human blood plasma and urine. *Biochemical Pharmacology* **43**, 137–145 (1992).

69. Pietraforte, D., Mallozzi, C., Scorza, G. & Minetti, M. Role of thiols in the targeting of S-nitroso thiols to red blood cells. *Biochemistry* **34**, 7177–7185 (1995).

70. Tuttle, R. R. ; D. R. E. ; R. C. D. ; R. M. M. Monitoring a MOF Catalyzed Reaction Directly In Blood Plasma. *ACS Applied Materials & Interfaces Just Accepted* (2021).

71. Huang, Y. *et al.* Size, separation, structural order, and mass density of molecules packing in water and ice. *Scientific Reports* **3**, 3005 (2013).

72. Thiele, E. W. Relation between Catalytic Activity and Size of Particle. *Industrial & Engineering Chemistry* **31**, 916–920 (1939).

73. Zhao, Y. H., Abraham, M. H. & Zissimos, A. M. Fast Calculation of van der Waals Volume as a Sum of Atomic and Bond Contributions and Its Application to Drug Compounds. *The Journal of Organic Chemistry* **68**, 7368–7373 (2003).

74. Wicholas, Mark. & Wolford, Thomas. Stable cyanide complexes of copper(II). *Inorganic Chemistry* **13**, 316–318 (1974).

75. Reisfeld, M. J. & Jones, L. H. Raman Spectra of Some Cyanide Complexes of Copper. *Journal of Molecular Spectroscopy* **18**, 222–226 (1965).

76. Chantry, G. W. & Plane, R. A. CN Stretching Bands in the Raman Spectra of Some Group Ib and Group IIb Compex Cyanides. *The Journal of Chemical Physics1* **33**, 736–739 (1960).

77. Penneman, R. A. & Jones, L. H. Infrared Absorption Studies of Aqueous Complex Ions. II. Cyanide Complexes of Cu(I) in Aqueous Solution. *The Journal of Chemical Physics* **24**, 293–296 (1956).

78. Jones, L. H. Vibrational Spectrum and Structure of Metal-Cyanide Complexes in the Solid State. IV. K3Cu(CN)4. *The Journal of Chemical Physics* **29**, 463–466 (1958).

79. Dincă, M. & Long, J. R. High-Enthalpy Hydrogen Adsorption in Cation-Exchanged Variants of the Microporous Metal−Organic Framework Mn3[(Mn4Cl)3(BTT)8(CH3OH)10]2. *Journal of the American Chemical Society* **129**, 11172–11176 (2007).

80. Demessence, A., D'Alessandro, D. M., Foo, M. L. & Long, J. R. Strong CO2 Binding in a Water-Stable, Triazolate-Bridged Metal−Organic Framework Functionalized with Ethylenediamine. *Journal of the American Chemical Society* **131**, 8784–8786 (2009).

81. Dincă, M. *et al.* Observation of Cu2+–H2 Interactions in a Fully Desolvated Sodalite-Type Metal–Organic Framework. *Angewandte Chemie International Edition* **46**, 1419–1422 (2007).

82. Bligaard, T. *et al.* Toward Benchmarking in Catalysis Science: Best Practices, Challenges, and Opportunities. *ACS Catalysis* **6**, 2590–2602 (2016).

83. Kao, P.-T., Lee, I.-J., Liau, I. & Yeh, C.-S. Controllable NO release from Cu(1.6)S nanoparticle decomposition of S-nitrosoglutathiones following photothermal disintegration of polymersomes to elicit cerebral vasodilatory activity. *Chemical science* **8**, 291–297 (2017).

II. COPPER ION VS COPPER METAL-ORGANIC FRAMEWORK CATALYZED NO RELEASE FROM BIOAVAILABLE S-NITROSOGLUATHIONE EN ROUTE TO BIOMEDICAL APPLICATIONS: DIRECT ^{1}H NMR MONITROING IN WATER ALLOWING IDENTIFICATION OF THE DISTINCT, TRUE REACTION STOICHIOMETRIES AND THIOL DEPENDENCIES[1]

Overview

Copper containing compounds catalyze the decomposition of *S*-Nitrosoglutathione (GSNO) in the presence of glutathione (GSH) to yield glutathione disulfide (GSSG) and nitric oxide (NO). Long term NO generation from an endogenous source is medically desirable to achieve vasodilation, reduction in biofilm formation on implanted medical devices, antibacterial activity, and other physiologically relevant effects. Homogeneous and heterogeneous copper species have been used to catalyze decomposition of endogenous GSNO for NO release. One heterogeneous catalyst used for GSNO decomposition in blood plasma is the metal-organic framework (MOF), $H_3[(Cu_4Cl)_3$-$(BTTri)_8$, H_3BTTri = 1,3,5-tris(^{1}H-1,2,3-triazol-5-yl) benzene] (CuBTTri). Fundamental questions about these catalytic systems remain unanswered, despite their use in biomedical applications, in part because no method has been developed previously for the simultaneous tracking of [GSNO], [GSH], and [GSSG] in water. Development of a technique to track these reactions in water is a necessary step towards study in biological media as blood is comprised of ca. 80% water, and NO release systems must eventually operate in blood. Even the true, balanced reaction stoichiometry remains unknown for copper-ion and CuBTTri catalyzed

[1] The work presented in Chapter II contains the entire published manuscript describing our first published work investigating the CuBTTri/NO/GSNO system (Tuttle, R. R.; Rubin, H. N.; Rithner, C. D.; Finke, R. G.; Reynolds, M. M. *J. Inorg. Biochem.* **2019**, *199*, No. 110760.). Minor formatting edits have been introduced to meet the dissertation requirements.

GSNO decomposition. Herein, we report a direct ^{1}H NMR method which: (i) allows simultaneous monitoring of [GSNO], [GSH], and [GSSG] in water; (ii) provides the experimentally determined, balanced reaction stoichiometry for copper-ion vs CuBTTri catalyzed GSNO decomposition; (iii) reveals that the CuBTTri-catalyzed reaction reaches only 10% GSNO decomposition in 16h without added GSH, yet the copper-ion catalyzed reaction reaches 100% GSNO decomposition within 16h without added GSH; and (iv) shows that 100% GSNO decomposition can be achieved upon addition of stoichiometric GSH to the CuBTTri catalyzed reaction. Importantly, (v) these observations provide compelling evidence that copper-ion and CuBTTri catalyzed GSNO decomposition in water operate through different reaction mechanisms, the details of which can now be probed by direct, ^{1}H NMR kinetics and other needed studies.

2.1 Introduction

Generation of NO carries great importance in medicine as NO is a vital signaling molecule in the human nervous,[1,2] immune,[3,4] and cardiovascular[5,6] systems, as well as an effective antibacterial agent.[7,8] *S*-Nitrosothiols (RSNOs)[9] such as *S*-Nitrosoglutathione (GSNO) have attracted attention as endogenous sources of NO, GSNO being of particular importance due to its presence in human blood.[10,11] One equivalent of NO is known to form per equivalent of GSNO decomposed along with disulfide (RSSR) formation.[12,13] Long-term NO generation for biomedical applications is desirable[14,15] and can be achieved by pairing an endogenous NO source such as GSNO with a catalyst that induces GSNO decomposition *in water* rather than organic solvents where RSNO decompositions have been studied. For example, the study of homogeneous copper model complexes in organic solvents such as dichloromethane[16] and toluene[17] have appeared. Relevant here is that water is an important solvent for RSNO studies given that blood is ca. 80% water, and blood is where NO release is important for applications under development.[18]

Copper-containing compounds are an important family of RSNO decomposition catalysts. Solvated Cu^{2+} is the most commonly studied copper ion pre-catalyst for RSNO conversion.[19] Reduction of Cu^{2+} to Cu^{+} is hypothesized as a necessary step in the reaction mechanism.[20] Thiols (RSH) have been used as reducing agents at sub stoichiometric concentrations to initiate the catalytic cycle and increase the rate of copper ion catalyzed RSNO decomposition.[21] Thiols are thought to play a dual role in these systems, as reducing agents to generate Cu^{+}, and as complexing agents for Cu^{2+}.[21,22] Interestingly, stoichiometric levels of RSH have been observed to *halt* copper-ion catalyzed RSNO decomposition, perhaps because of Cu^{2+} complexation by the corresponding thiolate (RS^{-}).[21,22] While extensive work done on copper-ion catalyzed RSNO conversion to NO has resulted in valuable insights,[16,17,20–24] even just the complete, balanced reaction stoichiometry for copper-ion catalyzed RSNO decomposition has not been experimentally determined, neither in the presence nor absence of added RSH. Of course, determination of the true reaction stoichiometry under the actual reaction conditions is *the necessary starting point* for any rigorous mechanistic study because the proposed mechanistic steps must, in turn, sum to the experimentally determined reaction stoichiometry. Without the true stoichiometry, one runs the risk of reporting the "mechanism" for a different reaction than is actually being investigated.

Due to the potentially toxic nature of freely diffusing copper ions in vitro, incorporation of copper ions into a solid support material for biomedical applications is desired.[25–28] Copper containing metal-organic frameworks (MOFs) are a class of porous solid materials containing organic linkers and copper cations that have been used to catalyze NO release from RSNO precursors.[12,13] The two copper based MOFs previously used in this regard are copper (II) benzene-1,3,5-tricarboxylate (Cu-BTC), and $H_3[(Cu_4Cl)_3$-$(BTTri)_8$, H_3BTTri = 1,3,5-tris(1*H*-1,2,3-triazol-5-yl) benzene] (CuBTTri), Figure 2.1. Of these two, CuBTTri is attractive for incorporation into

biomedical devices such as stents, catheters, and extracorporeal circuitry[29] because of its hydrothermal stability, its ability to catalyze GSNO decomposition in aqueous solutions, and because CuBTTri materials are compatible with human hepatocytes.[30]

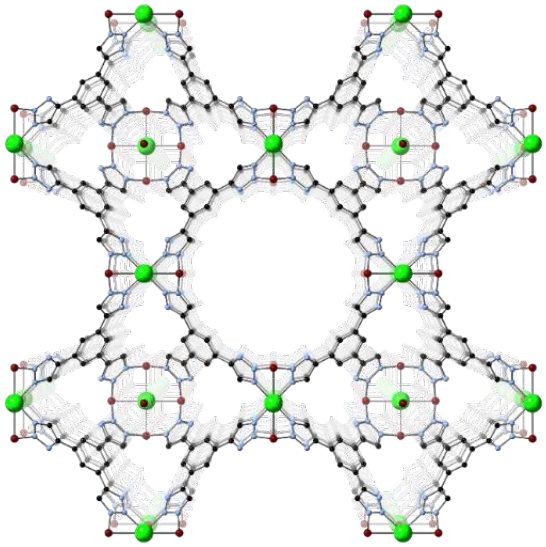

Figure 2.1. One plausible CuBTTri subunit structure.[42] Shown are carbon (black), nitrogen (blue), chlorine (green), and copper (red). The open channels formed in CuBTTri may allow for diffusion of GSNO substrate into MOF pores via the largest, central channel. Open copper sites both at the surface and inside the CuBTTri pores are the plausible, expected active sites for GSNO binding and catalysis for NO release.

Important prior work is available testing CuBTTri as a catalyst material for endogenous NO generation.[13,18,30] Although CuBTTri catalyzed decomposition of GSNO is known to produce NO, the formation of glutathione disulfide (GSSG) has not yet been experimentally confirmed—nor has the complete reaction stoichiometry been experimentally determined for any copper MOF system. Additionally, the effect(s) and fate of added glutathione (GSH) in the CuBTTri MOF-catalyzed NO release reaction have not been explored, an important point given the apparent importance of thiols to the copper-ion system.

The reason these basic pieces of information about copper MOF systems and their NOR release catalysis are missing is because no method enabling the *simultaneous, direct monitoring* of [GSNO], [GSH], and [GSSG] *in water* has been reported.[31] The previously proposed

stoichiometry[12–14,17,25–27,32] for both systems, Figure 2.1, is widely accepted, *but has actually never been experimentally verified*. RSNO decomposition catalyzed by solvated copper ions and CuBTTri have been traditionally studied via either ultraviolet-visible (UV-VIS) spectroscopy (via the intensity of a peak at 335 nm caused by a $\pi \rightarrow \pi^*$ transition in the S-N bond of the RSNO) or nitric oxide analyzers (NOAs)[12,13] to track NO release.[33,34] NOA experiments use chemiluminescence to quantify the amount of gaseous NO generated.[35] NOAs and UV-visible monitor only the concentration of one chemical species in the complex reaction mixture and hence, are unable to determine the true, balanced reaction stoichiometry. Specifically, the amount of GSSG formed per amount of GSNO decomposed has never been previously determined in either the CuBTTri or the copper-ion system—and we demonstrate herein that the prior, assumed stoichiometry in Figure 2.2 is not precisely correct. This in turn means that the prior mechanistic details for RSNO conversion to NO and the other products of the reaction cannot be exactly correct.

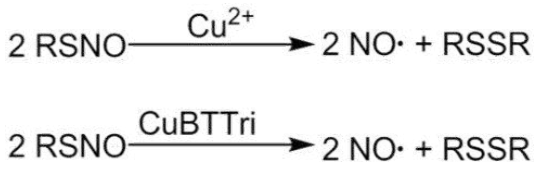

Figure 2.2. Idealized[12,14,15,17,25–27] stoichiometry for copper catalyzed decomposition of GSNO.

Herein, we report that solvent-suppressed ^{1}H nuclear magnetic resonance (^{1}H NMR) spectroscopy provides the needed ability to monitor GSNO decomposition catalyzed by either copper ion or CuBTTri in the blood-and hence biomedical applications-relevant solvent, *water*. Direct, simultaneous, and reliable quantification of [GSNO], [GSH], and [GSSG] in water is reported for the first time. Hydrogen bonding of RSNOs to water may, for example, account for part of RSNO *in vivo* stability.[36,37] We also compare copper-ion vs CuBTTri catalyzed release of

NO from GSNO, an important[38] comparison by our direct ^{1}H NMR methodology given that copper ions are currently the most efficient copper pre-catalyst for NO release from GSNO.[12,13,28]

2.2 Results and Discussion

^{1}H NMR of the Individual Reaction Components

Despite their structural similarities, each individual reaction component, GSNO, GSH, and GSSG, proved to contain distinguishable ^{1}H NMR signals, in 20 mM NaH_2PO_4 buffered 90% H_2O 10% D_2O, Figure 2.3. Specifically, GSSG displays two doublets of doublets at 3.15–3.19 ppm and 2.84–2.89 ppm identified as the protons on the carbon adjacent to the sulfur groups. GSH displays a multiplet at 4.40–4.48 ppm associated with the C-H two carbons away from the sulfur group and a multiplet at 2.80–2.88 ppm attributed to the protons adjacent to the sulfur group. The two protons on the carbon adjacent to the sulfur group in GSNO appear as two distinctly broad peaks at 4.00–4.03 ppm and 3.85–3.89 ppm. All individual peaks that were used for determining the concentration of reaction components are identified with boxes in Figure 2.3.

Initial attempts to determine reaction species concentration used benzene as an internal quantitative standard, but the significant difference in longitudinal relaxation time, T_1, among various reaction components and benzene protons afforded a large error under the conditions necessary for data acquisition. In response, efforts were directed to quantify the individual reaction components in solution directly by developing an absolute calibration curve based on known concentrations of authentic GSNO, GSH, and GSSG. The intensity of the signals used to quantify GSNO and GSH were affected by the solvent suppression method due to their proximity to the water peak. However, the magnitude of this effect was stable and consistent from experiment-to-experiment over a concentration range from 500 μM to 3 mM. Hence, the necessary calibration curves were generated using 4 different concentrations for each component (500 μM, 1 mM, 2

mM, and 3mM). A calibration curve was constructed whereby the intensity of the highest peak within the boxed regions shown in Figure 2.3 was plotted on the y-axis and concentration plotted on the x-axis (Appendix I, Figures S2.7-S2.9). A linear fit was applied yielding the following equations where y is signal intensity and x is species concentration (in mmol/L), all fits having R^2 values greater than 0.99:

$$[\text{GSNO}]: y = 28.4x - 2.05 \qquad \text{(eq. 2.1)}$$

$$[\text{GSH}]: y = 138x - 17.5 \qquad \text{(eq. 2.2)}$$

$$[\text{GSSG}]: y = 368x + 223 \qquad \text{(eq. 2.3)}$$

Buffering the system with NaH_2PO_4 for NMR analysis was critical to prevent peak broadening and unwanted competing reaction pathways that could arise from minor differences in pH. DMSO was also examined as a possible solvent, but proved inferior to water as it either prevented any decomposition or yielded unwanted oxidization of GSH to GSSG.[39] In short, a direct method has been developed that allows the quantitative analysis of the reactions of CuBTTri and Cu^{2+} with the biologically relevant GSNO, *all in water* as a preferred solvent, and which can simultaneously detect each of the reactions' starting material and products (other than NO, which is detected separately, *vide infra*) GSNO, GSH, and GSSG.

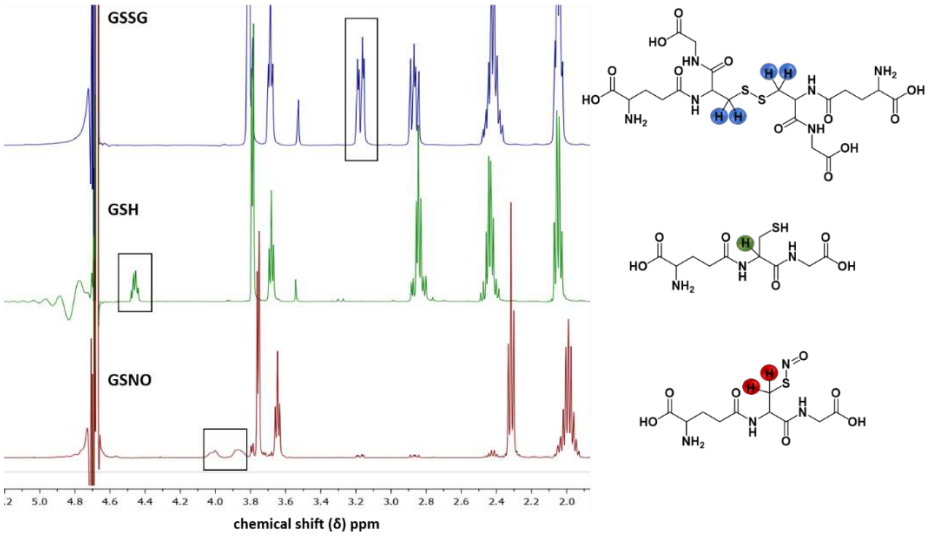

Figure 2.3. Structures and diagnostic peaks used for ^{1}H-NMR analysis of GSH (green), GSNO (red), and GSSG (blue) in 0.5 mL H_2O and 0.1 mL 20 mM NaH_2PO_4 buffered D_2O.

Cu^{2+} Pre-catalyst GSNO Decomposition, First *Without* Added GSH

With a reliable, quantitative ^{1}H NMR technique to monitor [GSNO], [GSH], and [GSSG], the ostensibly simplest, solvated copper-ion catalyzed decomposition of GSNO was investigated first, under N_2 (g) as noted in the Experimental section. Entry 2 in Table 2.1 summarizes the results of the reaction between GSNO (1 mM) and Cu^{2+} (0.2 mM) in water over 16 h *with no added GSH*. Complete decomposition of GSNO was observed within 16 h, as shown in Figure 2.5. The only detectable products by ^{1}H NMR from the conversion of GSNO are GSSG and what matches a GSSG-Cu^{2+} chelate complex (also previously reported in the literature by Noble et al, Kenche et al, and Gorren et al.[22,40,41] shown in boxes in Figure 2.5, right and left, respectively.

The amount of GSSG formed was quantified using the previously described calibration curves, while the concentration of the chelate complex was determined via the relative peak integrations between the GSSG signal and the GSSG-Cu^{2+} complex signal. Together, these two concentrations sum to $[GSSG]_{Total}$, which in turn is equal to half of the initial [GSNO] within experimental error, as expected based on mass balance. The chelate complex exhibits the same splitting pattern as GSSG, with shifts further downfield (3.40-3.58 ppm) upon chelation of GSSG

to Cu^{2+} ions, Figure 2.5. Furthermore, formation of a GSSG-Cu^{2+} chelate complex is supported by the observation that as the initial [Cu^{2+}] is increased, the relative concentration of the chelate complex increases rather than GSSG, as shown by the red trace in Figure 2.5. The net reaction stoichiometry is shown in Figure 2.4:

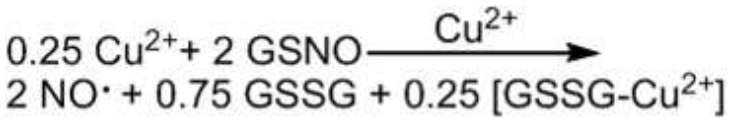

Figure 2.4. Reaction stoichiometry for Cu^{2+} (0.2 mM) catalyzed release of NO from GSNO (1 mM) *without added GSH*.

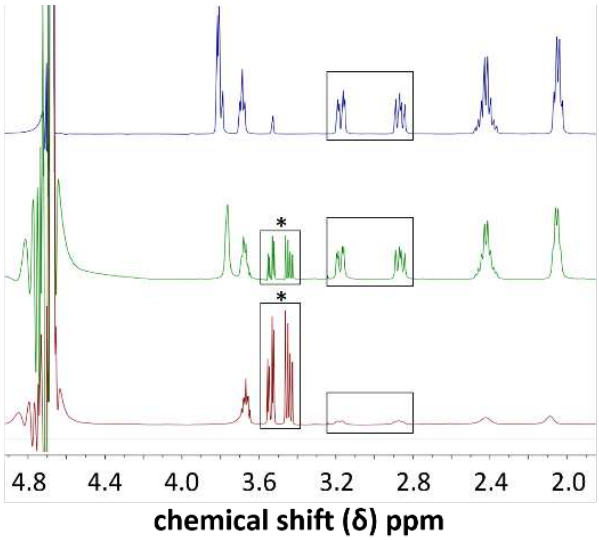

Figure 2.5. Blue: GSSG (2 mM) in H_2O. Decomposition of GSNO (1 mM) with Cu^{2+} (0.2 mM, green), (1 mM, red) in H_2O over 16 h. *Indicates a GSSG-Cu^{2+} complex.

Table 2.1. Concentration values (expressed in mmol/L) for reactants and products in the Cu^{2+} catalyzed system initially at 0 h and then after 16 h. All values at 16 h represent the average of three trials with standard deviation.

Entry	Initial Conditions, T=0h				T=16h				
	$[GSH]_{Added}$	[GSNO]	$[Cu^{2+}]$	[NO]	[GSH]	[GSNO]	$[GSSG]_{Total}$	[NO]	% loss GSNO
1	0.04	1.0	0	0	N/A	1.0±0.01	0±0.05	0	0
2	0	1.0	0.2	0	N/A	0	0.5±0.1	1.0±0.1	100
3	0.04	1.0	1.0	0	N/A	0	0.4±0.1	1.0±0.1	100
4	1.0	1.0	0.2	0	1.0	0.75±0.1	0.2±0.1	0.25±0.1	25

Of note here is that the ^1H NMR demonstrated stoichiometry in Figure 2.4 deviates from the previously hypothesized, idealized stoichiometry, Figure 2.2, in that 25% of the "RS•" by-product of NO release from GSNO winds up as GSSG-Cu^{2+}, that is, GSSG bound to Cu^{2+}. Overall, the observed reaction stoichiometry in Figure 2.4 is the first time the amount of GSSG and GSSG-Cu^{2+} formed have been quantified for copper-ion catalyzed GSNO decomposition towards release of NO.

Cu^{2+} Pre-catalyst GSNO Release of NO, *With* Added GSH

As noted in the Experimental section, the GSNO sample used herein is determined to be 97 ± 2% pure by UV-VIS spectroscopy (Appendix I, Table S2.1 and Figure S2.4). However, the literature suggests that small (≤5%) impurity of GSH present in all GSNO samples (leftover from the synthesis) could be sufficient to initiate the reaction via reduction of Cu^{2+} to Cu^{+}. Hence, this small GSH impurity could be critical to NO release catalysis, at least for the case of Cu^{2+}.

To probe the possible importance of GSH on the reaction, NO release from GSNO under Cu^{2+} pre-catalyst conditions was probed with 0.04 and then 1.0 equivalents of added GSH per equivalent of GSNO. The results are given in Table 2.1 entries 3 and 4, and Figures 2.6 and 2.7. A control showing no GSNO conversion over 16 h if Cu^{2+} is omitted (and with 0.04 equivalents GSH added) is summarized in Entry 1 of Table 2.1 and the resulting ^1H NMR is shown in Appendix I (Figure S2.11). The addition of sub-stoichiometric levels of GSH (1:5 ratio of

[GSH]:[Cu^{2+}]) did not prevent the reaction from reaching completion within 16 h (Entry 3, Table 2.1), in agreement with previous reports. The only products detectable by ^{1}H NMR are GSSG and the GSSG-Cu^{2+} chelate complex, as shown in Figure 2.6. The total concentration of GSSG containing species is equal to half of the initial [GSNO] within experimental error, as summarized in the stoichiometry reported in Figure 2.7.

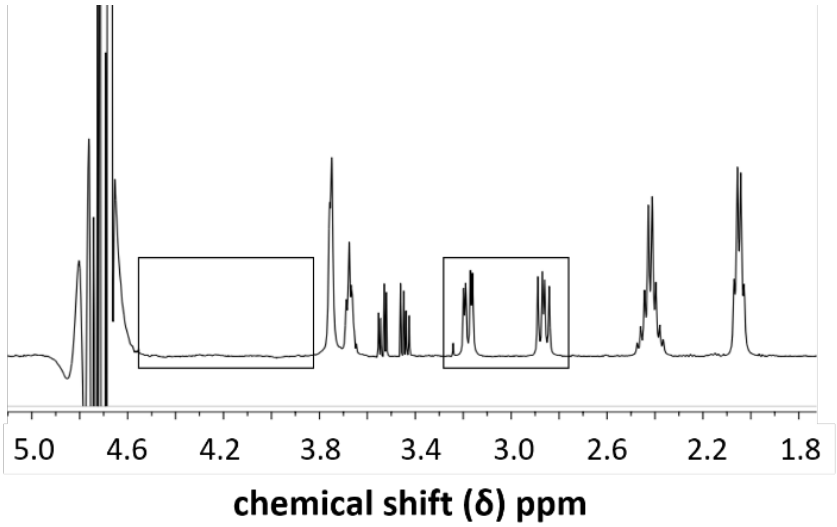

Figure 2.6. GSNO (1 mM) reaction in the presence of Cu^{2+} ions (0.2 mM) and GSH (0.04 mM) in H_2O after 16 h.

$$0.25\ Cu^{2+} + 2\ GSNO \xrightarrow{Cu^{2+},\ GSH} 2\ NO^{\cdot} + 0.75\ GSSG + 0.25\ [GSSG\text{-}Cu^{2+}]$$

Figure 2.7. Observed stoichiometry for Cu^{2+} (0.2 mM) catalyzed release of NO from GSNO (1 mM) with added sub stoichiometric GSH (0.04 mM).

On the other hand, the introduction of stoichiometric GSH (vs the amount of GSNO) to the reaction system, resulting in a 5:1 ratio of [GSH]:[Cu^{2+}], led to an incomplete reaction after 16 h (Appendix I, Figure S2.14). Excess GSH has previously been reported to halt GSNO decomposition, potentially via competitive complexation of Cu^{2+} and/or Cu^{+} ions by the carboxylate or thiolate of GSH, rendering the ions inactive for GSNO decomposition, Table 2.1, Entry 4 (Figure 2.8).[20–22,40,42] Our direct ^{1}H NMR- determined results on Cu^{2+} catalysis at various

[GSH] are, then, fully consistent with the prior literature in that sub-stoichiometric (0.04 mM) levels of GSH do not poison Cu^{2+} catalysis while stoichiometric (1mM) levels do .

Table 2.2. Concentration values (expressed in mmol/L) for reactants and products in the CuBTTri catalyzed system initially at 0 h and then after 16 h. All values at 16 h represent the average of three trials with standard deviation.

Entry	Initial Conditions, T=0h				T=16h				
	$[GSH]_{Added}$	[GSNO]	CuBTTri**	[NO]	[GSH]	[GSNO]	[GSSG]	[NO]	% loss GSNO
1	0	2.0	0.015	0	0	1.9±0.1	0±0.1	0.1±0.1	10
2	2.0	2.0	0.015	0	1.7±0.1	0	0.9±0.1	2.0	100

**Value expressed in mmol. Due to the heterogeneous nature of the MOF pre-catalyst the appropriate mass was added to yield a 2:1 ratio of GSNO molecules to copper MOF atoms to achieve catalytic conditions.

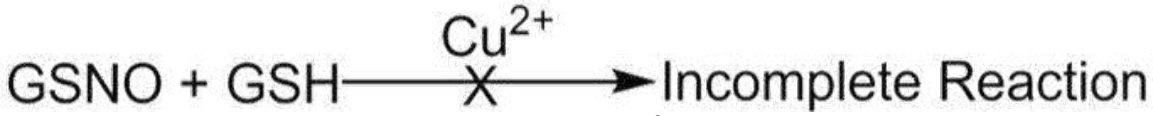

Figure 2.8. Observed, incomplete reaction between Cu^{2+} (0.2 mM) and GSNO (1 mM) with added *stoichiometric* GSH (1 mM).

CuBTTri Pre-catalyst GSNO to NO Conversion Catalysis, First *Without* Added GSH

Next, the CuBTTri catalyzed release of NO from GSNO was examined by ^1H NMR, first with no added GSH. All experiments were carried out with a 2:1 ratio of GSNO-to-copper centers in the MOF. Reaction supernatant and MOF samples used for the experiments were saved to test for framework stability over the course of the reaction.

Figure 2.9 depicts a ^1H NMR spectrum of the reaction between CuBTTri and GSNO (2 mM) in water taken at 16 h where the boxed peaks correspond to the unreacted GSNO on the left and GSSG product on the right. Entry 1 in Table 2.2 summarizes the results of the reaction after 16 h: the system did not reach completion, and instead resulted in only 10% GSNO decomposition. The resulting GSNO conversion stoichiometry is shown in Figure 2.9.

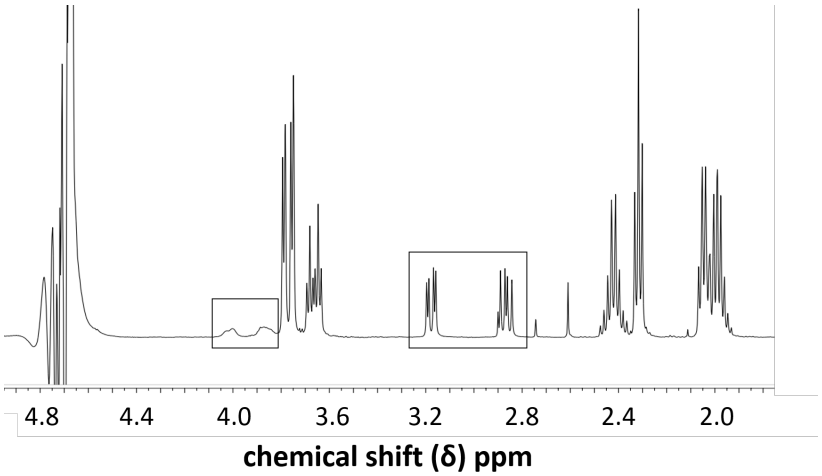

Figure 2.9. GSNO (2 mM) conversion after 16 h in the presence of CuBTTri in H_2O at a ratio of 2:1 mol GSNO:mol Cu atoms in the MOF sample.

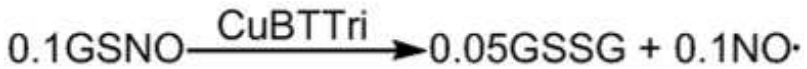

Figure 2.10. Observed, incomplete reaction between GSNO (2 mM) and CuBTTri *without added GSH.*

Clearly the low level of GSH inherently present in the GSNO samples is insufficient to activate CuBTTri for complete GSNO decomposition. This result is quite different than the reactions with Cu^{2+} ions, that went to 100% completion under analogous conditions (vide supra). Given the literature hypothesis that Cu^{+} is necessary for copper-ion catalyzed GSNO decomposition, it seemed prudent to introduce additional GSH in an attempt to activate the MOF pre-catalyst for GSNO decomposition, so those experiments were performed next.

CuBTTri Catalyzed GSNO to NO Conversion, *With* Added GSH

The next system examined was a CuBTTri catalyzed reaction in which a stoichiometric equivalent of GSH (2 mM) was added to a reaction mixture containing GSNO (2 mM) and CuBTTri in water, then examined after 16 h. Complete GSNO decomposition is observed within 16 h and GSSG is the only product detectable by ^{1}H NMR, Figure 2.11. One equivalent of GSSG is formed per two equivalents of GSNO decomposed. The resultant stoichiometry is reported in Figure 2.12, and the overall tabulated results are provided in Entry 2 of Table 2.2.

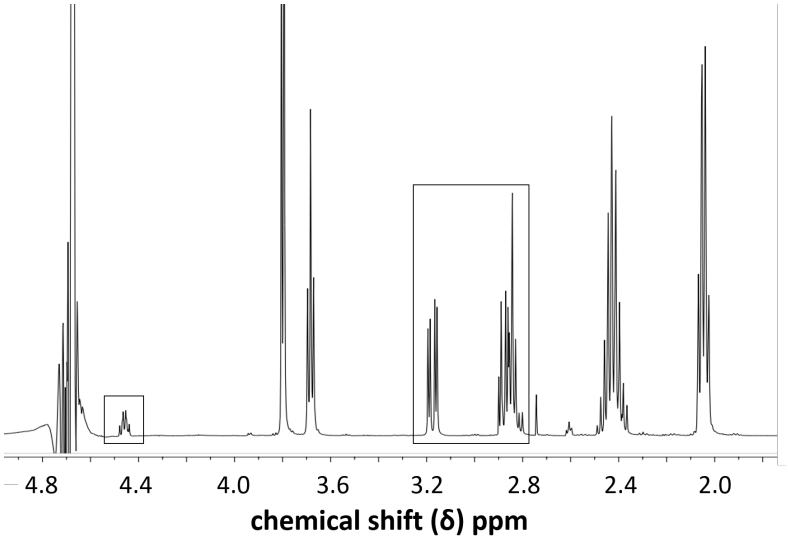

Figure 2.11. Conversion of GSNO (2 mM) in the presence of GSH (2 mM) and CuBTTri in H_2O over 16 h with 2:1 mol GSNO:mol Cu in the MOF sample.

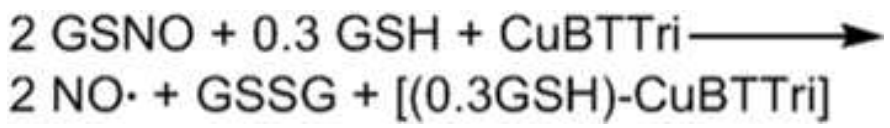

Figure 2.12. Observed stoichiometry for CuBTTri catalyzed GSNO (2 mM) decomposition with added *stoichiometric* GSH (2 mM).

Of considerable interest in the CuBTTri catalyzed reaction, and vs its Cu^{2+} ion counterpart, is that c*omplete GSNO decomposition is observed* even in the presence of stoichiometric GSH over 16 h. That is, unlike copper ions, *the active sites in CuBTTri are not deactivated by the introduction of stoichiometric GSH*. Moreover, the requirement for GSH is sub stoichiometric in the CuBTTri system, only 15% of the added 1.0 equivalent (0.3 equivalents in Figure 2.12 vs 2 GSNO) being consumed at the end of the full GSNO conversion and NO release reaction. Leftover GSH is shown in Figure 2.11 in the left-most box. A control experiment with no CuBTTri present was performed to ensure that observed reactivity was not solely induced by GSH.[43,44] No reaction within experimental error between GSNO (2 mM) and GSH (2 mM) over 14 h is observed in the absence of CuBTTri (Appendix I, Figure S2.12) supporting the hypothesis that CuBTTri is a necessary pre-catalyst, along with the GSH.

The sub-stoichiometric GSH requirement again looks to be involved in the activation of the Cu catalyst (in this case CuBTTri), since entry 1 of Table 2.2 shows only 10% reaction in the absence of added GSH. Indeed, one hypothesis is that the 0.3 GSH is activating (reducing, hence "titrating") a 0.3 fraction of Cu sites in the CuBTTri pre-catalyst (Figure 2.1, vide supra). Figure 2.12 is written to reflect this hypothesis, specifically presently as "[(0.3GSH)-CuBTTri]" which is meant to convey only the net composition of this complex. Further studies on the number and type of active sites in the CuBTTri are warranted and in progress. Note also, once again, that the true stoichiometry in Figure 2.12—and by necessity the underlying reactions that add up to this stoichiometry and, hence, the overall mechanism—are different than the prior literature's stoichiometry for RSNO conversion, Figure 2.2 (vide supra). Once again, the value of the presented direct ^{1}H NMR monitoring method for RSNO conversion in water is apparent.

Evidence Against Copper-Ion Leaching from CuBTTri

Tests were performed to determine if copper ions were leaching from the CuBTTri under the reaction conditions. Specifically, inductively coupled plasma atomic emission spectroscopy (ICP-AES) analysis of the reaction supernatant after 16 h indicated that less than 1% of the total copper from the MOF was in solution (Appendix I, Table S2.2). The lack of ≥1% copper in solution (≤~10^{-6} M Cu^{2+}) argues compellingly against GSNO conversion being catalyzed by Cu^{2+} ions released from the MOF. First, the [GSH]:[Cu^{2+}] ratio would be approximately 1000:1 and we have shown herein that even a 1:1 ratio poisons copper-ion catalysis, results consistent with the finding of others. Furthermore, no GSSG-Cu^{2+} complex is observed for incomplete or completed CuBTTri reactions (Figure 2.9 and Figure 2.11), further discrediting significant leaching of copper atoms from the framework. The MOF also retains crystallinity over the course of the reaction as verified by powder X-ray diffraction (pXRD) data (Appendix I, Figure S2.15). In short, the "leached Cu^{2+}

is the catalyst" hypothesis for the CuBTTri MOF is disproven (consistent with previous studies reported by our group).

2.3 Summary and Conclusions

The following are the key findings of the present studies:

(1) ^{1}H NMR with solvent suppression proves to be a valuable, direct technique to track copper catalyzed release of NO from bio-available GSNO in water, thereby making the results herein relevant at least in principle to other, aqueous-based systems such as blood with its ~80% water content.

(2) The ^{1}H NMR method allows each of [GSNO], [GSH], and [GSSG] to be monitored simultaneously and directly by their differentiable ^{1}H NMR signals. This tracking in turn led to four balanced reaction stoichiometries not previously available, those for GSNO conversion with Cu^{2+} or CuBTTri pre-catalysts, each with and without added GSH from sub-stoichiometric to stoichiometric levels, Figures 2.7, 2.8, 2.10, and 2.12.

(3) Importantly, in 3 cases those reaction stoichiometries—and, hence, the underlying mechanism adding up to those net reactions—are distinct vs the literature's assumed, idealized stoichiometry, Figure 2.2. The formation and quantification of GSSG-Cu^{2+}, and what we write compositionally as [(0.3GSH)-CuBTTri], are the primary differences vs what one finds in the literature.

(4) Significantly, copper-ion and CuBTTri catalyzed systems show key differences in reactivity towards the amount of GSH present initially: sub-stoichiometric levels of GSH are sufficient for 100% GSNO conversion by copper ions (Table 2.1, entries 2 and 3), but allow only 10% conversion of GSNO using CuBTTri (Table 2.2, entry 1). In stark contrast, when 1.0 equivalent of GSH is added only 25% GSNO conversion is seen using Cu^{2+} (Table 2.1, entry 4) while 100% GSNO conversion to NO is achieved by CuBTTri (Table 2.2, entry 2). The results between the

two pre-catalysts are essentially completely flipped by the absence or presence of more than trace GSH. These observations support computational studies by Kumar et. al. suggesting that RSH species can interact with coordinatively unsaturated copper centers in MOFs to activate them for RSNO decomposition.[45,46]

(5) Critically, taken together, the above findings lead to the inescapable conclusion that the copper-ion and CuBTTri catalyzed reactions *must be operating through different mechanistic pathways*. The Cu^{2+} precatlyst operates at a greater catalytic rate, the CuBTTri and Cu^{2+} exhibit inverse responses to the additional of stoichiometric and sub-stoichiometric GSH, and the reaction products of the two systems differ. Further investigation into why and how those mechanisms differ is a goal of our ongoing studies.

(6) Lastly, with the ^{1}H NMR methodology developed herein, kinetic and mechanistic studies of copper catalyzed GSNO release of NO become possible and can be based on a direct method. The comparison of the Cu^{2+} and CuBTTri based pathways promises to be an interesting comparison. Determining the number and type of active sites in the CuBTTri system is another important goal, with efforts in progress. Finally, application of the ^{1}H NMR method to reactions carried out in blood/biological milieu is another important future goal, one made eventually possible by the present study in water emphasizing the bio-available substrate, GSNO, and its complete reaction products upon the desired release of NO for medically important applications.

2.4 Experimental

Reagents. Diethylamine (99%), trimethylsilylacetylene (98%), trimethylsilylazide (94%), and 1,3,5- tribromobenzene (98%) were purchased from Alfa Aesar (Ward Hill, MA, USA). Glutathione (98%) was purchased from VWR (Radnor, PA, USA). Sodium nitrite (99.5%), oxidized glutathione (98%), copper (I) iodide (99.5%), bis(triphenylphosphine)palladium(II)

dichloride (99%), and dichloromethane (99%) were purchased from Sigma-Aldrich (St. Louis, MO, USA). HCl (1N), methanol (99%), and sodium hydroxide (98.9%) were purchased from Fisher Scientific (Hampton, NH, USA). Dimethylformamide (99%) and copper (II) chloride dihydrate (99%) were purchased from EMD Chemicals (Gibbstown, NJ, USA). Ultrahigh purity nitrogen gas was supplied by Airgas (Denver, CO, USA). Deionized water (18.2 MΩ·cm) was obtained from a Millipore Direct-Q water purification system (EMD Millipore, Billerica, MA, USA). All materials were used as received without any further purification.

Water Suppression ^{1}H NMR Methodology. All NMR experiments were performed using an Agilent Inova 500 equipped with a 5mm pulsed-field-gradient HCN probe. Samples were prepared in septa-capped Wilmad 528-PP 500 MHz tubes under inert conditions (N_2). For this, 0.5 mL of reaction supernatant was added into an NMR tube containing 0.1 mL of 20 mM NaH_2PO_4 buffered D_2O and mixed by hand, followed by 2 s of sonication to remove any air bubbles. Samples were kept dark, air-free, and analyzed as soon as possible. NMR experiments were run using PRESAT with PURGE solvent signal suppression available in VnmrJ version-4.2.[47] The system was buffered with NaH_2PO_4 to a pH of 4 due to the sensitivity of the compounds of interest (GSNO, GSH, GSSG) to the pH of the solvent. 512 transients were acquired for all samples, which took 35 minutes to complete. A 2 s square presat with a bandwidth of 100 Hz on resonance at 4.67 ppm (water) was used, followed by the PURGE crusher sequence and a pi/2 excitation pulse of 5.7 μs. Acquisition time was 2 s, so with the PRESAT delay the total time between transients was about 4 s.

GSNO Synthesis. GSNO was prepared following an established literature protocol.[48] In brief: a solution of glutathione (1.53 g, 4.99 mmol) was prepared in millipore filtered water (8 mL) containing 2 M HCl (2.5 mL). One equivalent of sodium nitrite (0.345 g, 4.99 mmol) was added

and the resulting mixture was stirred for 40 min at 5 °C. Acetone (10 mL) was added to the resulting red solution and the mixture was stirred for another 10 min. The red precipitate was collected via vacuum filtration and washed with ice-cold water (5 x 5 mL) and ice-cold acetone (3 x 10 mL). The precipitate was then dried on a high vacuum line for 4 h to afford *S*-nitrosoglutathione (1.31 g, 3.86 mmol, 77%) (λ_{max}) (H2O) 335, 550 nm (ε=922, 15.9 cm^{-1} mM^{-1}). The GSNO sample used herein was determined to be 97 ± 2% pure, (Appendix I, Table S2.1 and Figure S2.4). This will prove important because even a 3 ± 2% GSH impurity from GSNO is potentially capable of initiating copper catalyzed NO release from GSNO.

H_3BTTri Ligand Synthesis. The H_3BTTri ligand was prepared following an established literature protocol. In brief: solid 1,3,5-tribromobenzene (9.45 g, 30.0 mmol) was dissolved in diethylamine (250 mL) under inert conditions (N_2). Copper(I) iodide (50 mg, 0.26mmol) and dichlorobis(triphenylphosphine)palladium(II) (400 mg, 0.57 mmol) were added to the stirred solution. Trimethylsilylacetylene (10.6 g, 108. mmol) was added to the solution and the resulting mixture was heated at 50 °C for 6 h. Resulting diethylamine hydrobromide was removed by filtration and washed with ether (45 mL). Combined washings were evaporated to dryness in vacuo and the resulting product purified by a silica plug to yield 9.61 g (78%) 1,3,5-tris(trimethylsilylethynyl)benzene as an intermediate. ^{1}H-NMR (400 MHz, $CDCl_3$): δ = 7.43 (s), 0.23 (s) ppm.

The 1,3,5-tris(trimethylsilylethynyl)benzene intermediate (9.61 g, 26.3 mmol) was hydrolyzed by treatment with NaOH(aq) (30 mL, 1 M), CH_2Cl_2 (20 mL), and methanol (50 mL) via stirring at room temperature for 3 h. Work-up involving the evaporation of methanol, ether extraction of the residue, and evaporation of the solvent in vacuo yielded 2.68 g of white powder containing 1,3,5- triethynylbenzene. ^{1}H-NMR (400 MHz, $CDCl_3$): δ = 7.51 (s), 3.12 (s) ppm.

Trimethylsilylazide (9.26 g, 80.4 mmol) was added to a solution of Copper(I) iodide (510 mg, 2.63 mmol) and 1,3,5-triethynylbenzene (2.68 g, 17.8 mmol) under inert conditions in a mixture of dimethylformamide (DMF; 90 mL) and methanol (10 mL). The resulting mixture was stirred at 100 °C for 36 h. The mixture was then filtered and reduced to a volume of 10 mL via rotary evaporation. A pale-yellow precipitate was formed upon the addition of millipore filtered water (30 mL) to the resulting filtrate. The solid was collected by filtration, washed with ether and dried in vacuo to yield 4.1 g (83%) of the product. ^{1}H-NMR (400 MHz, $(CD_3)_2SO$): δ = 8.52 (s), 8.34 (s) ppm.

CuBTTri Choice and Synthesis. Choosing a MOF catalyst required careful consideration, as many MOF species are not stable in water or biological media[49–51] Hence, CuBTTri was used based on prior evidence that the MOF is stable in both water and biological media.[30,52] CuBTTri was synthesized following a previously reported procedure.

A solution of H_3BTTri (225 mg, 0.937 mmol) in DMF (40 mL) was prepared in a 250 mL Pyrex bottle $CuCl_2{\cdot}2H_2O$ (383 mg, 2.25 mmol) was added to the solution. The vial was heated at 100 °C for 72 h to afford $H_3[(Cu_4Cl)_3(BTTri)_8(DMF)_{12}]{\cdot}7DMF{\cdot}76H_2O$. The purple powder was washed with boiling DMF (10 x 10 mL) and allowed to dry under ambient conditions to yield 218 mg (76%) of product. Solvent exchange via Soxhlet was performed using millipore filtered water to yield $H_3[(Cu_4Cl)_3(BTTri)_8(DMF)_{12}]{\cdot}72H_2O$.

Reaction Setup. All reactions described herein were carried out under inert, N_2 gas, atmosphere, unless otherwise noted. GSNO and GSH solutions were prepared from millipore H_2O and solid GSNO or GSH powder under inert conditions (N_2) in a 200 mL round bottom flask. CuBTTri was weighed into a multi neck 100 mL round-bottomed flask and oven dried overnight at 110 °C. Following drying, the flask containing CuBTTri was placed under vacuum for 1 h on a

Schlenk line and backfilled with N_2 (g) prior to reaction. GSNO and GSH solutions were then injected into the reaction flasks containing dry CuBTTri. Vigorous bubbling in the solution was established. Reaction flasks were wrapped in aluminum foil to prevent exposure to light and reactions proceeded for a predetermined time. To quench the reaction once the reaction time had been reached, the exit needle was removed to stop bubbling and the supernatant was carefully decanted via a syringe, leaving the MOF particles in the flask. The quenched reaction solution was then kept cool and dark in a Cu-free glass vial under inert conditions (N_2) or added directly to an NMR tube. The ^{1}H-NMR sample was prepared in a septa capped sample tube under inert conditions (N_2) by injecting 0.5 mL of reaction supernatant into the NMR tube along with 0.1 mL of 20 mM NaH_2PO_4 buffered D_2O. An identical procedure as described was carried out for the reaction between GSNO and $CuCl_2$. No unanticipated safety hazards were encountered over the course of all experiments. All reactions reported in the results and discussion section of this work were performed in triplicate to obtain an average and standard deviation.

^{1}H NMR. All free induction decay (FID) spectra were processed using MestraNova® software to examine peak intensities and integration values. Data analysis and calculations were performed using Microsoft Excel®.

Nitric Oxide Analyzer (NOA) Detection of NO. Control experiments were performed for both the copper-ion and CuBTTri catalysis systems to confirm that the previously observed release of one mol NO per mol GSNO does in fact occur and is detectable in our hands for both catalysts systems. The details and results are provided in Appendix I (Figures S2.16 and S2.17). These reactions were performed under identical conditions to those described above in the Reaction Setup subsection of the Methods section (vide supra).

Supporting Information. The following are available in Appendix I: Supporting Information for Chapter II: Description of additional characterization methods used, ^{1}H NMR characterization data of the H_3BTTri linker, the powder X-ray diffraction pattern for CuBTTri before and after reactions were completed, scanning electron micrographs of CuBTTri, ^{1}H NMR peak assignments for GSH, elemental analysis of the reaction supernatant, 3-D figures of the CuBTTri crystal structure, ^{1}H NMR data used to construct calibration curves to quantify [GSNO], [GSH], and [GSSG], control experiments to test the reactivity of GSNO alone with no Cu present, GSNO and GSH with no Cu present, GSNO and GSH with no CuBTTri, reactions bubbled with house air instead of ultrahigh purity N_2 gas, and raw NOA data.

REFERENCES

1. Williams, D. R. *et al.* Synthetic Small Molecules that Induce Neurogenesis in Skeletal Muscle. *Journal of the American Chemical Society* **129**, 9258–9259 (2007).

2. Knott, A. B. & Bossy-Wetzel, E. Nitric oxide in health and disease of the nervous system. *Antioxidants & redox signaling* **11**, 541–554 (2009).

3. Bogdan, C. Nitric oxide and the immune response. *Nature Immunology* **2**, 907–916 (2001).

4. Coleman, J. W. Nitric oxide in immunity and inflammation. *International immunopharmacology* **1**, 1397–1406 (2001).

5. Palmer, R. M. J., Ferrige, A. G. & Moncada, S. Nitric oxide release accounts for the biological activity of endothelium-derived relaxing factor. *Nature* **327**, 524–526 (1987).

6. Marletta, M. A. Nitric oxide: biosynthesis and biological significance. *Trends in Biochemical Sciences* **14**, 488–492 (1989).

7. Carpenter, A. W. & Schoenfisch, M. H. Nitric oxide release: Part II. Therapeutic applications. *Chemical Society Reviews* **41**, 3742–3752 (2012).

8. Schairer, D. O., Chouake, J. S., Nosanchuk, J. D. & Friedman, A. J. The potential of nitric oxide releasing therapies as antimicrobial agents. *Virulence* **3**, 271–279 (2012).

9. Roy, B., du Moulinet d'Hardemare, A. & Fontecave, M. New Thionitrites: Synthesis, Stability, and Nitric Oxide Generation. *The Journal of Organic Chemistry* **59**, 7019–7026 (1994).

10. Tsikas, D. *et al.* UPLC-MS/MS measurement of S-nitrosoglutathione (GSNO) in human plasma solves the S-nitrosothiol concentration enigma. *Journal of chromatography. B, Analytical technologies in the biomedical and life sciences* **927**, 147–157 (2013).

11. Mengel, A. & Lindermayer, C. *Nitric Oxide: Methods and Protocols*. (Springer, 2018).

12. Harding, J. L. & Reynolds, M. M. Metal Organic Frameworks as Nitric Oxide Catalysts. *Journal of the American Chemical Society* **134**, 3330–3333 (2012).

13. Harding, J. L., Metz, J. M. & Reynolds, M. M. A Tunable, Stable, and Bioactive MOF Catalyst for Generating a Localized Therapeutic from Endogenous Sources. *Advanced Functional Materials* **24**, 7503–7509 (2014).

14. Kao, P.-T., Lee, I.-J., Liau, I. & Yeh, C.-S. Controllable NO release from Cu(1.6)S nanoparticle decomposition of S-nitrosoglutathiones following photothermal disintegration of polymersomes to elicit cerebral vasodilatory activity. *Chemical science* **8**, 291–297 (2017).

15. Pal, H. A., Mohapatra, S., Gupta, V., Ghosh, S. & Verma, S. Self-assembling soft structures for intracellular NO release and promotion of neurite outgrowth. *Chemical Science* **8**, 6171–6175 (2017).

16. Zhang, S., Çelebi-Ölçüm, N., Melzer, M. M., Houk, K. N. & Warren, T. H. Copper(I) nitrosyls from reaction of copper(II) thiolates with S-nitrosothiols: mechanism of NO release from RSNOs at Cu. *Journal of the American Chemical Society* **135**, 16746–16749 (2013).

17. Melzer, M. M. *et al.* A Copper(II) Thiolate from Reductive Cleavage of an S-Nitrosothiol. *Inorganic Chemistry* **51**, 8658–8660 (2012).

18. Neufeld, M. J., Lutzke, A., Jones, W. M. & Reynolds, M. M. Nitric Oxide Generation from Endogenous Substrates Using Metal–Organic Frameworks: Inclusion within Poly(vinyl alcohol) Membranes To Investigate Reactivity and Therapeutic Potential. *ACS Applied Materials & Interfaces* **9**, 35628–35641 (2017).

19. Askew, S. C., Barnett, D. J., McAninly, J. & Williams, D. L. H. Catalysis by Cu2+ of nitric oxide release from S-nitrosothiols (RSNO). *Journal of the Chemical Society, Perkin Transactions 2* 741–745 (1995) doi:10.1039/P29950000741.

20. Dicks, A. P. *et al.* Identification of Cu+ as the effective reagent in nitric oxide formation from S-nitrosothiols (RSNO). *Journal of the Chemical Society, Perkin Transactions 2* 481–487 (1996) doi:10.1039/P29960000481.

21. P. Dicks, A., Herves Beloso, P. & Lyn H. Williams, D. Decomposition of S-nitrosothiols: the effects of added thiols. *Journal of the Chemical Society, Perkin Transactions 2* 1429–1434 (1997) doi:10.1039/A701594A.

22. Gorren, A. C. F., Schrammel, A., Schmidt, K. & Mayer, B. Decomposition ofS-Nitrosoglutathione in the Presence of Copper Ions and Glutathione. *Archives of Biochemistry and Biophysics* **330**, 219–228 (1996).

23. Smith, J. N. & Dasgupta, T. P. Kinetics and Mechanism of the Decomposition of S-Nitrosoglutathione by l-Ascorbic Acid and Copper Ions in Aqueous Solution to Produce Nitric Oxide. *Nitric Oxide* **4**, 57–66 (2000).

24. Burg, A., Cohen, H. & Meyerstein, D. The reaction mechanism of nitrosothiols with copper(I). *JBIC Journal of Biological Inorganic Chemistry* **5**, 213–217 (2000).

25. Neufeld, M. J., Lutzke, A., Tapia, J. B. & Reynolds, M. M. Metal–Organic Framework/Chitosan Hybrid Materials Promote Nitric Oxide Release from S-Nitrosoglutathione in Aqueous Solution. *ACS Applied Materials & Interfaces* **9**, 5139–5148 (2017).

26. Luza, S. C. & Speisky, H. C. Liver copper storage and transport during development: implications for cytotoxicity. *The American journal of clinical nutrition* **63**, 812S–20S (1996).

27. Ren, H. *et al.* Electrochemically Modulated Nitric Oxide (NO) Releasing Biomedical Devices via Copper(II)-Tri(2-pyridylmethyl)amine Mediated Reduction of Nitrite. *ACS Applied Materials & Interfaces* **6**, 3779–3783 (2014).

28. Liu, K. & Meyerhoff, M. E. Preparation and characterization of an improved Cu2+–cyclen polyurethane material that catalyzes generation of nitric oxide from S-nitrosothiols. *Journal of Materials Chemistry* **22**, 18784–18787 (2012).

29. Roberts, T. R. *et al.* A metal organic framework reduces thrombus formation and platelet aggregation ex vivo. *The journal of trauma and acute care surgery* **85**, 572–579 (2018).

30. Neufeld, M. J., Ware, B. R., Lutzke, A., Khetani, S. R. & Reynolds, M. M. Water-Stable Metal–Organic Framework/Polymer Composites Compatible with Human Hepatocytes. *ACS Applied Materials & Interfaces* **8**, 19343–19352 (2016).

31. Broniowska, K. A., Diers, A. R. & Hogg, N. S-nitrosoglutathione. *Biochimica et biophysica acta* **1830**, 3173–3181 (2013).

32. Pettinari, C., Marchetti, F., Mosca, N., Tosi, G. & Drozdov, A. Application of metal − organic frameworks. *Polymer International* **66**, 731–744 (2017).

33. Williams, D. L. H. The Chemistry of S-Nitrosothiols. *Accounts of Chemical Research* **32**, 869–876 (1999).

34. Bartberger, M. D. *et al.* Theory, Spectroscopy, and Crystallographic Analysis of S-Nitrosothiols: Conformational Distribution Dictates Spectroscopic Behavior. *Journal of the American Chemical Society* **122**, 5889–5890 (2000).

35. Instruments, G. A. (2014).

36. Choi, L.-S. & Bayley, H. S-Nitrosothiol Chemistry at the Single-Molecule Level. *Angewandte Chemie International Edition* **51**, 7972–7976 (2012).

37. Baciu, C., Cho, K.-B. & Gauld, J. W. Influence of Cu+ on the RS-NO bond dissociation energy of S-nitrosothiols. *The journal of physical chemistry. B* **109**, 1334–1336 (2005).

38. García-García, P., Müller, M. & Corma, A. MOF catalysis in relation to their homogeneous counterparts and conventional solid catalysts. *Chemical Science* **5**, 2979–3007 (2014).

39. Homer, N. Z. M. *et al.* Dimethylsulfoxide oxidizes glutathione in vitro and in human erythrocytes: Kinetic analysis by 1H NMR. *Cryobiology* **50**, 317–324 (2005).

40. R. Noble, D., R. Swift, H. & Lyn H. Williams, D. Nitric oxide release from S-nitrosoglutathione (GSNO). *Chemical Communications* 2317–2318 (1999) doi:10.1039/A907891F.

41. Kenche, V. B. *et al.* Mixed Ligand Cu2+ Complexes of a Model Therapeutic with Alzheimer's Amyloid-β Peptide and Monoamine Neurotransmitters. *Inorganic Chemistry* **52**, 4303–4318 (2013).

42. Ngamchuea, K., Batchelor-McAuley, C. & Compton, R. G. The Copper(II)-Catalyzed Oxidation of Glutathione. *Chemistry – A European Journal* **22**, 15937–15944 (2016).

43. Pietraforte, D., Mallozzi, C., Scorza, G. & Minetti, M. Role of thiols in the targeting of S-nitroso thiols to red blood cells. *Biochemistry* **34**, 7177–7185 (1995).

44. Singh, S. P., Wishnok, J. S., Keshive, M., Deen, W. M. & Tannenbaum, S. R. The chemistry of the S-nitrosoglutathione/glutathione system. *Proceedings of the National Academy of Sciences of the United States of America* **93**, 14428–14433 (1996).

45. Taylor-Edinbyrd, K., Li, T. & Kumar, R. Effect of chemical structure of S-nitrosothiols on nitric oxide release mediated by the copper sites of a metal organic framework based environment. *Physical Chemistry Chemical Physics* **19**, 11947–11959 (2017).

46. Li, T., Taylor-Edinbyrd, K. & Kumar, R. A computational study of the effect of the metal organic framework environment on the release of chemically stored nitric oxide. *Physical Chemistry Chemical Physics* **17**, 23403–23412 (2015).

47. Simpson, A. J. & Brown, S. A. Purge NMR: Effective and easy solvent suppression. *Journal of Magnetic Resonance* **175**, 340–346 (2005).

48. Hart, T. W. Some Observations Concerning the S-Nitroso and S-Phenylsulphonyl Derivatives of L-Cysteine and G. *Tetrahedron Letters* **26**, 2013–2016 (1985).

49. Huang, L. *et al.* Synthesis, morphology control, and properties of porous metal-organic coordination polymers. *Microporous and Mesoporous Materials* **58**, 105–114 (2003).

50. Schoenecker, P. M., Carson, C. G., Jasuja, H., Flemming, C. J. J. & Walton, K. S. Effect of Water Adsorption on Retention of Structure and Surface Area of Metal–Organic Frameworks. *Industrial & Engineering Chemistry Research* **51**, 6513–6519 (2012).

51. Al-Janabi, N. *et al.* Mapping the Cu-BTC metal–organic framework (HKUST-1) stability envelope in the presence of water vapour for CO2 adsorption from flue gases. *Chemical Engineering Journal* **281**, 669–677 (2015).

52. Demessence, A., D'Alessandro, D. M., Foo, M. L. & Long, J. R. Strong CO2 Binding in a Water-Stable, Triazolate-Bridged Metal−Organic Framework Functionalized with Ethylenediamine. *Journal of the American Chemical Society* **131**, 8784–8786 (2009).

III. MONITORING A MOF CATALYZED REACTION DIRECTLY IN BLOOD PLASMA[1]

Overview

Herein, we establish a method to quantitatively monitor a metal–organic framework (MOF) catalyzed, biomedically-relevant reaction directly in blood plasma. Specifically, the generation of nitric oxide (NO) from the endogenous substrate *S*–Nitrosoglutathione (GSNO) catalyzed by $H_3[(Cu_4Cl)_3–(BTTri)_8]$ (CuBTTri). The reaction monitoring method uses UV-VIS and ^{1}H NMR spectroscopies along with a nitric oxide analyzer (NOA) to yield the reaction stoichiometry and catalytic rate for GSNO to NO conversion catalyzed by CuBTTri in blood plasma. Results show 100% loss of GSNO within 16 h and production of one equivalent of glutathione disulfide (GSSG) per two equivalents of GSNO. Only 78 ± 10% recovery of NO (g) was observed, indicating that blood plasma can scavenge the generated NO before it can escape the reaction vessel. The NO scavenging observed herein in blood plasma is the only difference from the stoichiometry previously determined in water for the same reaction. The rate of the loss of GSNO (–d[GSNO]/dt) measured in blood plasma ((6.8 ± 0.4) x 10^{-4} mM s^{-1}) is double the rate that was previously measured in water under otherwise identical experimental conditions ((2.9 ± 0.3) x 10^{-4} mM s^{-1}), within experimental error. Significantly, to best apply reaction systems with biomedical importance, such as NO release catalyzed by CuBTTri, methods to study the reaction directly in biological solvents must be developed. Tuttle, R. R., Daly, R. E., Rithner, C. D. & Reynolds, M. M. Monitoring a MOF Catalyzed Reaction Directly in Blood Plasma. ACS Applied Materials & Interfaces (2021) doi:10.1021/acsami.1c08917.

[1] The work presented in Chapter III is a direct follow-up to Chapter II where the CuBTTri/NO/GSNO system was studied in a much more complicated solvent matrix, blood plasma. This work is published (Tuttle, R. R.; Daly, R. E.; Rithner, C. D.; Reynolds, M. M. *ACS. Appl. Mater. Inter.* **2021**, doi:10.1021/acsami.1c08917). Minor formatting edits have been introduced to meet the dissertation requirements.

3.1 Introduction

Monitoring chemical reactions *in vitro*, directly in biological solvents (such as blood plasma) is a difficult but important, experimental challenge, especially for chemical reactions relevant to biomedical applications.[1,2] Blood plasma is a complex solvent matrix. Components of blood plasma can create interfering signals,[1–7] making it difficult to quantify, or even detect reactants or products in a given chemical reaction. Additionally, biological molecules, such as proteins, present in blood plasma can affect reactions of interest.[8–10] Hence, fundamental studies of biomedically relevant reactions carried out in biological solvents are rare.[11,12] Water is often used as an initial blood plasma-relevant solvent in attempts to mimic the effects of blood plasma and relieve these challenges (blood plasma being ~90% water).[13] However, monitoring biomedical reactions directly in blood plasma is desirable as it ensures that findings are more relevant to biological systems.

One biomedically relevant reaction that has not been studied *in blood plasma* is the generation of nitric oxide (NO)[14–20] from the endogenous substrate *S*–Nitrosoglutathione (GSNO) catalyzed by copper-based materials such as the metal–organic framework (MOF) $H_3[(Cu_4Cl)_3–(BTTri)_8$, where H_3BTTri = 1,3,5–tris(^{1}H–1,2,3–triazol–5–yl)benzene] (CuBTTri, Figure 3.1).[11,21,22] Polymer-based materials containing CuBTTri generate NO release, resulting in desirable vasodilation and biofilm reduction on implanted medical devices.[16,20,23] CuBTTri is a superior NO generation catalyst compared to other among copper-based materials (including other MOFs) as it is stable in biological media. Based upon Cu ion leaching and powder X-ray diffraction data, CuBTTri is stable in freshly citrated whole blood and phosphate buffered saline.[11] CuBTTri is also non-toxic to human hepatocytes[11,12] and catalyzes NO release *in vivo*.[11,17] Cu-MOF systems have also been shown to exhibit catalytic recyclability for NO generation.[24]

CuBTTri is known to catalyze generation of NO from GSNO via coordinatively unsaturated Cu sites present on the exterior surface of CuBTTri particles based upon previously reported catalyst kinetic poisoning and characterization studies.[25] Previous work has established that for 600 ± 300 nm octahedral particles, 1.3 ± 0.4 % of the total Cu sites are active for GSNO to NO conversion catalysis in water.[25] The CuBTTri catalyzed GSNO to NO conversion stoichiometry and rate have also been reported in water,[21,25] and NO generation via materials containing CuBTTri has been observed in blood.[11] However, no method has previously been reported to monitor [GSNO] or glutathione disulfide product ([GSSG]) in blood plasma. Hence, fundamental parameters (stoichiometry and rate) are unknown for CuBTTri catalyzed NO generation *in blood plasma*.

The CuBTTri GSNO to NO catalysis system is unique among NO generation strategies because of the synthetic MOF catalyst. Crystalline MOFs are porous materials constructed from organic linkers and metal cation or cluster nodes.[26] MOFs have garnered interest as catalytic materials for several reasons, arguably chief among them being that MOFs exhibit unparalleled synthetic and chemical tunability in comparison to other solid-state materials.[11,27–32] Synthetic tunability is often proposed as a route towards the design of next-generation MOF catalysts with greater catalytic activity.[33–36] However, the directed design of future Cu-MOF catalysts with improved catalytic properties versus CuBTTri *in vitro*[23–30] is precluded by the need to determine reaction parameters like stoichiometry and rate *in vitro* first. Determining these reaction parameters requires the development of a monitoring method for CuBTTri catalyzed GSNO to NO conversion in blood plasma. Without a method to directly monitor the reaction in blood plasma one cannot measure the reaction rates and rate constants necessary to set benchmark catalyst performance or make meaningful inter-catalyst comparisons.[34]

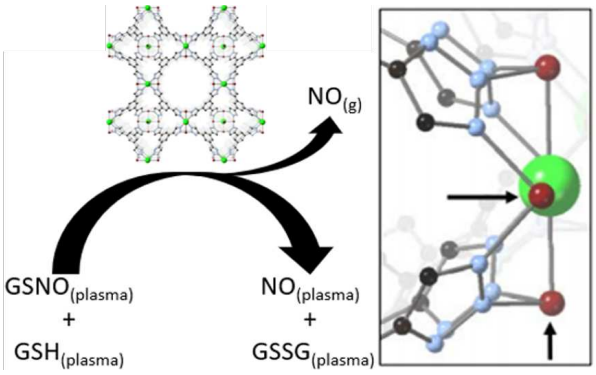

Figure 3.1. The reaction system investigated on the left. Generation of GSSG and NO (in the gas phase and scavenged by plasma) in blood plasma via reaction of GSNO and GSH with CuBTTri. CuBTTri unit cell shown on the [1, 1, 1] face with carbon (black), nitrogen (blue), chlorine (green), and copper (red). Shown on the right is the previously determined exterior surface Cu active site in CuBTTri for GSNO to NO conversion.[22,25,37,38]

Understanding how GSNO to NO conversion reaction catalyzed by CuBTTri operates *in vivo* requires that methods to comprehensively monitor the reaction in biological solvents (such as blood plasma) be developed. Towards that goal, we report herein a direct method to quantitatively monitor CuBTTri catalyzed GSNO to NO conversion in bovine blood plasma (serving to mimic human blood plasma[39–42]). Combining three analytical techniques (UV-VIS and ^{1}H NMR spectroscopies with a Nitric Oxide Analyzer) overcomes the challenges presented by the blood plasma solvent and allows for the comprehensive and quantitative monitoring of all relevant reactants and products in the NO release reaction. The method yields the balanced reaction stoichiometry and catalytic rate for the NO release reaction *in vitro*, fundamental parameters for this biomedically relevant reaction. Monitoring the NO release reaction in blood plasma is, to the best of our knowledge, the first report of quantitatively monitoring a MOF-catalyzed reaction in a biological solvent.

3.2 Results and Discussion

The catalytic reaction system studied herein is the release of NO from GSNO in the presence of GSH resulting in GSSG formation catalyzed by the MOF CuBTTri. All the reactions described were carried out in bovine blood plasma. Separate analytical techniques were used to

monitor each of the unique reactants and products. UV-VIS spectroscopy was utilized to monitor [GSNO] in blood plasma. ^{1}H NMR spectroscopy was used to monitor [GSSG] in blood plasma. The gaseous NO generated in the reaction was detected and quantified using a chemiluminescence technique selective for NO. Details for each of the separate analytical methods used to monitor the reactions follow below, as do an analysis of the results yielding the reaction stoichiometry and catalytic rate (*vide infra*).

Monitoring [GSNO] in Blood Plasma via UV-VIS Spectroscopy and NO Release via NOA

The concentration of GSNO in aqueous solutions has traditionally been monitored using UV-VIS spectroscopy. GSNO exhibits an electronic transition at 335 nm observable by UV-VIS spectroscopy ($\varepsilon = 922\ mM^{-1}\ cm^{-1}$).[43,44] UV-VIS spectroscopy cannot be used to monitor GSSG or GSH in blood plasma because GSH does not exhibit an observable UV-VIS signal, and baseline interference from the blood plasma solvent prevents measuring the UV signal associated with GSSG (Figure S3.2). Solutions of blood plasma containing GSNO at various concentrations were analyzed using UV-VIS spectroscopy (Figure 3.2A), and the absorbance at 335 nm increases with concentration of GSNO. The negative absorbance values in Figure 3.2A are the result of the intense baseline UV-VIS absorbance of the blood plasma solvent (Figure S3.5). However, the error introduced by the intense background UV-VIS signal from blood plasma is systematic and does not prevent one from quantifying [$GSNO_{(plasma)}$] in the concentration range utilized herein. Plotting the absorbance maximum at 335 nm vs [$GSNO_{(plasma)}$] yields the calibration curve in Figure 3.2B, which shows that the concentration of GSNO in blood plasma can be quantified using UV-VIS spectroscopy. Three separate experiments showed that within 16 h, 100% of GSNO initially present in solution is lost (Figure S3.7), as reported in Table 3.1.

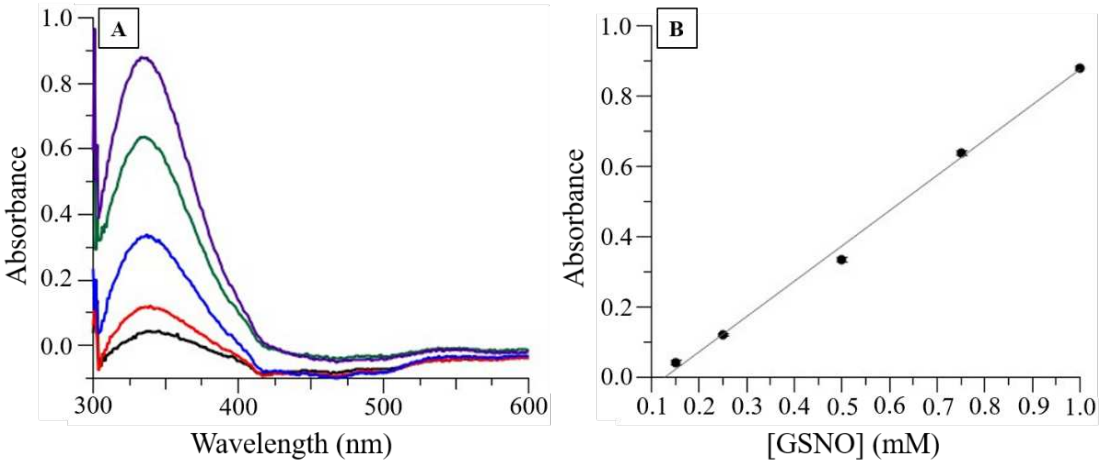

Figure 3.2. (A, left) UV-VIS absorbance spectrum of blood plasma with [$GSNO_{(plasma)}$] = 0.15, 0.25, 0.5, 0.75, and 1 mM (bottom to top; black, red, blue, green, purple). (B, right) Calibration curve comparing the absorbance at 335 nm and [$GSNO_{(plasma)}$]. The trend line is fit by $y = (1.00 \pm 0.04)x - (0.13 \pm 0.02)$, $R^2 = 0.99$. Data points correspond to the average and standard deviation of three trials. Data points are plotted as the average and standard deviation of three trials. In some cases, the y–axis error bars are smaller than the size of the data point.

Table 3.1. Total GSNO, NO, and GSSG present initially and after 16 h. GSH does not appear in the 16 h column as [$GSH_{(plasma)}$] cannot currently be tracked quantitatively. Each data point represents the average and standard deviation of n = 3.

mol/Time	**T = 0 h**	**T = 16 h**
mol GSNO	$1.0 \pm 0.1 \times 10^{-5}$	0
mol GSH	$1.0 \pm 0.1 \times 10^{-5}$	N/A
mol NO	0	$7.8 \pm 1.0 \times 10^{-6}$
mol GSSG	0	$5.5 \pm 0.5 \times 10^{-6}$

The amount of NO released from CuBTTri catalyzed GSNO to NO conversion is commonly quantified using a nitric oxide analyzer (NOA). NOA instruments detect and quantify gaseous NO released over the course of the reaction via chemiluminescence.[11,21,24] Figure 3.3 shows a representative NO release profile for GSNO to NO conversion catalyzed by CuBTTri in blood plasma. As reported in Table 3.1, the average mols of NO released over 16 h (based on three separate trials) was $7.8 \pm 1.0 \times 10^{-6}$ mol NO, corresponding to 78 ± 10% of the total mols of GSNO initially present in the reactions ($1.0 \pm 0.1 \times 10^{-6}$ mol). While one might expect 100% NO recovery along with 100% loss of GSNO, one possible explanation is that 22 ± 10% of the gaseous NO generated is scavenged by proteins in blood plasma.[45–49] Indeed, while Hb is the main scavenger

of NO in whole blood, several groups have reported the scavenging of NO by proteins. [45–49] The NO scavenging explanation is reflected in the stoichiometry (Figure 3.5) by the species written $NO_{(plasma)}$, while NO which escapes and is detected by the NOA is designated NO (g). While other NO scavenging processes are possible, the protein scavenging hypothesis fits the experimental data.

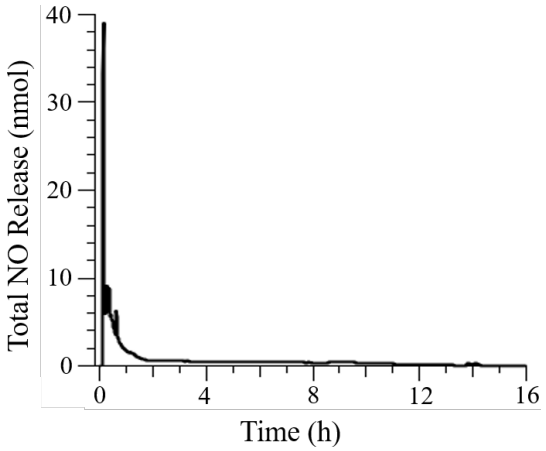

Figure 3.3. NO release profile from 0 to 16 h for an experiment with initial conditions: $[GSNO_{(plasma)}]$ = 2 mM, $[GSH_{(plasma)}]$ = 2 mM, at 25 °C, reaction bubbled with N_2 (g), and 4.05 mg CuBTTri. The average amount of NO released for three trials under identical conditions was 7.8 ± 1.0 x 10^{-6} mol.

Monitoring [GSSG] in Blood Plasma via ^{1}H NMR Spectroscopy

Tracking the generation of disulfide has been the most difficult challenge in comprehensively monitoring Cu-catalyzed NO release from nitrosated thiols. In fact, our previous work[21] using ^{1}H NMR was the first report of a method which could quantify the production of GSSG from GSNO catalyzed by CuBTTri. Hence, ^{1}H NMR was investigated as a possible method to track $[GSNO_{(plasma)}]$, $[GSH_{(plasma)}]$, and $[GSSG_{(plasma)}]$ (as reported in water[21]). Solvent signals prevent using ^{1}H NMR to follow $[GSNO_{(plasma)}]$ and $[GSH_{(plasma)}]$ (Appendix II, Figures S3.2 and S3.3). However, blood plasma exhibits a flat baseline signal in the ppm range (3.16–3.24)[21,50] where unique ^{1}H NMR signals are expected for GSSG (Appendix II, Figure S3.4). Figure 3.4A contains ^{1}H NMR data for samples of blood plasma with varying [GSSG] and shows that the signal

corresponding to GSSG is observable at 3.18 ppm, and as [GSSG] increases, so does the measured signal intensity. Figure 3.4B shows a calibration curve plotting signal intensity at 3.18 ppm vs [$GSSG_{(plasma)}$]. Intensity was measured as the difference between the baseline value of the ^1H NMR spectrum and the absolute intensity of the resonance at 3.18 ppm to obtain consistent values regardless of phasing. Figure 3.4B establishes linear agreement between [$GSSG_{(plasma)}$] and signal intensity, a linear working range (0.25–5 mM), and that [$GSSG_{(plasma)}$] can be quantified using ^1H NMR. The experimental section contains details of the ^1H NMR pulse sequence used to measure [$GSSG_{(plasma)}$]. Measuring [$GSSG_{(plasma)}$] after 16 h of reaction (Appendix II, Figure S3.8, Table S3.1) revealed that 5.5 ± 0.5 x 10^{-6} mols GSSG are produced upon the complete loss of 1.0 ± 0.1 x 10^{-5} mol GSNO, as reported in Table 3.1. The amount of GSSG generated is equal within experimental error to one half the amount of GSNO initially present. Hence, it is reasonable to conclude[51] that all GSNO lost over 16 h is converted into GSSG.

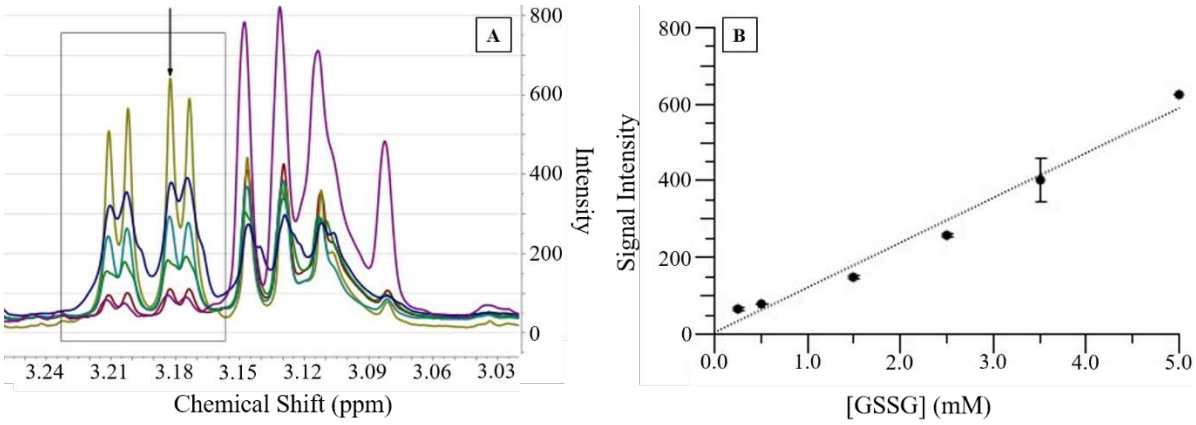

Figure 3.4. (A, Left) ^1H NMR spectra of blood plasma with [$GSSG_{(plasma)}$] = 0.25, 0.5, 1.5, 2.5, 3.5, and 5 mM (bottom to top; purple, red, green, teal, blue, yellow). The arrow indicates the 3.18 ppm resonance used for intensity measurements. (B, Right) Calibration curve comparing signal intensity at 3.18 ppm and [$GSSG_{(plasma)}$]. The trend line is fit by y = (118 ± 9)*x* + (2 ± 25), R^2 = 0.98. Data points correspond to the average and standard deviation of three trials. Data points are plotted as the average and standard deviation of three trials. In some cases, the y–axis error bars are smaller than the size of the data point.

The Reaction Stoichiometry in Blood Plasma

The data summarized in Table 3.1 allow one to write a balanced reaction for release of NO from GSNO catalyzed by CuBTTri in blood plasma (Figure 3.5). 2 equivalents of GSNO are lost for every 1 equivalent of GSSG generated. For every 2 equivalents of GSNO lost, 1.6 equivalents of NO are detected, and 0.4 equivalents of NO are scavenged by blood plasma. Table 3.1 does not list GSH concentration data at 16 h because no method currently exists to quantify [$GSH_{(plasma)}$] (Figure S3.6).[21,52,53] As summarized herein, neither UV-VIS nor ^{1}H NMR spectroscopy can be used to quantify [$GSH_{(plasma)}$]. However, GSH must be present to observe CuBTTri-based NO release catalysis,[21] and since GSH is only present at trace levels in bovine plasma,[54] additional GSH was added to the reaction mixture. No GSH oxidation to generate GSSG beyond half the amount of GSNO initially present is observed (Table 3.1). Therefore, GSH is not converted into a detectable reaction product and does not appear in Figure 3.5. The role of GSH in GSNO to NO conversion catalyzed by CuBTTri (or any Cu-based material) has not been established for this or any other GSNO to NO conversion catalyst. The fact that GSH must be present to observe GSNO to NO conversion when the reaction is carried out under anaerobic conditions (as the reactions described herein were) has led many, including us, to hypothesize that GSH acts as a reducing agent to generate catalytically active Cu(I) sites on the surface of CuBTTri. However, future work (ultimately made possible by the monitoring method established herein) is necessary to support or disprove this hypothesis.

$$2GSNO_{(plasma)} \xrightarrow[\text{Bovine Plasma}]{\text{CuBTTri}} 1.6NO\bullet_{(g)} + 0.4NO\bullet_{(plasma)} + GSSG_{(plasma)}$$

Figure 3.5. Reaction stoichiometry for GSNO to NO conversion catalyzed by CuBTTri in blood plasma.

The Catalytic Rate in Blood Plasma

The initial rate of CuBTTri catalyzed GSNO to NO conversion in blood plasma was also investigated. In blood plasma, it is advantageous to follow the rate of GSSG production (+d[GSSG]/dt) for kinetic study as opposed to following [$GSNO_{(plasma)}$]. The ^{1}H NMR spectrum of blood plasma exhibits a flat baseline in the region where the signal for GSSG is observed (Appendix II, Figure S3.4), whereas the UV-VIS spectrum for blood plasma exhibits an intense baseline signal at the wavelength where GSNO is observed (Appendix II, Figure S3.5).[43] Consequently, blood plasma introduces less solvent interference if following [$GSSG_{(plasma)}$] by ^{1}H NMR than following [$GSNO_{(plasma)}$] by UV-VIS. The measured value for $[+d[GSSG]/dt]_{plasma}$ can be converted into $[-d[GSNO]/dt]_{plasma}$ using statistical factors from the reaction stoichiometry (Figure 3.5). This conversion is shown below in equations 3.1-3.3. Figure 3.6 shows ^{1}H NMR data obtained from blood plasma supernatant after 0 min, 20 min, and 16 h of reaction. The experimentally determined value for $[+d[GSSG]/dt]_{plasma}$ (Appendix II, Table S3.1) and calculated $[-d[GSNO]/dt]_{plasma}$ are given in Table 3.2.

$$\left(\frac{+d[GSSG]}{dt}\right)_{plasma} = \frac{[GSSG]_t - [GSSG]_i}{t} \quad \text{(eq. 3.1)}$$

$$\frac{1}{2}\left(\frac{-d[GSNO]}{dt}\right)_{plasma} = \frac{1}{1}\left(\frac{+d[GSSG]}{dt}\right)_{plasma} \quad \text{(eq. 3.2)}$$

$$\left(\frac{-d[GSNO]}{dt}\right)_{plasma} = \frac{2}{1}\left(\frac{+d[GSSG]}{dt}\right)_{plasma} \quad \text{(eq. 3.3)}$$

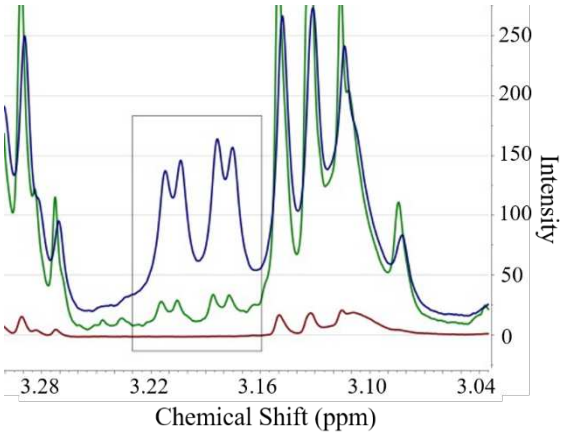

Figure 3.6. ^{1}H NMR spectra from aliquots of supernatant taken from separate reactions of GSNO with CuBTTri in blood plasma at 0 min (red, bottom), 20 min (green, middle), and 16 h (blue, top).

Table 3.2. Comparison of initial rates determined for GSNO to NO conversion catalyzed by CuBTTri at 20 min. Each data point represents the average and standard deviation of n = 3.

Solvent	**[+d[GSSG]/dt] (mM s^{-1})**	**[–d[GSNO]/dt] (mM s^{-1})**
Bovine Plasma (this work)	(3.4 ± 0.2) x 10^{-4}	(6.8 ± 0.4) x 10^{-4}
Water (previous work)[21,24]	n/a	(2.9 ± 0.3) x 10^{-4}

Comparing Results in Blood Plasma to Results Previously Obtained in Water

Comparing the reaction parameters determined in blood plasma to those previously determined in water is useful to evaluate water as a model solvent for the much more complicated case of blood plasma for GSNO to NO conversion catalyzed by CuBTTri. In previous studies carried out in water, 100% recovery of NO is observed from catalysis of GSNO with CuBTTri (Figure 3.7).[21] The only difference observed when the reaction is carried out in blood plasma is the scavenging of NO (Figures 3.5 and 3.7). Adsorption of GSH onto the CuBTTri framework was also hypothesized to occur in water,[21] and while GSH may also adsorb onto CuBTTri in blood plasma, it is currently unknown if any such adsorption occurs. However, the physical adsorption of GSH onto CuBTTri is a minor feature of the stoichiometry in Figure 3.7, as it is not an elementary step in the NO release reaction mechanism. Previous experiments in water determined the rate of reaction by following the loss of GSNO (–d[GSNO]/dt) via ^{1}H NMR.[25] Using ^{1}H NMR

once again to measure the catalytic rate in blood plasma ($[+d[GSSG]/dt]_{plasma}$) mimics instrumental precision and maximizes reliability of comparisons presented between the solvent systems. The measured catalytic rate in blood plasma at 20 min is double that previously measured in water, within experimental error (Table 3.2). It is important to note here that these comparisons are made under the assumption that the rate law for the NO release reaction does not change when moving the reaction from water to blood plasma. We are currently working to test this assumption to best understand the comparison between the rates in Table 3.2. Importantly, if the statistical factors from Figure 3.5 are not used, the calculated value for $[-d[GSNO]/dt]_{plasma}$ appears (incorrectly) equal to $[-d[GSNO]/dt]_{water}$.

$$2GSNO_{(aq)} + 0.3GSH_{(aq)} + CuBTTri_{(s)} \longrightarrow$$
$$2NO\bullet_{(g)} + GSSG_{(aq)} + [(0.3GSH)\text{-}CuBTTri]_{(s)}$$

Figure 3.7. The stoichiometry for GSNO to NO conversion catalyzed by CuBTTri in water determined in previous work.[21]

3.3 Summary and Conclusions

Results presented herein yield the stoichiometry and rate for CuBTTri catalyzed generation of NO from GSNO *in vitro*. Combining three separate experimental techniques (UV-VIS and ^{1}H NMR spectroscopies with an NOA) to monitor the reaction comprehensively and quantitatively was necessary to overcome the difficulties presented by blood plasma as a solvent. One equivalent of GSSG is formed per two equivalents of GSNO lost in blood plasma. Scavenging of NO by blood plasma is evidenced by the fact that only 78 ± 10% NO recovery is observed in blood plasma when 100% of the GSNO is lost. The rate of the GSNO to NO reaction catalyzed by CuBTTri was measured in blood plasma to be (6.8 ± 0.4) x 10^{-4} mM s^{-1}. Future work can focus on using the monitoring method developed herein to determine the reasons why the measured rate in blood plasma is double that for the rate measured in water ((2.9 ± 0.3) x 10^{-4} mM s^{-1}). The only difference in the reaction stoichiometries for the two solvents is that minor NO scavenging is observed in

blood plasma, but not in water. Hence, while the elementary steps of the NO release reaction mechanism are likely the same in water and blood plasma, the rate constants associated with the elementary steps are different in the two solvents. Full kinetic and mechanistic studies of NO release from GSNO with any Cu-based catalyst can be performed *in vitro* in the future with the monitoring method in hand. Additionally, the ^{1}H NMR method reported herein can likely quantify other disulfides than GSSG generated from *S*-Nitrosothiols (RSNOs) other than GSNO, and the UV-VIS method is certainly capable of quantifying the concentration of other RSNOs. Hence, the monitoring method established herein can be used to quantitatively study other catalytic RSNO to NO systems directly in blood plasma.

3.4 Experimental

Reagents. Diethylamine (99%), trimethylsilylacetylene (98%), trimethylsilylazide (94%), and 1,3,5- tribromobenzene (98%) were purchased from Alfa Aesar (Ward Hill, MA, USA). Glutathione (98%) was purchased from VWR (Radnor, PA, USA). Sodium nitrite (99.5%), copper (I) iodide (99.5%), bis(triphenylphosphine)palladium(II) dichloride (99%), and dichloromethane (99%). HCl (1 N), methanol (99%), and sodium hydroxide (98.9%) were purchased from Fisher Scientific (Hampton, NH, USA). Dimethylformamide (99%) and copper (II) chloride dihydrate (99%) were purchased from EMD Chemicals (Gibbstown, NJ, USA). Ultrahigh purity nitrogen gas was supplied by Airgas (Denver, CO, USA). Deionized water (18.2 MΩ·cm) was obtained from a Millipore Direct-Q water purification system (EMD Millipore, Billerica, MA, USA). Bovine blood plasma containing fluoride as an anticoagulant was purchased from Hemostat Laboratories (Greely, CO, USA). All materials were used as received without any further purification.

Instrumentation. UV-VIS data was acquired using a Thermo Scientific Evolution 300 UV-Vis Spectrophotometer. Samples were prepared in quartz cuvettes. Powder X-Ray diffraction (PXRD) patterns were obtained using a Bruker D8 Discover DaVinci Powder X-ray Diffractometer with CuKα radiation operated at 40 kV and 40 mA. A typical scan rate was 0.3 sec/step with a step size of 0.02 deg. ^{1}H NMR spectra were acquired using a Varian / Agilent Inova 500 MHz spectrometer equiped with a sensitive 5mm pulse-field-gradient (PFG), room-temperature inverse detection (ID) probe. The probe was not a cryo-probe. All NMR measurements were made at 25˚C by using the Varian / Agilent VnmrJ 4.2 pulse sequence library software provided for Inova spectrometers, without modification. The spectral width was 8 kHz, the acquisition time was 2.0 sec, the combined relaxation and pre-saturation delay was 1.5 sec, the π/2 pulse width was 7.2 μs, 512 signal averaging transients were acquired, 0.3 Hz exponential line-broadening was applied to the time-domain and the digital resolution after Fourier transformation was 0.12 Hz. ^{1}H NMR data was processed in MestraNova using the phasing and baseline correction tools available in the software. All values reported correspond to, at minimum, the average and standard deviation of three identical experiments. Software: MestraNova, IgorPro, OriginPro, and Microsoft Excel, and Powerpoint.

GSNO Synthesis and Characterization. GSNO was synthesized and characterized according to previously established[43] literature procedures. Briefly, a solution of glutathione (1.53 g, 4.99 mmol) was prepared in millipore filtered water (8 mL) containing 2 M HCl (2.5 mL, 10.5 mL total volume). One equivalent of sodium nitrite (0.345 g, 4.99 mmol) was added, and the resulting mixture was stirred for 40 min at 5 °C. Acetone (10 mL) was added to the resulting red solution and the mixture was stirred for another 10 min. The red precipitate was collected via vacuum filtration and washed with ice-cold water (5 × 5 mL) and ice-cold acetone (3 × 10 mL).

The precipitate was then dried on a high vacuum line for 4 h to afford *S*-Nitrosoglutathione (1.40 g, 4.12 mmol, 82%) (λ_{max}) (H_2O) 335, 550 nm (ε=922, 15.9 cm^{-1} mM^{-1}). The GSNO sample used herein was determined to be 97 ± 2% pure by the established method of UV-VIS spectroscopy.[40]

H_3BTTri Synthesis and Characterization. H_3BTTri was synthesized and characterized according to previously established[22] literature procedures. Briefly, solid 1,3,5-tribromobenzene (9.45 g, 30.0 mmol) was dissolved in diethylamine (250 mL) under inert conditions (N_2). Copper(I) iodide (50 mg, 0.26 mmol) and dichlorobis(triphenylphosphine)palladium(II) (400 mg, 0.57 mmol) were added to the stirred solution. Trimethylsilylacetylene (10.6 g, 108. mmol) was added to the solution and the resulting mixture was heated at 50 °C for 6 h. Resulting diethylamine hydrobromide was removed by filtration and washed with ether (45 mL). Combined washings were evaporated to dryness in vacuo and the resulting product purified by a silica plug to yield 9.61 g (78%) 1,3,5-tris(trimethylsilylethynyl)benzene as an intermediate. ^{1}H NMR (400 MHz, $CDCl_3$): δ = 7.43 (s), 0.23 (s) ppm.

The 1,3,5-tris(trimethylsilylethynyl)benzene intermediate (9.61 g, 26.3 mmol) was hydrolyzed by treatment with NaOH (aq) (30 mL, 1 M), CH_2Cl_2 (20 mL), and methanol (50 mL) via stirring at room temperature for 3 h. Evaporation of methanol, ether extraction of the residue, and evaporation of the solvent in vacuo yielded 2.68 g of white powder containing 1,3,5-triethynylbenzene. ^{1}H NMR (400 MHz, $CDCl_3$): δ = 7.51 (s), 3.12 (s) ppm.

Trimethylsilylazide (9.26 g, 80.4 mmol) was added to a solution of copper(I) iodide (510 mg, 2.63 mmol) and 1,3,5-triethynylbenzene (2.68 g, 17.8 mmol) under inert conditions in a mixture of dimethylformamide (DMF; 90 mL) and methanol (10 mL). The resulting mixture was stirred at 100 °C for 36 h. The mixture was then filtered and reduced to a volume of 10 mL via rotary evaporation. A pale-yellow precipitate was formed upon the addition of millipore filtered

water (30 mL) to the resulting filtrate. The solid was collected by filtration, washed with ether, and dried in vacuo to yield 4.1 g (83%) of 1,3,5-tris(^{1}H-1,2,3-triazol-5-yl)benzene. ^{1}H NMR (400 MHz, $(CD_3)_2SO$): δ = 8.52 (s), 8.34 (s) ppm. The H_3BTTri used in this work is from the same batch made and used for previous publications.[21,24]

CuBTTri Synthesis and Characterization. CuBTTri was synthesized and characterized according to previously established[22] literature procedures. A solution of H_3BTTri (225 mg, 0.937 mmol) in DMF (40 mL) was prepared in a 250 mL Pyrex bottle $CuCl_2{\cdot}2H_2O$ (383 mg, 2.25 mmol) was added to the solution. The vial was heated at 100 °C for 72 h to afford $H_3[(Cu_4Cl)_3(BTTri)_8(DMF)_{12}]$. The purple powder was washed with boiling DMF (10 × 10 mL) and allowed to dry under ambient conditions to yield 218 mg (76%) of product. Solvent exchange was performed using millipore filtered water to yield $H_3[(Cu_4Cl)_3(BTTri)_8(H_2O)_{12}]$. The resulting light purple powder was analyzed by powder X-ray diffraction (pXRD). The diffraction pattern collected matched a literature standard (Figure S3.9).[22] CuBTTri particles are known to exhibit a largest pore size of approximately 2 nm, measured BET surface area of 1770 to 1900 m^2/g , and to be stable in both boiling water and in solutions where pH = 3.[22,25,55] The CuBTTri particles used in this work are from the same batch of prepared and used in a previous publication.[25]

Reaction Procedure. Reactions were carried out using an identical procedure to previously established methods, [21] with the only meaningful difference being the substitution of blood plasma for water as the solvent in the reaction system. All reactions described herein were stirred by bubbling the solution vigorously with N_2 (g). CuBTTri was massed into a three-neck 50 mL round-bottomed flask and oven dried overnight at 110 °C. Following drying, the flask containing CuBTTri was placed under vacuum for 1 h on a Schlenk line, capped with rubber septa, and backfilled with N_2 (g) prior to reaction. GSNO and GSH solutions (prepared from blood

plasma and solid GSNO or GSH under ambient conditions in 100 mL round-bottomed flasks capped with rubber septa) were then injected into the flasks containing dry CuBTTri. Vigorous bubbling in the round-bottomed flask using an N_2 (g) flow was established, and an exit needle was added to one arm of the reaction flask to allow generated NO (g) to escape. Reaction flasks were wrapped in aluminum foil to prevent exposure to light and reactions proceeded for a predetermined time. To quench the reaction, the exit needle was removed to stop bubbling and the supernatant was immediately decanted via a syringe and injected directly into an NMR tube or quartz UV-VIS cuvette. The ^1H NMR samples contained 0.5 mL of reaction supernatant and 0.1 mL of 20 mM NaH_2PO_4 buffered D_2O. No unanticipated safety hazards were encountered over the course of all experiments. All reactions reported were performed in triplicate.

Reaction Conditions for Measuring the NO Release in Blood Plasma. Three separate trials were completed with standard conditions of: i) 2 mM GSNO, ii) 2 mM GSH, iii) 4.05 mg CuBTTri (for a 2:1 ratio of GSNO molecules to Cu atoms), iv) 25 °C, v) 5 mL reaction volume, and vi) bubbled by N_2 (g). The amounts of each reagent added are summarized in Table 3.3 below. All solutions for this set of experiments were prepared in bovine blood plasma.

Table 3.3. Amounts of each reagent added and the reaction time of experiments where the data collected was used to determine the NO release reaction stoichiometry in blood plasma.

Volume 4 mM GSNO Added (mL)	Volume 4 mM GSH Added (mL)	Mass CuBTTri (mg)	Time (h)
2.5	2.5	4.05	16

Reaction Conditions for Determining the Catalytic Rate in Bovine Blood Plasma. Three separate trials were completed with standard conditions of: i) 1 mM GSNO, ii) 1 mM GSH, iii) 2.7 mg CuBTTri (for a 2:1 ratio of GSNO molecules to Cu atoms), iv) 25 °C, v) 15 mL reaction volume, and vi) bubbled by N_2 (g). The reaction conditions for determining the rate were change

for those used to measure NO release to mimic reaction conditions previously used to measure the catalytic rate in water.[25] The amounts of each reagent added are summarized in Table 3.4 below. All solutions for this set of experiments were prepared in bovine blood plasma.

Table 3.4. Amounts of each reagent added and the reaction time of experiments where the data collected was used to determine the NO release reaction rate in blood plasma.

Volume 3 mM GSNO Added (mL)	Volume 3 mM GSH Added (mL)	Volume Bovine Blood Plasma Added (mL)	Mass CuBTTri (mg)	Time (min)
5	5	5	2.7	20

Details of the ^{1}H NMR Method Used to Measure [$GSSG_{(plasma)}$]. ^{1}H NMR data collection was challenging for several reasons. Blood plasma was a complex matrix containing hundreds of individual components, many overlapping in the visible spectrum that contributed to the observed NMR spectral pattern. It was difficult to quantify the baseline under these conditions and achieve reproducible, quantitative analysis. Fortunately, it was possible to discriminate against many of these species based on differing T_2 relaxation times. For example, for relatively large molecules such as proteins and lipids, an appropriate T_2-weighted pulse-sequence allowed their response to relax more rapidly and vanish from the final spectrum while signals of interest (arising from the GSSG product of the NO release reaction) would survive the filter and be refocused with good intensity. Water itself was also an obstacle since it makes up most of the bulk sample and the NMR response is proportional to the concentration of the molecule measured. This was a dynamic range problem since the H_2O response will be at least 10^4 times more intense than signals of interest. Fortunately, NMR practices exist for managing concerns both concerns (signals arising from components of blood plasma and the intensity of the water signal) at the same time. We used the Varian CPMG-T2 Weighted pulse sequence with pre-saturation (PRESAT) to make measurements. PRESAT provides a weak (50 Hz in our case) RF pulse fixed on the water

resonance (for 1.5 seconds in our case), prior to each pulse-train transient, which improved the dynamic range substantially. We were not interested in following any water exchangeable protons (NH, OH, or SH) so there are no deleterious effects from PRESAT. We next tuned the CPMG portion of the sequence experimentally and found that a CPMG-T2 weighted pulse train with a 250 μs *tau* period and 75 ms re-focusing train provided the best compromise between good intensity of our analyte molecule (GSSG) and a flat baseline (Appendix II, Figure S3.1).

Supporting Information. The following are available in Appendix II: Supporting Information for Chapter III: raw ^{1}H NMR data array of GSSG in blood plasma used to determine the optimal re-focusing train times in the CPMG-T2 weighted pulse sequence, raw ^{1}H NMR data of GSNO in blood plasma, raw ^{1}H NMR data of GSH in blood plasma, UV-VIS data of blood plasma alone, UV-VIS data confirming the loss of GSNO over 16 h, ^{1}H NMR data used to quantify GSSG in blood plasma after 16 h and 20 min, example determination of the catalytic rate in blood plasma, and powder X-ray diffraction data used to characterize the CuBTTri.

REFERENCES

1. Mason, G. F., Behar, K. L., Rothman, D. L. & Shulman, R. G. NMR Determination of Intracerebral Glucose Concentration and Transport Kinetics in Rat Brain. *Journal of Cerebral Blood Flow & Metabolism* **12**, 448–455 (1992).

2. Jian, W., Edom, R. W., Wang, D., Weng, N. & Zhang, S. (Weihua). Relative Quantitation of Glycoisoforms of Intact Apolipoprotein C3 in Human Plasma by Liquid Chromatography–High-Resolution Mass Spectrometry. *Analytical Chemistry* **85**, 2867–2874 (2013).

3. Bligh, S. W. A., Boyle, H. A., Mcewen, A. B., Sadler, P. J. & Woodham, R. H. 1H NMR studies of reactions of copper complexes with human blood plasma and urine. *Biochemical Pharmacology* **43**, 137–145 (1992).

4. Nicholson, J. K., Foxall, P. J. D., Spraul, Manfred., Farrant, R. Duncan. & Lindon, J. C. 750 MHz 1H and 1H-13C NMR Spectroscopy of Human Blood Plasma. *Analytical Chemistry* **67**, 793–811 (1995).

5. de Graaf, R. A. & Behar, K. L. Quantitative 1H NMR Spectroscopy of Blood Plasma Metabolites. *Analytical Chemistry* **75**, 2100–2104 (2003).

6. Ji, Q. C., Rodila, R., Gage, E. M. & El-Shourbagy, T. A. A Strategy of Plasma Protein Quantitation by Selective Reaction Monitoring of an Intact Protein. *Analytical Chemistry* **75**, 7008–7014 (2003).

7. Heinig, K. & Wirz, T. Determination of Taspoglutide in Human and Animal Plasma Using Liquid Chromatography−Tandem Mass Spectrometry with Orthogonal Column-Switching. *Analytical Chemistry* **81**, 3705–3713 (2009).

8. Freeborn, D., Cunningham, L. & LoCicero, R. What Is Plasma? *Health Encyclopedia* (2020).

9. What Is Plasma? *Standford Children's Health*.

10. Sarode, R. Components of Blood. *Merck Manual* (2018).

11. Harding, J. L., Metz, J. M. & Reynolds, M. M. A Tunable, Stable, and Bioactive MOF Catalyst for Generating a Localized Therapeutic from Endogenous Sources. *Advanced Functional Materials* **24**, 7503–7509 (2014).

12. Neufeld, M. J., Ware, B. R., Lutzke, A., Khetani, S. R. & Reynolds, M. M. Water-Stable Metal–Organic Framework/Polymer Composites Compatible with Human Hepatocytes. *ACS Applied Materials & Interfaces* **8**, 19343–19352 (2016).

13. The Human Heart: Blood. *The Franklin Institute* https://web.archive.org/web/20090305043654/http://www.fi.edu/learn/heart/blood/blood.html (2009).

14. Carpenter, A. W. & Schoenfisch, M. H. Nitric oxide release: Part II. Therapeutic applications. *Chemical Society Reviews* **41**, 3742–3752 (2012).

15. Paricio, L., Neufeld, B. & Reynolds, M. Combined influence of nitric oxide and surface roughness in biofilm reduction across bacteria strains. *Biointerphases* **14**, 21004 (2019).

16. Palmer, R. M. J., Ferrige, A. G. & Moncada, S. Nitric oxide release accounts for the biological activity of endothelium-derived relaxing factor. *Nature* **327**, 524–526 (1987).

17. Neufeld, M. J., Lutzke, A., Jones, W. M. & Reynolds, M. M. Nitric Oxide Generation from Endogenous Substrates Using Metal–Organic Frameworks: Inclusion within Poly(vinyl alcohol) Membranes To Investigate Reactivity and Therapeutic Potential. *ACS Applied Materials & Interfaces* **9**, 35628–35641 (2017).

18. Schairer, D. O., Chouake, J. S., Nosanchuk, J. D. & Friedman, A. J. The potential of nitric oxide releasing therapies as antimicrobial agents. *Virulence* **3**, 271–279 (2012).

19. Marletta, M. A. Nitric oxide: biosynthesis and biological significance. *Trends in Biochemical Sciences* **14**, 488–492 (1989).

20. Neufeld, B. H. & Reynolds, M. M. Critical nitric oxide concentration for Pseudomonas aeruginosa biofilm reduction on polyurethane substrates. *Biointerphases* **11**, 31012 (2016).

21. Tuttle, R. R., Rubin, H. N., Rithner, C. D., Finke, R. G. & Reynolds, M. M. Copper ion vs copper metal–organic framework catalyzed NO release from bioavailable S-Nitrosoglutathione en route to biomedical applications: Direct 1H NMR monitoring in water allowing identification of the distinct, true reaction stoichiometries and thio. *Journal of Inorganic Biochemistry* **199**, 110760 (2019).

22. Demessence, A., D'Alessandro, D. M., Foo, M. L. & Long, J. R. Strong CO2 Binding in a Water-Stable, Triazolate-Bridged Metal−Organic Framework Functionalized with Ethylenediamine. *Journal of the American Chemical Society* **131**, 8784–8786 (2009).

23. Paricio, L., Neufeld, B. & Reynolds, M. Combined influence of nitric oxide and surface roughness in biofilm reduction across bacteria strains. *Biointerphases* **14**, 021004 (2019).

24. Harding, J. L. & Reynolds, M. M. Metal Organic Frameworks as Nitric Oxide Catalysts. *Journal of the American Chemical Society* **134**, 3330–3333 (2012).

25. R Tuttle, R., J Folkman, S., N Rubin, H., G. Finke, R. & M. Reynolds, M. Copper Metal–Organic Framework Surface Catalysis: Catalyst Poisoning, IR Spectroscopic, and Kinetic Evidence Addressing the Nature and Number of the Catalytically Active Sites En Route to Improved Applications. *ACS Applied Materials & Interfaces* **0**, (2020).

26. Furukawa, H., Cordova, K. E., O'Keeffe, M. & Yaghi, O. M. The Chemistry and Applications of Metal-Organic Frameworks. *Science* **341**, 1230444 (2013).

27. Cheetham, A. K., Bennett, T. D., Coudert, F.-X. & Goodwin, A. L. Defects and disorder in metal organic frameworks. *Dalton Transactions* **45**, 4113–4126 (2016).

28. Rasheed, T., Rizwan, K., Bilal, M. & Iqbal, H. M. N. Metal-Organic Framework-Based Engineered Materials—Fundamentals and Applications. *Molecules* **25**, 1598 (2020).

29. Yang, J. & Yang, Y.-W. Metal–Organic Frameworks for Biomedical Applications. *Small* **16**, 1906846 (2020).

30. Wu, H. *et al.* Unusual and Highly Tunable Missing-Linker Defects in Zirconium Metal–Organic Framework UiO-66 and Their Important Effects on Gas Adsorption. *Journal of the American Chemical Society* **135**, 10525–10532 (2013).

31. Chen, X. *et al.* Tuning Zr12O22 Node Defects as Catalytic Sites in the Metal–Organic Framework hcp UiO-66. *ACS Catalysis* **10**, 2906–2914 (2020).

32. Li, X. *et al.* Direct Imaging of Tunable Crystal Surface Structures of MOF MIL-101 Using High-Resolution Electron Microscopy. *Journal of the American Chemical Society* **141**, 12021–12028 (2019).

33. Xiao, D. J., Oktawiec, J., Milner, P. J. & Long, J. R. Pore Environment Effects on Catalytic Cyclohexane Oxidation in Expanded Fe2(dobdc) Analogues. *Journal of the American Chemical Society* **138**, 14371–14379 (2016).

34. Bligaard, T. *et al.* Toward Benchmarking in Catalysis Science: Best Practices, Challenges, and Opportunities. *ACS Catalysis* **6**, 2590–2602 (2016).

35. Yang, D. & Gates, B. C. Catalysis by Metal Organic Frameworks: Perspective and Suggestions for Future Research. *ACS Catalysis* **9**, 1779–1798 (2019).

36. Metzger, E. D., Comito, R. J., Hendon, C. H. & Dincă, M. Mechanism of Single-Site Molecule-Like Catalytic Ethylene Dimerization in Ni-MFU-4l. *Journal of the American Chemical Society* **139**, 757–762 (2017).

37. Dincă, M. & Long, J. R. High-Enthalpy Hydrogen Adsorption in Cation-Exchanged Variants of the Microporous Metal−Organic Framework Mn3[(Mn4Cl)3(BTT)8(CH3OH)10]2. *Journal of the American Chemical Society* **129**, 11172–11176 (2007).

38. Dincă, M. *et al.* Observation of Cu2+–H2 Interactions in a Fully Desolvated Sodalite-Type Metal–Organic Framework. *Angewandte Chemie International Edition* **46**, 1419–1422 (2007).

39. Stone, W. H. The Relation of Human and Cattle Blood Groups. *Transfusion* **2**, 172–177 (1962).

40. Steinhardt, J., Krijn, J. & Leidy, J. G. Differences between bovine and human serum albumins. Binding isotherms, optical rotatory dispersion, viscosity, hydrogen ion titration, and fluorescence effects. *Biochemistry* **10**, 4005–4015 (1971).

41. Amin, T. M. & Sirs, J. A. The Blood Rheology of Man and Various Animal Species. *Quarterly Journal of Experimental Physiology* **70**, 37–49 (1985).

42. Raus, J. & Love, D. N. Comparison of the Affinities to Bovine and Human Prothrombin of the Staphylocoagulases from Staphylococcus intermedius and Staphylococcus aureus of Animal Origin. *Journal of Clinical Microbiology* **29**, 570–572 (1991).

43. Hart, T. W. Some Observations Concerning the S-Nitroso and S-Phenylsulphonyl Derivatives of L-Cysteine and G. *Tetrahedron Letters* **26**, 2013–2016 (1985).

44. Dicks, A. P. *et al.* Identification of Cu+ as the effective reagent in nitric oxide formation from S-nitrosothiols (RSNO). *Journal of the Chemical Society, Perkin Transactions 2* 481–487 (1996) doi:10.1039/P29960000481.

45. Seneviratne, U. *et al.* S-nitrosation of proteins relevant to Alzheimer's disease during early stages of neurodegeneration. *Proceedings of the National Academy of Sciences* **113**, 4152 LP – 4157 (2016).

46. Miersch, S. & Mutus, B. Protein S-nitrosation: Biochemistry and characterization of protein thiol–NO interactions as cellular signals. *Clinical Biochemistry* **38**, 777–791 (2005).

47. Iyer, A. K. V, Rojanasakul, Y. & Azad, N. Nitrosothiol signaling and protein nitrosation in cell death. *Nitric oxide : biology and chemistry* **42**, 9–18 (2014).

48. Price, M. E. *et al.* S-nitrosation of protein phosphatase 1 mediates alcohol-induced ciliary dysfunction. *Scientific Reports* **8**, 9701 (2018).

49. Wohuter, K. *et al.* Evidence Against Stable Protein S-Nitrosylation as a Widespread Mechanism of Post-Translational Regulation. *Molecular Cell* **69**, 438–450 (2018).

50. Choi, L.-S. & Bayley, H. S-Nitrosothiol Chemistry at the Single-Molecule Level. *Angewandte Chemie International Edition* **51**, 7972–7976 (2012).

51. Hoffman, R., Minkin, V. I. & Carpenter, B. K. Ockham's Razor and Chemistry. *International Journal for Philosophy of Chemistry* **3**, 3–28 (1997).

52. Broniowska, K. A., Diers, A. R. & Hogg, N. S-nitrosoglutathione. *Biochimica et biophysica acta* **1830**, 3173–3181 (2013).

53. Keszler, A., Zhang, Y. & Hogg, N. Reaction between nitric oxide, glutathione, and oxygen in the presence and absence of protein: How are S-nitrosothiols formed? *Free radical biology & medicine* **48**, 55–64 (2010).

54. Pocius, P. A., Clark, J. H. & Baumrucker, C. R. Glutathione in Bovine Blood: Possible Source of Amino Acids for Milk Protein Synthesis. *Journal of Dairy Science* **64**, 1151–1154 (1981).

55. Zhao, Y. H., Abraham, M. H. & Zissimos, A. M. Fast Calculation of van der Waals Volume as a Sum of Atomic and Bond Contributions and Its Application to Drug Compounds. *The Journal of Organic Chemistry* **68**, 7368–7373 (2003).

IV. COPPER METAL-ORGANIC FRAEWORK SURFACE CATALYSIS: CATALYST POISONING, IR SPECTROSCOPIC, AND KINETIC EVIDENCE ADDRESSING THE NATURE AND NUMBER OF THE CATALYTICALLY ACTIVE SITES EN ROUTE TO IMPROVED APPLICATIONS[1]

Overview

The metal–organic framework (MOF) $H_3[(Cu_4Cl)_3–(BTTri)_8$, H_3BTTri = 1,3,5–tris(^{1}H–1,2,3–triazol–5–yl)benzene] (CuBTTri) is a precatalyst for biomedically relevant nitric oxide (NO) release from *S*–Nitrosoglutathione (GSNO). The questions of the number and nature of the catalytically most active, kinetically dominant sites are addressed. Also addressed is whether or not the well–defined structural geometry of MOFs (as solid–state analogues of molecular compounds) can be used to generate specific, testable hypotheses about, for example, if intrapore vs exterior surface metal sites are more catalytically active. Studies of initial catalytic rate vs CuBTTri particle external surface area to interior volume ratio show that intrapore copper sites are *inactive* within experimental error ($\leq 1.7 \times 10^{-5}$ % of the observed catalytic activity)—restated, the traditional *MOF intrapore metal site catalysis* hypothesis is disproven for the current system. *All* observed catalysis occurs at exterior surface Cu sites, within experimental error. FT–IR analysis of CN^- poisoned CuBTTri reveals just two *detectable* Cu sites at a ca. ≥0.5% detection limit, those which bind 3 or 1 CN^- ("$Cu(CN)_3$" and "CuCN"), corresponding to CN^- binding expected for exterior surface, 3–coordinate ($Cu_{surface}$) and intrapore, 5–coordinate (Cu_{pore}) sites predicted by the idealized, metal–terminated crystal structure. Two coordinate Cu defect sites are ruled out at the

[1] The work presented in Chapter IV contains the entire published manuscript describing our investigations into the location, proportion, and identity of the catalytically active copper sites in CuBTTri for GSNO to NO conversion catalysis (Tuttle, R. R.; Folkman, S. J.; Rubin, H. N.; Finke, R. G.; Reynolds, M. M. *ACS Appl. Mater. Interfaces* **2020**, *35*, 39043-39055.). Minor formatting edits have been introduced to meet the dissertation requirements.

≥0.5% FT–IR detection limit as such defect sites would have been detectable by the FT–IR studies of the CN^- poisoned catalyst. Size–selective poisoning studies of CuBTTri exterior surface sites reveal that 1.3(±0.4)% of total copper in 0.6 ± 0.4 μm particles is active. That counting of active sites yields a normalized TOF, $TOF_{norm} = (4.9 \pm 1.2) \times 10^{-2}$ mol NO (mol $Cu_{surface})^{-1}$ s^{-1} (in water, at 20 min, 25 °C, 1 mM GSNO, 30% loss of GSNO, and 1.3 ± 0.4 mol% $Cu_{surface}$)—a value ~100× higher than the TOF calculated without active site counting. Overall, the Ockham's razor interpretation of the data is that exterior surface, $Cu_{surface}$ sites are the catalytically most active sites present at a 1.3(±0.4)% level of total Cu.

4.1 Introduction

Crystalline metal–organic frameworks (MOFs) can be viewed as extended, solid–state versions of discrete coordination complexes. As such, they offer special opportunities rare in even all of catalysis.[1,2] From their synthesis and well–defined structures, MOFs permit an upfront, *a priori*[3,4] estimation of the location / type of each metal site—and, hence, an upfront idea of at least the primary possibilities for the catalytically active sites—based on an idealized MOF crystal structure and ignoring the important possibility of defect active sites for the moment. This level of upfront information allows the construction of more specific hypotheses about what might, or might not, be the true catalytically active site in MOFs compared to traditional heterogeneous catalysts composed of metals on oxide supports, for example. Knowledge of at least what is not the active site, en route to better ideas about the true active site, in any catalyst is, in turn, central information relevant to that catalyst system, its applications, and its rational improvement.

However, despite over 60,000 MOF structures being known at present[5] and many uses of MOFs in catalysis, no prior study exists which both quantifies the number of active sites in MOF–based catalysts, and also provides evidence for the catalytically active site(s), including at least

consideration of defects as the possible kinetically dominant active site. This means, in turn, that fundamental values in catalysis such as the turnover frequency (TOF, moles product/(moles active sites • time))[6] are not precisely known for most MOF catalysts because the number of active sites is not known.[7–12] Indeed, Boudart long ago noted that catalyst TOF values should be normalized to the percentage of active sites for all catalysts.[13] The work that follows also addresses the open question in MOF catalysis of if, for a given catalytic reaction, the intrapore metal sites are more active—the traditional *MOF intrapore metal site catalysis* hypothesis—or if those intrapore sites are actually inconsequential in comparison to exterior surface or to some unknown defect site(s).

Fully consistent with the above statements, Yang and Gates note in their insightful review of MOF catalysis that, "research is needed to… identify catalytic sites, and determine intrinsic catalytic reaction rates."[14] They also note that, "A few researchers have reported turnover frequencies of MOF catalyzed reactions,[15] but often questions have remained about whether the sites were identified and counted correctly, whether they were all equivalent, and whether they were all fully accessible."[14] In short, determination of the number, and ideally at least some information about the identity of MOF active sites while testing the hypothesis of MOF intrapore metal site catalysis, and at least including the possibility of defect active sites[16] is an important, fundamental problem in MOF catalysis. Also noteworthy is that the number and at least some idea of the possible identity of the catalytically most active sites is needed before more meaningful full rate law and associated mechanistic studies can be performed. That mechanistic insight is then in turn required for mechanistically guided design of the next generation of MOF–based catalysts, studies that then ideally exploit the enormous synthetic variability and fine–tunability of MOF–based systems (discussion of the valuable reference #18 is provided in the References section for the interested reader).[4,17,18]

Copper–based MOF $H_3[(Cu_4Cl)_3–(BTTri)_8]$: A Catalyst for Biomedical Applications

Incorporation of the copper–based MOF $H_3[(Cu_4Cl)_3–(BTTri)_8$, where H_3BTTri = 1,3,5–tris(^{1}H–1,2,3–triazol–5–yl)benzene] (CuBTTri, Figure 4.1) into biomedical devices has been shown to be effective for catalyzing for nitric oxide (NO) release *in vivo*.[19–23] The controlled release of NO results in the desired effects of vasodilation,[24,25] reduction in biofilm formation on implanted medical devices,[26,27] and also antibacterial activity.[28,29] Among copper–based MOFs, CuBTTri is unique in its high hydrothermal stability,[30] in its ability to catalyze NO release from the endogenous, nitrosated tripeptide *S*–Nitrosoglutathione (GSNO),[22,21] and in its compatibility with human blood and hepatocytes.[20,23]

The effectiveness of CuBTTri catalysis for NO release from the bulky GSNO substrate is actually a surprising result, at least if one is expecting CuBTTri intrapore Cu sites to be the dominant catalytically active site, given that the large GSNO tripeptide substrate should experience relatively slow to no diffusion into (and glutathione disulfide (GSSG) product, which is twice as large as GSNO, out of) the pores of CuBTTri. Additionally a Cu(II)/Cu(I) redox reaction is at least presently suspected as the most probable mechanism,[31–35] so that 5–6 coordinate Cu(II) intrapore sites in CuBTTri (Cu_{pore}) should then be *largely unreactive* due to an anticipated prohibitive Marcus–type intrinsic barrier for rearrangement of a 5–6 coordinate Cu(II) to a 4–coordinate Cu(I) site.[36] Restated, little to no CuBTTri catalysis of NO release from GSNO is expected *if* Cu_{pore} sites are the dominant catalytically active sites. Experimentally, the *opposite* result is observed: CuBTTri is an effective precursor for catalysis of NO release from GSNO[20,37], an observation that by itself strongly suggests that the catalytically most active sites are exterior surface Cu sites[30,38,39] that we will label $Cu_{surface}$, or possibly some other type of surface defect site that we label Cu_{defect}. Noteworthy here is that the surface metal sites in CuBTTri can be described as naturally occurring,

particle-termination sites or missing-linker sites[40], so in that sense "defect" sites. However, we will retain the descriptor Cu_{defect} to sites *different than* $Cu_{surface}$ sites (*vide infra*).

Given the open question of how active intrapore vs exterior surface or defect sites are in a given MOF–catalyzed reaction, the CuBTTri catalysis examined herein is an interesting if not prototype system with which to probe the number and nature of the catalytically active site(s). The next question is how should one think about the possible types of active sites, and their relative number, even if in a basic, initial way? This is where MOFs as three-dimensional solids with repeating structural units would seem to have an upfront advantage, at least ideally and if one again ignores for the moment defects that one expects to be present. Although no single–crystal x–ray diffraction data has been obtained specifically for CuBTTri, a matching powder X–ray diffraction (P–XRD) pattern[30] between CuBTTri and the X–ray diffraction crystallographically characterized[38] Cu–MOF $H[(Cu(DMF)_6][(Cu_4Cl)_3(BTT)_8–(H_2O)_{12}]•3.5HCl•12H_2O•16CH_3OH$ confirms that these two MOFs are isostructural save their different organic linker. From that structural data, the idealized, starting structural model for CuBTTri shown in Figure 4.1 can be generated.

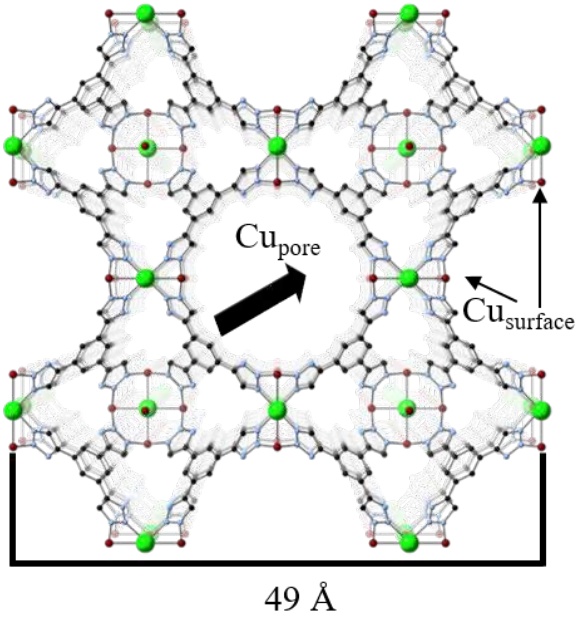

Figure 4.1. Idealized, defect-free view of one layer of the metal–terminated CuBTTri unit cell showing Cu_{pore} and $Cu_{surface}$ sites with carbon (black), nitrogen (blue), chlorine (green), and copper (red).[30,38,39] One question the current work will address is "how useful is it to design and interpret experiments at least to start based on this idealized view of the structure and the Cu sites shown?"

Using the idealized, metal–terminated structure in Figure 4.1 as a starting point, two types of copper sites are apparent in Figure 4.1: (i) intrapore, 5–coordinate Cu sites (defined as Cu_{pore} to denote *any and all 5–coordinate Cu sites),* and (ii) 3–coordinate Cu sites at the particle exterior surface (defined as $Cu_{surface}$ to denote *any and all 3–coordinate Cu sites*), ignoring *for the moment* (*vide infra*) complicating issues such as the possibility that surface Cu atoms could be terminated by the H_3BTTri ligand,[41] Cl^-, or solvent ligands. Hence, using the structural model in Figure 4.1 as an initial working hypothesis, we have at minimum two types of possible active sites, Cu_{pore} and $Cu_{surface}$ sites. We can then add to this a third category, Cu_{defect}, defined as any and all defect sites. A fourth possibility for the active catalyst, that of Cu leached from the MOF, has already been ruled out at the <<1% level in previous studies.[37]

Questions Addressed in the Present Studies

The questions addressed in the work that follows are: (i) the number of active sites, and hence in turn (ii) the question of can one obtain a normalized TOF (TOF_{norm}), computed using the experimentally determined number of active sites from catalyst poisoning studies. Our results also address (iii) the question of whether or not one can distinguish exterior surface from intrapore catalytic sites in the CuBTTri / GSNO system, and also (iv) the issue of if some defect site (i.e., perhaps formed mechanochemically as a result of grinding particles to generate higher surface area), *that by definition has to be distinguishable experimentally* from the Cu_{pore} and $Cu_{surface}$ sites, is the kinetically dominant catalyst. Additionally, our results address (v) the question of what methods and spectroscopies might best probe both exterior surface vs intrapore sites as well as their relative activity, and (vi) the related question of the number of vacant coordination sites in $Cu_{surface}$ and Cu_{pore} sites. Additionally, we address (vii) the question of how useful, or perhaps misleading, is the idealized structure of the MOF–based catalyst (Figure 4.1) and the therefore *a priori* identifiable, possible active sites[6,14,16,17,40] of $Cu_{surface}$ and Cu_{pore}? That is, does using the 5–coordinate Cu_{pore} and 3–coordinate $Cu_{surface}$ sites as defined above as a starting, working hypothesis to be tested prove useful in trying to understand the CuBTTri MOF based catalysis? Does it aid or mislead one in the design of effective experiments and their, at least, initial interpretation? Overall, five specific hypotheses for the number and type of catalytically Cu active sites within CuBTTri will be tested in what follows, hypotheses that will be listed after the Experimental section provided next, but at the start of the Results and Discussion section.

4.2 Results and Discussion

Five Hypotheses for the Type and Hence Relative Number of Catalytically Active Copper Sites Derived From CuBTTri

Five hypotheses, for the number and location of active copper sites for GSNO to NO conversion catalyzed by CuBTTri, are the following:

1) That leached Cu is the actual, true catalyst. As already mentioned in the Introduction, this initial hypothesis was definitively ruled out previously, by glutathione (GSH) poisoning of Cu^{n+} catalysis and inductively coupled plasma atomic emission spectroscopy. Hence, it need not be considered further.[37]

2) That 100% of the active copper sites are 5–coordinate $Cu(II)_{pore}$ sites close to if not indistinguishable from those predicted by the CuBTTri crystal structure, Figure 4.2B. This is essentially the traditional *MOF intrapore metal site catalysis* hypothesis;

3) That 100% of the active copper sites are 3–coordinate, what we have labeled $Cu(II)_{surface}$, sites close to if not indistinguishable from those in the simplified, idealized metal–terminated CuBTTri structure, Figure 4.2A, 4.2C;

4) That 100% of the observed catalysis is caused by defect sites in CuBTTri (Cu_{defect}) that are, as defined in this manuscript, not among the *a priori* identifiable 5– or 3–coordinate sites in hypotheses **2** and **3**; and then the possibility

5) That some combination of Cu_{pore}, $Cu_{surface}$, and Cu_{defect} sites are active.

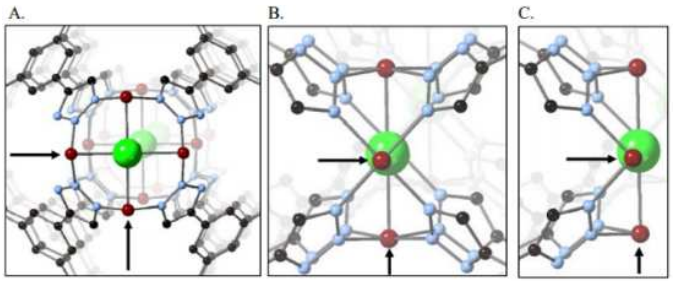

Figure 4.2. Finer, more detailed view than provided in Figure 4.1 of nominally 3–coordinate $Cu_{surface}$ (A and C) and nominally 5–coordinate Cu_{pore} (B) (red = copper, green = chlorine, blue = nitrogen, black = carbon) based on the x–ray structure of an isostructural MOF[38] and assuming to start an idealized, metal–terminated surface of CuBTTri.[30,39] All Cu atoms indicated with arrows in each respective figure have equivalent coordination numbers. Vacant coordination sites within CuBTTri would presumably be occupied by H_2O pre–reaction while surface Cu sites could be coordinated by anything from H_3BTTri ligand[41] to Cl^- to H_2O, ligands that, however, are expected (and hence assumed in what follows) to be displaced by GSNO or GSH in the catalytic reaction—an assumption supported quantitatively by the results that follow, *vide infra*. Hydrogen atoms have been omitted for clarity. Reproduced with permission from the Supporting Information of reference 38. Copyright 2019 Elsevier.

A key experiment to start is to find a way to vary the ratio of exterior surface to intrapore Cu sites in a given CuBTTri MOF sample, and to see if doing that increases, decreases, or does not affect the catalytic rate. The ideal approach to generate Cu–MOF particles of designed and desired size would be to synthesize / grow them in a controlled fashion across a wide range of particle sizes. That, however, is itself an unsolved, state–of–the–art problem.[42–44] Hence, one currently available option is grinding and sieving / filtering the ground particle to change the CuBTTri sample particle size and, hence, also the ratio of the exterior surface area to the interior volume. Doing so also changes the ratio of exterior surface Cu sites vs Cu_{pore} sites (and possibly if not probably introduces Cu_{defect} sites of some unknown specific coordination number and associated ligands). The resultant study of particle size / external surface area vs initial catalytic rate proved quite interesting, as discussed next.

Grinding and Filtration of CuBTTri to Generate Three Different Particle Size Domains with Associated Increasing External Surface Area

Three sets of CuBTTri particles were obtained for measuring the catalytic rate versus particle size. First, large particles in the millimeter range (MOF_{Large}, ~1 mm, Table 4.1) were picked out from CuBTTri samples by hand using tweezers. Second, hand–ground CuBTTri particles (MOF_{Ground}) were obtained by hand–grinding the MOF powder in a mortar and pestle for 5 min. Third, filtered CuBTTri particles ($MOF_{Filtered}$) were obtained by gravity filtering suspensions of MOF_{Ground} samples in water through a cell strainer with a mesh size of 1 μm. The yield of $MOF_{Filtered}$ was maximized by sonication (10 min) of the MOF_{Ground} samples from which the finer $MOF_{Filtered}$ was obtained. The efficacy of these cell strainers for filtering out particles equal to or larger than 1 μm in length was evaluated via scanning electron microscopy (SEM, Table 4.1, Appendix III, Figures S4.6-S4.11) and dynamic light scattering (DLS). The DLS showed that particles larger than 1 μm are effectively removed by the strainers employed (Appendix III, Figure S4.3). Analysis of SEM micrographs yields average particle sizes of 1.5 ± 0.4 μm for MOF_{Ground} samples (100 particles counted) and 0.6 ± 0.4 μm for $MOF_{Filtered}$ samples (100 particles counted). While even more particle size distributions could in principle be obtained and would lower the error estimates on the particle size distributions, the samples prepared proved adequate for the purposes of this study and the conclusions drawn, *vide infra*.

Table 4.1. Optical microscope image of a MOF_{Large} particle, SEM micrographs of MOF_{Ground} and $MOF_{Filtered}$ particles, method of generation, average size, exterior surface area (ExSurArea) to interior volume (IntVol) ratio, and the initial observed catalytic rate ($[-d[GSNO]/dt]_i$) for each particle set.

Sample	MOF_{Large}	MOF_{Ground}	$MOF_{Filtered}$
Image	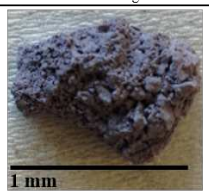	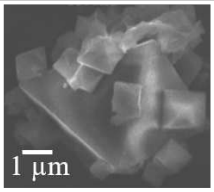	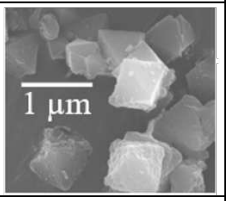
Method of Generation	CuBTTri as Synthesized	Hand Ground CuBTTri	Gravity Filtered CuBTTri
Average Size	~ 1 mm	1.5 ± 0.4 µm	0.6 ± 0.4 µm
ExSurArea/IntVol (m^{-1})	1.0×10^{-5}	$0.7 \pm 0.1 \times 10^{-2}$	$1.9 \pm 0.6 \times 10^{-2}$
$[-d[GSNO]/dt]_i$	0 mM s^{-1}	$1.6 \pm 0.25 \times 10^{-4}$ mM s^{-1}	$2.9 \pm 0.3 \times 10^{-4}$ mM s^{-1}

Observed Initial Catalytic Rate versus CuBTTri Particle Size

Studies of the observed initial catalytic rate for GSNO to NO conversion ($[-d[GSNO]/dt]_i$) vs CuBTTri MOF particle size and associated external surface area were performed and are summarized in Figures S4.4-S4.5 of Appendix III.[14,16,45] First, when the MOF_{Large}, ~1 mm particles (with their low exterior surface area to interior volume ratio) are used, *no detectable loss of GSNO (or generation of GSSG product) is observable by ^1H NMR over 20 min*, $[-d[GSNO]/dt]_{i,MOF\textbf{Large}}$ = 0 mM s^{-1}. However, to determine if the larger particles are actually contain active sites as anticipated, but just slow (e.g., due to a low number of active sites due to their low exterior surface area to interior volume ratio, *vide infra*) control experiments were run with the MOF_{Large} particles over 6 to 9-fold longer times of 120 and 180 min. Those experiments show 8% and 14% loss of GSNO over the 120 and 180 min reaction times, respectively. Hence, some—but still relatively slow—NO release catalysis is observed for MOF_{Large} particles. This important observation supports the hypothesis that the MOF_{Large} particles contain naturally occurring active sites for GSNO to NO conversion (Appendix III, Figure S4.16), but just low numbers of them. This result rules out the limiting alternative hypothesis (raised by an insightful referee's query) that *all* of the

catalytically active sites could be created solely by mechano-chemistry as a result of the grinding process. The answer is "no", because at least some activity is present before any grinding to increase the surface area is performed.

Next, MOF_{Ground} particles with their ~10^3–fold increase in external surface area (Table 4.1) over MOF_{Large} particles were examined for their GSNO conversion and associated NO release catalysis. GSNO loss *is* now observed on the 20 min timescale when using the higher surface area MOF_{Ground} particles, $[-d[GSNO]/dt]_{i,MOF\mathbf{Ground}} = (1.6 \pm 0.25) \times 10^{-4}$ mM s^{-1}. Control shows that no effect of grinding the CuBTTri particles is detectable by P–XRD (Appendix III, Figure S4.2), although this only shows that the Cu-MOF is still mostly "bulk" sample structurally. In a third set of experiments using the even higher surface area $MOF_{Filtered}$ particles (with their ~2–fold increase in exterior surface area to interior volume ratio compared to MOF_{Ground}, Table 4.1), the initial rate of GSNO substrate loss once again increased, *approximately double* in comparison to that for MOF_{Ground} particles, $[-d[GSNO]/dt]_{i,MOF\mathbf{Filtered}} = (2.9 \pm 0.3) \times 10^{-4}$ mM s^{-1}, implying a linear dependence of the catalytic rate on the surface area.

The increase in $[-d[GSNO]/dt]_i$ at 20 min as particle size decreases (last row of Table 4.1), and therefore as the exterior surface area to interior volume ratio increases, is consistent with and supportive of catalysis occurring at $Cu_{surface}$ sites,[46–48] or conceivably at a surface Cu_{defect} site that scales linearly in production with $Cu_{surface}$ sites as particle exterior surface area increases (hypotheses **3** and **4**, *vide supra***)**. The results strongly suggest that low coordinate $Cu_{surface}$ sites or equivalent Cu_{defect} sites (either *exposed* or *created* by the grinding process to break up the aggregated MOF_{Large} particles) are more active than Cu_{pore} sites. This valuable result in turn disproves hypotheses **2** and **5**, that is, disproves the traditional *MOF intrapore metal site catalysis* hypothesis. Hence, Cu_{pore} sites are *not* the kinetically dominant active sites.

Plot of the Catalytic Rate vs Exterior Surface Area to Interior Volume Ratio

It proved instructive to analyze the catalytic rate vs particle size and associated surface area in more detail, in particular the catalytic rate vs the external surface area to interior volume ratio. The volume denominator is required because although a constant total mass was used between samples of $MOF_{Large/Ground/Filtered}$, the total number of particles in each MOF_{Ground} or $MOF_{Filtered}$ sample is not known. Figure 4.3 shows a plot of the calculated exterior surface area to interior volume ratio vs the particle size for octahedral symmetry particles (O_h symmetry being observed in the particle's SEM images over the size range of MOF_{Ground} and $MOF_{Filtered}$ samples; see calculation S4.2 in Appendix III). The bar diagrams show the ranges spanned by $MOF_{Filtered}$ and MOF_{Ground} particles.

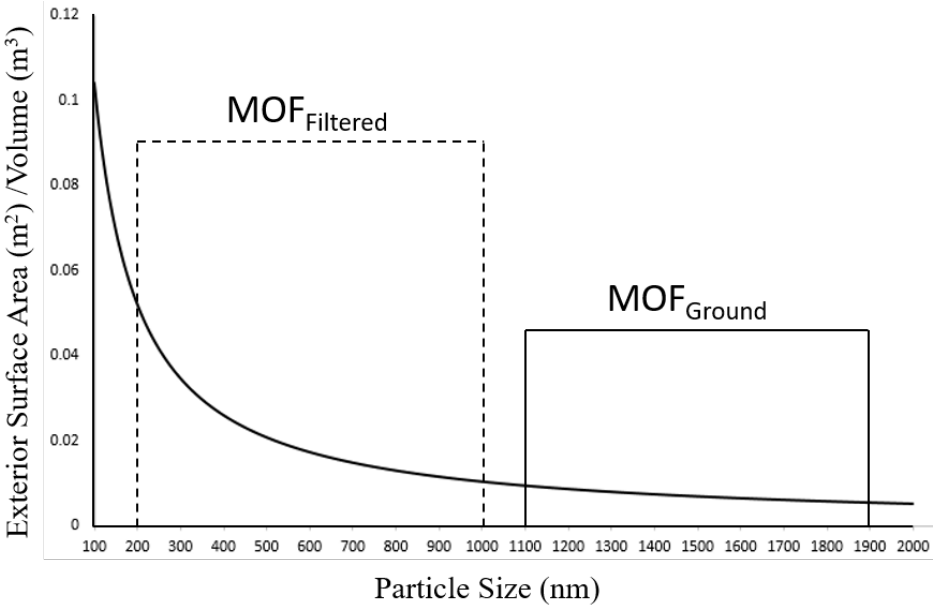

Figure 4.3. The ratio of exterior surface area to interior volume at varying octahedral particle size. This curve is fit by an empirical inverse power function equal to $y = 9.8x^{-0.992}$, $R^2 = 0.98$.

Next, in a plot with a telling result, the experimentally observed catalytic rate was then plotted against the calculated exterior surface area to interior volume ratio for all three particle sizes studied, Figure 4.4. *The plot in Figure 4.4, while showing only 3 data points and larger than*

ideal error bars on the $MOF_{Filtered}$ data, demonstrates a first–order dependence of the catalytic rate, $[-d[GSNO]/dt]_i$, on the exterior surface area / interior volume ratio:

$$\left[-\frac{\mathrm{d[GSNO]}}{\mathrm{dt}}\right] = k_{1,obs}[\text{Exterior Surface Area}] \cdot \left[\frac{1}{\text{Interior Volume}}\right] \quad \text{(eq. 4.1)}$$

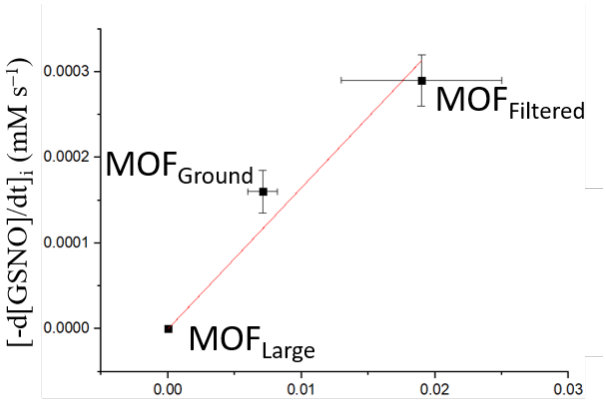

Figure 4.4. Plot of $[-d[GSNO]/dt]_i$ as a function of the external surface area to interior volume ratio for octahedral CuBTTri particles in the size domains studied. The data point for MOF_{Large} is not at the origin (0 m^{-1}, 0 mM s^{-1}), but corresponds to the calculated exterior surface area to interior volume ratio and the experimentally observed catalytic rate (1.0×10^{-5} m^{-1}, 0 mM s^{-1}). The linear trend line is fit by the equation $y = ((1.8 \pm 0.4) \times 10^{-2})\boldsymbol{x} - (1.7 \pm 0.3) \times 10^{-7}$, $R^2 = 0.97$. Physically, the intercept cannot be negative ($-(1.7 \pm 0.3) \times 10^{-7}$ mM s^{-1}). Hence, and at 3 sigma, the error is taken to be $(\pm(1.7 \pm 0.3)) \times 10^{-7}$ mM s^{-1}. All values of $[-d[GSNO]/dt]_i$ were measured at 20 min reaction time and all values represent the average and standard deviation of three trials.

In equation 4.1, the observed rate constant ($k_{1,obs}$) is equal to the slope of the line in Figure 4.4 ($(1.8 \pm 0.4) \times 10^{-2}$ mM s^{-1} m^{-1}). Importantly, the y–intercept in Figure 4.4 ($\pm(1.7 \pm 0.3) \times 10^{-7}$ mM s^{-1}) *has information about where 100* $\pm$ ~(1.7×10^{-5})*% of the catalytic activity comes from.* As surface area / volume approaches zero (as in MOF_{Large} particles) , the type of available Cu sites approaches only Cu_{pore} sites, and the resulting catalytic activity expressed by the intercept is zero within experimental error. The inescapable implication is that the Cu_{pore} sites carry zero of the catalytic activity—to quantitate it, precisely $0 \pm ((1.7 \pm 0.3) \times 10^{-7})$ mM s^{-1} of the catalytic activity. As a control, we estimated the error in the intercept a second way, using the maximum and minimum lines possible from the data in Figure 4.4. Doing so provided an intercept of $\pm(2.9 \pm 0.3) \times 10^{-5}$ mM s^{-1} and, hence, once again zero within a very small experimental error.

Figure 4.4 provides further disproof of the classic hypothesis of MOF intrapore metal-site catalysis, disproof at the level of $\leq \pm 10^{-5}$ mM s^{-1} of the catalytic activity. Hence, either the $Cu_{surface}$ or putative Cu_{defect} sites that correlate with the amount of external surface area (or conceivably some combination of these two) are implicated as the kinetically dominant, catalytically active site in CuBTTri-based conversion of GSNO to NO.[37]

Equation 4.1 can be rewritten to yield a rate equation that more directly reflects the proportion(s) of Cu sites (Equation 4.2) using the fact that the proportion of $Cu_{surface}$ (or, conceivably, Cu_{defect}) sites scales linearly with exterior surface area and the proportion of Cu_{pore} sites scales linearly with interior volume in a sample of CuBTTri.

$$\left[-\frac{d[GSNO]}{dt}\right] = k_2[\text{Exterior Surface Cu}] \cdot [\frac{1}{Cu_{pore}}] \text{ (eq. 4.2)}$$

This formulation of the results once again makes clear that the activity of Cu_{pore} sites is very low (zero within experimental error), and leaves $Cu_{surface}$ as well as Cu_{defect} sites of some unspecified nature but that are produced in the grinding process (in that hypothesis) as the remaining possibilities for the kinetically dominant active site(s).

Unselective Poisoning of MOF_{Ground} and $MOF_{Filtered}$ Particles with KCN

Quantitative catalyst poisoning was turned to next because studies using the proper poisons can offer insight into the number of active sites. First, the anticipated unselective catalyst poison CN^- was used, CN^- being a strong sigma–donor and hence good Cu(II) poison that should also be able to diffuse at least some length into the largest central channel of CuBTTri (unhydrated diameter ~20 Å vs CN^- unhydrated van der Waals diameter of ~4 Å as its K^+ salt).[49] CN^- is therefore expected to *unselectively bind and hence irreversibly poison both intrapore and exterior surface Cu sites*.[50,51]

Quantitative, kinetic poisoning studies using KCN were carried out on MOF_{Ground} and $MOF_{Filtered}$ samples—from the same batch of CuBTTri as used to generate the data in Table 4.1 to provide consistency in the data and avoid unnecessary complications in its analysis. An initial experiment revealed that CN^- poisoning is, as expected, very effective: 2 equivalents of CN^- added per total Cu in a given CuBTTri MOF_{Ground} sample resulted in *complete poisoning*, with no catalysis observed within the normal initial time point of 30 min (Appendix III, Figure S4.12). Figure 4.5 shows the experimental $[-d[GSNO]/dt]_i$ as a function of equivalents of KCN added per total copper for MOF_{Ground} and $MOF_{Filtered}$ samples. Based on linear fits of the data in Figure 4.5, approximately 1.6 and 2.6 equivalents of CN^- per total Cu atoms are required to completely poison the Cu–MOF_{Ground} and Cu–$MOF_{Filtered}$ particles, respectively.

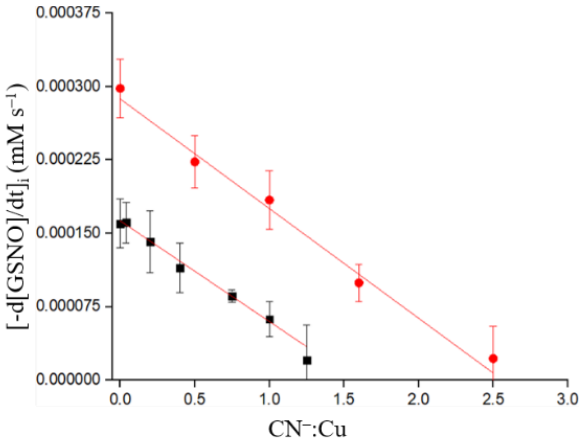

Figure 4.5. KCN poisoning curves for MOF_{Ground} (square, black) and for the finer, higher exterior surface area to interior volume ratio $MOF_{Filtered}$ (circle, red) particles. All values of $[-d[GSNO]/dt]_i$ were measured at 20 min reaction time. All experiments were conducted using the same mass of CuBTTri (~2.7 mg). Each data point represents the average and standard deviation of three trials.

Given the catalytic rate vs MOF external surface area evidence provided previously indicating that $Cu_{surface}$ sites (and / or linearly correlating Cu_{defect} sites) are the kinetically dominant active sites, if CN^- were poisoning *only* those active sites, then the x–intercepts of the curves would be lower by *approaching an order of magnitude* (exterior surface area is less than 3% of interior volume in both MOF_{Ground} and $MOF_{Filtered}$ samples). Hence, the observed, much larger x–intercepts

(1.6 and 2.6 equivalents / total Cu) are fully consistent with the anticipated result that CN^- is *unselectively binding* both the $Cu_{surface}$ and at least the Cu_{pore} sites CN^- is able to reach by diffusion in 30 minutes and under the other reaction conditions provided in the Experimental section.

Very interesting in Figure 4.5 is that significantly more CN^- (2.6 vs 1.6 equivalents / total Cu) is required to completely poison the smaller, higher surface area, $MOF_{Filtered}$ particle samples in comparison to the larger, lower surface area MOF_{Ground} samples. We hypothesize that the difference in x–intercepts occurs not because all Cu_{pore} sites can be reached by CN^- in the 30 min chosen for the poisoning experiment, but that in the smaller particle size samples more Cu_{pore} sites are accessible in 30 minutes. FT–IR results to follow will support the thesis that even the relatively small CN^- cannot readily diffuse deep into the CuBTTri, at least in 30 min at 25 °C in unstirred solutions.

FT–IR Analysis of the Poisoned Catalyst

At this point, we returned to the idealized MOF structural geometry in the CuBTTri catalyst system and the predicted, if idealized, $Cu_{surface}$ and Cu_{pore} sites to see what type of spectroscopy could be used to identify the types of sites present. The $Cu_{surface}$ and Cu_{pore} sites in Figure 4.2 *have 3–coordinate and 5–coordinate geometries*, respectively. Additionally, a search of FT–IR stretching frequencies of $Cu(CN)_x$ complexes revealed that they are known to be quite sensitive to the number of coordinated cyanides.[52,53] Hence, if there is any reliability of the idealized structures in Figures 4.1 and 4.2, $Cu_{surface}$ and Cu_{pore} will bind more vs less CN^-, and presumably X = 3 vs 1 CN^-, respectively. That is*, one expects that the coordination number and Cu site location of the CN^- poison can be probed directly by FT–IR analysis of the poisoned catalyst*. The more detailed prediction is that at least two CN^- to Cu binding modes within CN^- poisoned CuBTTri should be present, one for 3–coordinate $Cu_{surface}$ sites, nominally "$Cu(CN)_3$", and one for 5–coordinate Cu_{pore}

sites, nominally "$Cu(CN)_1$" —plus possibly a third band if any Cu_{defect} site is present with a coordination number not predicted by the metal–terminated CuBTTri crystal structure, for example 2–coordinate Cu poisoned as "$Cu(CN)_4$" (≥0.5% should be detectable, *vide infra*).

To start and as a control, the FT–IR spectrum of a KCN poisoned $MOF_{Filtered}$ CuBTTri sample (Figure 4.6) was compared to the known complexes[54–59] KCN, $[CuCN]^+$, $[Cu(CN)_2]$, $[Cu(CN)_3]^-$, and $[Cu(CN)_4]^{2-}$ as KBR pellets and homogeneous complexes.

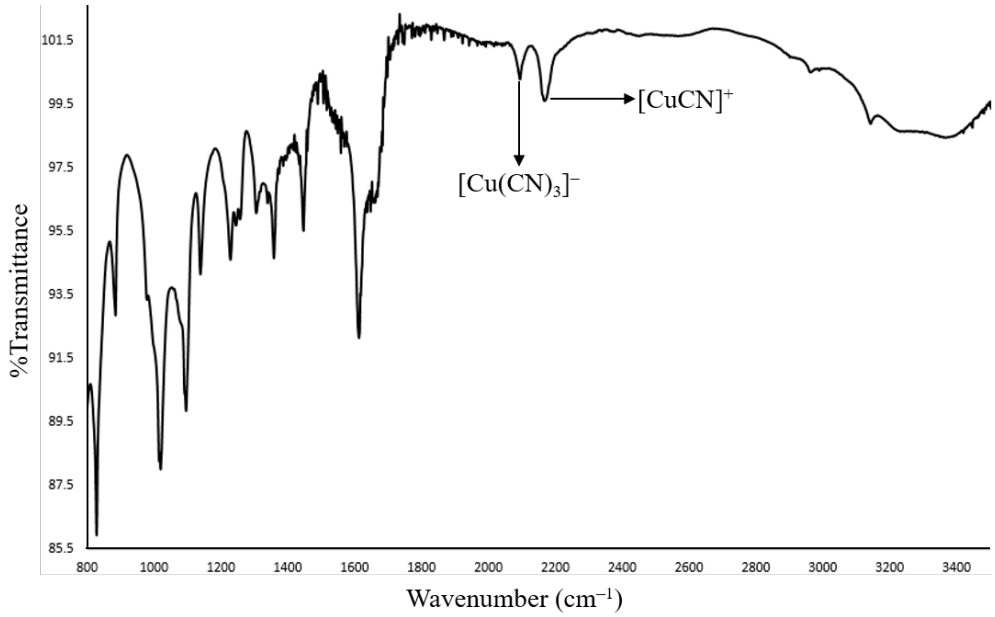

Figure 4.6. FT–IR spectrum of $MOF_{Filtered}$ CuBTTri poisoned with 1.5 equivalents of CN^- from 800 to 3400 cm^{-1}. The expected $Cu_{surface}$ ($3CN^-$:1Cu) binding mode is observed at 2093 cm^{-1}. The expected Cu_{pore} ($1CN^-$:1Cu) binding mode is observed at 2169 cm^{-1}. No other cyanide to copper binding mode stretches are observed. Signals between 800 and 1800 cm^{-1} are attributed to vibrational modes of GSH and GSSG adsorbed onto the CuBTTri surface.

$MOF_{Filtered}$ samples of the CuBTTri powder poisoned with 1.5 equivalents of CN^- were used directly post–reaction for FT–IR measurements (Figure 4.6). Vibrational modes in Figure 4.6 are observed at 2093 and 2169 cm^{-1}, consistent with *just* $[Cu(CN)_3]^-$ *and* $[CuCN]^+$, respectively (literature values for these two species being at 2094 and 2170 cm^{-1}, respectively).[54–59] Absent (not observed) were any of the vibrational modes for free KCN, **$[Cu(CN)_2]$, or $[Cu(CN)_4]^{2-}$** (2070, 2125, and 2075 cm^{-1}).[54–59] Absent (≥0.5% detection limit) is any third peak that might be a

detectable Cu_{defect} site with coordination number different from that of $Cu_{surface}$ or Cu_{pore} sites. For example, neither a 2–coordinate nor 4–coordinate Cu_{defect} site that would—especially in light of the results in Figure 4.6—be expected to generate a $Cu(CN)_4$ or a $Cu(CN)_2$ band is observable down to a ≥0.5% level.

The FT–IR frequencies observed (and those absent) are summarized in Table 4.2. In short, the predicted 3:1 and 1:1 binding ratios and associated stoichiometry (Figure 4.1, Figure 4.7-4.8) for the metal–terminated 3–coordinate $Cu_{surface}$ and 5–coordinate Cu_{pore} CN^- poisoned sites *are observed directly by FT–IR*. The evidence is direct and compelling that CN^- binds unselectively to, and "poisons" what we have denoted $Cu_{surface}$ and Cu_{pore} sites in CuBTTri. Note that the quantitation of the two IR bands in Figure 4.6 is about 1 $Cu(CN)_3$ to 2 Cu(CN), so much more than the ratio expected based on exterior surface area to interior volume ratio for $MOF_{Filtered}$ samples of CuBTTri (Table 4.1). This is likely the case because even CN^- can only diffuse a short distance into the MOF even over 30 min and in an unstirred solution (IR radiation can fully penetrate the $MOF_{Filtered}$ crystals of the present size,[60,61] so that is not the origin of the difference).

Table 4.2. Observed and (Absent) FT–IR Stretching Frequencies for $MOF_{Filtered}$ CuBTTri Poisoned with KCN.

CN^- Species (frequency)	Observed / Absent	Predicted/ Not Predicted
KCN Stretch (2070 cm^{-1})[51–56]	(Absent)	N/A
$[CuCN]^+$ Stretch (2170 cm^{-1})[51–56]	**Observed**	**Predicted (Cu_{pore} site)**
$[Cu(CN)_2)$ Stretch (2125 cm^{-1})[51–56]	(Absent)	Not Predicted (Cu_{defect} site)
$[Cu(CN)_3]^-$ Stretch (2094 cm^{-1})[51–56]	**Observed**	**Predicted ($Cu_{surface}$ site)**
$[Cu(CN)_4]^-$ Stretch (2075 cm^{-1})[51–56]	(Absent)	Not Predicted (Cu_{defect} site)

Hence, the IR studies of the CN^- poisoned catalyst are of fundamental interest in that they show that even just $K^+(H_2O)_n$ $CN^-(H_2O)_m$ (estimated unhydrated dimeter of ~4 Å and hydrated

diameter of ~10 Å[49,62] with two waters of hydration) cannot readily find its way fully into the center of the MOF particles via the largest CuBTTri pores (unhydrated diameter ~20 Å; estimated hydrated diameter, 14 to 16 Å for 4 waters of hydration[49,62]) in 30 min at 25 °C in unstirred solution. As expected, FT–IR spectra for CN^- poisoned CuBTTri of all particle size ranges studied show that $MOF_{Filtered}$ samples have more detectable $Cu(CN)_3$ sites than MOF_{Ground} samples. Additionally, $MOF_{Filtered}$ samples show more *total* detectable $Cu(CN)_x$ sites than either MOF_{Ground} or MOF_{Large} particles, unsurprisingly (Appendix III, Figure S4.15). This further supports our earlier conclusion that GSNO cannot enter the CuBTTri pores for reaction with Cu_{pore} sites.

Importance of the FT–IR of the CN^- Poisoned Catalyst to the Cu_{defect} Active Site Hypothesis

A very important part of the data in Figure 4.6 and Table 4.2 is that no third, Cu_{defect} species is seen to an estimated detection limit of ≥0.5%. Specifically, the lack of detectable 2– or 4–coordinate Cu corresponding to CN^- poisoned $Cu(CN)_4$ or $Cu(CN)_2$ even down to the ≥0.5% level of the total Cu present puts, in turn, a huge restriction on any putative "Cu_{defect}" site. Either such a putative, postulated site is present at ≤0.5% level of the total Cu present, or it has a 3–coordinate or 5– coordinate geometry, yet is >200-fold faster *for some unknown reason* compared to all other, normal $Cu_{surface}$ and Cu_{pore} sites (≥200-fold so that ≤0.5% can carry 100% of the catalysis in the Cu_{defect} hypothesis). We cannot come up with any reasonable explanation why a 2nd type of 3– or 5–coordinate Cu would have a ≥200 fold reactivity than the 3– and 5–coordinate Cu sites expected from the X-ray structure-based, even if simplified and idealized, model back in Figure 4.1. Put another way, the IR of the CN^- poisoned catalyst *provides direct spectroscopic evidence against the defect hypothesis **4** provided previously,* at least at the ≥0.5% level for $MOF_{Filtered}$ samples. The *working hypothesis* for the structure of the 3–coordinate surface active site (and the 5–coordinate inactive site) has at present to be close to that that shown in Figure 4.1 based on the idealized 3–

and 5–coordinate structures back in Figure 4.1. While we cannot unequivocally rule out that what we are actually detecting is a Cu_{defect} site that has the IR signal of "$Cu(CN)_3$", yet has different ligands than those expected from the synthesis and shown in Figure 4.1, there is no evidence for that more complex hypothesis. The simplest—Ockham's razor—explanation is that the structures in Figure 4.1 are at least good initial, working hypotheses for at least the poisoned form of the Cu–MOF catalyst.

$$\text{(a) } Cu^{II}_{\text{surface MOF}} + 3CN^- \rightarrow [Cu^{II}_{\text{surface MOF}}(CN)_3]^-$$

$$\text{(b) } Cu^{II}_{\text{pore MOF}} + CN^- \rightarrow [Cu^{II}_{\text{pore MOF}}(CN)]^+$$

Figure 4.7. CN^- Binding Stoichiometry to (a) $Cu_{surface}$ and (b) Cu_{pore} revealed by FT–IR Studies of CN^- Poisoned CuBTTri Catalyst.

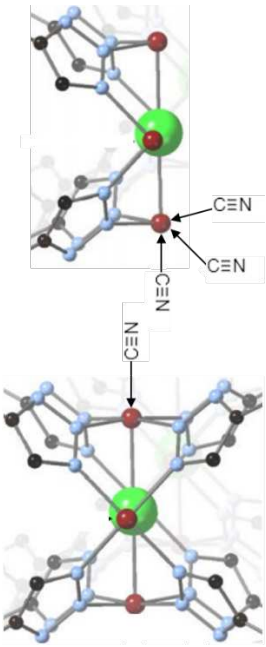

Figure 4.8. View of the binding of 3 CN^- to a $Cu_{surface}$ site predicted by the metal–terminated CuBTTri idealized structure to generate $Cu(CN)_3$ as observed by FT–IR in Figure 4.6 (Top). The binding of 1 CN^- to a Cu_{pore} site predicted by the CuBTTri idealized structure to generate Cu(CN) as observed by FT–IR in Figure 4.6 (Bottom). Shown are carbon (black), nitrogen (blue), chlorine (green), and copper (red).

Selective, Size–Based 3,3',3"–Phosphanetriyltris–Benzene Sulfonic Acid (TPPTS) Poisoning of $MOF_{Filtered}$ Particles

The bulky ligand 3,3',3"–phosphanetriyltris benzene sulfonic acid (TPPTS, Figure 4.9) (unhydrated van der Waals diameter of ~14 Å, hydrated diameter of 18 to 20 Å for 3 waters of hydration[49,62]) was chosen next as a *selective poison* for only exterior, $Cu_{surface}$ sites because it cannot enter the CuBTTri pores (unhydrated diameter ~20 Å, hydrated diameter ca 14 to 16 Å for 4 waters of hydration[62]). Hence, TPPTS can only interact with the CuBTTri exterior surface, and cannot enter the pores to bind Cu_{pore} sites.[77]

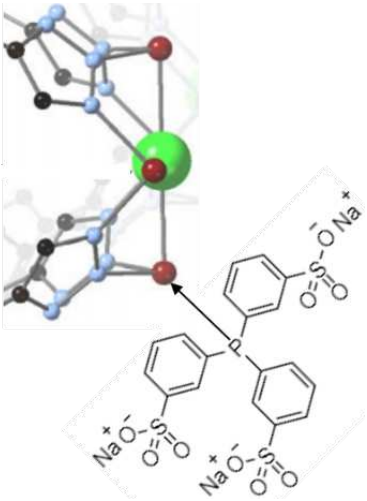

Figure 4.9. TPPTS poisoning of a $Cu_{surface}$ site modeled by the metal–terminated CuBTTri crystal structure. The Tolman cone angle of TPPTS falls between 160–180°.[63,64]

A plot of the $[-d[GSNO]/dt]_i$ values as a function of equivalents of TPPTS added per total copper in a given $MOF_{Filtered}$ sample is shown in Figure 4.10. Based on a linear fit of the data, a mere $(1.3 \pm 0.4) \times 10^{-2}$ equivalents of TPPTS per total Cu are required to poison the $MOF_{Filtered}$ particles completely. In control experiments, the amount of TPPTS required to completely poison $MOF_{Filtered}$ samples obtained by the alternative method of UV–VIS spectroscopy is consistent with that determined by ^1H NMR (Appendix III, Figure S4.14).

The finding that only (1.3 ± 0.4) × 10^{-2} equivalents of TPPTS per total Cu is required to fully poison the CuBTTri catalyst is a telling result that further compellingly rules out Cu_{pore} as the active site. This valuable selective poisoning with TPPTS implicates a species present at 1.3(±0.4)% of the total Cu as the kinetically dominant form. The idealized CuBTTri structure reveals that there is at most 270° present at the $Cu_{surface}$ sites while the Tolman cone angle for TPPTS[63,64] is ca. 160–180° (Figure 4.9). Hence, a 1 TPPTS:1 $Cu_{surface}$ binding stoichiometry is supported (and the 1.3(±0.4)% active Cu metric generated), a valuable result given that a lack of knowledge of the ratio of poison to active site is the Achilles Heel of the otherwise powerful catalyst–poisoning method.[7] Cu_{defect} sites with a coordination number lower than 3 could in theory accommodate multiple TPPTS ligands, but no, for example, 2–coordinate Cu sites (which should have generated $Cu(CN)_4$) are observed by FT–IR at the already cited ≥0.5% detection limit (Figure 4.6, Table 4.2). Hence, again no evidence for a putative Cu_{defect} site over and above the idealized $Cu_{surface}$ site is seen in the TPPTS poisoning experiments down to a ~0.5% level of the total Cu present.

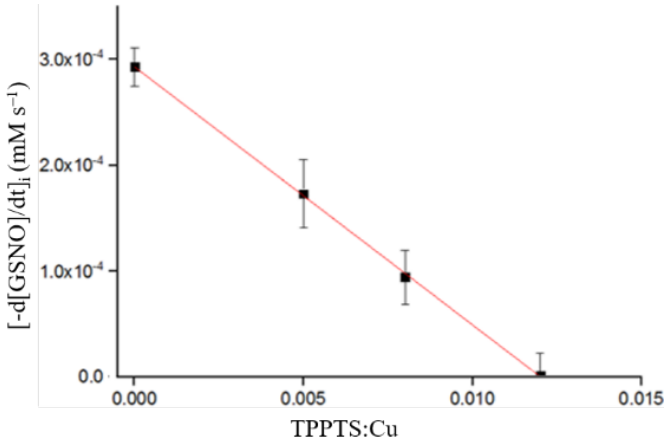

Figure 4.10. TPPTS poisoning curves for $MOF_{Filtered}$ particles. The critical finding is that 1.3(±0.4)% the larger, selective poison (TPPTS) per amount of Cu present in the MOF CuBTTri completely inhibits the catalysis of NO release from GSNO. All values of $[-d[GSNO]/dt]_i$ were measured at20 min reaction time. Each data point represents the average and standard deviation of three measurements.

In summary, all the evidence so far points towards the 3–coordinate $Cu_{surface}$ sites present in the $MOF_{Filtered}$ samples at 1.3(±0.4)% of total Cu sites as being the kinetically dominant catalyst for GSNO to NO conversion catalysis beginning with CuBTTri.

Calculation of a TOF Normalized to the Number of Active Sites, TOF_{norm}

The TPPTS poisoning–determined number of active sites in a given MOF sample (i.e., and a 1:1 TPPTS:Cu binding ratio) was used to calculate a TOF_{norm} (Appendix III, Calculation S4.1). The resulting $TOF_{norm} = (4.9 \pm 1.2) \times 10^{-2}$ mol NO (mol $Cu_{surface})^{-1}$ s^{-1} (in water, at 20 min, 25 °C, 1mM GSNO, 30% loss of GSNO, and 1.3 ± 0.4 mol% $Cu_{surface}$). This TOF_{norm} value is reported with the reaction conditions included as those factors (time, temperature, substrate concentration, catalyst loading, and so on) are known to influence experimentally determined TOF values.[65] TOF_{norm} values are required to make reliable comparisons to other catalysts, but are relatively rarely reported. Without such TOF_{norm} values inter–catalyst comparison are meaningless, and even then one should take care to not inadvertently compare different rate laws when comparing TOFs (i.e. for processes with different rate laws) as G. Lente has cautioned.[65]

Comments on the Alternative Hypothesis of Cu_{defect} as the True Active Site

We end with some comments on the Cu_{defect} active site hypothesis—the available evidence disfavors it, but it has not been unequivocally disproven. As is the case in science in general and certainly in catalytic and mechanistic chemistry, the Cu_{defect} hypothesis is a good example of the fact that there is always one or more additional, often more complicated hypotheses one can think of that cannot be conclusively disproven by the methodology or precision of the measurements available at the time. Indeed, an omnipresent alternative hypothesis for any solid catalyst is that an alternative site—one indistinguishable from $Cu_{surface}$ at least by IR of the CN^- poisoned catalysis in the present case—is actually the true, kinetically dominant catalyst. For example and for the

sake of illustration, a defect which exists at a trace 0.1% level but is 10^5 more reactive than any other metal site present would, then, carry ~100% of the catalytic activity. The defect hypothesis in catalysis is typically difficult if not approaching impossible to completely rule out, perhaps why many studies fail to consider it. This is where we believe studies of MOF–based catalysts have a sizable intrinsic advantage—we can at least start with the structural knowledge shown back in Figures 4.1 and 4.2 for example, and even if those structures are idealized and oversimplified.

The results of the present studies are able, however, to put some strict requirements and limits on a putative Cu_{defect} active site: (i) that Cu_{defect} site must scale linearly with $Cu_{surface}$ production as CuBTTri particle size decreases—and is not the $Cu_{surface}$ site by definition, (ii) the putative Cu_{defect} active site must generate a FT–IR signal of its CN^- poisoned adduct that is either (iia) indistinguishable from those for the $Cu_{surface}$ (and/or Cu_{pore}) sites predicted from the metal–terminated CuBTTri crystal structure, or (iib) is simply below the 0.5% level of total Cu that our IR studies have been able to detect. (iii) The hypothetically active, putative Cu_{defect} site is not a 2–coordinate Cu site (the one potentially more active site we could come up with) because we have shown that 1.3(±0.4)% of the total Cu is the (low) level of active sites, and any Cu site present at 1.3(±0.4)% should be detectable by FT–IR (where the detection limit is ≥0.5% of total Cu). Hence, (iv) the postulated Cu_{defect} active site must exhibit must greater activity than all the other Cu sites combined in order to carry 100% of the catalysis; and (v) postulating such a Cu_{defect} sites carries the burden of coming up with a reasonable chemical idea and structure for why the putative Cu_{defect} has a ≥200-fold increased activity over the expected 3–coordinate $Cu_{surface}$ sites—and yet is not a 2–coordinate site, as one reasonable hypothesis that has been disproved. All of the above *could* be true, but intellectually we are manufacturing a "special type of highly active site" for which we have zero experimental evidence. Our bet is with the hypothesis that stands up to the application

of Ockham's razor, namely that the kinetically dominant active site is surface Cu that looks a lot like $Cu_{surface}$ back in Figures 4.1 and 4.2. This is certainly the working hypothesis going forward that is most consistent with and supported by the present studies.

4.3 Summary and Conclusions

The present studies utilize multiple, previously uncombined methods to study MOF CuBTTri catalysis of biomedically relevant conversion of GSNO to NO and to establish the following conclusions:

• Quantitative, size–selective poisoning studies establish that only 1.3(±0.4)% of the total Cu present in $MOF_{Filtered}$ samples is catalytically active;

• The amount of active Cu allows a more reliable TOF than previously available to be calculated for this MOF catalyzed reaction, $TOF_{norm} = (4.9 \pm 1.2) \times 10^{-2}$ mol NO (mol $Cu_{surface})^{-1}$ s^{-1} (in water, at 20 min, 25 °C, 1mM GSNO, 30% loss of GSNO, and 1.3 ± 0.4 mol% $Cu_{surface}$). This TOF_{norm} is, accordingly, *~100x greater than the TOF one calculates in the absence of the present studies* (i.e., and under the otherwise normal but unsupported assumption that 100% of the Cu sites in the MOF are active).

• A linear dependence of $[-d[GSNO]/dt]_i$ α (exterior surface area / interior volume) was established, one that provides compelling evidence disproving the traditional hypothesis of *MOF intrapore metal site catalysis* for the present example, and to zero activity ($\pm 10^{-5}$ mM s^{-1}) for all the pore sites combined.

• Hence, a simple but valuable lesson from the current work is that active site density in at least CuBTTri for NO release catalysis depends on the particle size and morphology.

• Another important result of the present work is the finding that either the $Cu_{surface}$ or putative Cu_{defect} sites (or some combination of them) are implicated as the kinetically dominant active site.

• The above finding has significant implications for the design of better, more active Cu–MOF based catalysts for at least the present NO release reaction—and by implication for other MOF catalyzed reactions that may be untenable for MOF intrapore metal sites: namely find ways to increase the external surface area and, hence, increase the number of active sites and resultant activity of such MOF based catalysts.

• KCN catalyst poisoning and FT–IR analysis of the CN^- poisoned catalyst ($MOF_{Filtered}$ samples) were performed and two distinct CN^- to Cu binding ratios were observed, $Cu(CN)_3$ and Cu(CN)—the two binding modes expected based upon admittedly idealized, metal–terminated CuBTTri structure. No other Cu to CN^- binding modes are observed, at an estimated detection limit of ≥0.5%. Hence, no site such as a 2–coordinate Cu_{defect} site (which should generate a $Cu(CN)_4$ species observable by FT–IR) that might have been produced by grinding of the CuBTTri particles and might have had some unusually high activity could be detected. Any Cu_{defect} site has to have an IR signal indistinguishable from the IR signal of the CN^- poisoned catalyst expected based on the idealized 3– and 5–coordinate sites in Figure 4.1 and yet has to be ≥200-fold more reactive than those sites for some unspecified reason that at least we cannot see at present.

• Therefore, despite their clearly idealized, oversimplified nature, the structural model in Figures 4.1 and 4.2 of CuBTTri and its Cu_{pore} and $Cu_{surface}$ sites proved valuable in designing and interpreting experiments including catalytic activity vs surface area, CN^- poisoning, and experiments involving FT–IR analysis of the CN^- poisoned catalyst. This is not meant to claim that this work has determined the true nature of the $Cu_{surface}$ site at atomic resolution nor that Cu_{defect} sites do not exist. However, we certainly have a much better idea of what a $Cu_{surface}$ site might actually look like compared to the hypothesis of a putative Cu_{defect} site of totally unknown nature: namely the working hypothesis of the 3–coordinate, $Cu_{surface}$ site back in Figure 4.2.

• Finally, the present studies set the stage for improved, rational applications of these Cu–MOF based catalysts as well as three additional, future studies. One study in progress involves additional poisoning studies of a wider range of particle sizes and associated surface areas for the current CuBTTri catalyst, studies that are testing predictions from the structural model in Figure 4.1 of the percentage of surface sites expected vs particle size. Also in progress is the determination of the more detailed reaction mechanism of the CuBTTri catalyzed GNSO to NO conversion catalysis. The starting mechanistic hypotheses to be tested are clear, namely that the GSNO to NO conversion is catalyzed by either a Cu(II)/Cu(I) redox mechanism, or by a Cu(II) Lewis acid mechanism.[31–33] A third important implication of the present studies—one with significant implications for practical applications—has already been briefly mentioned: the idea of synthesizing *low dimension, Cu–based MOF nano sheets* to yield catalyst materials with a greater proportion of the copper present as exterior surface, low coordinate, Cu sites. The needed studies are in progress, promise to prove interesting, and will be reported in due course.

4.4 Experimental

Reagents. Diethylamine (99%), trimethylsilylacetylene (98%), trimethylsilylazide (94%), and 1,3,5– tribromobenzene (98%) were purchased from Alfa Aesar (Ward Hill, MA, USA). Glutathione (98%) was purchased from VWR (Radnor, PA, USA). Sodium nitrite (99.5%), copper (I) iodide (99.5%), bis(triphenylphosphine)palladium(II) dichloride (99%), dichloromethane (99%), monobasic sodium phosphate (≥98%), 3, 3', 3"–phosphanetriyltris benzene sulfonic acid (TPPTS) (97%), and potassium cyanide (>97%), were purchased from Sigma–Aldrich (St. Louis, MO, USA). HCl (1 N), methanol (99%), and sodium hydroxide (98.9%) were purchased from Fisher Scientific (Hampton, NH, USA). Dimethylformamide (99%) and copper (II) chloride dihydrate (99%) were purchased from EMD Chemicals (Gibbstown, NJ, USA). One micron mesh

cell strainers were obtained from Pluriselect (Germany). Ultrahigh purity nitrogen gas was supplied by Airgas (Denver, CO, USA). Deionized water (18.2 MΩ·cm) was obtained from a Millipore Direct–Q water purification system (EMD Millipore, Billerica, MA, USA). All materials were used as received without any further purification.

GSNO Synthesis. GSNO was prepared following an established literature protocol.[66] Briefly, a solution of glutathione (1.53g, 4.99 mmol) was prepared in millipore filtered water (8 mL) containing 2M HCl (2.5 mL, 10.5 mL total volume). One equivalent of sodium nitrite (0.345 g, 4.99 mmol) was added and the resulting mixture was stirred for 40 min at 5 °C. Acetone (10 mL) was added to the resulting red solution and the mixture was stirred for another 10min. The red precipitate was collected via vacuum filtration and washed with ice–cold water (5 × 5 mL) and ice–cold acetone (3 × 10 mL). The precipitate was then dried on a high vacuum line for 4h to afford *S*–Nitrosoglutathione (1.31 g, 3.86 mmol, 77%) (λ_{max}) (H_2O) 335, 550 nm (ε=922, 15.9 cm^{-1} mM^{-1}). The GSNO sample used herein was determined to be (97 ± 2)% pure by UV–VIS spectroscopy (Appendix III, Table S4.1, Figure S4.1). The small impurity present is glutathione (GSH) or glutathione disulfide (GSSG) left over from the synthesis. We have shown previously that added levels of GSH in greater concentration than the inherent 1–5% impurity in our as–prepared GSNO are required to initiate measurable CuBTTri catalyzed GSNO to NO conversion within 20 min.[35]

H_3BTTri Ligand Synthesis. The H_3BTTri ligand was prepared following an established literature protocol.[30] Briefly, solid 1,3,5–tribromobenzene (9.45 g, 30.0 mmol) was dissolved in diethylamine (250 mL) under inert conditions (N_2). Copper(I) iodide (50 mg, 0.26 mmol) and dichlorobis(triphenylphosphine)palladium(II) (400 mg, 0.57 mmol) were added to the stirred solution. Trimethylsilylacetylene (10.6 g, 108. mmol) was added to the solution and the resulting

mixture was heated at 50 °C for 6 h. Resulting diethylamine hydrobromide was removed by filtration and washed with ether (45 mL). Combined washings were evaporated to dryness in vacuo and the resulting product purified by a silica plug to yield 9.61 g (78%) 1,3,5–tris(trimethylsilylethynyl)benzene as an intermediate. ^{1}H NMR (400 MHz, $CDCl_3$): δ = 7.43(s), 0.23(s) ppm.

Hydrolysis of the Trimethylsilylethynyl Intermediate. The 1,3,5–tris(trimethylsilylethynyl)benzene intermediate (9.61 g, 26.3 mmol) was hydrolyzed by treatment with NaOH (aq) (30 mL, 1M), CH_2Cl_2 (20 mL), and methanol (50 mL) via stirring at room temperature for 3h. Evaporation of methanol, ether extraction of the residue, and evaporation of the solvent in vacuo yielded 2.68 g of white powder containing 1,3,5– triethynylbenzene. ^{1}H NMR (400 MHz, $CDCl_3$): δ =7.51(s), 3.12(s) ppm.

Click Reaction to Form 1,3,5–tris(^{1}H–1,2,3–triazol–5–yl)benzene. Trimethylsilylazide (9.26 g, 80.4 mmol) was added to a solution of copper(I) iodide (510mg, 2.63 mmol) and 1,3,5–triethynylbenzene (2.68 g, 17.8 mmol) under inert conditions in a mixture of dimethylformamide (DMF; 90 mL) and methanol (10 mL). The resulting mixture was stirred at 100 °C for 36 h. The mixture was then filtered and reduced to a volume of 10 mL via rotary evaporation. A pale–yellow precipitate was formed upon the addition of millipore filtered water (30 mL) to the resulting filtrate. The solid was collected by filtration, washed with ether and dried in vacuo to yield 4.1 g (83%) of 1,3,5–tris(^{1}H–1,2,3–triazol–5–yl)benzene. ^{1}H NMR (400 MHz, $(CD_3)_2SO$): δ = 8.52(s), 8.34(s) ppm.

CuBTTri Synthesis. CuBTTri was synthesized following a previously reported procedure.[30] A solution of H_3BTTri (225 mg, 0.937 mmol) in DMF (40 mL) was prepared in a 250mL Pyrex bottle $CuCl_2 \cdot 2H_2O$ (383 mg, 2.25 mmol) was added to the solution. The vial was

heated at 100 °C for 72 h to afford $H_3[(Cu_4Cl)_3(BTTri)_8(DMF)_{12}]\cdot 7DMF\cdot 76H_2O$. The purple powder was washed with boiling DMF (10 × 10 mL) and allowed to dry under ambient conditions to yield 218 mg (76%) of product. Solvent exchange was performed using millipore filtered water to yield $H_3[(Cu_4Cl)_3(BTTri)_8(DMF)_{12}]\cdot 72H_2O$. The resulting light purple powder was hand ground and analyzed by powder X–ray diffraction (pXRD). The observed diffraction pattern matched a literature standard (Figure S4.2).[30]

Water Suppression ^{1}H NMR. These experiments follow our protocol for direct, *in situ* monitoring the release of NO from GSNO in water by solvent suppressed ^{1}H NMR.[37] All NMR experiments were performed using an Agilent Inova 500 equipped with a 5 mm pulsed–field–gradient HCN probe. Samples were prepared in septa–capped Wilmad 528–PP 500 MHz tubes under inert conditions (N_2) by adding 0.5 mL of reaction supernatant to an NMR tube containing 0.1 mL of 20 mM NaH_2PO_4 buffered D_2O. Samples were mixed by hand, followed by 2 s of sonication to remove N_2 bubbles. Samples were kept dark, air–free, and analyzed as soon as possible. NMR experiments were run using PRESAT with PURGE solvent signal suppression available in VnmrJ version–4.2.[67] The system was buffered with NaH_2PO_4 to pH 4 due to the sensitivity of the compounds of interest (GSNO, GSH, and GSSG) to the pH of the solvent. Five hundred and twelve transients were acquired for all samples, which took 35 min to complete. A 2 s square presat with a bandwidth of 100 Hz on resonance at 4.67 ppm (water) was used, followed by the PURGE crusher sequence and a pi/2 excitation pulse of 5.7 µs. Acquisition time was 2 s, with the PRESAT delay the total time between transients was about 4 s. All free induction decay (FID) spectra were processed using MestraNova® software to examine peak intensities and integration values. Data analysis and calculations were performed using Microsoft Excel®.

Reaction Design, Particle Size Studies, KCN Poisoning, and TPPTS Poisoning. All reactions described herein were carried out under an inert N_2 atmosphere. GSNO, GSH, KCN, and TPPTS solutions were prepared from millipore H_2O and solid GSNO, GSH, KCN, or TPPTS under inert conditions (N_2) in a 200 mL round–bottomed flask capped with a rubber septum. CuBTTri was massed into a three–neck 100 mL round–bottomed flask and oven dried overnight at 110 °C. Following drying, the flask containing CuBTTri was placed under vacuum for 1 h on a Schlenk line and backfilled with N_2 (g) prior to reaction. GSNO, GSH, KCN, or TPPTS solutions were then injected into the reaction flasks containing dry CuBTTri. For poisoning experiments, a KCN, or in separate experiments TPPTS, solution in millipore water was allowed to react with CuBTTri for 30 min to ensure completed binding to the Cu centers. Vigorous bubbling in the round–bottomed flask using an N_2 (g) flow was established. Reactions were bubbled vigorously to mitigate mass transport limitations and ensure the measured value for $[-d[GSNO]/dt]_i$ was not simply the rate of substrate diffusion to the MOF active sites.[68,69] Reaction flasks were wrapped in aluminum foil to prevent exposure to light and reactions proceeded for a predetermined time. To quench the reaction once at predetermined times, the exit needle was removed to stop bubbling and the supernatant was immediately decanted via a syringe, leaving the MOF particles in the flask. The quenched reaction solution was then kept cool and dark in an EPA certified Cu–free glass vial under inert conditions (N_2) or added directly to an NMR tube or UV–VIS quartz cuvette for analysis. The ^{1}H NMR sample was prepared in a septa capped sample tube under inert conditions (N_2) by injecting 0.5mL of reaction supernatant into the NMR tube along with 0.1 mL of 20mM NaH_2PO_4 buffered D_2O due to the sensitivity of GSNO to the pH of the solvent. ^{1}H NMR were taken at 20 min to allow sufficient loss of GSNO and GSSG product formation to be detectable, yet to remain relatively early in the reaction progress to determine what is designated

as an initial rate. Practically and given the ca. ± 5% precision of the ^{1}H NMR data under our conditions, the trade–off between measurable reaction vs more points meant that taking 1 point in the first ca. 30% reaction was a good compromise that allowed good initial rate measurements. Furthermore, the plots (*vide infra*) using these data demonstrate they are more than adequate for the purposes of the present study. Catalytic loss of GSNO for MOF_{Large} particles was followed by UV–VIS spectroscopy because ^{1}H NMR and UV–VIS spectroscopies have been determined to be equivalent techniques for monitoring loss of GSNO in the current system and because of the longer timescales required for the slow reaction with the low surface area, larger particles. No unanticipated safety hazards were encountered over the course of all experiments. Glassware contaminated with KCN was washed (3 × 20 mL) with a pH = 10 sodium bicarbonate buffer. All reactions reported were performed in triplicate. The reported average and standard deviation were calculated from those three trials.

Supporting Information. The following are available in Appendix III: Supporting Information for Chapter IV: additional characterization methods, GSNO purity assay using UV-VIS spectroscopy, CuBTTri synthesis characterization, particle size analysis by DLS, raw ^{1}H NMR data comparing particle size and the reaction rate, example calculation for initial rate, additional SEM micrographs of MOF_{Ground} and $MOF_{Filtered}$ samples, raw ^{1}H NMR data for KCN and TPPTS poisoning experiments, raw UV-VIS data for TPPTS poisoning experiments, additional FT-IR spectra for MOF_{Large}, MOF_{Ground}, and $MOF_{Filtered}$ particles exposed to KCN, raw UV-VIS data examining MOF_{Large} particles for GSNO to NO conversion catalysis over longer time periods than 20 min, example calculation for a TOF value, and calculation of the ratio between exterior surface area and interior volume of an octahedron.

REFERENCES

1. Furukawa, H., Cordova, K. E., O'Keeffe, M. & Yaghi, O. M. The Chemistry and Applications of Metal-Organic Frameworks. *Science* **341**, 1230444 (2013).

2. Gascon, J., Corma, A., Kapteijn, F. & Llabrés i Xamena, F. X. Metal Organic Framework Catalysis: Quo vadis? *ACS Catalysis* **4**, 361–378 (2014).

3. Furukawa, H., Müller, U. & Yaghi, O. M. "Heterogeneity within Order" in Metal–Organic Frameworks. *Angewandte Chemie International Edition* **54**, 3417–3430 (2015).

4. Metzger, E. D., Comito, R. J., Hendon, C. H. & Dincă, M. Mechanism of Single-Site Molecule-Like Catalytic Ethylene Dimerization in Ni-MFU-4l. *Journal of the American Chemical Society* **139**, 757–762 (2017).

5. How many MOFs are there in the CSD? *Cambridge Crystallographic Data Centre* (2016).

6. Gates, B. C. Catalytic Chemistry. in *Catalytic Chemistry* 385 (Wiley, 1992).

7. Hornstein, B. J., Aiken, J. D. & Finke, R. G. Nanoclusters in Catalysis: A Comparison of CS2 Catalyst Poisoning of Polyoxoanion- and Tetrabutylammonium-Stabilized 40 ± 6 Å Rh(0) Nanoclusters to 5 Rh/Al2O3, Including an Analysis of the Literature Related to the CS2 to Metal Stoichiometry Issue. *Inorganic Chemistry* **41**, 1625–1638 (2002).

8. Bayram, E. & Finke, R. G. Quantitative 1,10-Phenanthroline Catalyst-Poisoning Kinetic Studies of Rh(0) Nanoparticle and Rh4 Cluster Benzene Hydrogenation Catalysts: Estimates of the Poison Kassociation Binding Constants, of the Equivalents of Poison Bound and of the Number of Cata. *ACS Catalysis* **2**, 1967–1975 (2012).

9. Hagen, C. M., Vieille-Petit, L., Laurenczy, G., Süss-Fink, G. & Finke, R. G. Supramolecular Triruthenium Cluster-Based Benzene Hydrogenation Catalysis: Fact or Fiction? *Organometallics* **24**, 1819–1831 (2005).

10. Bayram, E. *et al.* Is It Homogeneous or Heterogeneous Catalysis Derived from [RhCp*Cl2]2? In Operando XAFS, Kinetic, and Crucial Kinetic Poisoning Evidence for Subnanometer Rh4 Cluster-Based Benzene Hydrogenation Catalysis. *Journal of the American Chemical Society* **133**, 18889–18902 (2011).

11. Della Pina, C., Falletta, E., Rossi, M. & Sacco, A. Selective deactivation of gold catalyst. *Journal of Catalysis* **263**, 92–97 (2009).

12. Gorunova, O. N. *et al.* When Applying the Mercury Poisoning Test to Palladacycle-Catalyzed Reactions, One Should Not Consider the Common Misconception of Mercury(0) Selectivity. *Organometallics* **37**, 2842–2858 (2018).

13. Boudard, M., Aldag, A., Benson, J. E., Dougharty, N. A. & Girvin Harkins, C. No Title. *Journal of Catalysis* **6**, 92–99 (1966).

14. Yang, D. & Gates, B. C. Catalysis by Metal Organic Frameworks: Perspective and Suggestions for Future Research. *ACS Catalysis* **9**, 1779–1798 (2019).

15. García-García, P., Müller, M. & Corma, A. MOF catalysis in relation to their homogeneous counterparts and conventional solid catalysts. *Chemical Science* **5**, 2979–3007 (2014).

16. Yang, D. *et al.* Structure and Dynamics of Zr6O8 Metal–Organic Framework Node Surfaces Probed with Ethanol Dehydration as a Catalytic Test Reaction. *Journal of the American Chemical Society* **140**, 3751–3759 (2018).

17. Simons, M. C. *et al.* Structure, Dynamics, and Reactivity for Light Alkane Oxidation of Fe(II) Sites Situated in the Nodes of a Metal–Organic Framework. *Journal of the American Chemical Society* **141**, 18142–18151 (2019).

18. Xiao, D. J., Oktawiec, J., Milner, P. J. & Long, J. R. Pore Environment Effects on Catalytic Cyclohexane Oxidation in Expanded Fe2(dobdc) Analogues. *Journal of the American Chemical Society* **138**, 14371–14379 (2016).

19. Harding, J. L. & Reynolds, M. M. Metal Organic Frameworks as Nitric Oxide Catalysts. *Journal of the American Chemical Society* **134**, 3330–3333 (2012).

20. Harding, J. L., Metz, J. M. & Reynolds, M. M. A Tunable, Stable, and Bioactive MOF Catalyst for Generating a Localized Therapeutic from Endogenous Sources. *Advanced Functional Materials* **24**, 7503–7509 (2014).

21. Neufeld, M. J., Lutzke, A., Tapia, J. B. & Reynolds, M. M. Metal–Organic Framework/Chitosan Hybrid Materials Promote Nitric Oxide Release from S-Nitrosoglutathione in Aqueous Solution. *ACS Applied Materials & Interfaces* **9**, 5139–5148 (2017).

22. Neufeld, M. J., Lutzke, A., Jones, W. M. & Reynolds, M. M. Nitric Oxide Generation from Endogenous Substrates Using Metal–Organic Frameworks: Inclusion within Poly(vinyl alcohol) Membranes To Investigate Reactivity and Therapeutic Potential. *ACS Applied Materials & Interfaces* **9**, 35628–35641 (2017).

23. Neufeld, M. J., Ware, B. R., Lutzke, A., Khetani, S. R. & Reynolds, M. M. Water-Stable Metal–Organic Framework/Polymer Composites Compatible with Human Hepatocytes. *ACS Applied Materials & Interfaces* **8**, 19343–19352 (2016).

24. Palmer, R. M. J., Ferrige, A. G. & Moncada, S. Nitric oxide release accounts for the biological activity of endothelium-derived relaxing factor. *Nature* **327**, 524–526 (1987).

25. Marletta, M. A. Nitric oxide: biosynthesis and biological significance. *Trends in Biochemical Sciences* **14**, 488–492 (1989).

26. Paricio, L., Neufeld, B. & Reynolds, M. Combined influence of nitric oxide and surface roughness in biofilm reduction across bacteria strains. *Biointerphases* **14**, 21004 (2019).

27. Neufeld, B. H. & Reynolds, M. M. Critical nitric oxide concentration for Pseudomonas aeruginosa biofilm reduction on polyurethane substrates. *Biointerphases* **11**, 31012 (2016).

28. Carpenter, A. W. & Schoenfisch, M. H. Nitric oxide release: Part II. Therapeutic applications. *Chemical Society Reviews* **41**, 3742–3752 (2012).

29. Schairer, D. O., Chouake, J. S., Nosanchuk, J. D. & Friedman, A. J. The potential of nitric oxide releasing therapies as antimicrobial agents. *Virulence* **3**, 271–279 (2012).

30. Demessence, A., D'Alessandro, D. M., Foo, M. L. & Long, J. R. Strong CO2 Binding in a Water-Stable, Triazolate-Bridged Metal−Organic Framework Functionalized with Ethylenediamine. *Journal of the American Chemical Society* **131**, 8784–8786 (2009).

31. Singh, R. J., Hogg, N., Joseph, J. & Kalyanaraman, B. Mechanism of Nitric Oxide Release from S-Nitrosothiols. *Journal of Biological Chemistry* **271**, 18596–18603 (1996).

32. Burg, A., Cohen, H. & Meyerstein, D. The reaction mechanism of nitrosothiols with copper(I). *JBIC Journal of Biological Inorganic Chemistry* **5**, 213–217 (2000).

33. Smith, J. N. & Dasgupta, T. P. Kinetics and Mechanism of the Decomposition of S-Nitrosoglutathione by l-Ascorbic Acid and Copper Ions in Aqueous Solution to Produce Nitric Oxide. *Nitric Oxide* **4**, 57–66 (2000).

34. Taylor-Edinbyrd, K., Li, T. & Kumar, R. Effect of chemical structure of S-nitrosothiols on nitric oxide release mediated by the copper sites of a metal organic framework based environment. *Physical Chemistry Chemical Physics* **19**, 11947–11959 (2017).

35. Li, T., Taylor-Edinbyrd, K. & Kumar, R. A computational study of the effect of the metal organic framework environment on the release of chemically stored nitric oxide. *Physical Chemistry Chemical Physics* **17**, 23403–23412 (2015).

36. Marcus, R. A. Chemical and Electrochemical Electron-Transfer Theory. *Annual Review of Physical Chemistry* **15**, 155–196 (1964).

37. Tuttle, R. R., Rubin, H. N., Rithner, C. D., Finke, R. G. & Reynolds, M. M. Copper ion vs copper metal–organic framework catalyzed NO release from bioavailable S-Nitrosoglutathione en route to biomedical applications: Direct 1H NMR monitoring in water allowing identification of the distinct, true reaction stoichiometries and thio. *Journal of Inorganic Biochemistry* **199**, 110760 (2019).

38. Dincă, M. *et al.* Observation of Cu2+–H2 Interactions in a Fully Desolvated Sodalite-Type Metal–Organic Framework. *Angewandte Chemie International Edition* **46**, 1419–1422 (2007).

39. Dincă, M. & Long, J. R. High-Enthalpy Hydrogen Adsorption in Cation-Exchanged Variants of the Microporous Metal−Organic Framework Mn3[(Mn4Cl)3(BTT)8(CH3OH)10]2. *Journal of the American Chemical Society* **129**, 11172–11176 (2007).

40. Chen, X. *et al.* Tuning Zr12O22 Node Defects as Catalytic Sites in the Metal–Organic Framework hcp UiO-66. *ACS Catalysis* **10**, 2906–2914 (2020).

41. Li, X. *et al.* Direct Imaging of Tunable Crystal Surface Structures of MOF MIL-101 Using High-Resolution Electron Microscopy. *Journal of the American Chemical Society* **141**, 12021–12028 (2019).

42. Feng, X. *et al.* Size, Shape, and Porosity Control of Medi-MOF-1 via Growth Modulation under Microwave Heating. *Crystal Growth & Design* **19**, 889–895 (2019).

43. Kaur, G. *et al.* Controlling the Synthesis of Metal–Organic Framework UiO-67 by Tuning Its Kinetic Driving Force. *Crystal Growth & Design* **19**, 4246–4251 (2019).

44. Lan, X., Huang, N., Wang, J. & Wang, T. A general and facile strategy for precisely controlling the crystal size of monodispersed metal–organic frameworks via separating the nucleation and growth. *Chemical Communications* **54**, 584–587 (2018).

45. Wang, B., Liu, W., Zhang, W. & Liu, J. Nanoparticles@nanoscale metal-organic framework composites as highly efficient heterogeneous catalysts for size- and shape-selective reactions. *Nano Research* **10**, 3826–3835 (2017).

46. Thiele, E. W. Relation between Catalytic Activity and Size of Particle. *Industrial & Engineering Chemistry* **31**, 916–920 (1939).

47. Wu, Z. & Overbury, S. H. *Catalysis by Materials with Well-Defined Structures*. (2015).

48. Somorjai, G. A. & Li, Y. Impact of surface chemistry. *Proceedings of the National Academy of Sciences* **108**, 917 LP – 924 (2011).

49. Zhao, Y. H., Abraham, M. H. & Zissimos, A. M. Fast Calculation of van der Waals Volume as a Sum of Atomic and Bond Contributions and Its Application to Drug Compounds. *The Journal of Organic Chemistry* **68**, 7368–7373 (2003).

50. Wicholas, Mark. & Wolford, Thomas. Stable cyanide complexes of copper(II). *Inorganic Chemistry* **13**, 316–318 (1974).

51. Duke, F. R. & Courtney, W. G. Complexes in Oxidation–Reduction Reactions. The Copper(II)–Cyanide Reaction. *The Journal of Physical Chemistry* **56**, 19–21 (1952).

52. Jones, J. *et al.* Thermally stable single-atom platinum-on-ceria catalysts via atom trapping. *Science* **353**, 150 LP – 154 (2016).

53. Wöll, C. Structure and Chemical Properties of Oxide Nanoparticles Determined by Surface-Ligand IR Spectroscopy. *ACS Catalysis* 168–176 (2019) doi:10.1021/acscatal.9b04016.

54. Chantry, G. W. & Plane, R. A. CN Stretching Bands in the Raman Spectra of Some Group Ib and Group IIb Compex Cyanides. *The Journal of Chemical Physics1* **33**, 736–739 (1960).

55. Bowmaker, A. G., Kennedy, B. J. & Reid, J. C. Crystal Structures of AuCN and AgCN and Vibrational Spectroscopic Studies of AuCN, AgCN, and CuCN. *Inorganic Chemistry* **37**, 3968–3974 (1998).

56. Penneman, R. A. & Jones, L. H. Infrared Absorption Studies of Aqueous Complex Ions. II. Cyanide Complexes of Cu(I) in Aqueous Solution. *The Journal of Chemical Physics* **24**, 293–296 (1956).

57. Miller, F. A. & Wilkins, C. H. Infrared Spectra and Characteristic Frequencies of Inorganic Ions. *Analytical Chemistry* **24**, 1253–1294 (1952).

58. Reisfeld, M. J. & Jones, L. H. Raman Spectra of Some Cyanide Complexes of Copper. *Journal of Molecular Spectroscopy* **18**, 222–226 (1965).

59. Jones, L. H. Vibrational Spectrum and Structure of Metal-Cyanide Complexes in the Solid State. IV. K3Cu(CN)4. *The Journal of Chemical Physics* **29**, 463–466 (1958).

60. Padalkar, M. V & Pleshko, N. Wavelength-dependent penetration depth of near infrared radiation into cartilage. *The Analyst* **140**, 2093–2100 (2015).

61. Huang, M. *et al.* Penetration Depth Measurement of Near-Infrared Hyperspectral Imaging Light for Milk Powder. *Sensors* **16**, 1–11 (2016).

62. Huang, Y. *et al.* Size, separation, structural order, and mass density of molecules packing in water and ice. *Scientific Reports* **3**, 3005 (2013).

63. Tolman, C. A. Steric effects of phosphorus ligands in organometallic chemistry and homogeneous catalysis. *Chemical Reviews* **77**, 313–348 (1977).

64. Tolman, C. A. Phosphorus ligand exchange equilibriums on zerovalent nickel. Dominant role for steric effects. *Journal of the American Chemical Society* **92**, 2956–2965 (1970).

65. Lente, G. Comment on "'Turning Over' Definitions in Catalytic Cycles." *ACS Catalysis* **3**, 381–382 (2013).

66. Hart, T. W. Some Observations Concerning the S-Nitroso and S-Phenylsulphonyl Derivatives of L-Cysteine and G. *Tetrahedron Letters* **26**, 2013–2016 (1985).

67. Simpson, A. J. & Brown, S. A. Purge NMR: Effective and easy solvent suppression. *Journal of Magnetic Resonance* **175**, 340–346 (2005).

68. Wang, C., Wang, J.-L. & Lin, W. Elucidating Molecular Iridium Water Oxidation Catalysts Using Metal–Organic Frameworks: A Comprehensive Structural, Catalytic, Spectroscopic, and Kinetic Study. *Journal of the American Chemical Society* **134**, 19895–19908 (2012).

69. Notheisz, F., Zsigmond, A., Barto´k, M., Szegletes, Z. & V. Smith, G. Mass transfer test and maximum rate determination during liquid-phase hydrogenations. *Applied Catalysis A: General* **120**, 105–114 (1994).

V. A CU^{II} TO FORMALLY CU^{III} REDOX, PROTON-COUPLED ELECTRON TRANSFER MECHANISM FOR CUBTTRI CATALYZED NO RELEASE FROM S-NITROSOGLUTATHIONE[1]

Overview

Evidence is provided for an unprecedented, formally Cu^{II} to Cu^{III} redox, proton-coupled electron transfer (PCET) mechanism for nitric oxide (NO) release from endogenous *S*-Nitrosoglutathione (GSNO) in the presence of glutathione (GSH) catalyzed by the metal-organic framework (MOF) $H_3[(Cu_4Cl)_3(BTTri)_8]$ (CuBTTri). The balanced reaction stoichiometry, active site characterization, and experimental rate law are used to systematically disprove competing mechanistic hypotheses, leading to Cu^{II} to Cu^{III} PCET as a proposed minimal mechanism. The PCET steps and tripeptide structures of the endogenous GSNO and GSH are exploited by the CuBTTri catalyst to affect S-N bond homolysis and NO release in the proposed mechanism. The Cu^{II} to Cu^{III} mechanism contrasts traditionally proposed, either Cu^{II} to Cu^{I} redox or Cu^{II} Lewis acid mechanisms for NO generation using other Cu-based catalysts but may be unique to the GSNO/GSH tripeptides and CuBTTri. The proposed mechanism sets the stage for future computational experiments on the CuBTTri/GSNO/GSH/NO system which will leverage the well-defined structure of CuBTTri, structures of hypothesized reaction intermediates, and specific questions/hypotheses generated in the mechanism. Mechanistically guided synthesis of improved Cu-MOF catalysts for GSNO to NO conversion is now also possible via the experimentally based mechanism detailed in the present studies. Prior to the present work, the minimum, classic requirements for establishing a more reliable mechanism of a catalytic reaction had not been

[1] The work presented in Chapter V contains work currently in final preparation for submission to a peer reviewed journal. Minor formatting edits have been introduced to meet the dissertation requirements.

achieved for any MOF catalysis system, to the best of our knowledge, and if one includes the requirement of experimentally establishing the active site in the MOF.

5.1 Introduction

CuBTTri: A MOF Catalyst for Biomedically-Important Nitric Oxide Generation from Endogenous Sources.

The catalytic generation of nitric oxide (NO) from endogenous sources such as *S*-Nitrosothiols (RSNO) by solid-state, copper-based materials carries great importance in applications involving implanted medical devices.[1–4] Generating NO *in vivo* stimulates vasodilation for improved blood flow at medical device surfaces and increases the lifetime of implanted devices.[5–14] One NO release system that is known to operate *in vivo* is the generation of NO from the endogenous, nitrosated tripeptide *S*-Nitrosoglutathione (GSNO, Figure 5.1) in the presence of the corresponding thiol glutathione (GSH, Figure 5.1), catalyzed by the Cu-based metal-organic framework (MOF) $H_3[(Cu_4Cl)_3(BTTri)_8]$ (CuBTTri, Figure 5.3).[2,15–22] Glutathione disulfide (GSSG) has been established as the other main product of the reaction (Figure 5.1)[21] for the CuBTTri/GSNO/GSH/NO system in water. CuBTTri is a promising MOF for biomedical applications because of its stability it biological media, ability to generate NO from an endogenous source (GSNO), and because CuBTTri is a solid-state NO generation catalyst that avoids problems with soluble Cu-based NO release catalysts (e.g., acute liver toxicity due to free Cu ions).[2,23] However, the reaction mechanism of CuBTTri catalyzed GSNO to NO conversion with GSH is poorly understood, limiting both the most efficient use of Cu-MOF NO-release catalysts as well as the directed design of future CU-MOF catalysts with even better NO release properties.

CuBTTri Catalyzed GSNO to NO Conversion: Reaction Stoichiometry and Thiol Dependence Have Been Established in Prior Work.

The balanced reaction stoichiometry for GSNO to NO conversion catalyzed by CuBTTri in H_2O was previously established by us and is shown in Figure 5.2.[21] Investigating the reaction stoichiometry revealed that GSH must be added at stoichiometric levels to observe GSNO to NO catalysis by CuBTTri at a reasonable rate.[19,21] Without added GSH only 10% loss of GSNO is observed over 16 h, but when one equivalent of GSH (relative to GSNO) is added, then 100% loss of GSNO is observed within 16 h, an apparent 10-fold acceleration of the reaction.[21] Indeed, the dependence of CuBTTri on added GSH for NO release catalysis will turn out to be very important in formulating mechanistic hypotheses consistent with the experimental evidence (*vide infra*).

Others, as well as ourselves, have hypothesized that, for both CuBTTri and solvated Cu ions, Cu-catalyzed GSNO to NO conversion operates through a mechanism involving a redox reaction at Cu and that GSH is critical in initiating that redox event.[22,24,25] Investigations into RSNO to NO conversion, at least as catalyzed by *solvated copper ions*, have suggested that the *reduction* of Cu^{II} to Cu^{I} appears to be a necessary step for that particular reaction.[24,25] Selective Cu^{I} ion poisoning experiments using the selective Cu^{I} chelator neocuproine have been shown to halt the reaction completely when the *solvated copper ion catalyst* starts as Cu^{II}.[25] The Cu^{II} to Cu^{I} redox catalysis hypothesis for GSNO to NO conversion is, also, at least sensible as one begins to write proposed mechanisms for NO release from GSNO with a Cu^{II} precatalyst because, without electron transfer at the Cu site, it is difficult to generate a driving force for S-N bond homolysis (*vide infra*).

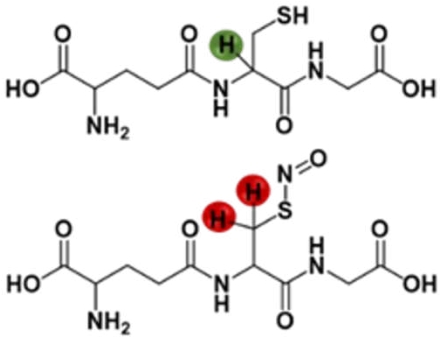

Figure 5.1. Structures and diagnostic protons used in ^{1}H NMR to detect and quantify GSH (green, top) and GSNO (red, bottom) in H_2O. It will become apparent from the work presented herein that the structural uniqueness of the GSH/GSNO tripeptide structures explains, in part, the unique reactivity of the CuBTTri/GSNO/GSH/NO catalysis system in comparison to the generation of NO from other *S*-Nitrosothiol/thiol pairs.

$$2GSNO_{(aq)} + 0.3GSH_{(aq)} + CuBTTri_{(s)} \longrightarrow GSSG_{(aq)} + 2NO_{(g)} + [(0.3GSH)\text{-}CuBTTri]_{(s)}$$

Figure 5.2. The balanced reaction for GSNO to NO conversion catalyzed by CuBTTri determined previously.[21] Work from several groups, including our own, has conclusively disproven the hypothesis that leached copper ions from the CuBTTri framework are the source of GSNO to NO catalysis.[2,21,22,26–28]

For other MOF-based systems researchers have reasonably proposed that reaction mechanisms for solid-state MOFs and analogous homogeneous catalysts are the same based for example on identical observed reaction stoichiometries, as in the case of Nickel-MOF catalyzed ethylene dimerization.[29] However, the experimentally observed reaction stoichiometries for solid CuBTTri versus solvated Cu ion catalyzed GSNO to NO conversion *are different*.[21] The addition of stoichiometric levels of GSH to the reaction mixture is required to observe NO release catalysis for CuBTTri, but the opposite result is observed for solvated Cu ions—stoichiometric levels of GSH *effectively poison* Cu ion catalyzed GSNO to NO conversion in H_2O.[21,24,30,31] Hence, the different thiol dependencies of CuBTTri and solvated Cu ions as GSNO to NO conversion catalysts as well as their different stoichiometries demand that that the two NO-release catalysts employ different reaction mechanisms.

Noteworthy here is that different RSNO substrates (of which GSNO is one endogenous example)[15,20,32,33] respond differently to the addition of their corresponding thiol (RSH) in the presence of Cu-based catalysts for NO release. For example, *S*-Nitrosocysteamine (CysamNO) readily releases NO in the presence of CuBTTri *without* the addition of its corresponding thiol (cysteamine).[2] It follows those mechanistic findings for even one RSNO / RSH system may not be applicable to other NO release systems, such as the CuBTTri/GSNO/GSH/NO system investigated herein. In fact, we will see that the unique reactivity of GSNO and GSH in CuBTTri catalyzed NO release is both an important part of the current contribution and leads to a unique, previously unknown proposed mechanism (*vide infra*).

The Catalytically Active Cu Sites in CuBTTri for GSNO to NO Conversion.

The active Cu sites in CuBTTri for GSNO to NO conversion catalysis have been studied by us in our prior work and shown to be: 1) located on CuBTTri particle exterior surfaces; 2) low-coordinate, naturally-occurring, particle-termination $Cu_{surface}$ sites which can bind 3 equivalents of cyanide per Cu site (Figure 5.3); and 3) are active sites that are present at 1.3 ± 0.4% of total Cu for CuBTTri particles 600 ± 400 nm in size.[22] Such low-coordinate, exterior-surface $Cu^{II}_{surface}$ sites should exhibit relatively low Marcus-type reorganization energy barriers for any geometric rearrangement required for a Cu redox step, either the Cu^{II} to Cu^{I} mechanism, or alternatively (and as our evidence will lead us to herein) a Cu^{II} to Cu^{III} redox-based mechanism.[34,35] In short, the hypothesis that the active sites in CuBTTri for GSNO to NO conversion may operate via a redox mechanism is therefore supported, in at least a general sense, by Marcus-theory type considerations.

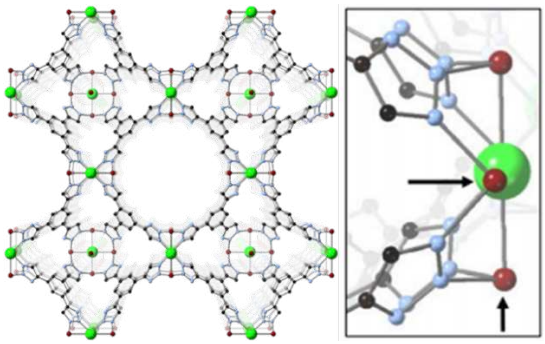

Figure 5.3. (Left) The CuBTTri unit cell showing carbon (black), nitrogen (blue), chlorine (green), and copper (red). (Right) Finer, more detailed view of nominally 3–coordinate $Cu_{surface}$ site (indicated with arrows) previously determined to be active for GSNO to NO conversion catalysis.

Minimum Requirements for Establishing a Reliable, Ockham's Razor-Obeying Reaction Mechanism in any Catalytic System.

Before establishing what is unknown about the CuBTTri/GSNO/GSH/NO catalysis system, it is useful at this point to list the five requirements that any experimentally determined reaction mechanism for a catalyst system should meet, at a minimum and ideally speaking.

1) *Determination of the kinetically dominant active site(s).*[22,36–42] Active site investigation in MOFs, for example, will ideally determine the location, number, and include some structural information of the active sites.[43–45] Active site studies require extensive work, represent a broad topic in the literature, and ideally might best be performed before additional kinetics and mechanistic studies. Knowledge of the active site(s) in MOF catalysts, in turn, allows one to design the most efficient studies necessary to address the four following requirements.

2) *The full catalytic reaction stoichiometry, including mass and charge balance.*[21,39] Often, the critical requirement of a balanced reaction is not reported in investigations of MOF catalysts.[46,47] Without a balanced reaction in hand, one cannot write the correct series of elementary steps that sum to the observed stoichiometry. Without a balanced reaction, the possibility also exists of proposing a mechanism that is simply wrong because it is, then, for another (i.e., the wrong) reaction.

3) *Kinetics data must be obtained for all reactants present using direct physical handles if possible.*[21] Comparing the experimentally observed rate law to rate laws derived for proposed mechanisms is an essential part of disproving or, if not, supporting competing mechanistic hypotheses.

4) *Elementary (or pseudo-elementary) steps which sum to the observed balanced reaction are required.* These elementary or pseudo-elementary steps define the rate constants for each step of the reaction. Elementary steps also eliminate any possible language-based confusion about

reaction mechanisms by defining the concepts and associated language needed to describe the mechanism unequivocally via those pseudo-elementary steps.

5) *Consideration, and attempted disproof, of multiple, competing, deliberately minimalistic mechanistic hypotheses*.[48] Initial mechanistic hypotheses should only contain the minimal elementary steps and assumptions necessary to explain all data; that is, proposed mechanisms should obey Ockham's razor.[49]

Previous work discussed earlier in this introduction (Figures 5.1-5.3) has satisfied requirements 1 and 2 in the above list.[21,22] Specifically, balanced reaction stoichiometry (Figure 5.2) and the Cu active sites (Figure 5.3) are known for CuBTTri catalyzed GSNO to NO conversion in the presence of added GSH. The previously unsatisfied requirements to a reliable initial mechanism, 3, 4, and 5 in the above list, are what the present work aims to address for the CuBTTri/GSNO/GSH/NO system.

Focal Points Herein and For Addressing the CuBTTri/GSNO/NO Mechanism of NO Release Catalysis.

Prior to the present work, to the best of our knowledge no study into the mechanism of a MOF catalyst had fulfilled all five of the above requirements for a minimum, more reliable reaction mechanism.[46,47,50] This is unfortunate because, due to unparalleled chemical and physical tunability, MOFs stand to benefit greatly from reliable-mechanism- directed design of improved, future catalysts.[43,51–54]

For the current system and getting back to requirements 3, 4, and 5 in the above list, the reaction orders were unknown with respect to GSNO, GSH, amount of Cu, and pH (requirement 3 in the above list). We reasoned that reaction pH would be an important parameter to investigate—as proved true, *vide infra*—because GSNO and GSH are both tripeptides with multiple sites which could participate in the reaction that will be protonated/deprotonated depending on the solution pH (Figure 5.1). Looking through the literature of Cu ion catalyzed GSNO to NO conversion in water,

we were unable to find any prior report where the rate of the reaction had been studied as a function of pH. As for the dependence of the rate on the "amount of Cu", while one cannot vary the [Cu-ion] the same way one can in solution, we can and have varied the amount and hence effectively the "concentration" of Cu active sites ([$Cu_{surface}$], Figure 5.3) in the reaction mixture by varying the amount of solid CuBTTri of known particle size (and hence surface area and surface active sites) added to the well-stirred reaction solution. Supporting our approach is a relevant hypothesis prevalent in the literature of MOF catalysts, namely that proposed catalytic cycles for MOF systems are often written under the assumption that the metal sites determined from MOF crystal structures can be treated as discreet, homogeneous metal complexes.[29,51,54–56] The results which follow will support the hypothesis viewing "MOFs as extended solid-state structures composed of homogenous metal sites" (*vide infra*), at least for the present, specific case of $Cu_{surface}$ sites for GSNO to NO conversion.

For the present Cu-MOF catalyst system it was also unknown previously if the kinetically dominant reaction mechanism is one of two main types previously discussed and proposed in the Cu-catalyzed (both Cu ion and solid Cu materials) RSNO to NO literature: i) a Cu^{II} Lewis acid mechanism (where the Cu active sites remain as Cu^{II} throughout the reaction), or ii) a more favored Cu^{II} redox mechanism, where there is a step involving reduction of Cu^{II}—or as proposed herein *oxidation* of Cu^{II} .[24,25,57–60]

Hence, herein we report the experimental rate law for CuBTTri catalyzed GSNO to NO conversion with respect to GSNO, GSH, total Cu, and pH. We considered six main competing mechanistic hypotheses that seemed appropriate *a priori* (two Cu^{II} Lewis acid mechanisms, three Cu^{II} to Cu^{I} redox mechanisms, and one Cu^{II} to Cu^{III} mechanism). Of course, as is always the case in studying reaction mechanisms, the hypotheses considered initially are chosen from a

theoretically infinite list based upon what is deemed reasonable using one's knowledge of the system of interest[48,49] as well as one's broader chemical and mechanistic knowledge. Our currently favored, disproof-based, proposed mechanistic hypothesis is shown in the first reaction mechanism in the Discussion (i.e., and if one wishes to look ahead to that mechanism). It is a Cu^{II} to Cu^{III} redox mechanism with two proton-coupled electron transfer (PCET) steps. The proposed mechanism satisfies all five of the requirements previously listed for proposing reliable reaction mechanisms and is a minimalistic explanation that can explain the observed kinetic and other mechanistic data that follow.

5.2 Results

As noted in a section of the Introduction, our previous work on CuBTTri catalyzed GSNO to NO conversion determined the balanced reaction stoichiometry (Figure 5.2) and provided compelling evidence for exterior surface Cu sites as the kinetically dominant, catalytically most active site (Figure 5.3) in the CuBTTri/GSNO/GSH/NO system.[22] Those studies thereby satisfy requirements 1 and 2, respectively, en route to more reliable minimum reaction mechanisms. Hence, we turned our efforts towards requirement 3 (*vide supra*), namely obtaining experimental kinetics data for the rate law with respect to [GSH], [GSNO], $[Cu]_T$, as well as the reaction pH.

Figure 5.4 shows the first-order integrated rate plot for $\ln[GSNO]_t$ vs the reaction time. [GSNO] was monitored using the previously reported solvent suppression ^{1}H NMR method.[21] Figure 5.4 shows that the reaction is first order in [GSNO] under the standard reaction conditions reported herein (i.e., when $[GSNO]_i$ is between 1 and 1.5 mM and at 20 min reaction time). The linear fit of the data where $[GSNO]_i$ = 1 mM yields the empirical rate law (equation 5.1):

$$\frac{-d[GSNO]}{dt} = k_{GSNO,obs}[GSNO]^1 \text{ (eq. 5.1)}$$

Where $k_{GSNO,obs}$ is the observed first-order rate constant $(1.92 \pm 0.11) \times 10^{-2}\ s^{-1}$.

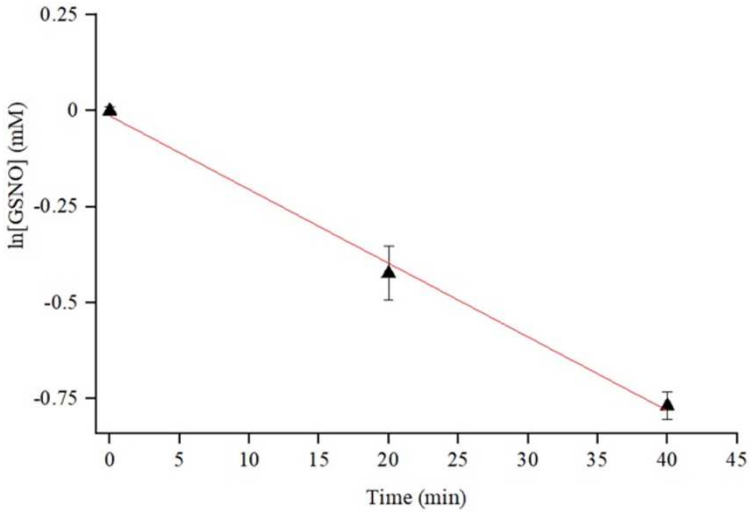

Figure 5.4. First-order integrated rate plot of $\ln[GSNO]_t$ versus reaction time for experiments where $[GSNO]_i = 1$ mM. The linear trend line is fit by the equation $y = ((-1.92 \pm 0.11) \times 10^{-2})\boldsymbol{x} - ((1.32 \pm 2.94) \times 10^{-2})$, $R^2 = 0.99$. The reaction is first order in GSNO in at 1 mM and at 20 min reaction time (the standard reaction conditions described herein). Additional experiments where $[GSNO]_i = 1.5$ mM (Appendix IV, Figure S5.2) show that the reaction is 1st order in GSNO at a range of $[GSNO]_i$, and that the results shown here where $[GSNO]_i = 1$ mM are not unique.

Next, Figure 5.5 shows the relationship between the reaction rate (-d[GSNO]/dt) and the initial concentration of GSH added to GSNO release reactions with CuBTTri. The reaction is 1st order in [GSH] in the lower range of concentrations studied (0.025 to 0.15 mM). For higher levels of [GSH] the reaction becomes saturated and appears 0th order in [GSH]. Figure 5.6 shows a linear fit of the 1st order portion of the plot in Figure 5.5 (the first four points). Figure 5.5 yields the empirical rate law (equation 5.2):

$$\frac{-d[GSNO]}{dt} = k_{GSH,obs}[GSH]^{1\rightarrow 0} \quad \text{(eq. 5.2)}$$

Where $k_{GSH,obs}$ is equal to the observed first order rate constant ($(1.76 \pm 0.1) \times 10^{-3}$ s^{-1}) defined by the slope of the line in Figure 5.6. The GSH present in experiments with the lowest level of [GSH] in Figure 5.6 ([GSH] = 0.025 mM) is a ~1-5% GSH impurity in the GSNO sample leftover from the GSNO synthesis (as summarized in the experimental section). All other experiments contain added GSH beyond that baseline-impurity level.

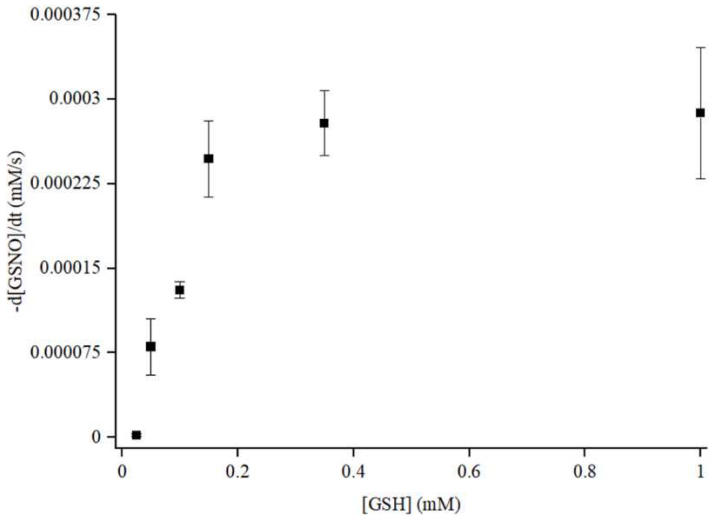

Figure 5.5. Plot of -d[GSNO]/dt measured at 20 min reaction time versus $[GSH]_i$ added to the reaction mixture. There are two distinct domains shown on this plot. In the first domain, the reaction is first order in [GSH]; in the second domain the reaction is zeroth order in [GSH] and shows saturated kinetics with respect to [GSH]. The first point of the plot corresponds to a set of experiments where no GSH was added to the reaction, so that the only present is ca. 1-5 % GSH present as an impurity from the GSNO synthesis.

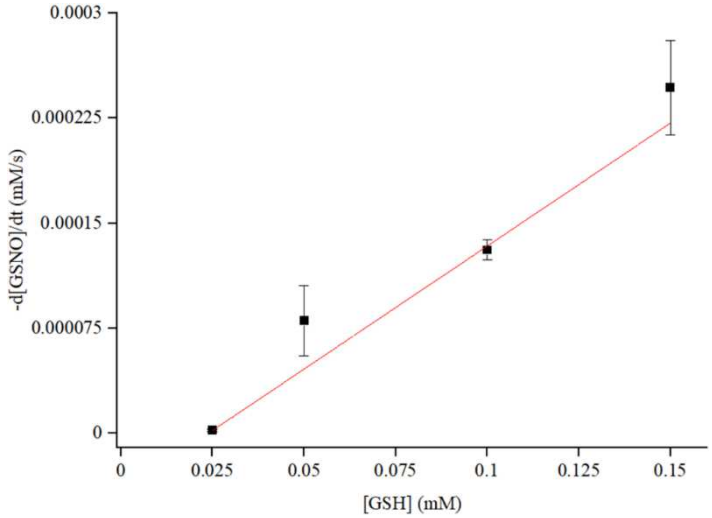

Figure 5.6. Plot of the 1st order portion of Figure 5.5 (the first four points) with a linear least-squares fit (all linear fits herein were obtained with a least-squares fit). The line is fit by the equation $y = ((1.76 \pm 0.1) \times 10^{-3})\boldsymbol{x} - ((4.17 \pm 0.29) \times 10^{-5})$, $R^2 = 0.99$. Physically, the intercept cannot be negative ($-(4.17 \pm 0.29) \times 10^{-5}$ mM s^{-1}), so that at 3 sigma the error is taken to be ($\pm(4.17 \pm 0.29)) \times 10^{-5}$ mM s^{-1}. This plot demonstrates that GSH must be present, even if in small amounts, to observe CuBTTri catalyzed GSNO to NO conversion.

Third, Figure 5.7 shows the relationship between -d[GSNO]/dt and the amount of exterior surface Cu sites in CuBTTri (reported as mol % of GSNO). Previous work has shown that the NO release reaction is first order in CuBTTri particle exterior surface area.[22] The plot in Figure 5.7

also shows that the reaction is first order in catalytically active $Cu_{surface}$ sites, as expected. The number of $Cu_{surface}$ sites present in each experiment was calculated based upon the previously determined Cu active site density in 600 ± 300 nm CuBTTri particles.[22] The linear relationship in Figure 5.7 yields the empirical rate law for just the Cu-catalyst (equation 5.3):

$$\frac{-d[GSNO]}{dt} = k_{Cu,obs}[Cu_{surface}]^1 \text{ (eq. 5.3)}$$

The observed first-order rate constant, $k_{Cu,obs}$, set by the slope of the line in Figure 5.7 is $k_{Cu,obs}$ = (1.06 ± 0.04) × 10^{-4}) s^{-1}. The [$Cu_{surface}$] term in equation 5.3 reflects the total number of $Cu_{surface}$ sites, that is the "concentration" of insoluble Cu sites suspended in the volume of solution by vigorous stirring as detailed in the Experimental section.

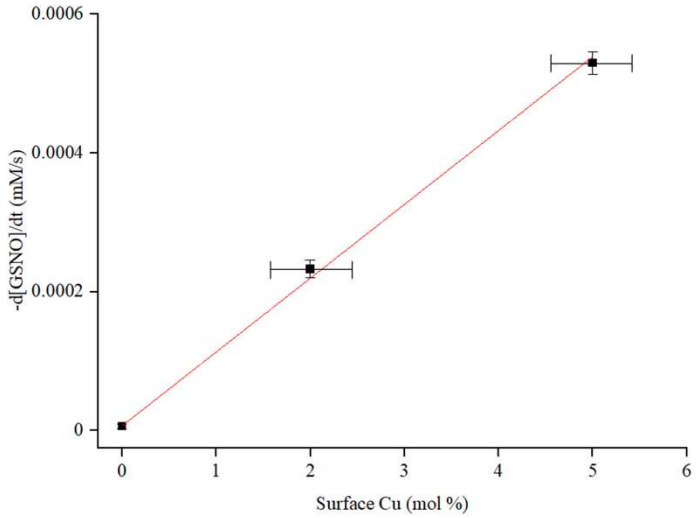

Figure 5.7. Plot of -d[GSNO]/dt measured at 20 min versus $Cu_{surface}$ sites added into the reaction (Cu reported in mol % of GSNO). The line is fit by the equation y = ((1.06 ± 0.04) × 10^{-4})***x*** + ((6.74 ± 3.98) × 10^{-6}), R^2 = 0.99. The horizontal error bars represent the previously determined experimental error in the active site density of the CuBTTri particle used herein. High CuBTTri mass loadings required for greater than 5 mol % $Cu_{surface}$ resulted in artificially lowered experimental -d[GSNO]/dt], apparently due to mass-transport limitations in the turbid, suspended-solid solution.

Lastly, the effect of pH on reaction rate was also investigated. Relevant here is that GSNO and GSH are endogenous tripeptides with multiple exchangeable, carboxylate and thiol protons

(Figure 5.1, *vide supra*). Hence, varying the reaction pH was investigated to see what insights such pH changes might teach about the reaction mechanism.

Figure 5.8 shows -d[GSNO]/dt as a function of reaction pH in buffered solutions prepared using non-coordinating buffers as detailed in the Experimental section. Decrease in -d[GSNO]/dt as reaction pH increases suggests that OH^- is involved in catalyst deactivation. Further discussion of the apparent catalyst poisoning at higher pH values will be presented in the Discussion section and is an important piece of evidence in support of our currently favored mechanism that has a Cu^{II}-bound GSH that can be deprotonated, and then poison, the proposed catalytic pathway. All -d[GSNO]/dt versus pH studies were carried out under conditions where the reaction was saturated in [GSH]. Therefore, the maximum number of $Cu^{II}_{surface}$ sites available were coordinated with GSH for all the data points in Figure 5.8.

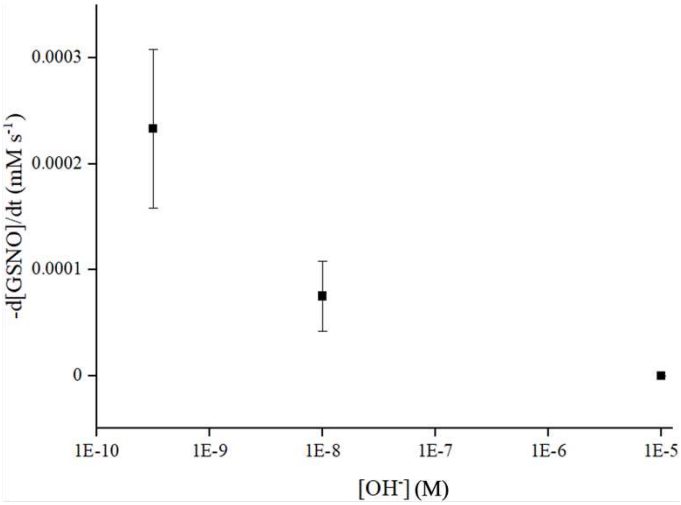

Figure 5.8. Plot of -d[GSNO]/dt versus $[OH^-]$. The x-axis is presented on a $\log_{10}$ scale to reflect the fact that $[OH^-]$ was varied over several orders of magnitude by altering the reaction pH. However, the data points correspond to the true, numerical value for $[OH^-]$ and *not* $\log[OH^-]$. The measured value for -d[GSNO]/dt at pH = 9 is equal to zero (the furthest right point on the plot). The data were fit to estimate reaction parameters (summarized in Appendix IV).

Overall, the kinetics data reported in Figures 5.4-5.8 reveal that the rate law for CuBTTri catalyzed GSNO to NO conversion is: a) first order in [GSNO], b) first order initially, but the

exhibiting saturation kinetics, in [GSH] c) first order in [$Cu_{surface}$], and d) inversely dependent on [OH^-]. The kinetics data reported herein yield the experimental rate law shown in equation 5.4:

$$\frac{-d[GSNO]}{dt} = k_{obs}\frac{[GSNO][Cu_{surface}][GSH]^{1\rightarrow 0}}{[OH^-]^{1\rightarrow 0}} \quad \text{(eq. 5.4)}$$

At pH = 4.5 the apparent rate law simplifies to equation 5.5, where the small, constant denominator $[OH]^{-1}$ term has been absorbed into k'_{obs}:

$$\frac{-d[GSNO]}{dt} = k'_{obs}[GSNO][Cu_{surface}][GSH]^{1\rightarrow 0} \quad \text{(eq. 5.5)}$$

Equations 5.4 and 5.5 satisfy the third requirement for determining a catalytic reaction mechanism (*vide supra*), namely obtaining an experimental rate law for the reaction. It is important to note here that this treatment of the -d[GSNO]/dt versus pH data operates under the assumption that the reaction mechanism does not change when moving from pH = 4.5 to 6 to 9. However, based upon the relative pK_a values of the protons available in GSH and GSNO (Figure 5.1, discussed in greater detail in the following Discussion section), we propose it is reasonable to assume that the reaction mechanism is the same for all three pH values tested in Figure 5.8.

A Summary of the Key Experimental Evidence That Must Be Accounted for by Any Proposed Initial, Minimum Mechanism.

The Results section combined with our prior work[21,22] establishes five key pieces of evidence that any proposed GSNO to NO catalytic cycle must meet. That evidence, items A through E below, is of course specific to the CuBTTri/GSNO/GSH/NO system and satisfies (but is not identical in its order) to the list in the Introduction (*vide supra*) of requirements a proposed reaction mechanism needs to meet:

A. Copper ions leached from CuBTTri have been ruled out as the active catalyst.[1,2,21] Previously reported results detail the following evidence inconsistent with Cu ions as being the kinetically dominant catalyst: (i) the lack of catalytic activity of the reaction supernatant; (ii) catalyst poisoning by TPPTS; (iii) solvated Cu ion poisoning by GSH; and (iv) the surface sites

detected by FT-IR spectroscopic analysis of CuBTTri poisoned by cyanide. A more detailed discussion of the four points listed here can be found in Appendix IV. Hence, the proposed mechanism uses a Cu-MOF (surface) active site provided by CuBTTri solid catalyst.

B. The proposed mechanisms must operate via the previously characterized $Cu_{surface}$ active sites on CuBTTri. Those catalytically $Cu_{surface}$ sites have 3 open coordination sites to accept ligands other than solvent and are bound to two nitrogen atoms from the H_3BTTri linker and one interstitial chlorine atom.[26–28] The $Cu_{surface}$ active sites can by poisoned by cyanide, by 3,3′,3″-phosphanetriyltris (benzenesulfonic acid) trisodium salt (TPPTS) and the results herein suggest by GS^- (*vide infra* and *vide supra*).[22]

C. The proposed mechanism must of course sum to the experimentally observed reaction stoichiometry (Figure 5.2, *vide supra*).

D. The mathematically derived rate law for proposed mechanisms must of course match the experimentally observed rate law given in equations 5.4 and 5.5. That is, the proposed mechanism must be 1st order in GSNO, GSH (with the possibility of saturation in each, implying they are involved in prior binding K_{eq}), 1st order in $Cu_{surface}$ atoms, and inverse order in OH^- up to a zero-order dependence at pH ≥ ca. 6.7.

E. The proposed mechanism must be able to be written as catalytic cycle, so that for example after NO release from GSNO, the Cu active site must be back in the starting state where it then bound GSNO.

5.3 Discussion

The Discussion section which follows contains four stages en route to establishing a best mechanistic working hypothesis for going forward for CuBTTri catalyzed GSNO to NO conversion that is consistent with and supported by the above-summarized experimental data. First, we provide a brief discussion of the alternative mechanistic hypotheses considered, but which did not fit the observed data. Second, we present the presently favored, proposed mechanism and compare it to the observed rate law and other data. Third, key features of the catalytic cycle are then explained in more depth. The special properties of GSNO and GSH as substrates in the NO release reaction turn out to be an important part of that discussion—consistent with the literature where the endogenous tripeptides GSNO and GSH are known to exhibit unique behavior in comparison to other Cu/RSNO/RSH/NO release systems.[16–19,24,25,30,32,58,61–63] Fourth, we will

present specific hypotheses about the exact nature of observed catalyst poisoning at alkaline pH (Figure 5.8).

Problems with Cu^{II} Lewis acid and Cu^{II} to Cu^{I} Redox Mechanisms.

Table 5.1. Considered, but disproven, mechanistic hypotheses for CuBTTri catalyzed GSNO to NO conversion in the presence of GSH in water. The requirements listed at the top of the second through fifth columns in Table 5.1 are requirements A-E listed at the end of the Results section, respectively. Each disproven hypothesis fails to satisfy one or more of the requirements in the list A-E, disproving all four listed mechanisms en route to the proposed mechanism that will be given, *vide infra*.

(#) Mechanistic Hypothesis/Specific Requirement	A) Does this hypothesis make use of Cu active sites within the CuBTTri framework?	B) Does this hypothesis make use of the previously characterized Cu active sites?	C) Can this hypothesis be written to sum to the observed reaction stoichiometry?	D) Does the derived rate law for this hypothesis match what is observed experimentally?	E) Can this hypothesis be written as a reasonable, minimalistic catalytic cycle?
1) Cu^{II} Lewis acid, S-N homolysis resulting from inductive effects	Yes, requirement A is satisfied	Yes, requirement B is satisfied	No, requirement C is *not* satisfied	No, requirement D is *not* satisfied	No, requirement E is *not* satisfied
2) Cu^{II} Lewis acid, thiol coupling	Yes, requirement A is satisfied	Yes, requirement B is satisfied	No, requirement C is *not* satisfied	No, requirement D is *not* satisfied	Yes, requirement E is satisfied
3) Cu^{II} to Cu^{I} redox, GS^- is the reductant	Yes, requirement A is satisfied	Yes, requirement B is satisfied	No, requirement C is *not* satisfied	No, requirement D is *not* satisfied	Yes, requirement E is satisfied
4) Cu^{II} to Cu^{I} redox, GS• forms from GSH	Yes, requirement A is satisfied	Yes, requirement B is satisfied	No, requirement C is *not* satisfied	Yes, requirement D is *not* satisfied	No, requirement E is *not* satisfied

The alternative mechanistic hypotheses we considered, but which could be ruled out, are described briefly in Table 5.1 and the text that follows. Disproven mechanisms are discussed in greater detail in Appendix IV for the interested reader.

First, we considered two Cu^{II} Lewis acid mechanisms for CuBTTri catalyzed GSNO to NO conversion. Ultimately, it proved difficult to write a chemically reasonable, minimalistic reaction

mechanism for a Cu^{II} Lewis acid pathway. One possible Cu^{II} Lewis acid pathway involves coordination of GSNO and then GSH to Cu^{II}, followed by homolysis of the S-N bond to release a thiyl radical (GS•) and NO from GSNO (Appendix IV, Figure S5.9). *However*, this first Cu^{II} Lewis acid mechanism could be discarded because: (i) it did not explain the requirement that GSH must be added to the reaction at stoichiometric levels to observe catalysis with CuBTTri, and (ii) it could not be written, at least in our hands, as a reasonable catalytic cycle.

A second class of Cu^{II} Lewis acid mechanism that was considered and is listed in Table 5.1 as entry #2 is based on the well-known Cu-catalyzed thiol-coupling reactions (Appendix IV, Figure S5.10).[59,61] However, this second class of Cu^{II} Lewis acid mechanisms can be ruled out because it is not consistent with the observed reaction stoichiometry, as it predicts GSSG formation *from GSH* (which Figure 5.2 rules out) and rather than from GSNO as observed. The second class of Cu^{II} Lewis acid mechanisms also requires the formation of either Cu^{I} or $[NO]^{-}$ as reaction products (Appendix IV, Figure S5.10). *All but one of the Cu^{II} Lewis acid mechanisms considered* (Figure 5.10, *vide infra*) *failed to provide a reasonable explanation for the homolysis of the S-N bond*. In short, the Cu^{II} Lewis acid mechanisms provided no clear explanation for the essential feature of the reaction of interest, namely NO release from GSNO, at least in our hands and as we wrote each mechanism in Table 5.1 (see Appendix IV if additional details are desired).

The prevailing hypothesis for solvated Cu ion catalyzed GSNO to NO conversion, Cu^{II} reduction to Cu^{I}, was also carefully considered to see if it could explain our observed stoichiometry and kinetics entries #3 and #4 in Table 5.1. However, we encountered several problems in trying to write a reasonable Cu^{II} to Cu^{I} mechanism for CuBTTri catalyzed GSNO to NO conversion. First, if one writes a mechanism where thiolate (GS^{-}) is the reducing agent (Appendix IV, Figure S5.11), the derived rate law for such a mechanism predicts that the reaction rate will increase as

pH increases, *but the exact opposite effect is observed,* as seen in Figure 5.8. Second, Cu^{II} to Cu^{I} mechanisms can be written which include an identical intramolecular deprotonation to step 3 in the currently favored mechanism shown in Figure 5.9. Following GSH deprotonation, GS^- performs a one electron transfer to Cu^{II} and generates a thiyl radical (GS•, Appendix IV, Figure S5.12). However, mechanisms where GS•, and thus GSSG, are generated from *both* GSH and GSNO are ruled out by the observed reaction stoichiometry (Figure 5.2) in which the amount of GSSG corresponds to only one-half the amount of starting GSNO.[21] Furthermore, it is difficult to explain the driving force for why Cu^{I} is oxidized back to Cu^{II} in any of the Cu^{II} to Cu^{I} pathways considered. Again, these alternative mechanistic hypotheses that were considered are presented in greater depth in Appendix IV for the interested readers' perusal. Ultimately, it appears that placing the active Cu site within the solid framework of the CuBTTri surface prevents the catalyst from operating through a Cu^{II} to Cu^{I} redox mechanism, a point expected given the large if not prohibitive Marcus barrier expected for a Cu^{II} to Cu^{I} redox pathway within at least the internal Cu^{II} sites in a MOF.

The Currently Favored, Proposed Cu^{II} to Cu^{III} Redox, Proton-Coupled Electron-Transfer Mechanism.

Eventually—to our surprise—we wound up at the Cu^{II} to Cu^{III}, proton-coupled electron-transfer (PCET) redox mechanism in Figure 5.9 as our proposed catalytic cycle for GSNO to NO conversion catalyzed by CuBTTri. The Cu^{II} pre-active site in Figure 5.9 is drawn and written as $Cu^{II}(N_2)(Cl)(OH_2)$ to reflect the hypothesis that each $Cu^{II}_{surface}$ site (Figure 5.3) is coordinated to one chlorine and two nitrogen atoms within the framework.[26–28] We note here that the pre-active site is formally a net +1 cation complex, at least locally, as indicated by the "$[\ ]^+$" nomenclature around key species in Figure 5.9. The structures in the catalytic cycle are drawn with trigonal

bipyramidal geometry because steric effects resulting from the bulky nature of the GSH/GSNO tripeptide ligands (Figure 5.1) are minimized by placing one tripeptide in an axial position and the other in an equatorial position, a detail that is reasonable but not known absolutely, of course. The Cu site in Figure 5.9 exists as either a Cu^{II} site (d^9) or Cu^{III} site (d^8), lending further support to drawing the sites as trigonal bipyramidal. Metal complexes with d^9 or d^8 electron counts are known to exhibit little to no structural preference energy for a D_{3h} (trigonal bipyramidal) compared to the often slightly electronically favored C_{4v} (square pyramidal) geometry.[64,65] The elementary steps of Figure 5.9 are described in a list below and in more detail in what follows. The catalyst poisoning step in Figure 5.9 is not included in the list (as it exists outside the catalytic cycle) and is discussed in its own separate section later in this Discussion (*vide infra*).

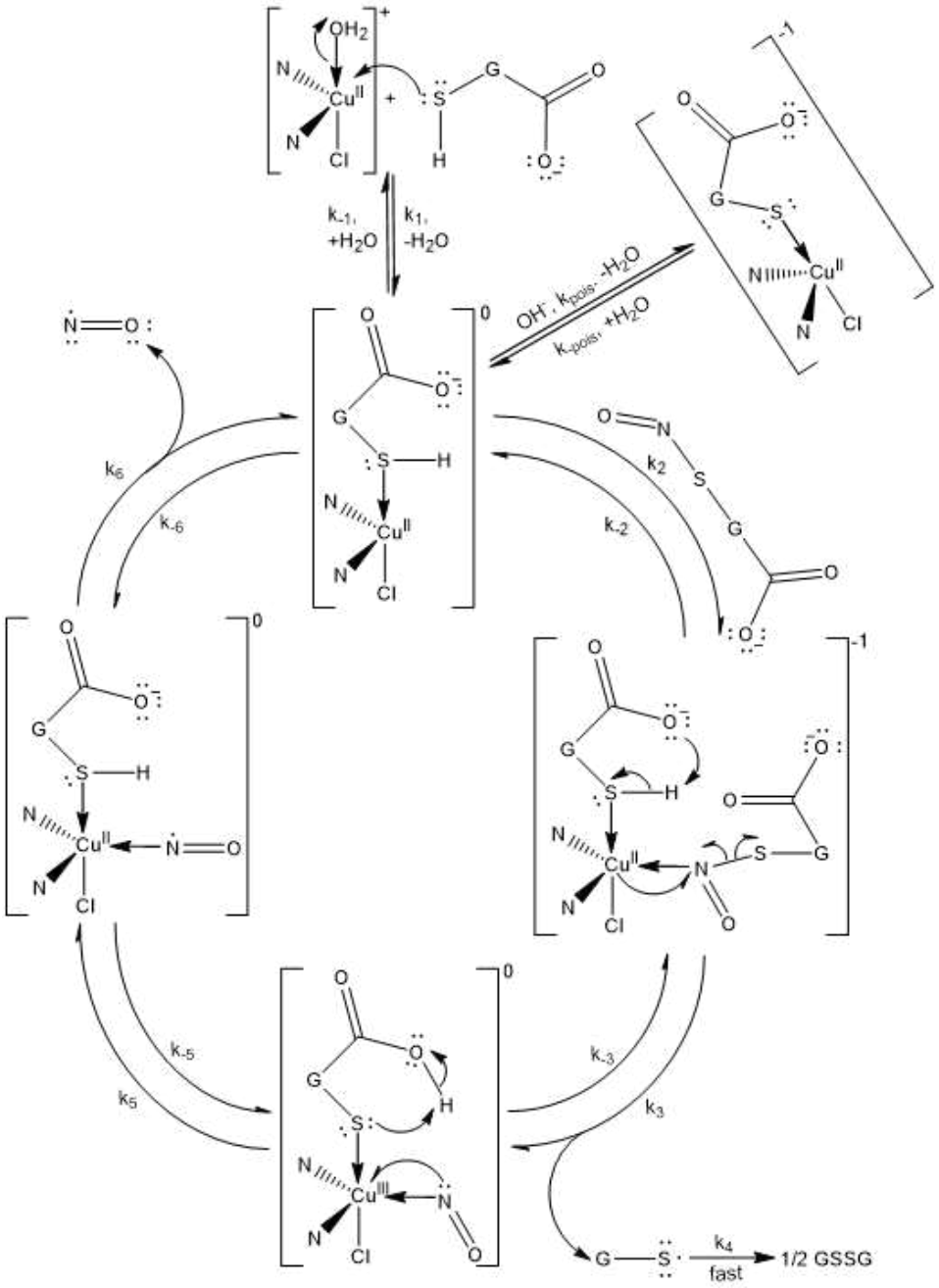

Figure 5.9. Proposed catalytic cycle for GSNO to NO conversion catalyzed by CuBTTri in water. The mechanism begins with GSH and GSNO coordination to the Cu^{II} pre-active site (steps 1 and 2), followed by Cu^{II} oxidation to what is formally Cu^{III} and S-N bond homolysis in GSNO resulting in GSSG formation (steps 3 and 4), and is completed by Cu^{III} reduction back to Cu^{II} along with release of NO which closes the catalytic cycle (steps 5 and 6). While each GSH/GSNO molecule contains *two* terminal carboxylate groups (Figure 5.1), only one has been drawn on each molecule in this Figure for the sake of simplicity and because only one carboxylate is involved in the proposed mechanism. The character "G" in the GSH and GSNO structures represents the identical tripeptide backbone in each molecule. Catalyst poisoning occurs via abstraction of the thiol proton by OH^- in GSH coordinated to the Cu^{II} site, effectively preventing at least steps 5 and 6 in the catalytic cycle and stopping NO release.

Step 1) Rate constants k_1 and k_{-1}. Reversible coordination of GSH to Cu^{II} through sulfur displaces H_2O and initiates the catalytic cycle. Coordination from sulfur to Cu^{II} is represented using a dative bond formalism, that is without a $–S^+–Cu^–$ charge implied in a valance bonding formalism, as that that avoids the otherwise resultant confusion of an implied reduction to Cu^I (i.e., in a valance bonding oxidation-state formalism vs the traditional "even electron" Cu^{II} oxidation-state formalism typically employed and utilized herein).[66] Step 1 forms a net neutral intermediate Cu site. Figure 5.9 shows GSH coordination to Cu^{II} first for the sake of simplicity, however it is possible that instead GSNO coordinates to Cu^{II} before GSH. The timing of steps in reaction mechanisms before or after the t.l.s. cannot be determined with kinetics studies and is rarely, if ever, conclusively established. Which species coordinates to Cu^{II} first may vary depending on the relative concentrations of GSH/GSNO and impacts the derived rate law for Figure 5.9. The interested reader is directed to Appendix IV for further details.

Step 2) Rate constants k_2 and k_{-2}. Reversible coordination of GSNO to Cu^{II} through nitrogen. Mechanisms analogous to Figure 5.9 can be drawn where GSNO coordinates to Cu^{II} through sulfur. Overall, N vs S coordination of GSNO to Cu^{II} is a detail in the mechanism in Figure 5.9 that will be addressed via future, needed computational studies. The intermediate formed in Step 2 is formally a net -1 anionic complex.

Step 3) Rate constants k_3 and k_{-3}. Proposed *intramolecular* deprotonation of the thiol proton in GSH by the terminal carboxylate in GSH (Figure 5.1). The deprotonation increases electron density around sulfur and Cu^{II} and helps drive the, at least formal, oxidation of Cu^{II} to Cu^{III} via an inner-sphere one electron transfer from Cu^{II} to nitrogen. *Critically, this proton-coupled electron transfer (PCET) provides the driving force for homolysis of the S-N bond in GSNO* and release of a thiyl radical (GS•). Furthermore, step 3 is favorable in part because the intermediate formed is a net neutral complex. Step 3 is assumed to be the turnover limiting step (t.l.s.), which means that $k_{-3} << k_4$ and k_5. Further support for the hypothesis that step 3 is the t.l.s. is presented later in this discussion section when analyzing the catalyst poisoning data in Figure 5.8 (*vide infra*). The concentration dependencies in the derived rate law for Figure 5.9 (equation 5.6) do not change if steps 2, 3, 5, or 6 are set as the t.l.s., only the constants making up the net "k_{obs}" change. Hence, we present step 3 as the t.l.s. at this time for the sake of simplicity and given point 4 discussed next.

Step 4) Rate constant k_4. Radical recombination of GS• to generate GSSG product. Note that step 4 is unlikely to be the t.l.s. because k_4 (the rate constant for thiyl radical recombination) is known to be diffusion controlled, $>10^9$ s^{-1} in H_2O for GS•.[61,67]

Step 5) Rate constants k_5 and k_{-5}. Reduction of Cu^{III} back to Cu^{II} via an inner-sphere one electron transfer from nitrogen to Cu^{II} coupled to a reverse of the intramolecular deprotonation in step 3, that is sulfur anion ligand ($GS^–$) deprotonation of the terminal carboxylate group in GSH. Electron transfer in step 5 is proposed to result concomitant with a change in NO ligand geometry from bent (formally $[NO]^–$) to near-linear (formally •NO) driven by the higher reduction potential at Cu^{III} due to conversion of a formally $–GS^–(COOH)$ ligand to a $–GSH(COO^–)$ ligand. The intermediate formed from step 5 retains the net neutral charge formed in steps 3 and 4. The proposed catalytic cycle shows that the *synthetic* CuBTTri NO release

catalyst utilizes what appears to be *nature's* elegant PCET chemistry for GS-NO bond activation.

Step 6) Rate constants k_6 and k_{-6}. Dissociation of NO from Cu^{II}. Dissociation of the neutral NO ligand results in the release of NO product and regeneration of the Cu^{II} site generated in step 1 of Figure 5.9. It is possible of course that the intermediate shown in between steps 5 and 6 is not needed, or at most a very transient intermediate, another topic worthy of planned computational investigations.

The derived rate law for the mechanism shown in Figure 5.9 with k_3 as the turnover-limiting step at reaction pH = 4.5 (Appendix IV, Derivation S5.1) is given below in equation 5.6 and matches the experimental rate law (equation 5.5).

$$\frac{-d[GSNO]}{dt} = k_3 K_{eq,1} K_{eq,2} [GSNO]^1 [Cu]_T [GSH(COO^-)]^{1\rightarrow 0} \text{ (eq. 5.6)}$$

The mechanism in Figure 5.2 can be written (by manipulating the coefficients of each elementary step) to sum to the experimentally observed reaction stoichiometry (Figure 5.2). Previously, it was established that each equivalent of GSNO lost produced one equivalent of NO and one half of an equivalent of GSSG.[21] However, our previous work did not have an explanation for the disappearance of ~15% of the GSH over the course of the reaction. The proposed mechanism in Figure 5.9 explains that GSH loss naturally, however, as it is due to GSH bound to the Cu^{II} resting state of the catalyst. The loss of GSH may also occur by physisorption to CuBTTri over and above the binding of GSH to Cu^{II} shown in Figure 5.9.[68]

The Question of Formal Cu^{III} vs Physically More Correct Cu Oxidation State In Figure 5.9

What is formally Cu^{III} is written in Figure 5.9 in conjunction with the normal, U.S. "even" (vs European "odd") formalism of bookkeeping electrons.[66] We are aware of Pauling's electroneutrality principle[69] which states that the charge on the central metal ion in a complex lies between ±1 (others say ±0.5). We are also aware of work that provides XAFS as well as DFT evidence that Cu^{III} physically likely never exists, an unsurprising result again in light of both

Pauling's electroneutrality principle as well in light of molecular orbital population analyses on even some of the very earliest quantum mechanical calculations of transition-metal species that are in general agreement with Pauling's principle.[70] In short, it is not our intention to say that a physically truly Cu^{III} species is formed as written using the oxidation-state formalism employed in Figure 5.9.

It is our intent to show arrow pushing and a general flow of electrons that will drive the key GS-NO bond cleavage. Our hypothesis is that the Cu active site in Figure 5.9 is if anything oxidized*, not reduced*, en route to providing the driving force for S-N bond homolysis in GSNO. It is entirely possible, however, that more especially S-ligand-based orbitals are what is oxidized while the Cu site in Figure 5.9 acts mainly as a conduit for charge transfer, with overall little true redox change at Cu. Just such a "ligand-based redox, PCET, all Cu^{II} mechanism" is shown below in Figure 5.10. One key point to make clear here is that Figures 5.9 and 5.10 are resonance forms of one another, and hence both contribute to some extent to the overall, "true" mechanism. Additionally, a limiting case of an all Cu^{I} mechanism is provided in Appendix IV for the interested reader. DFT calculations, followed by population analysis of the resulting molecular orbitals, as well as studies by methods such as XAFS able to address the net charge at Cu are needed, some of which are already in progress.

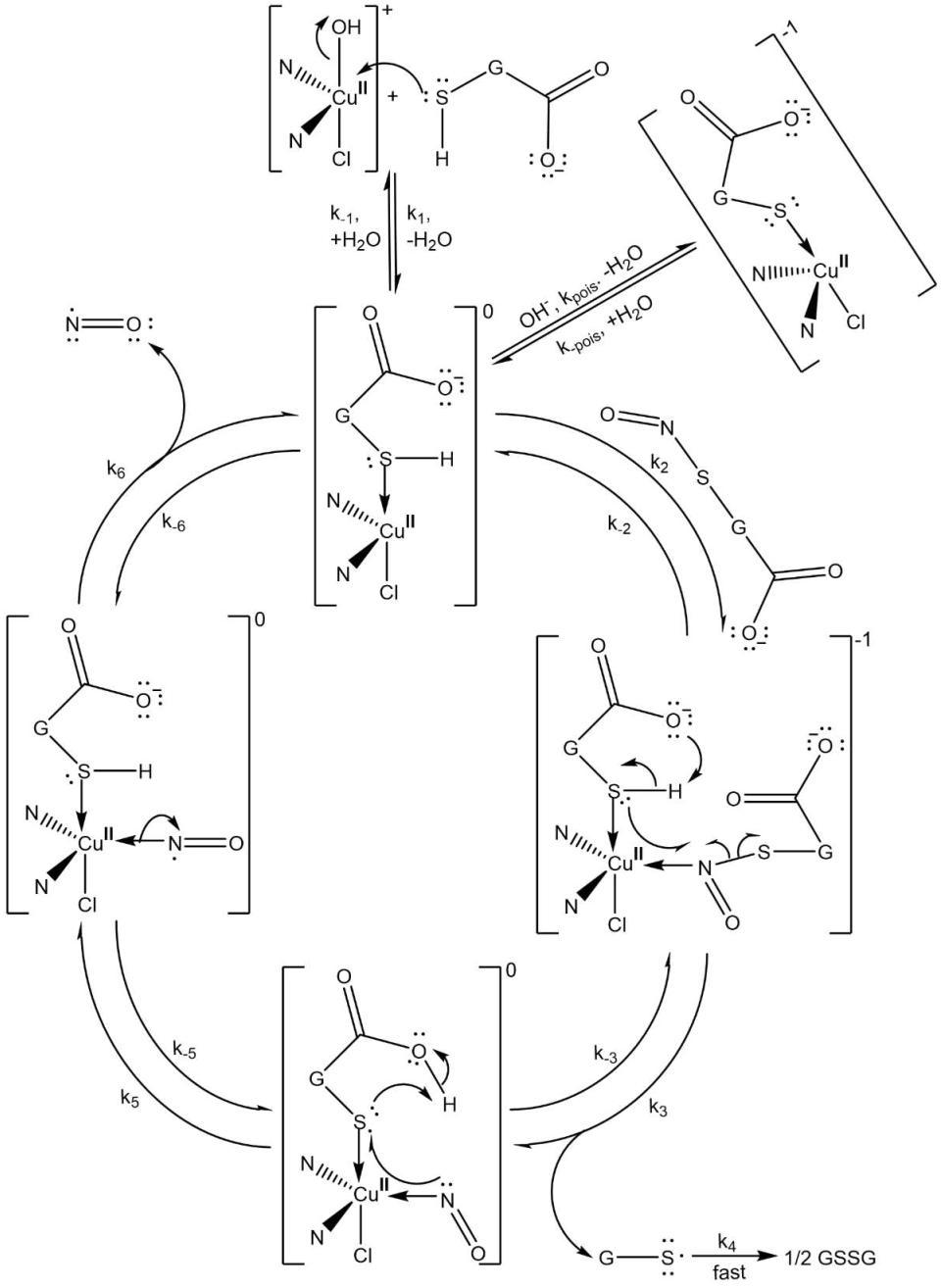

Figure 5.10. Proposed alternative mechanistic hypothesis for GSNO to NO conversion catalyzed by CuBTTri in water. In this mechanism (which matches the experimentally observed rate law and stoichiometry) the *formal oxidation state* of Cu^{II} remains unchanged throughout the catalytic cycle. Cu^{II} (d^9) acts as a conduit for e^- transfer between S (in the GSH ligand) and N (from the GSNO ligand). Steps 3 and 5 are PCET, as in the $Cu^{II/III}$ Figure 5.9. The above mechanism can be considered a ligand-dominated, charge-transfer mechanism. Ultimately, the above mechanism is a resonance form of the $Cu^{II/III}$ mechanism (Figure 5.9) where Cu^{II} is never formally oxidized or reduced by the gain or loss of a full e^-. The mechanism above addresses the question of: is the Cu^{II} site in CuBTTri formally oxidized or reduced to catalyze S-N bond homolysis or does the Cu^{II} site merely act as a "conduit" for e^- transfer between the ligands? Evidence that Cu^{III} sites do, in general, not form supports the ligand-dominated e^- transfer shown above.[70]

Estimating Thermodynamic/Kinetic Parameters in Figures 5.9-5.10

Using the data in Figures 5.5, 5.6, and 5.8 and the predicted rate law as given by the derivation in S5.1 in Appendix IV, one can estimate the following thermodynamic/kinetic parameters for Figure 5.9-5.10 from the resultant analysis of the kinetics data: (1) the equilibrium constant for Step 1, $K_{eq,1}$, (2) the equilibrium constant for the poisoning step, $K_{eq,pois}$, and (3) the product of the rate constant for Step 3 and the equilibrium constant for Step 2, $k_3*K_{eq,2}$. What follows in this section is a brief discussion of how each of the parameters listed above was estimated (summarized in Table 5.2). Appendix IV contains the full details of how the data in each figure was analyzed to obtain the estimated parameters. It is worth pointing out here that successful fitting of kinetics data to obtain the reaction equilibrium constant and rate constant parameters suggests that the mechanistic hypotheses in Figures 5.9-5.10 are, at the very least, decent initial mechanistic hypotheses. Moreover, the equilibrium and rate constants obtained from fits of the kinetics data in Figures 5.5, 5.6, and 5.8 to the predicted rate law(s) corresponding to Figures 5.9-5.10 make physical sense (Table 5.2, *vide infra*), further supporting the at least reasonableness of the working mechanistic hypotheses presented as Figures 5.9-5.10.

Table 5.2. Estimated reaction parameters for Figures 5.9-5.10 and the kinetics data used to calculate the estimates. The full details of how each of the estimated parameters was calculated can be found in Appendix IV. The values for $K_{eq,1}$ and $K_{eq,pois}$ are dimensionless.

Reaction Parameter	Data Used for Estimation	Value
$\mathbf{k_3*K_{eq,2}}$	Figure 5.5-5.6	$(5.6 \pm 1.6) \times 10^{-4}$ s^{-1}
$\mathbf{K_{eq,1}}$	Figure 5.5-5.6	6.1
$\mathbf{k_3*K_{eq,2}}$	Figure 5.8	$(5.02 \pm 0.2) \times 10^{-4}$ s^{-1}
$\mathbf{K_{eq,pois}}$	Figure 5.8	$(2.34 \pm 0.05) \times 10^{8}$

The data in Figures 5.5 and 5.6 yield estimates for both $K_{eq,1}$ and $k_3*K_{eq,2}$. The slope of the line of Figure 5.6 where -d[GSNO]/dt is 1st order in $[GSH]_i$ is equal to $k_3*K_{eq,1}*K_{eq,2}*[Cu]_T*[GSNO]$ (as explained in the derivation S5.1 in Appendix IV). The levels of $[Cu]_T$ and [GSNO] were held constant at 0.5 and 1 mM, respectively, for the experiments summarized in Figure 5.6. Therefore, one can use the slope of the line in Figure 5.6 to estimate $k_3*K_{eq,1}*K_{eq,2}$. The portion of the data in Figure 5.5 where -d[GSNO]/dt is 0th order in [GSH] (and -d[GSNO]/dt is a constant) is equal to $k_3*K_{eq,2}*[Cu]_T*[GSNO]$ (as explained in the derivation S5.1 in Appendix IV). Therefore, one can calculate an estimate for $K_{eq,1}$ and $k_3*K_{eq,2}$ using the data in Figures 5.5 and 5.6 (Table 5.2, explained in full detail in Appendix IV). The estimates for $K_{eq,1}$ and $k_3*K_{eq,2}$ given in Table 5.2 are, again, physically reasonable: the association of GSH to Cu^{II} is mildly favorable ($K_{eq,1} = 6.1$), thiols such as the bulky GSH being only a moderate ligand. The value for $k_3*K_{eq,2}$ ($(5.9 \pm 0.08) \times 10^{-4}\ s^{-1}$) is expected to be small based upon the hypothesis that k_3 corresponds to the turn-over limiting step in Figures 5.9-5.10.

The data in Figure 5.8 can be fit using non-linear least squares to yield estimates for both $K_{eq,pois}$ and $k_3*K_{eq,2}$ (full details are available in Appendix IV). The experimentally observed (*vide infra*) and derived (Appendix IV) rate laws for the reaction run at pH > 4.5 and saturated in [GSH] is given in equations 5.4 and 5.7 (*vide infra*). Using a general form of the derived rate law where one fit parameter is set equal to $K_{eq,pois}$ and one fit parameter is set equal to $k_3*K_{eq,2}$ yields the estimates for these two parameters shown in Table 5.2. Pleasingly, the value of $k_3*K_{eq,2}$ estimated from the data in Figure 5.8 ($(5.02 \pm 0.2) \times 10^{-4}\ s^{-1}$ matches, within experimental error, the estimate for $k_3*K_{eq,2}$ from the data in Figures 5.5 and 5.6 ($(5.6 \pm 1.6) \times 10^{-4}\ s^{-1}$)). The good agreement between these two estimates for $k_3*K_{eq,2}$ from two different sets of data supports the proposed

mechanism, the treatment of the data, and argues for reasonable at least precision if not accuracy for the estimates of $k_3*K_{eq,2}$ herein.

The value estimated for $K_{eq,pois}$ from the data in Figure 5.8 is large, on the order of 10^8. The large magnitude $K_{eq,pois}$ is reasonable as the deprotonation in the poisoning step (Figures 5.9-5.10) is energetically favorable (especially given the fact that the pK_a of the thiol proton in GSH bound to Cu^{II} is expected to drop 2-4 orders of magnitude compared to the unbound thiol, *vide infra*) and given that the resulting thiolate ligand is expected to be strongly bound to what is formally Cu^{II}.

Additional Discussion of the Cu^{II}/Cu^{III} and Then Cu^{III}/Cu^{II}, PCET Steps.

As we struggled to find a reasonable driving force and associated mechanism for the crucial S-N bond homolysis in GSNO, we were—quite unexpectedly, as noted above—driven to the Cu^{II} to Cu^{III}, and then reverse Cu^{III} back to Cu^{II}, steps with their accompanying PCET shown in Figure 5.9 (steps 3 and 5, respectively). Both proposed PCET steps[71,72] are intimately dependent on the molecular structures of GSH and GSNO. Figure 5.9 also explains why the relatively simple pH studies shown in Figure 5.8 are so important for discovering the PCET steps in the CuBTTri/GSNO/GSH/NO system. Searching for evidence of a PCET step requires that one either: a) alter the concentration of electrons available for the reaction or, b) alter the concentration of protons available for the reaction. Altering the concentration of protons available in the CuBTTri/GSNO/GSH/NO system in water through pH is much easier experimentally and the observed pH dependence of the reaction is consistent with and supportive of the proposed PCET mechanism.

Some additional details of the catalytic cycle and proposed PCET steps merit discussion. In step 3 the terminal carboxylate groups of GSH and GSNO should both be deprotonated when the reaction pH is 4.5 given that their respective pKa values are 2.12 and 3.53.[73] Increasing the

electron density around the Cu^{II} site in step 3 via the deprotonation of a –SH to a $–S^-$ by a $–COO^-$ decreases (shifts negatively) the Cu^{II} to Cu^{III} oxidation potential thereby driving the transfer of an electron from Cu^{II} to nitrogen, formally forming Cu^{III}. Formation of Cu^{III} in step 3 of Figure 5.9 is also favorable in part because it eliminates the net -1 formal charge formed on the active site in step 2. The thiol proton in GSH is known to have a pK_a of 9.12 when GSH is unbound.[73] However, upon binding to Cu^{II}, the pK_a of the thiol proton is expected to drop between roughly 2-4 orders of magnitude,[74] making the deprotonation as shown in step 3 more favorable (discussed in greater detail below, *vide infra*). We note that the deprotonations in steps 3 and 5, now written for simplicity as intramolecular deprotonations, assume the GSH tripeptide backbone (Figure 5.1) completely coils around to a conformation able to perform an intramolecular deprotonation. The currently written intramolecular deprotonations are possible oversimplifications of what, instead, could be a proton relay via one or more H_2O molecules in a Grotthus-type, proton hopping mechanism[75]—another topic we will test computationally. Steps 3 and 5 explain why GSH must be added to the CuBTTri/GSNO/NO system to observe NO release catalysis: *without GSH, no electron transfer between Cu^{II} and GSNO occurs in the proposed mechanism nor experimentally*.

The Cu^{III} intermediate that forms in step 3 is then reduced back to Cu^{II} in step 5 of Figure 5.9 in a reverse of the original PCET. The Cu^{III} intermediate contains what is formally a bent $[NO]^-$ ligand. Vibration of the formally $[NO]^-$ ligand into a more linear geometry is the implied nucleation motion driving the transfer of one electron from nitrogen to Cu^{III}, regenerating Cu^{II} and forming a near-linear, neutral •NO ligand (in reality, the bound •NO is perhaps likely to be somewhere between bent and linear). Reduction of Cu^{III} back to Cu^{II} increases electron density around sulfur in Cu^{II}←(SG(COO**H**)), and in part drives the deprotonation of the terminal carboxylate group, reforming the –SH ligand. The active site net charge may be neutral both before

and after step 5 in Figure 5.9, but the arrow pushing in step 5 is favorable because it reduces the total local charge on Cu and the NO ligand. Before step 5, Cu is in the Cu^{III} oxidation state and NO is formally an $[NO]^-$ ligand, and after step 5 Cu is in the Cu^{II} oxidation state and the NO ligand is neutral. Post •NO dissociation, the reformed Cu^{II}←(S(**H**)G) restarts the catalytic cycle at step 2 with a new equivalent of GSNO.

One final important point to make about the PCET steps in Figure 5.9 is that there should be a low Marcus type reorganization energy barrier for any geometric rearrangements required for the $Cu^{II\rightarrow III}/Cu^{III\rightarrow II}$ steps because Cu complexes in both oxidation states readily adopt either trigonal bipyramidal or square pyramidal geometry (*vide supra*). The predicted low reorganization energy barrier of the Cu^{II} to Cu^{III} mechanism proposed herein for CuBTTri emerges as another factor favoring Figure 5.9 over the traditionally hypothesized Cu^{II} to Cu^{I} mechanism (which requires a $\leq$6 to $\leq$4 coordinate geometry change).

Steps 3 and 5 of Figure 5.9 highlight the importance of the GSNO/GSH tripeptide structures for their unique behavior in Cu-catalyzed NO release. Previous literature reporting Cu-ion catalyzed GSNO to NO release highlights the unique nature of GSNO among other NO donors of the broad *S*-Nitrosothiol (RSNO) variety.[16,17,24,30,76] GSNO is exceptionally stable in solution in comparison to other small molecule RSNOs, even in the presence of Cu ions. The stability of GSNO, and the revealed mechanism for NO release by Cu^{II} are not surprising when one realizes that GSNO has been designed by nature over time to act as a metastable NO transport vessel in the human body.[20] Without the terminal carboxylate group and thiol proton in GSH, all the steps in Figure 5.9 are not possible as written. Other RSNO/RSH pairs which do not exhibit the same type of structural complexity of GSNO and GSH cannot operate via a mechanism such as Figure 5.9 for NO release in the presence of Cu-containing catalysts. RSH species without the terminal

carboxylate group of GSH may not be able to shuttle protons back and forth to the sulfur atom coordinating to the Cu site, making conversion back and forth between Cu^{II} and Cu^{III} not possible when using other RSH species. Hence, a general prediction of the proposed mechanism is that other RSNO to NO systems may release NO via different mechanistic pathways from the Cu^{II} to Cu^{III} redox mechanism proposed herein.

Explaining the pH-Dependent Results via the Coordination of GSH and Its Deprotonation at the –SH Moiety.

Figure 5.8 shows that Cu^{II} site poisoning occurs via deprotonation of GSH *bound* to a Cu^{II} site and *not* as a result of the deprotonation of unbound GSH. The only other protons present for abstraction by OH^- at pH = 6 (amines in GSH/GSNO and water) can be ruled out based on their relative pK_a values.[73] If deprotonation of unbound GSH (forming thiolate, GS^-) were the cause of the active site poisoning, then one would *not* expect to observe a ~67% decrease in -d[GSNO]/dt between pH = 4.5 and pH = 6 (Figure 5.8). Based on the ratio of GS^- to Cu^{II} active sites, strong binding poisoning of Cu^{II} sites by GS^- should result in a ~12% decrease in -d[GSNO]/dt at pH = 6 (Appendix IV, Calculation S5.1). The ~67% decrease in -d[GSNO]/dt at pH = 6 therefore indicates that OH^- is abstracting a more acidic proton than the thiol proton in unbound GSH (pK_a = 9.12).[73] The poisoning of the Cu active sites at alkaline pH may result from the deprotonation of the thiol proton in GSH bound to a Cu^{II} site. One can estimate the apparent pK_a of the Cu^{II}←(S(**H**)G) intermediate using the data in Figure 5.8 (Appendix IV, Calculation S5.2). Operating under the assumptions that: i) poisoning by OH^- is a strong-binding poisoning event, and ii) the reaction rate observed at pH = 4.5 represents 100% of the possible catalytic activity, then the apparent pK_a of the Cu←(S(**H**)G) intermediate is 5.6 (again, Appendix IV contains the details for how this value was obtained). The apparent pK_a of 5.6 for the thiol proton in

Cu^{II}←(S(**H**)G) is reasonable, as pK_a values for thiols bound to metal sites are known to decrease by 2-4 orders of magnitude compared to unbound thiols.[74] The apparent pK_a of Cu←(S(**H**)G) fits well with the mechanistic hypothesis shown in Figure 5.9. The deprotonation of Cu^{II}←(S(**H**)G) (pK_a of ~5.6) in step 3 of Figure 5.9 by $-COO^-$ (pK_a of 2.12 to 3.53) is energetically uphill by 2-3 orders of magnitude at room temperature but should still be a viable pathway and intermediate. Therefore, the hypothesis that step 3 of Figure 5.9 is the t.l.s. is supported by the apparent pK_a of Cu←(S(**H**)G) of 5.6.

Figure 5.11 shows the poisoning steps in Figure 5.9 in isolation. In Figure 5.11, the deprotonation of the thiol proton in Cu^{II}←(S(**H**)G) by hydroxide occurs before coordination of GSNO to the Cu^{II} site, resulting in the formation of a net -1 complex. In this hypothesis, GSNO coordination may still occur after the deprotonation and a single half-equivalent of GSSG could be formed at each active Cu site, but only once. In other words, steps 3 and 4 of Figure 5.9 may still occur *a single time* at each active site after the proton in Cu^{II}←(S(**H**)G) has been abstracted by OH^- (meaning that trace levels of GSNO and GSSG would be lost and generated, respectively). As reaction pH increases, the thiol proton will not be available again after the poisoning step. Therefore, steps 5 and 6 of Figure 5.9 cannot occur as written at alkaline pH. Without a proton available to balance the electron transfer in step 5 of Figure 5.9, the Cu^{III} site will not be reduced back to Cu^{II} and release NO. When the reaction is run at pH = 9, the active site may be trapped as the intermediate shown after either the poisoning step or step 3 in Figure 5.9. We discuss in Appendix IV how one can potentially further test the state of the poisoned active site, an interesting but relatively minor mechanistic detail.

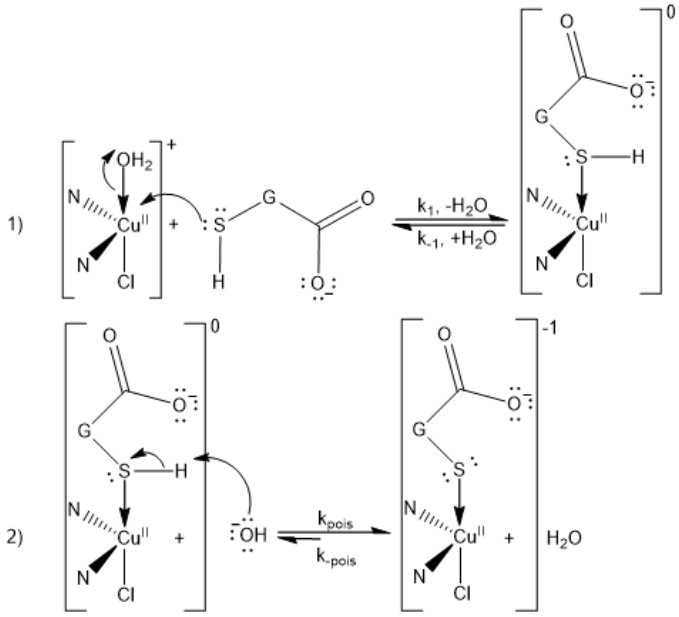

Figure 5.11. Proposed Active Site Poisoning Forming $Cu^{II}(N)_2(Cl)(SG)$ at pH = 9**.** The elementary steps to explain the poisoning at alkaline pH shown in Figure 5.9. At pH = 9, the thiol proton in Cu←(S(**H**)G) will be abstracted by hydroxide, and the resulting $[Cu^{II}(N)_2(Cl)(SG)]^-$ site will be poisoned and, hence, unable to complete a full catalytic cycle.

The derived rate law at pH = 9 for Figure 5.11 under reaction conditions where the system is saturated in [GSH] (Appendix IV, Derivation S5.1) is given below in equation 5.7 and matches the experimentally observed rate law (equation 5.4):

$$\frac{-d[GSNO]}{dt} = \frac{k_3 K_{eq,2}[Cu]_T[GSNO][GSH]^0}{1 + K_{eq,pois}[OH^-]} \quad \text{(eq. 5.7)}$$

Equation 5.7 will become equal to zero as the concentration of hydroxide increases. Once again, the $[Cu]_T$ term in equation 5.7 only refers to the total number of catalytically active Cu sites.

Possible Future Experiments Based on Predictions Derived from Figure 5.9.

Any more reliable mechanism can both explain all the current data, but also makes predictions that can be tested in future studies. The mechanism in Figure 5.9 is no exception. Some predictions based on the novel Cu^{II} to Cu^{III} redox PCET mechanism,[71,72] and hence aims of future studies, are detailed in Appendix IV for the interested reader.

5.4 Summary and Conclusions

A novel Cu^{II} to Cu^{III} redox, PCET mechanism that is the key behind the GS-NO bond homolysis catalyzed by CuBTTri is proposed as a working mechanistic hypothesis (Figure 5.9). That proposed mechanism satisfies both five minimum requirements listed in the introduction for establishing reliable reaction mechanisms in catalytic systems and explains the five critical experimental findings specific to the CuBTTri/GSNO/GSH/NO system established in the Results section. Figure 5.9 is offered as the simplest working mechanistic hypothesis for moving forward. As with all especially new, unprecedented mechanisms, future further experimental as well as computational testing of the proposed mechanism is needed as well as planned. The work presented here is a good example of how once the catalytically active sites in a MOF catalyst have been established,[21,43–45,50] then the reaction mechanism can be investigated with greater confidence. The present work also shows that one can treat at least exterior surface MOF active sites as if they were discreet, ostensibly homogenous, metal complexes,[55] another valuable result from the present studies.

The work reported herein is, to the best of our knowledge, the first example where a reaction mechanism for a MOF catalyst has been elucidated based upon both first establishing the active sites within the catalyst and then also ensuring that the classic requirements for establishing a disproof-based, Ockham's razor obeying, hence more reliable reaction mechanism have been met.[49] Due to their exceptional chemical and physical tunability, MOF catalysts stand to benefit considerably from mechanistic insight for catalyst improvements and mechanism-directed catalyst design. Hence, it is hoped that both the approach employed to elucidate the mechanism, as well as the proposed unprecedented Cu^{II} to Cu^{III} redox PCET mechanism, will prove of value to the communities connected to MOF literature, biomedical NO generation, heterogeneous catalysis,

and workers generally interested in kinetic and mechanistic analyses and the results of those efforts.

5.5 Experimental

Reagents. Diethylamine (99%), trimethylsilylacetylene (98%), trimethylsilylazide (94%), and 1,3,5– tribromobenzene (98%) were purchased from Alfa Aesar (Ward Hill, MA, USA). Glutathione (98%) was purchased from VWR (Radnor, PA, USA). Sodium nitrite (99.5%), copper (I) iodide (99.5%), bis(triphenylphosphine)palladium(II) dichloride (99%), dichloromethane (99%), and monobasic sodium phosphate (≥98%) were purchased from Sigma–Aldrich (St. Louis, MO, USA). HCl (1 N), methanol (99%), and sodium hydroxide (98.9%) were purchased from Fisher Scientific (Hampton, NH, USA). Dimethylformamide (99%) and copper (II) chloride dihydrate (99%) were purchased from EMD Chemicals (Gibbstown, NJ, USA). 2-(N-morpholino)ethanesulfonic acid (MES) (99%) was purchased from VWR (Radnor, PA, USA). Piperazine-N,N′-bis(3-propanesulfonic acid) (PIPPS) (≥97%) was purchased from MilliporeSigma (Burlington, MA, USA). Ultrahigh purity nitrogen gas (99%) was supplied by Airgas (Denver, CO, USA). Deionized water (18.2 MΩ·cm) was obtained from a Millipore Direct–Q water purification system (EMD Millipore, Billerica, MA, USA). All materials were used as received without any further purification.

GSNO Synthesis. GSNO was prepared, and its purity verified, following an established literature protocol (Figure 5.12).[77] Briefly, a solution of glutathione (1.60 g, 5.21 mmol) was prepared in millipore filtered water (8 mL) containing 2M HCl (2.5 mL, 10.5 mL total volume). One equivalent of sodium nitrite (0.361 g, 5.21 mmol) was added, and the resulting mixture was stirred for 40 min at 5 °C. Acetone (10 mL) was added to the resulting red solution and the mixture was stirred for another 10min. The red precipitate was collected via vacuum filtration and washed

with ice–cold water (5 × 5 mL) and ice–cold acetone (3 × 10 mL). The precipitate was then dried on a high vacuum line for 4 h to afford *S*–Nitrosoglutathione (1.43 g, 4.22 mmol, 81%) (λ_{max}) (H_2O) 335, 550 nm (ε=922 cm^{-1} mM^{-1}). The GSNO sample used herein was determined to be (97 ± 2) % pure by UV–VIS spectroscopy. The GSNO sample used to collect the data reported herein comes from the same batch of GSNO used in previously published work.[22] The small, 4 ± 2 %, impurity present is glutathione (GSH) leftover from, or glutathione disulfide generated from (GSSG) the synthesis. Relevant here is that previous work on GSNO to NO conversion catalyzed by CuBTTri established that GSH must be present to initiate measurable CuBTTri catalyzed GSNO to NO conversion within 20 min.[21,30]

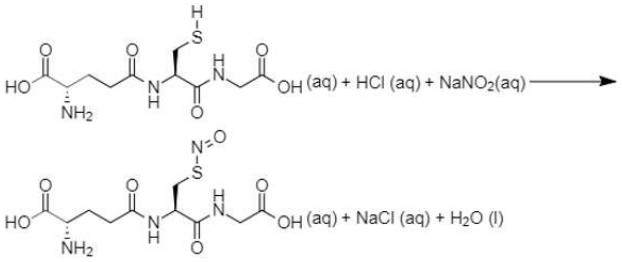

Figure 5.12. Synthesis of GSNO from GSH.

H_3BTTri Ligand Synthesis. The H_3BTTri ligand was prepared and characterized following an established literature protocol (Figures 5.13-5.15).[27] Briefly, solid 1,3,5–tribromobenzene (9.45 g, 30.0 mmol) was dissolved in diethylamine (250 mL) under inert conditions (N_2). Copper(I) iodide (50 mg, 0.26 mmol) and dichlorobis(triphenylphosphine)palladium(II) (400 mg, 0.57 mmol) were added to the stirred solution. Trimethylsilylacetylene (10.6 g, 108. mmol) was added to the solution and the resulting mixture was heated at 50 °C for 6 h. Resulting diethylamine hydrobromide was removed by filtration and washed with ether (45 mL). Combined washings were evaporated to dryness in vacuo at 30 °C and the resulting product purified by a silica plug to yield 9.61 g (78%) 1,3,5–

tris(trimethylsilylethynyl)benzene as an intermediate. ^{1}H NMR (400 MHz, $CDCl_3$): δ = 7.43(s), 0.23(s) ppm.

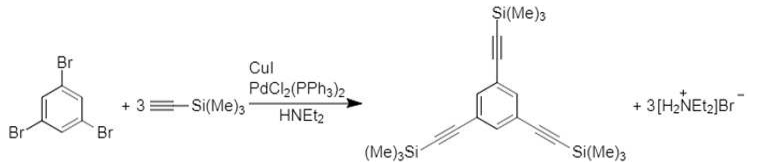

Figure 5.13. Coupling Aryl Halide and Trimethylsilylacetylene.

The 1,3,5–tris(trimethylsilylethynyl)benzene intermediate (9.61 g, 26.3 mmol) was hydrolyzed by treatment with NaOH (aq) (30 mL, 1M), CH_2Cl_2 (20 mL), and methanol (50 mL) via stirring at room temperature for 3h. Evaporation of methanol, extraction of the residue by ether, and evaporation of the solvent in vacuo at 30 °C yielded 2.68 g of white powder containing 1,3,5–triethynylbenzene. ^{1}H NMR (400 MHz, $CDCl_3$): δ =7.51(s), 3.12(s) ppm.

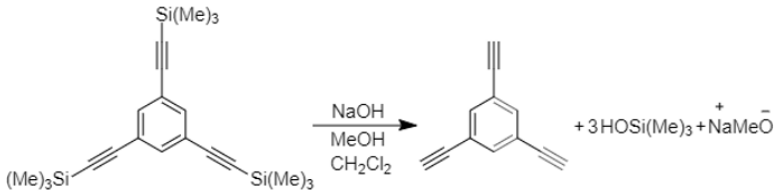

Figure 5.14. Hydrolysis of the Trimethylsilylethynyl Intermediate.

Trimethylsilylazide (9.26 g, 80.4 mmol) was added to a solution of copper(I) iodide (510mg, 2.63 mmol) and 1,3,5–triethynylbenzene (2.68 g, 17.8 mmol) under N_2 gas in a mixture of dimethylformamide (DMF; 90 mL) and methanol (10 mL). The resulting mixture was heated to 100 °C using a hot plate and stirred for 36 h. The mixture was then filtered using a vacuum filter and filter paper and reduced to a volume of 10 mL via rotary evaporation at 30 °C. A pale–yellow precipitate was formed upon the addition of millipore filtered water (30 mL) to the resulting filtrate. The solid was collected by filtration, washed with ether, and dried in vacuo at °C to yield 4.1 g (83%) of 1,3,5–tris(^{1}H–1,2,3–triazol–5–yl)benzene. ^{1}H NMR (400 MHz, $(CD_3)_2SO$): δ =

8.52(s), 8.34(s) ppm. The H_3BTTri used in this work is from the same batch prepared and used in two previous publications.[21,24]

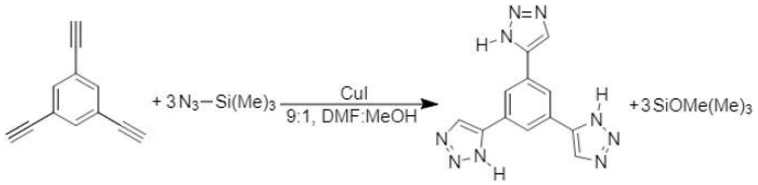

Figure 5.15. Click Reaction to Form 1,3,5–tris(^{1}H–1,2,3–triazol–5–yl)benzene.

CuBTTri Synthesis. CuBTTri was synthesized and characterized following a previously reported procedure (Figure 5.16).[27] A solution of H_3BTTri (225 mg, 0.937 mmol) in DMF (40 mL) was prepared in a 250mL Pyrex bottle. $CuCl_2 \cdot 2H_2O$ (383 mg, 2.25 mmol) was added to the solution. The vial was heated at 100 °C for 72 h in an oven to afford $H_3[(Cu_4Cl)_3(BTTri)_8(DMF)_{12}] \cdot 7DMF \cdot 76H_2O$. The purple powder was washed with boiling DMF (10 × 10 mL) and DMF was allowed to evaporate under ambient conditions for 18 h to yield 218 mg (76%) of product. Solvent exchange was performed using a Soxhlet extractor and millipore filtered water to yield $H_3[(Cu_4Cl)_3(BTTri)_8(DMF)_{12}] \cdot 72H_2O$. The resulting light purple powder was hand ground for five minutes, gravity filtered through 1 micrometer mesh, and analyzed by powder X–ray diffraction (pXRD). The batch of CuBTTri used to collect the data reported herein comes from the same batch used in previously published work.[22] The observed diffraction pattern matched a literature standard (Appendix IV, Figure S5.1).[27]

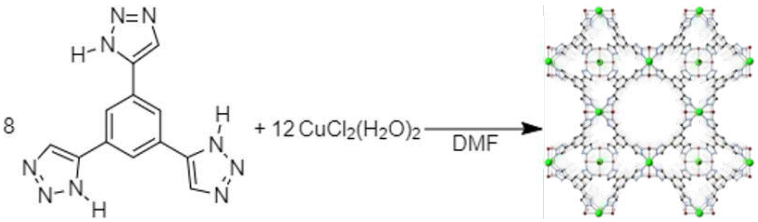

Figure 5.16. CuBTTri Synthesis.

Buffered Reactions. Measuring the reaction rate at different pH levels required that the reaction solutions be buffered to specific pH values. These experiments required the use of a buffer

which would not coordinate to the Cu sites in CuBTTri, hence we chose to use dissolving solid N,N′-bis(3-propanesulfonic acid) (PIPPS) and 2-(N-morpholino)ethanesulfonic acid (MES).[26] The buffered solutions were prepared by dissolving solid PIPPS or MES powders or in millipore water to achieve a 0.5 M solution. Then, a 10 N NaOH solution was added dropwise to the PIPPS or MES buffer solution until the desired pH was achieved. The buffered PIPPS and MES solutions were then used to prepare GSNO and GSH solutions from solid GSNO or GSH powder. These solutions were then used in an identical reaction procedure to the one described below to measure the reaction rate at different pH levels. All the reaction rate versus pH studies were carried out under conditions where the reaction was saturated in [GSH] (*vide infra*). Therefore, the maximum number of Cu active sites available were coordinated with GSH for all the data points reported in Figure 5.8 (*vide supra*).

Reaction Procedure. All reactions described herein were carried out under an N_2 (g) atmosphere to minimize the presence of O_2 (g) in the reactions. GSNO and GSH solutions were prepared using millipore H_2O and solid GSNO or GSH under inert conditions (N_2) in a 200 mL round–bottomed flask capped with a rubber septum and flushed with N_2. CuBTTri (600 ± 300 nm octahedral particles) was massed into a three–neck 100 mL round–bottomed flask and oven dried overnight at 110 °C. The CuBTTri samples used in this work are the same batch of particles previously employed in prior work.[22] Following the oven drying, the flask containing CuBTTri was placed under vacuum for 1 h on a Schlenk line and backfilled with N_2 (g) prior to reaction. GSNO or GSH solutions were then injected into the reaction flasks containing the dried CuBTTri. For buffered reactions, the GSNO or GSH solutions were prepared using buffered millipore H_2O. Vigorous bubbling in the round–bottomed flask was established using an inlet N_2 (g) flow needle and an outlet needle. Reactions were bubbled vigorously to mitigate mass transport limitations and

to ensure the measured value for $[-d[GSNO]/dt]_i$ was not simply the rate of substrate diffusion to the MOF active sites.[78,79] Reaction flasks were completely covered in aluminum foil to minimize exposure to light and reactions were left to proceed for a predetermined time. Wrapping the reactions in aluminum foil may not actually be necessary, and no more rigorous light blocking method (such as the use of black tape or cloth) was required. The outlet needle was removed to stop bubbling at a predetermined time and once all visible CuBTTri particles had settled to the bottom of the flask (~30 s) the supernatant was decanted via a syringe. The quenched reaction solution was then kept cool and dark in an EPA certified Cu–free glass vial under inert conditions (N_2) or added directly to an NMR tube or UV–VIS quartz cuvette within less than one minute. ^{1}H NMR or UV-VIS spectra were collected at 20 min to allow sufficient loss of GSNO to be detectable, yet to remain relatively early in the reaction progress to determine what is designated as an initial rate (-d[GSNO]/dt). Practically and given the ca. ± 5% precision of the ^{1}H NMR data under our conditions, the trade–off between measurable reaction vs more points meant that taking 1 point in the first ca. 30% reaction was a good compromise that allowed reasonable initial rate measurements. ^{1}H NMR and UV–VIS spectroscopies have been determined to be equivalent techniques for monitoring loss of GSNO in the current system. All reactions reported were performed in triplicate with the reported average and standard deviation calculated from those three trials.

Water Suppression ^{1}H NMR. These experiments follow our protocol for direct, *in situ* monitoring the release of NO from GSNO in water by solvent suppressed ^{1}H NMR.[21] All NMR experiments were performed using an Agilent Inova 500 equipped with a 5 mm pulsed–field–gradient HCN probe. Samples were prepared in septa–capped Wilmad 528–PP 500 MHz tubes under inert conditions (N_2) by adding 0.5 mL of reaction supernatant to an NMR tube containing

0.1 mL of 20 mM NaH_2PO_4 buffered D_2O. Samples were mixed by hand, followed by 2 s of sonication to remove N_2 bubbles. Samples were kept dark, air–free, and analyzed as soon as possible, typically within 5 minutes. NMR experiments were run using PRESAT with PURGE solvent signal suppression available in VnmrJ version–4.2.[80] The system was buffered with NaH_2PO_4 due to the sensitivity of the compounds of interest (GSNO, GSH, and GSSG) to the pH of the solution. 512 transients were acquired for all samples, which took 35 min to complete. A 2 s square presat with a bandwidth of 100 Hz on resonance at 4.67 ppm (water) was used, followed by the PURGE crusher sequence and a pi/2 excitation pulse of 5.7 μs. Acquisition time was 2 s, with the PRESAT delay the total time between transients was about 4 s. All free induction decay (FID) spectra were processed using MestraNova® software to examine peak intensities and integration values. Data analysis and calculations were performed using Microsoft Excel and OriginPro.

Supporting Information. The following are available in Appendix IV: Supporting Information for Chapter V: the powder X-ray diffraction pattern for CuBTTri, examining -d[GSNO]/dt versus $[GSNO]_i$ at two concentrations, derivation for the rate law associated with Figure 5.9., disproven mechanistic hypotheses and analysis, calculating the ratio between thiolate and $Cu^{II}_{surface}$ at varying reaction pH, calculating the apparent pK_a of the thiol proton in GSH bound to $Cu^{II}_{surface}$, and future experiments based on predictions derived from Figure 5.9.

REFERNCES

1. Harding, J. L. & Reynolds, M. M. Metal Organic Frameworks as Nitric Oxide Catalysts. *Journal of the American Chemical Society* **134**, 3330–3333 (2012).

2. Harding, J. L., Metz, J. M. & Reynolds, M. M. A Tunable, Stable, and Bioactive MOF Catalyst for Generating a Localized Therapeutic from Endogenous Sources. *Advanced Functional Materials* **24**, 7503–7509 (2014).

3. Liu, K. & Meyerhoff, M. E. Preparation and characterization of an improved Cu2+–cyclen polyurethane material that catalyzes generation of nitric oxide from S-nitrosothiols. *Journal of Materials Chemistry* **22**, 18784–18787 (2012).

4. Ren, H. *et al.* Electrochemically Modulated Nitric Oxide (NO) Releasing Biomedical Devices via Copper(II)-Tri(2-pyridylmethyl)amine Mediated Reduction of Nitrite. *ACS Applied Materials & Interfaces* **6**, 3779–3783 (2014).

5. Mengel, A. & Lindermayer, C. *Nitric Oxide: Methods and Protocols*. (Springer, 2018).

6. Marletta, M. A. Nitric oxide: biosynthesis and biological significance. *Trends in Biochemical Sciences* **14**, 488–492 (1989).

7. Coleman, J. W. Nitric oxide in immunity and inflammation. *International immunopharmacology* **1**, 1397–1406 (2001).

8. Bogdan, C. Nitric oxide and the immune response. *Nature Immunology* **2**, 907–916 (2001).

9. Carpenter, A. W. & Schoenfisch, M. H. Nitric oxide release: Part II. Therapeutic applications. *Chemical Society Reviews* **41**, 3742–3752 (2012).

10. Knott, A. B. & Bossy-Wetzel, E. Nitric oxide in health and disease of the nervous system. *Antioxidants & redox signaling* **11**, 541–554 (2009).

11. Schairer, D. O., Chouake, J. S., Nosanchuk, J. D. & Friedman, A. J. The potential of nitric oxide releasing therapies as antimicrobial agents. *Virulence* **3**, 271–279 (2012).

12. Neufeld, B. H. & Reynolds, M. M. Critical nitric oxide concentration for Pseudomonas aeruginosa biofilm reduction on polyurethane substrates. *Biointerphases* **11**, 31012 (2016).

13. Paricio, L., Neufeld, B. & Reynolds, M. Combined influence of nitric oxide and surface roughness in biofilm reduction across bacteria strains. *Biointerphases* **14**, 21004 (2019).

14. Palmer, R. M. J., Ferrige, A. G. & Moncada, S. Nitric oxide release accounts for the biological activity of endothelium-derived relaxing factor. *Nature* **327**, 524–526 (1987).

15. Neufeld, M. J., Lutzke, A., Jones, W. M. & Reynolds, M. M. Nitric Oxide Generation from Endogenous Substrates Using Metal–Organic Frameworks: Inclusion within Poly(vinyl alcohol) Membranes To Investigate Reactivity and Therapeutic Potential. *ACS Applied Materials & Interfaces* **9**, 35628–35641 (2017).

16. Singh, S. P., Wishnok, J. S., Keshive, M., Deen, W. M. & Tannenbaum, S. R. The chemistry of the S-nitrosoglutathione/glutathione system. *Proceedings of the National Academy of Sciences of the United States of America* **93**, 14428–14433 (1996).

17. Broniowska, K. A., Diers, A. R. & Hogg, N. S-nitrosoglutathione. *Biochimica et biophysica acta* **1830**, 3173–3181 (2013).

18. R. Noble, D., R. Swift, H. & Lyn H. Williams, D. Nitric oxide release from S-nitrosoglutathione (GSNO). *Chemical Communications* 2317–2318 (1999) doi:10.1039/A907891F.

19. Gorren, A. C. F., Schrammel, A., Schmidt, K. & Mayer, B. Decomposition ofS-Nitrosoglutathione in the Presence of Copper Ions and Glutathione. *Archives of Biochemistry and Biophysics* **330**, 219–228 (1996).

20. Tsikas, D. *et al.* UPLC-MS/MS measurement of S-nitrosoglutathione (GSNO) in human plasma solves the S-nitrosothiol concentration enigma. *Journal of chromatography. B, Analytical technologies in the biomedical and life sciences* **927**, 147–157 (2013).

21. Tuttle, R. R., Rubin, H. N., Rithner, C. D., Finke, R. G. & Reynolds, M. M. Copper ion vs copper metal–organic framework catalyzed NO release from bioavailable S-Nitrosoglutathione en route to biomedical applications: Direct 1H NMR monitoring in water allowing identification of the distinct, true reaction stoichiometries and thio. *Journal of Inorganic Biochemistry* **199**, 110760 (2019).

22. R Tuttle, R., J Folkman, S., N Rubin, H., G. Finke, R. & M. Reynolds, M. Copper Metal–Organic Framework Surface Catalysis: Catalyst Poisoning, IR Spectroscopic, and Kinetic Evidence Addressing the Nature and Number of the Catalytically Active Sites En Route to Improved Applications. *ACS Applied Materials & Interfaces* **0**, (2020).

23. Neufeld, M. J., Ware, B. R., Lutzke, A., Khetani, S. R. & Reynolds, M. M. Water-Stable Metal–Organic Framework/Polymer Composites Compatible with Human Hepatocytes. *ACS Applied Materials & Interfaces* **8**, 19343–19352 (2016).

24. Baciu, C., Cho, K.-B. & Gauld, J. W. Influence of Cu+ on the RS-NO bond dissociation energy of S-nitrosothiols. *The journal of physical chemistry. B* **109**, 1334–1336 (2005).

25. Dicks, A. P. *et al.* Identification of Cu+ as the effective reagent in nitric oxide formation from S-nitrosothiols (RSNO). *Journal of the Chemical Society, Perkin Transactions 2* 481–487 (1996) doi:10.1039/P29960000481.

26. Dincă, M. & Long, J. R. High-Enthalpy Hydrogen Adsorption in Cation-Exchanged Variants of the Microporous Metal−Organic Framework Mn3[(Mn4Cl)3(BTT)8(CH3OH)10]2. *Journal of the American Chemical Society* **129**, 11172–11176 (2007).

27. Demessence, A., D'Alessandro, D. M., Foo, M. L. & Long, J. R. Strong CO2 Binding in a Water-Stable, Triazolate-Bridged Metal−Organic Framework Functionalized with Ethylenediamine. *Journal of the American Chemical Society* **131**, 8784–8786 (2009).

28. Dincă, M. *et al.* Observation of Cu2+–H2 Interactions in a Fully Desolvated Sodalite-Type Metal–Organic Framework. *Angewandte Chemie International Edition* **46**, 1419–1422 (2007).

29. Metzger, E. D., Comito, R. J., Hendon, C. H. & Dincă, M. Mechanism of Single-Site Molecule-Like Catalytic Ethylene Dimerization in Ni-MFU-4l. *Journal of the American Chemical Society* **139**, 757–762 (2017).

30. P. Dicks, A., Herves Beloso, P. & Lyn H. Williams, D. Decomposition of S-nitrosothiols: the effects of added thiols. *Journal of the Chemical Society, Perkin Transactions 2* 1429–1434 (1997) doi:10.1039/A701594A.

31. Broniowska, K. A., Diers, A. R. & Hogg, N. S-nitrosoglutathione. *Biochimica et biophysica acta* **1830**, 3173–3181 (2013).

32. Keszler, A., Zhang, Y. & Hogg, N. Reaction between nitric oxide, glutathione, and oxygen in the presence and absence of protein: How are S-nitrosothiols formed? *Free radical biology & medicine* **48**, 55–64 (2010).

33. Pocius, P. A., Clark, J. H. & Baumrucker, C. R. Glutathione in Bovine Blood: Possible Source of Amino Acids for Milk Protein Synthesis. *Journal of Dairy Science* **64**, 1151–1154 (1981).

34. Marcus, R. A. Chemical and Electrochemical Electron-Transfer Theory. *Annual Review of Physical Chemistry* **15**, 155–196 (1964).

35. Bernasconi, C. F. Intrinsic barriers of reactions and the principle of nonperfect synchronization. *Accounts of Chemical Research* **20**, 301–308 (1987).

36. Danilina, N., Krumeich, F., Castelanelli, S. A. & van Bokhoven, J. A. Where Are the Active Sites in Zeolites? Origin of Aluminum Zoning in ZSM-5. *The Journal of Physical Chemistry C* **114**, 6640–6645 (2010).

37. Behrens, M. *et al.* The Active Site of Methanol Synthesis over Cu/ZnO/Al₂O₃ Industrial Catalysts. *Science* **336**, 893 LP – 897 (2012).

38. Bayram, E. & Finke, R. G. Quantitative 1,10-Phenanthroline Catalyst-Poisoning Kinetic Studies of Rh(0) Nanoparticle and Rh4 Cluster Benzene Hydrogenation Catalysts: Estimates of the Poison Kassociation Binding Constants, of the Equivalents of Poison Bound and of the Number of Cata. *ACS Catalysis* **2**, 1967–1975 (2012).

39. Hornstein, B. J., Aiken, J. D. & Finke, R. G. Nanoclusters in Catalysis: A Comparison of CS2 Catalyst Poisoning of Polyoxoanion- and Tetrabutylammonium-Stabilized 40 ± 6 Å Rh(0) Nanoclusters to 5 Rh/Al2O3, Including an Analysis of the Literature Related to the CS2 to Metal Stoichiometry Issue. *Inorganic Chemistry* **41**, 1625–1638 (2002).

40. Hagen, C. M., Vieille-Petit, L., Laurenczy, G., Süss-Fink, G. & Finke, R. G. Supramolecular Triruthenium Cluster-Based Benzene Hydrogenation Catalysis: Fact or Fiction? *Organometallics* **24**, 1819–1831 (2005).

41. Bayram, E. *et al.* Mononuclear Zeolite-Supported Iridium: Kinetic, Spectroscopic, Electron Microscopic, and Size-Selective Poisoning Evidence for an Atomically Dispersed True Catalyst at 22 °C. *ACS Catalysis* **2**, 1947–1957 (2012).

42. Bayram, E. *et al.* Is It Homogeneous or Heterogeneous Catalysis Derived from [RhCp*Cl2]2? In Operando XAFS, Kinetic, and Crucial Kinetic Poisoning Evidence for Subnanometer Rh4 Cluster-Based Benzene Hydrogenation Catalysis. *Journal of the American Chemical Society* **133**, 18889–18902 (2011).

43. Chen, X. *et al.* Tuning Zr12O22 Node Defects as Catalytic Sites in the Metal–Organic Framework hcp UiO-66. *ACS Catalysis* **10**, 2906–2914 (2020).

44. Yang, D. *et al.* Structure and Dynamics of Zr6O8 Metal–Organic Framework Node Surfaces Probed with Ethanol Dehydration as a Catalytic Test Reaction. *Journal of the American Chemical Society* **140**, 3751–3759 (2018).

45. Simons, M. C. *et al.* Structure, Dynamics, and Reactivity for Light Alkane Oxidation of Fe(II) Sites Situated in the Nodes of a Metal–Organic Framework. *Journal of the American Chemical Society* **141**, 18142–18151 (2019).

46. Gascon, J., Corma, A., Kapteijn, F. & Llabrés i Xamena, F. X. Metal Organic Framework Catalysis: Quo vadis? *ACS Catalysis* **4**, 361–378 (2014).

47. Yang, D. & Gates, B. C. Catalysis by Metal Organic Frameworks: Perspective and Suggestions for Future Research. *ACS Catalysis* **9**, 1779–1798 (2019).

48. Scott, S. L. The Burden of Disproof. *ACS Catalysis* **9**, 4706–4708 (2019).

49. Hoffman, R., Minkin, V. I. & Carpenter, B. K. Ockham's Razor and Chemistry. *International Journal for Philosophy of Chemistry* **3**, 3–28 (1997).

50. Bligaard, T. *et al.* Toward Benchmarking in Catalysis Science: Best Practices, Challenges, and Opportunities. *ACS Catalysis* **6**, 2590–2602 (2016).

51. Xiao, D. J., Oktawiec, J., Milner, P. J. & Long, J. R. Pore Environment Effects on Catalytic Cyclohexane Oxidation in Expanded Fe2(dobdc) Analogues. *Journal of the American Chemical Society* **138**, 14371–14379 (2016).

52. Kaur, G. *et al.* Controlling the Synthesis of Metal–Organic Framework UiO-67 by Tuning Its Kinetic Driving Force. *Crystal Growth & Design* **19**, 4246–4251 (2019).

53. Furukawa, H., Müller, U. & Yaghi, O. M. "Heterogeneity within Order" in Metal–Organic Frameworks. *Angewandte Chemie International Edition* **54**, 3417–3430 (2015).

54. Furukawa, H., Cordova, K. E., O'Keeffe, M. & Yaghi, O. M. The Chemistry and Applications of Metal-Organic Frameworks. *Science* **341**, 1230444 (2013).

55. García-García, P., Müller, M. & Corma, A. MOF catalysis in relation to their homogeneous counterparts and conventional solid catalysts. *Chemical Science* **5**, 2979–3007 (2014).

56. Metzger, E. D. *et al.* Highly Selective Heterogeneous Ethylene Dimerization with a Scalable and Chemically Robust MOF Catalyst. *ACS Sustainable Chemistry & Engineering* **7**, 6654–6661 (2019).

57. Burg, A., Cohen, H. & Meyerstein, D. The reaction mechanism of nitrosothiols with copper(I). *JBIC Journal of Biological Inorganic Chemistry* **5**, 213–217 (2000).

58. Singh, R. J., Hogg, N., Joseph, J. & Kalyanaraman, B. Mechanism of Nitric Oxide Release from S-Nitrosothiols. *Journal of Biological Chemistry* **271**, 18596–18603 (1996).

59. Zhang, S., Çelebi-Ölçüm, N., Melzer, M. M., Houk, K. N. & Warren, T. H. Copper(I) nitrosyls from reaction of copper(II) thiolates with S-nitrosothiols: mechanism of NO release from RSNOs at Cu. *Journal of the American Chemical Society* **135**, 16746–16749 (2013).

60. Smith, J. N. & Dasgupta, T. P. Kinetics and Mechanism of the Decomposition of S-Nitrosoglutathione by l-Ascorbic Acid and Copper Ions in Aqueous Solution to Produce Nitric Oxide. *Nitric Oxide* **4**, 57–66 (2000).

61. Ngamchuea, K., Batchelor-McAuley, C. & Compton, R. G. The Copper(II)-Catalyzed Oxidation of Glutathione. *Chemistry – A European Journal* **22**, 15937–15944 (2016).

62. Williams, D. L. H. The Chemistry of S-Nitrosothiols. *Accounts of Chemical Research* **32**, 869–876 (1999).

63. Askew, S. C., Barnett, D. J., McAninly, J. & Williams, D. L. H. Catalysis by Cu2+ of nitric oxide release from S-nitrosothiols (RSNO). *Journal of the Chemical Society, Perkin Transactions 2* 741–745 (1995) doi:10.1039/P29950000741.

64. Xiang, J. Y. & Ponder, J. W. An Angular Overlap Model for Cu(II) Ion in the AMOEBA Polarizable Force Field. *Journal of Chemical Theory and Computation* **10**, 298–311 (2014).

65. Suta, M., Cimpoesu, F. & Urland, W. The angular overlap model of ligand field theory for f elements: An intuitive approach building bridges between theory and experiment. *Coordination Chemistry Reviews* **441**, 213981 (2021).

66. Collman, J. ; H. L. ; N. J. ; F. R. *Principles and Applications of Organotransition Metal Chemistry*. (1987).

67. Homer, N. Z. M. *et al.* Dimethylsulfoxide oxidizes glutathione in vitro and in human erythrocytes: Kinetic analysis by 1H NMR. *Cryobiology* **50**, 317–324 (2005).

68. Jones, W. M., Tapia, J. B., Tuttle, R. R. & Reynolds, M. M. Thermogravimetric Analysis and Mass Spectrometry Allow for Determination of Chemisorbed Reaction Products on Metal Organic Frameworks. *Langmuir* **36**, (2020).

69. Pauling, L. *The Nature of the Chemical Bond*. (Cornell University Press, 1960).

70. DiMucci, I. M. *et al.* The Myth of d8 Copper(III). *Journal of the American Chemical Society* **141**, 18508–18520 (2019).

71. Hammes-Schiffer, S. Theoretical Perspectives on Proton-Coupled Electron Transfer Reactions. *Accounts of Chemical Research* **34**, 273–281 (2001).

72. Hammes-Schiffer, S. & Stuchebrukhov, A. A. Theory of Coupled Electron and Proton Transfer Reactions. *Chemical Reviews* **110**, 6939–6960 (2010).

73. Tummanapelli, A. K. & Vasudevan, S. Ab Initio MD Simulations of the Brønsted Acidity of Glutathione in Aqueous Solutions: Predicting pKa Shifts of the Cysteine Residue. *The Journal of Physical Chemistry B* **119**, 15353–15358 (2015).

74. Graminski, G. F., Kubo, Y. & Armstrong, R. N. Spectroscopic and kinetic evidence for the thiolate anion of glutathione at the active site of glutathione S-transferase. *Biochemistry* **28**, 3562–3568 (1989).

75. Agmon, N. The Grotthuss mechanism. *Chemical Physics Letters* **244**, 456–462 (1995).

76. Choi, L.-S. & Bayley, H. S-Nitrosothiol Chemistry at the Single-Molecule Level. *Angewandte Chemie International Edition* **51**, 7972–7976 (2012).

77. Hart, T. W. Some Observations Concerning the S-Nitroso and S-Phenylsulphonyl Derivatives of L-Cysteine and G. *Tetrahedron Letters* **26**, 2013–2016 (1985).

78. Wang, C., Wang, J.-L. & Lin, W. Elucidating Molecular Iridium Water Oxidation Catalysts Using Metal–Organic Frameworks: A Comprehensive Structural, Catalytic, Spectroscopic, and Kinetic Study. *Journal of the American Chemical Society* **134**, 19895–19908 (2012).

79. Notheisz, F., Zsigmond, A., Barto´k, M., Szegletes, Z. & V. Smith, G. Mass transfer test and maximum rate determination during liquid-phase hydrogenations. *Applied Catalysis A: General* **120**, 105–114 (1994).

80. Simpson, A. J. & Brown, S. A. Purge NMR: Effective and easy solvent suppression. *Journal of Magnetic Resonance* **175**, 340–346 (2005).

VI. SUMMARY AND CONCLUSIONS

This dissertation establishes the reaction stoichiometry, GSH dependence, Cu active site within the CuBTTri solid, experimental rate law, and proposes a reliable mechanism for CuBTTri catalyzed GSNO to NO conversion in water in the presence of GSH. All the conclusions were established from data collected using a direct monitoring method to quantify [GSNO], [GSH], and [GSSG] in H_2O.[1,2] The monitoring method was also adapted to monitor the same reaction directly in blood plasma.[3] Monitoring the reaction in blood plasma established that conclusions developed in water are likely relevant *in vivo*. Chapters II-IV are peer reviewed publications primarily written by R. Tuttle. Chapter V is in final preparation for submission to a peer-reviewed journal. The main findings of each chapter are discussed in this final section.

Solvent-suppressed ^{1}H NMR quantitatively, directly monitors [GSNO], [GSH], and [GSSG] in H_2O (as shown in Chapter II). The spectroscopic monitoring method allows for real time quantification of reactants and products in the CuBTTri/GSNO/GSH/NO system for kinetic and mechanistic studies. The monitoring method can also be applied to other RSNO/RSH/RSSR systems because ^{1}H NMR spectroscopy detects protons unique to each *class* of molecule.[1,4] The thiol dependence of CuBTTri and solvated Cu^{2+} as NO release catalysts are inverse of one another. GSH must be added to the reaction to observe significant NO release using CuBTTri, while GSH is an effective catalyst poison for solvated Cu^{2+}.[5] The reaction stoichiometries observed when using CuBTTri versus solvated Cu^{2+} for NO release catalysis are also different. Differences in stoichiometry and thiol dependence for CuBTTri and solvated Cu^{2+} indicate that the two catalysts operate via different mechanisms for GSNO to NO conversion. Hence, one cannot assume that

solid-state MOF catalysts operate via the same reaction mechanisms as their homogeneous counterparts.[6,7]

Combining solvent-suppressed ^{1}H NMR, UV-VIS, and NOA monitors the NO release reaction catalyzed by CuBTTri in blood plasma.[3] Monitoring the reaction in blood plasma (as demonstrated in Chapter III) is a true *in operando* monitoring method, which is rare and desirable in catalysis.[8–15] Monitoring biomedically relevant catalysis directly in a biological solvent is essential because that is the solvent matrix where the reaction must eventually operate.[16–19] The stoichiometry and rate for the NO release reaction were measured in blood plasma and we make initial comparisons to water. Because the stoichiometry observed in blood plasma is effectively identical to water, it appears the mechanism of NO release does not change in blood plasma. Although, the observed value for -d[GSNO]/dt at 20 min is double in blood plasma as compared to water under identical experimental conditions for CuBTTri catalyzed NO generation. The reason for the observed change in rate remains to be determined. Monitoring biological reactions *in operando* (i.e., in biological solvents) is possible and desirable despite the anticipated difficulty, because then one can assess how biologically meaningful results obtained in water are.

Establishing the catalytically active Cu sites in CuBTTri is another major outcome of this work.[20] The relationship between -d[GSNO]/dt and CuBTTri octahedral particle external surface area to interior volume ratio (ESA/IV) was investigated by varying CuBTTri particle size through grinding and filtering. Plotting -d[GSNO]/dt versus ESA/IV shows that ~100% of the catalytic activity comes from $Cu_{surface}$ sites on external surfaces of CuBTTri particles. Demonstrating that $Cu_{surface}$ is the kinetically dominant catalyst in CuBTTri for NO release disproves, for this system, the "MOF intrapore catalysis" hypothesis prevalent in the literature.[21–24] Although, the relatively low density of active sites in a given MOF sample is likely a more general result, as it is often

assumed in the literature that 100% of the metal sites are active when catalyst performance metrics are calculated for MOFs.[21,25,26] The kinetic catalytic poisoning data is well fit by a linear least-squares function, showing that the Cu active sites are kinetically, if not also structurally, identical.[8,20,27–29] Two Cu to CN binding modes are observed by FT-IR spectroscopy, $Cu(CN)_3$ and Cu(CN). These binding ratios correspond to the idealized, metal-terminated crystal structure of CuBTTri.[30–32] Catalytically active $Cu_{surface}$ sites bind 3 equivalents of cyanide and inactive Cu_{pore} sites bind 1. Hence, the CuBTTri MOF catalyst is heterogenous by one definition (it is insoluble), but homogeneous by another (there is only one kinetically dominant active site). Active site density in CuBTTri was measured using size-selective poisoning.[20,29] Employing TPPTS (which cannot diffuse into CuBTTri) as a poison showed that for 600 ± 400 nm CuBTTri particles (1.3 ± 0.4)% of the total Cu sites are active for GSNO to NO conversion catalysis. The measured active site density was used to calculate a normalized, true TOF value.

Chapter V establishes the experimental rate law and proposes a Cu^{II} to Cu^{III}, PCET reaction mechanism. The currently favored mechanism is the only one of five total hypotheses considered which: i) meets all 5 requirements for a reliable reaction mechanism (given in the introduction and chapter V), and ii) provides a reasonable driving force for S-N bond homolysis in GSNO. The PCET mechanism highlights the special nature of substrates designed by nature, such as GSH and GSNO.[33,34] The reactivity of GSNO/GSH for NO release with CuBTTri appears to be highly dependent on the tripeptide structure of GSNO/GSH.[5,35–40] One prediction of the mechanism proposed in Chapter V (supported by prior literature on solvated Cu^{2+} catalyzed NO release from RSNOs) is that RSNO/RSH pairs without the tripeptide backbone in GSNO/GSH may react with Cu sites through different reaction mechanisms. Additionally, it appears to be valid to treat the $Cu_{surface}$ active sites as discreet, homogenous molecular complexes based on experimental kinetic

results.[6] Treating the $Cu_{surface}$ sites as homogenous metal complexes further strengthens the notion that MOF catalysts can be thought of as exhibiting the advantages traditionally associated with both insoluble and soluble catalysts. Combining $Cu_{surface}$ site structure with the predictive power of mechanism suggests several interesting future experiments. One particularly exciting avenue are computational studies of the Cu^{II} to Cu^{III} PCET mechanism.[33,34] These computational studies would be especially powerful because they will be directed by mechanism. Hence, atomic positions and specific questions to be tested computationally will be known up front.[41] Obtaining reliable mechanisms for MOF catalysts enables computational experiments which offer the chance to, in turn, establish a level of mechanistic understanding previously not accessible for solid-state catalyst materials.

REFERENCES

1. Tuttle, R. R., Rubin, H. N., Rithner, C. D., Finke, R. G. & Reynolds, M. M. Copper ion vs copper metal–organic framework catalyzed NO release from bioavailable S-Nitrosoglutathione en route to biomedical applications: Direct 1H NMR monitoring in water allowing identification of the distinct, true reaction stoichiometries and thio. *Journal of Inorganic Biochemistry* **199**, 110760 (2019).

2. Simpson, A. J. & Brown, S. A. Purge NMR: Effective and easy solvent suppression. *Journal of Magnetic Resonance* **175**, 340–346 (2005).

3. Tuttle, R. R., Daly, R. E., Rithner, C. D. & Reynolds, M. M. Monitoring a MOF Catalyzed Reaction Directly in Blood Plasma. *ACS Applied Materials & Interfaces* (2021) doi:10.1021/acsami.1c08917.

4. Choi, L.-S. & Bayley, H. S-Nitrosothiol Chemistry at the Single-Molecule Level. *Angewandte Chemie International Edition* **51**, 7972–7976 (2012).

5. Gorren, A. C. F., Schrammel, A., Schmidt, K. & Mayer, B. Decomposition ofS-Nitrosoglutathione in the Presence of Copper Ions and Glutathione. *Archives of Biochemistry and Biophysics* **330**, 219–228 (1996).

6. García-García, P., Müller, M. & Corma, A. MOF catalysis in relation to their homogeneous counterparts and conventional solid catalysts. *Chemical Science* **5**, 2979–3007 (2014).

7. Metzger, E. D., Comito, R. J., Hendon, C. H. & Dincă, M. Mechanism of Single-Site Molecule-Like Catalytic Ethylene Dimerization in Ni-MFU-4l. *Journal of the American Chemical Society* **139**, 757–762 (2017).

8. Bayram, E. *et al.* Is It Homogeneous or Heterogeneous Catalysis Derived from [RhCp*Cl2]2? In Operando XAFS, Kinetic, and Crucial Kinetic Poisoning Evidence for Subnanometer Rh4 Cluster-Based Benzene Hydrogenation Catalysis. *Journal of the American Chemical Society* **133**, 18889–18902 (2011).

9. Freeborn, D., Cunningham, L. & LoCicero, R. What Is Plasma? *Health Encyclopedia* (2020).

10. de Graaf, R. A. & Behar, K. L. Quantitative 1H NMR Spectroscopy of Blood Plasma Metabolites. *Analytical Chemistry* **75**, 2100–2104 (2003).

11. Nicholson, J. K., Foxall, P. J. D., Spraul, Manfred., Farrant, R. Duncan. & Lindon, J. C. 750 MHz 1H and 1H-13C NMR Spectroscopy of Human Blood Plasma. *Analytical Chemistry* **67**, 793–811 (1995).

12. Ji, Q. C., Rodila, R., Gage, E. M. & El-Shourbagy, T. A. A Strategy of Plasma Protein Quantitation by Selective Reaction Monitoring of an Intact Protein. *Analytical Chemistry* **75**, 7008–7014 (2003).

13. Bligh, S. W. A., Boyle, H. A., Mcewen, A. B., Sadler, P. J. & Woodham, R. H. 1H NMR studies of reactions of copper complexes with human blood plasma and urine. *Biochemical Pharmacology* **43**, 137–145 (1992).

14. Jian, W., Edom, R. W., Wang, D., Weng, N. & Zhang, S. (Weihua). Relative Quantitation of Glycoisoforms of Intact Apolipoprotein C3 in Human Plasma by Liquid Chromatography–High-Resolution Mass Spectrometry. *Analytical Chemistry* **85**, 2867–2874 (2013).

15. Tsikas, D. *et al.* UPLC-MS/MS measurement of S-nitrosoglutathione (GSNO) in human plasma solves the S-nitrosothiol concentration enigma. *Journal of chromatography. B, Analytical technologies in the biomedical and life sciences* **927**, 147–157 (2013).

16. Roberts, T. R. *et al.* A metal organic framework reduces thrombus formation and platelet aggregation ex vivo. *The journal of trauma and acute care surgery* **85**, 572–579 (2018).

17. Harding, J. L. & Reynolds, M. M. Metal Organic Frameworks as Nitric Oxide Catalysts. *Journal of the American Chemical Society* **134**, 3330–3333 (2012).

18. Neufeld, B. H. & Reynolds, M. M. Critical nitric oxide concentration for Pseudomonas aeruginosa biofilm reduction on polyurethane substrates. *Biointerphases* **11**, 31012 (2016).

19. Paricio, L., Neufeld, B. & Reynolds, M. Combined influence of nitric oxide and surface roughness in biofilm reduction across bacteria strains. *Biointerphases* **14**, 21004 (2019).

20. R Tuttle, R., J Folkman, S., N Rubin, H., G. Finke, R. & M. Reynolds, M. Copper Metal–Organic Framework Surface Catalysis: Catalyst Poisoning, IR Spectroscopic, and Kinetic Evidence Addressing the Nature and Number of the Catalytically Active Sites En Route to Improved Applications. *ACS Applied Materials & Interfaces* **0**, (2020).

21. Xiao, D. J., Oktawiec, J., Milner, P. J. & Long, J. R. Pore Environment Effects on Catalytic Cyclohexane Oxidation in Expanded Fe2(dobdc) Analogues. *Journal of the American Chemical Society* **138**, 14371–14379 (2016).

22. Yang, D. & Gates, B. C. Catalysis by Metal Organic Frameworks: Perspective and Suggestions for Future Research. *ACS Catalysis* **9**, 1779–1798 (2019).

23. Bligaard, T. *et al.* Toward Benchmarking in Catalysis Science: Best Practices, Challenges, and Opportunities. *ACS Catalysis* **6**, 2590–2602 (2016).

24. Furukawa, H., Cordova, K. E., O'Keeffe, M. & Yaghi, O. M. The Chemistry and Applications of Metal-Organic Frameworks. *Science* **341**, 1230444 (2013).

25. Metzger, E. D. *et al.* Highly Selective Heterogeneous Ethylene Dimerization with a Scalable and Chemically Robust MOF Catalyst. *ACS Sustainable Chemistry & Engineering* **7**, 6654–6661 (2019).

26. Noh, H. *et al.* An Exceptionally Stable Metal–Organic Framework Supported Molybdenum(VI) Oxide Catalyst for Cyclohexene Epoxidation. *Journal of the American Chemical Society* **138**, 14720–14726 (2016).

27. Bayram, E. & Finke, R. G. Quantitative 1,10-Phenanthroline Catalyst-Poisoning Kinetic Studies of Rh(0) Nanoparticle and Rh4 Cluster Benzene Hydrogenation Catalysts: Estimates of the Poison Kassociation Binding Constants, of the Equivalents of Poison Bound and of the Number of Cata. *ACS Catalysis* **2**, 1967–1975 (2012).

28. Gonzalez-Tejuca, L., Aika, K., Namba, S. & Turkevich, J. Poisoning titration technique for determining the number of active centers in a supported platinum catalyst. *The Journal of Physical Chemistry* **81**, 1399–1406 (1977).

29. Bayram, E. *et al.* Mononuclear Zeolite-Supported Iridium: Kinetic, Spectroscopic, Electron Microscopic, and Size-Selective Poisoning Evidence for an Atomically Dispersed True Catalyst at 22 °C. *ACS Catalysis* **2**, 1947–1957 (2012).

30. Dincă, M. & Long, J. R. High-Enthalpy Hydrogen Adsorption in Cation-Exchanged Variants of the Microporous Metal−Organic Framework Mn3[(Mn4Cl)3(BTT)8(CH3OH)10]2. *Journal of the American Chemical Society* **129**, 11172–11176 (2007).

31. Demessence, A., D'Alessandro, D. M., Foo, M. L. & Long, J. R. Strong CO2 Binding in a Water-Stable, Triazolate-Bridged Metal−Organic Framework Functionalized with Ethylenediamine. *Journal of the American Chemical Society* **131**, 8784–8786 (2009).

32. Dincă, M. *et al.* Observation of Cu2+–H2 Interactions in a Fully Desolvated Sodalite-Type Metal–Organic Framework. *Angewandte Chemie International Edition* **46**, 1419–1422 (2007).

33. Hammes-Schiffer, S. Theoretical Perspectives on Proton-Coupled Electron Transfer Reactions. *Accounts of Chemical Research* **34**, 273–281 (2001).

34. Hammes-Schiffer, S. & Stuchebrukhov, A. A. Theory of Coupled Electron and Proton Transfer Reactions. *Chemical Reviews* **110**, 6939–6960 (2010).

35. Singh, S. P., Wishnok, J. S., Keshive, M., Deen, W. M. & Tannenbaum, S. R. The chemistry of the S-nitrosoglutathione/glutathione system. *Proceedings of the National Academy of Sciences of the United States of America* **93**, 14428–14433 (1996).

36. R. Noble, D., R. Swift, H. & Lyn H. Williams, D. Nitric oxide release from S-nitrosoglutathione (GSNO). *Chemical Communications* 2317–2318 (1999) doi:10.1039/A907891F.

37. Smith, J. N. & Dasgupta, T. P. Kinetics and Mechanism of the Decomposition of S-Nitrosoglutathione by l-Ascorbic Acid and Copper Ions in Aqueous Solution to Produce Nitric Oxide. *Nitric Oxide* **4**, 57–66 (2000).

38. Baciu, C., Cho, K.-B. & Gauld, J. W. Influence of Cu+ on the RS-NO bond dissociation energy of S-nitrosothiols. *The journal of physical chemistry. B* **109**, 1334–1336 (2005).

39. Dicks, A. P. *et al.* Identification of Cu+ as the effective reagent in nitric oxide formation from S-nitrosothiols (RSNO). *Journal of the Chemical Society, Perkin Transactions 2* 481–487 (1996) doi:10.1039/P29960000481.

40. Taylor-Edinbyrd, K., Li, T. & Kumar, R. Effect of chemical structure of S-nitrosothiols on nitric oxide release mediated by the copper sites of a metal organic framework based environment. *Physical Chemistry Chemical Physics* **19**, 11947–11959 (2017).

41. Hoffman, R., Minkin, V. I. & Carpenter, B. K. Ockham's Razor and Chemistry. *International Journal for Philosophy of Chemistry* **3**, 3–28 (1997).

APPENDIX I. SUPPORTING INFORMATION FOR CHAPTER II.

Additional Characterization Methods

UV-VIS data was acquired using a Thermo Scientific Evolution 300 UV-Vis Spectrophotometer. Samples were prepared using millipore water in quartz cuvettes. Elemental analysis was performed using ICP-AES provided by the Colorado State University Soil, Water and Plant Testing Laboratory. Powder X-Ray diffraction (PXRD) patterns were obtained using a Bruker D8 Discover DaVinci Powder X-ray Diffractometer with CuKα radiation operated at 40 kV and 40 mA. A typical scan rate was 0.3 sec/step with a step size of 0.02 deg. Ligand characterization ^{1}H NMR spectra was acquired using an Agilent (Inova) 400MHz spectrometer. SEM images were aquired using a JEOL JSM-6500F field emission scanning electron microscope.

H_3BTTri Ligand ^{1}H NMR

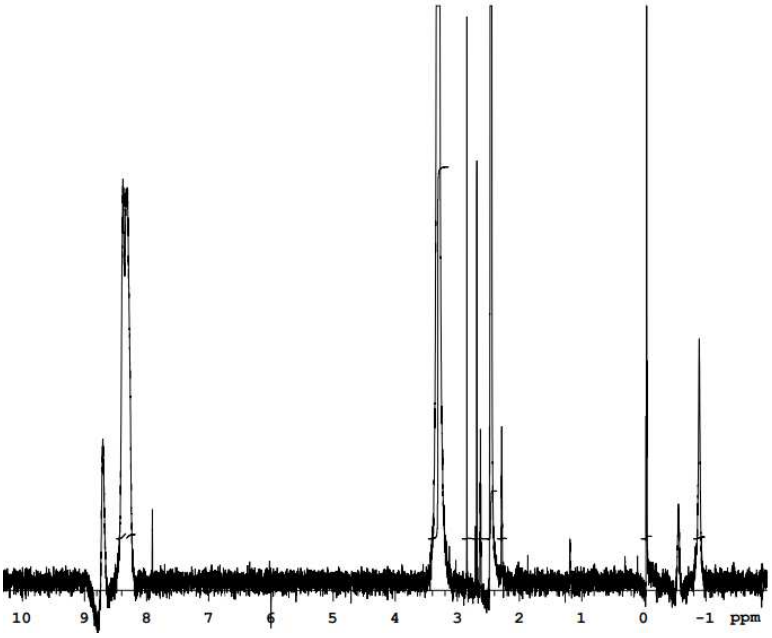

Figure S2.1. ^{1}H NMR spectrum of synthesized H_3BTTri ligand in DMSO.

PXRD Characterization of Cu-BTTri

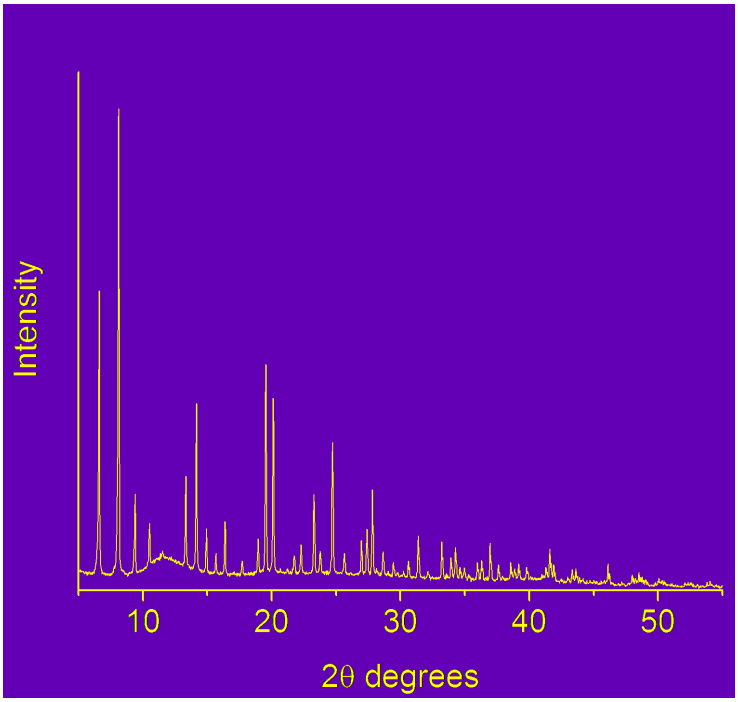

Figure S2.2. PXRD of synthesized CuBTTri.

SEM Image of Synthesized CuBTTri

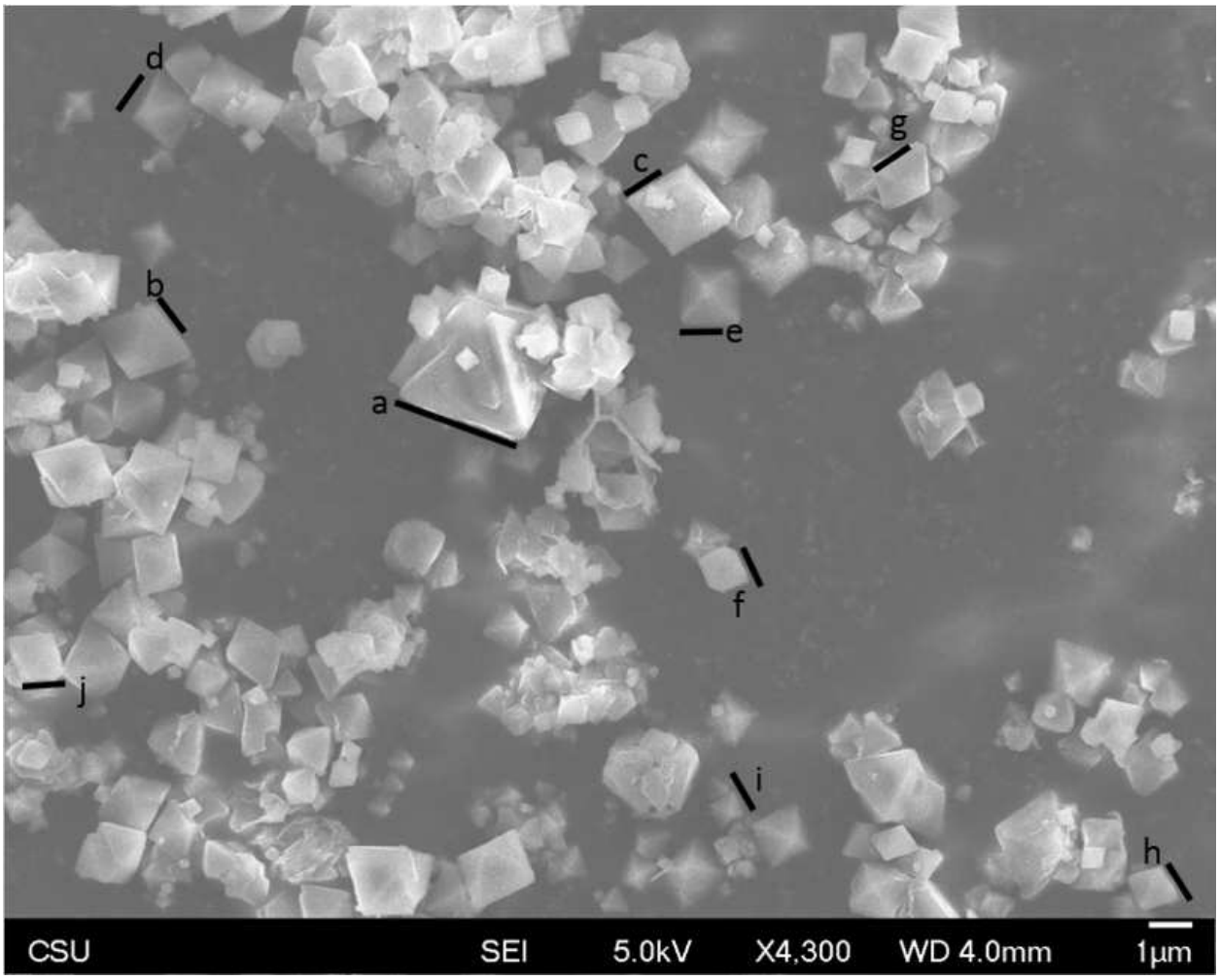

Figure S2.3. SEM image of as synthesized CuBTTri post Soxhlet exchange with H_2O.

UV-VIS Characterization of GSNO

Table S2.1. Average absorbance values and concentration data of synthesized GSNO used in all studies.

Trial	[GSNO] (mM)	Absorbance at 335 nm
1	1.11	0.993
2	1.11	0.992
3	1.11	0.991
4	0.75	0.68
5	0.75	0.68
6	0.75	0.68
7	0.50	0.453
8	0.50	0.453
9	0.50	0.453
10	0.25	0.225
11	0.25	0.226
12	0.25	0.225
13	0.10	0.089
14	0.10	0.088
15	0.10	0.089

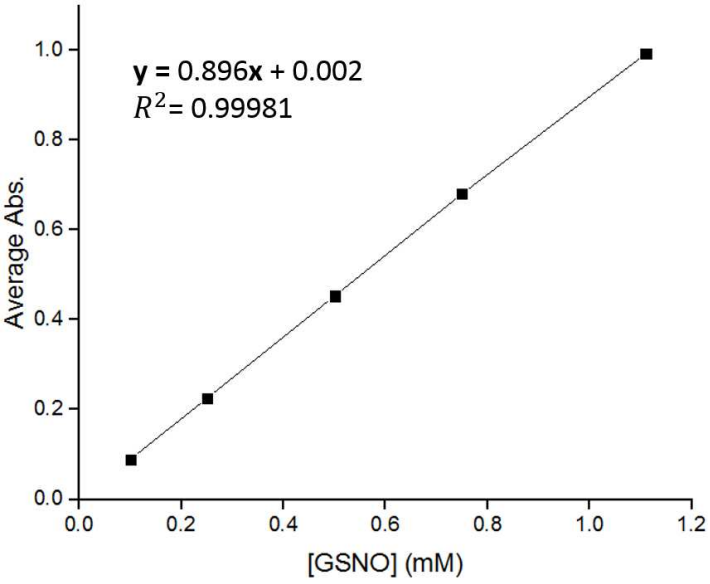

Figure S2.4. Average absorbance vs [GSNO] where slope=molar extinction coefficient (ε). Purity of GSNO assessed by comparison of observed ε versus literature value.[1,2] Resulting purity determined to be 97%.

^{1}H NMR Peak Assignments of GSH

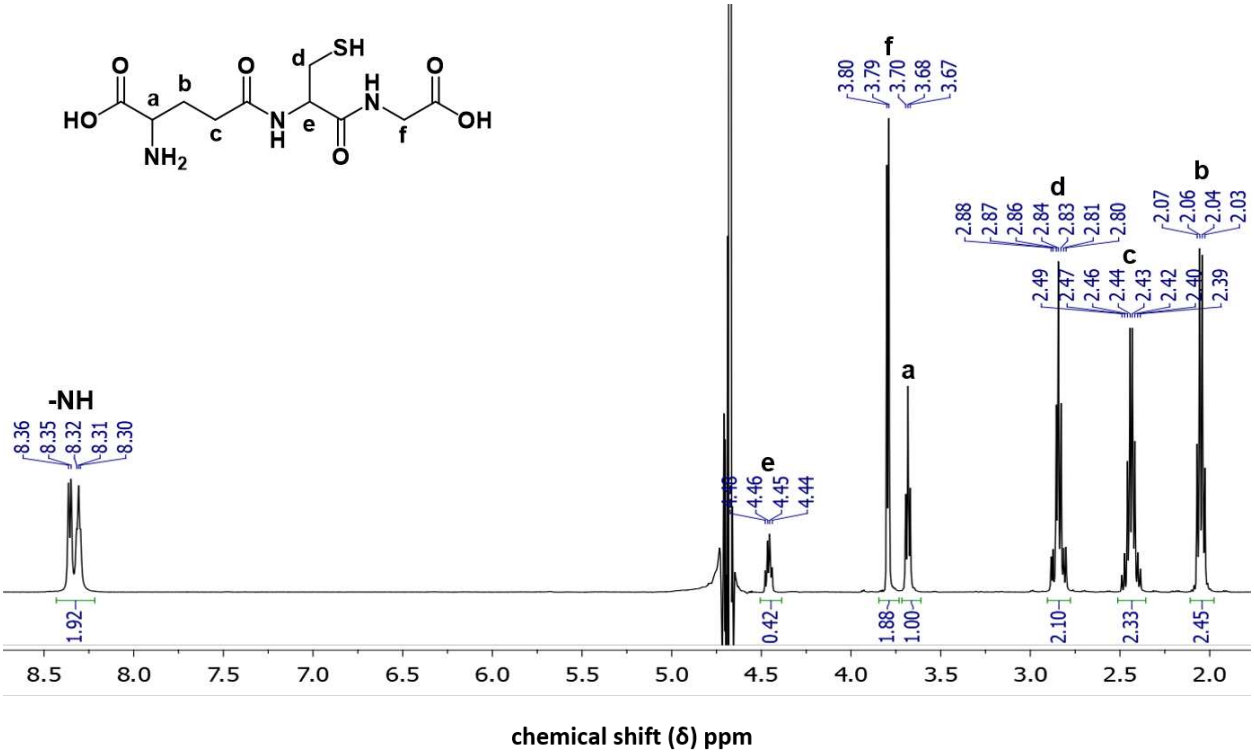

Figure S2.5. ^{1}H NMR peak assigned spectra of GSH.

ICP-AES Analysis of Reaction Supernatant

Table S2.2. ICP-AES analysis for total copper content present in reaction supernatant of CuBTTri catalyzed reactions.

Sample	[GSNO] (mmol/L)	[GSH] (mmol/L)	Reaction Time (h)	Cu (mg/L)	Cu (mg)	MOF (mg)	mg Cu (MOF)	%Cu lost	%Cu left	[Cu] mol/L
1A	2	0	16	0.64	0.0096	5.84	1.03	0.93	99.07	1.00E-05
2A	2	0	16	0.13	0.0020	4.07	0.72	0.28	99.72	2.09E-06
3A	2	0	16	0.58	0.0087	5.78	1.02	0.85	99.15	9.12E-06
1B	2	2	16	0.22	0.0033	4.37	0.77	0.44	99.56	3.49E-06
2B	2	2	16	0.44	0.0066	5.54	0.98	0.68	99.32	6.95E-06
3B	2	2	16	0.16	0.0025	4.26	0.75	0.33	99.67	2.58E-06

3-D Drawings of Cu-BTTri

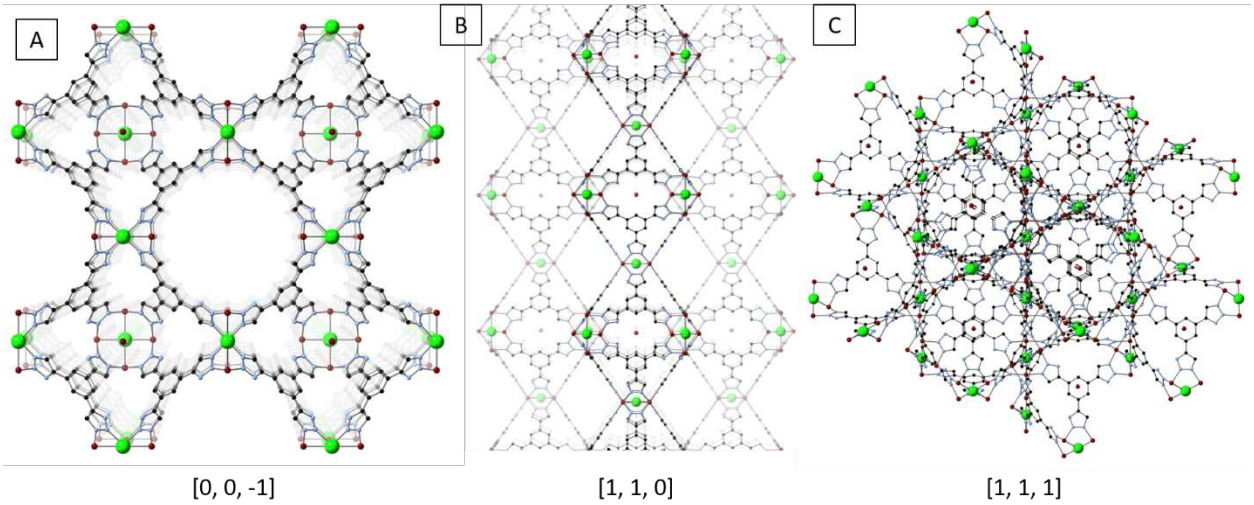

Figure S2.6. CrystalMaker drawings of Cu-BTTri along the (A) [0, 0, -1], (B) [1, 1, 0], and (C) [1, 1, 1] planes.

Calibration ^{1}H NMR Spectra and Resulting Calibration Curves

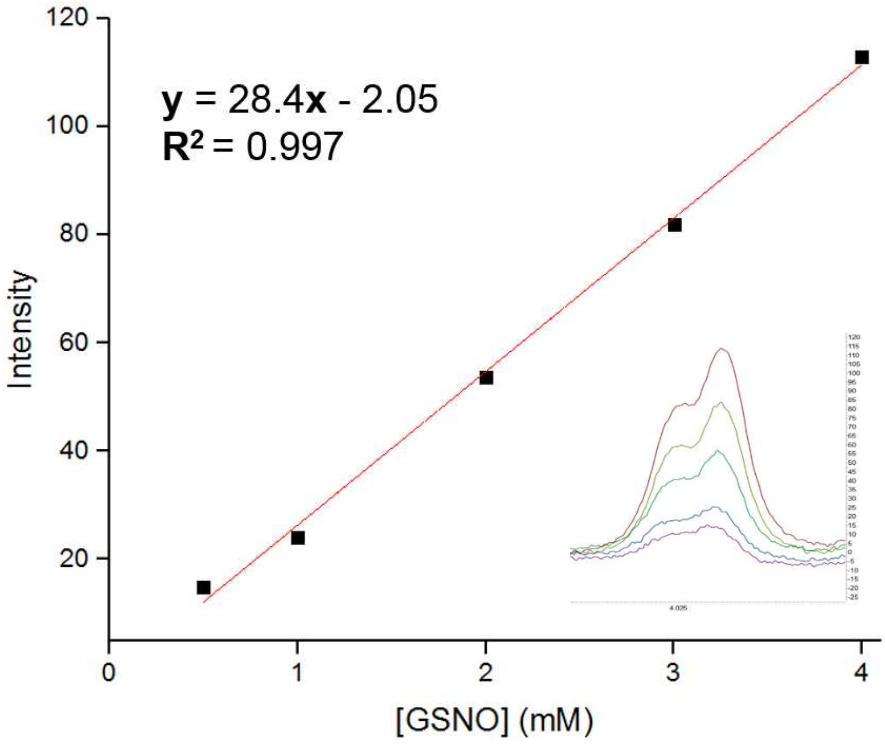

Figure S2.7. Calibration curve used to calculate [GSNO] in reaction samples. Inset, ^{1}H NMR data used to generate calibration curve (Red = 4 mM, Yellow = 3mM, Green = 2mM, Blue = 1 mM, Purple = 0.5 mM).

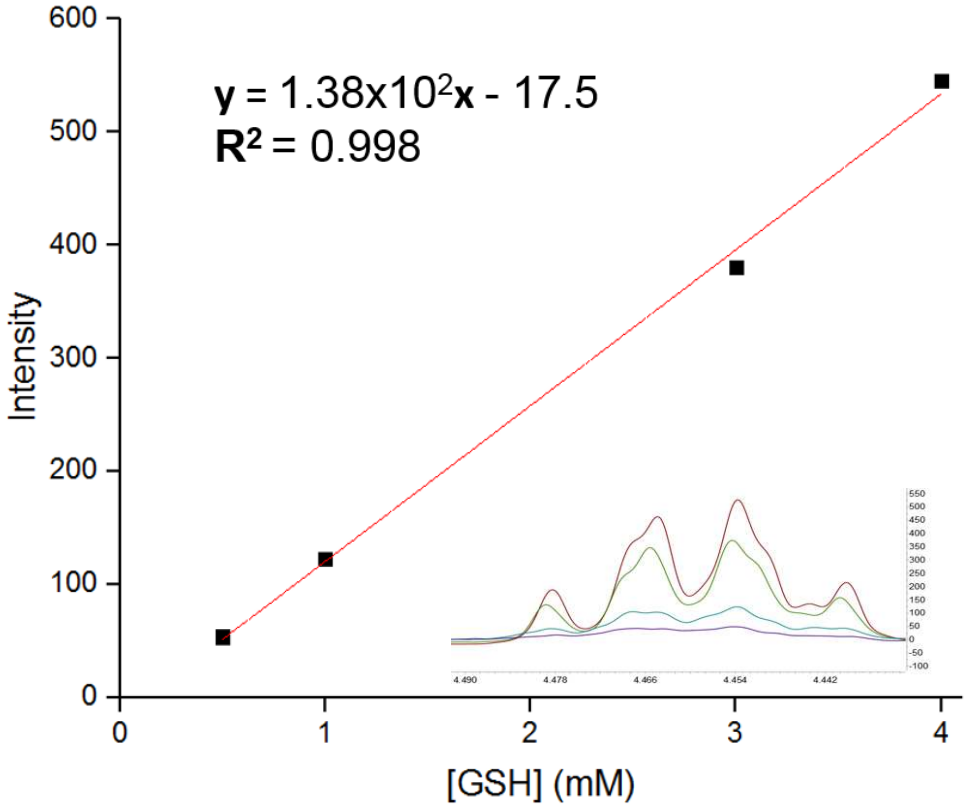

Figure S2.8. Calibration curve used to calculate [GSH] in reaction samples. Inset, ^{1}H NMR data used to generate calibration curve (Red = 4 mM, Yellow = 3mM, Blue = 1 mM, Purple = 0.5 mM).

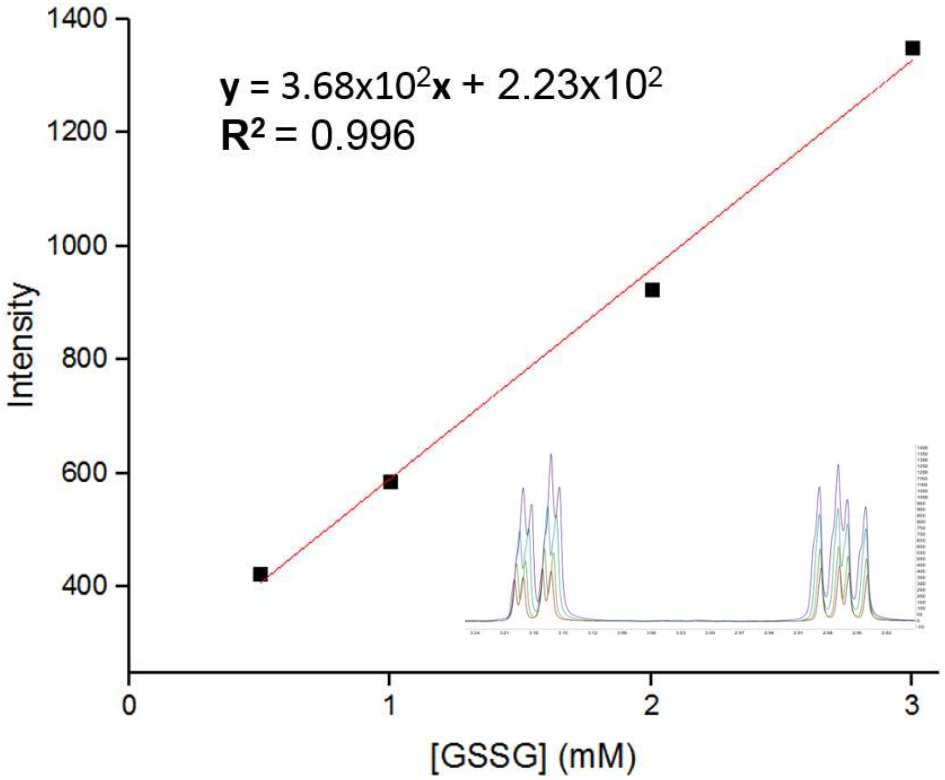

Figure S2.9. Calibration curve used to calculate [GSSG] in reaction samples. Inset, ^{1}H NMR data used to generate calibration curve (Purple = 3 mM, Blue = 2mM, Green = 1 mM, Red = 0.5 mM).

Control Reactions

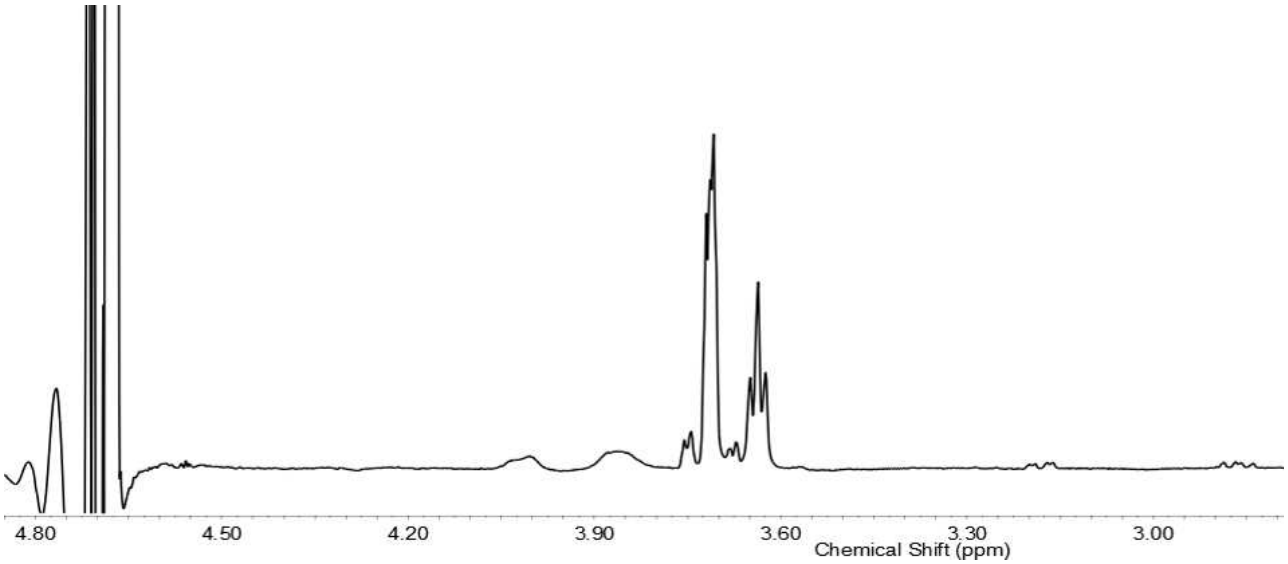

Figure S2.10. Resulting ^{1}H NMR spectra of GSNO (1 mM) alone without Cu^{2+} or Cu-BTTri present after 16 h. Spectra provided to indicate the stability of GSNO alone in the absence of copper containing species, supporting that the observed GSNO decomposition was not simply due to experimental conditions and that a copper catalyst is indeed required for decomposition.

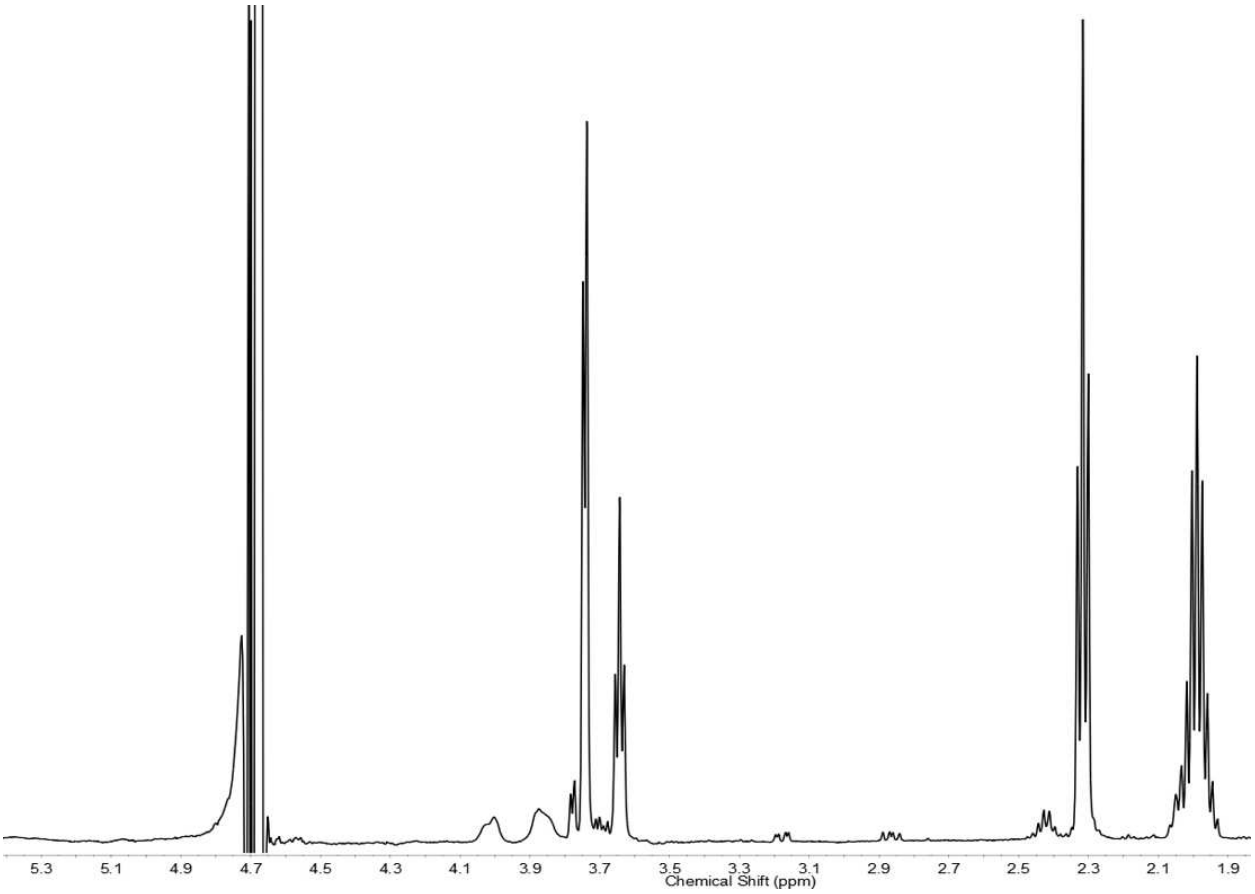

Figure S2.11. Resulting ^{1}H NMR spectra of GSNO (1 mM) and GSH (0.04 mM) alone without Cu^{2+} present after 16 h. Spectra provided to support the need for Cu^{2+} to observe GSNO decomposition. Low levels of GSH alone do not induce significant GSNO decomposition without Cu^{2+} present.

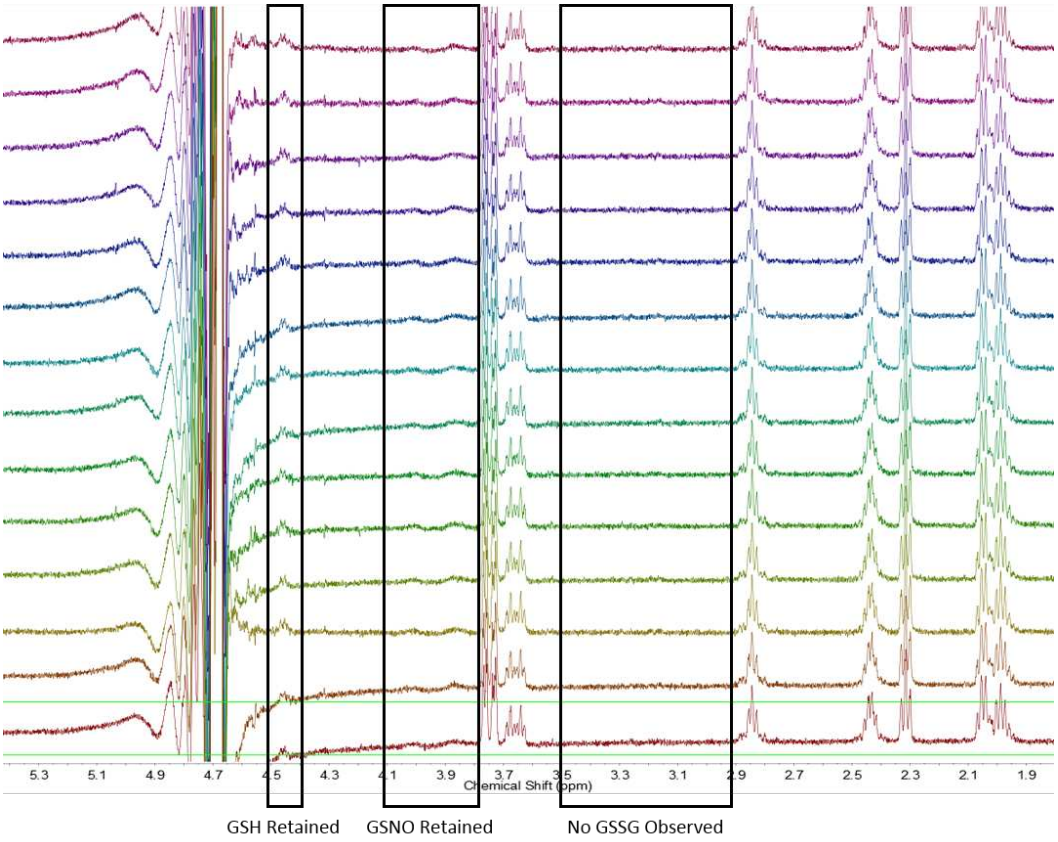

Figure S2.12. Reaction between GSNO (2 mM) and GSH (2 mM) over the course of 14 h. Spectra were collected at 1 h intervals. Each spectrum was collected with 8 transients. Spectra provided to support the need for CuBTTri to observe GSNO decomposition. GSH alone does not induce significant GSNO decomposition without CuBTTri present.

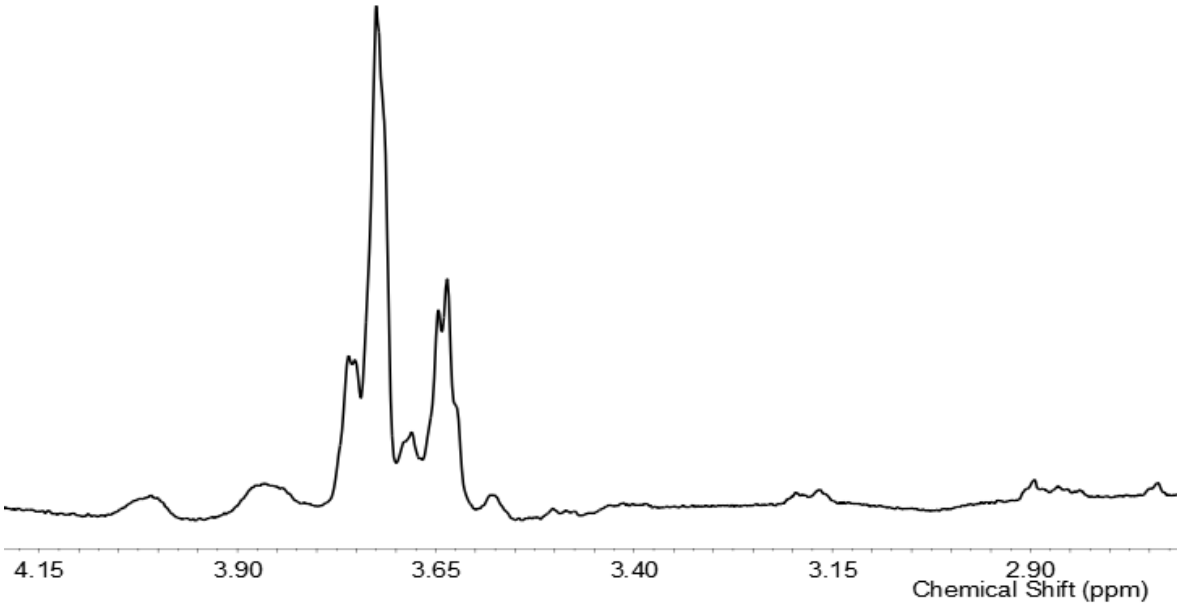

Figure S2.13. Resulting ^{1}H NMR spectra of reaction between GSNO (2mM) and Cu-BTTri (2:1 mol ratio GSNO:Cu) bubbled with house air after 1 h. Spectra provided to show the effect of introducing a chemical oxidant (O_2) into the reaction system. Little to no GSNO decomposition occurs, the opposite effect is observed when compared to the introduction of GSH into the reaction. These tests were performed to further support the importance of the redox chemistry in the CuBTTri catalyzed system.

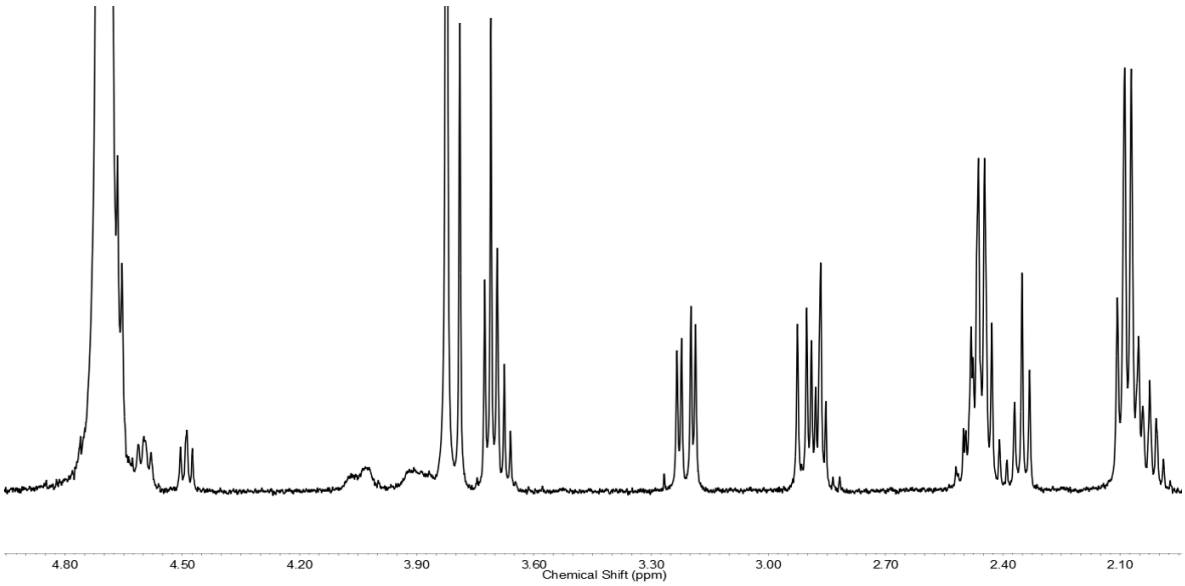

Figure S2.14. Resulting ^{1}H NMR spectra of reaction between GSNO (1 mM) and Cu^{2+} (0.2 mM) in the presence of GSH (1 mM) after 16 h. Based upon the relative concentrations determined, the reaction reaches 25% completion after approximately 1 h, and then does not proceed further in the next 11 h.

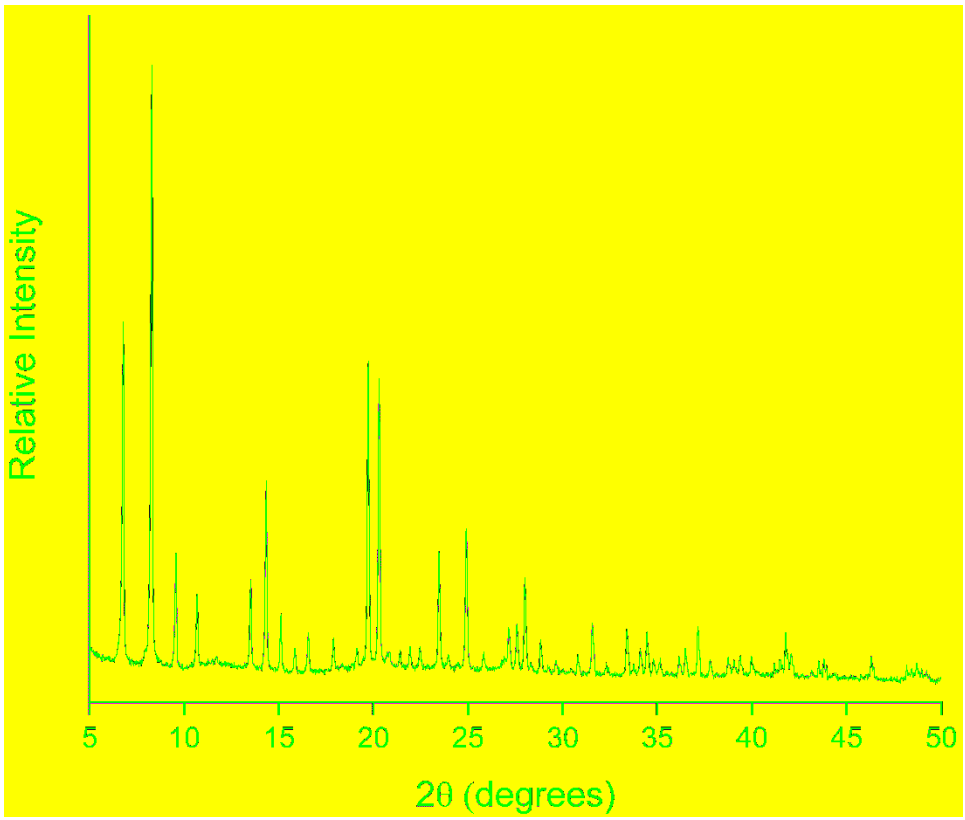

Figure S2.15. Post reaction PXRD characterization of CuBTTri for a reaction with GSNO (2 mM) and GSH (2mM).

NOA Experiments Using Cu^{2+} and CuBTTri

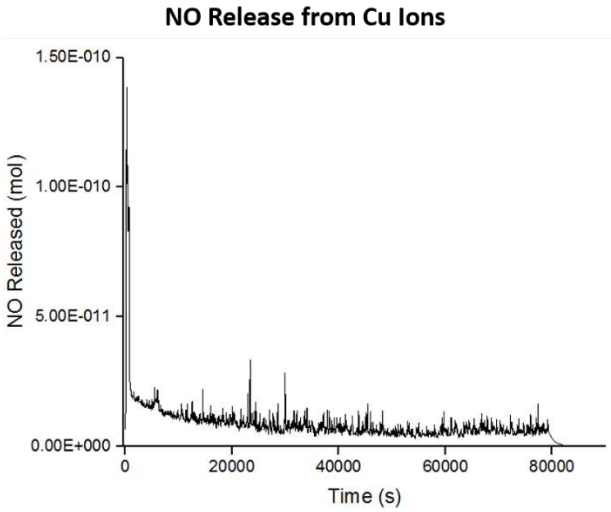

Figure S2.16. NO release profile for GSNO (1mM) decomposition catalyzed by copper ions (0.2 mM) in water. Total mols of NO generated (2.4 x 10^{-8}) correspond in a 1:1 ratio to the mols of GSNO initially present (2.5 x 10^{-8}).

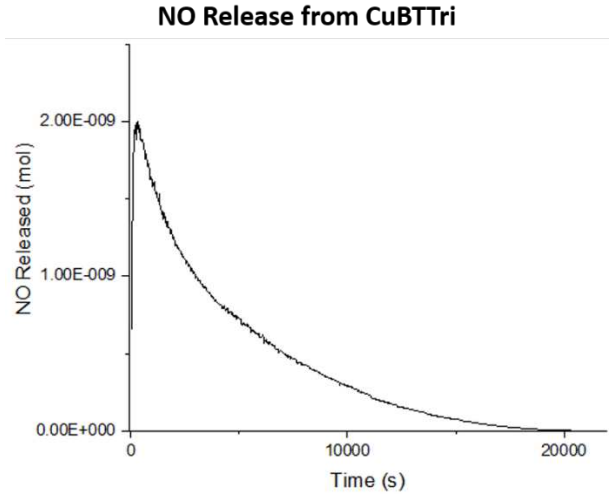

Figure S2.17. NO release profile for GSNO (2mM) decomposition catalyzed by CuBTTri in the presence of GSH (2mM) in water. Total mols of NO generated (3.1 x 10^{-7}) correspond in a 1:1 ratio to the mols of GSNO initially present (3.0 x 10^{-7}).

REFERENCES

1. Broniowska, K. A., Diers, A. R. & Hogg, N. S-nitrosoglutathione. *Biochimica et biophysica acta* **1830**, 3173–3181 (2013).

2. Hart, T. W. Some Observations Concerning the S-Nitroso and S-Phenylsulphonyl Derivatives of L-Cysteine and G. *Tetrahedron Letters* **26**, 2013–2016 (1985).

APPENDIX II. SUPPORTING INFORMATION FOR CHAPTER III.

^{1}H-NMR Spectra Array of GSSG in Blood Plasma

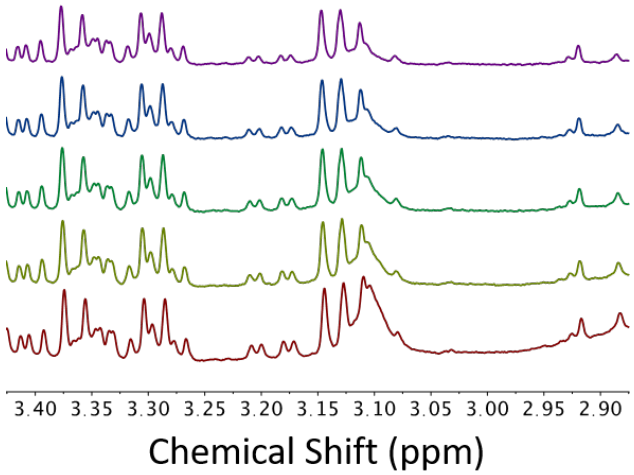

Figure S3.1. ^{1}H–NMR spectra of 0.5mM GSSG solution in bovine plasma collected using a CPMG-T2 weighted pulse sequence with PRESAT, as described in the experimental section of Chapter III. The signal of interest corresponding to GSSG can be observed at 3.2 ppm. The different spectra correspond to different re-focusing train times in the CPMG-T2 weighted pulse sequence (red = 50 ms , light green = 75 ms, dark green = 100 ms, blue = 125 ms, purple = 150 ms). It was determined that 75 ms provided measurable intensity while minimizing the baseline signal from blood plasma. Without using this ^{1}H NMR experimental method, the signal arising from GSSG cannot be observed.

^{1}H-NMR Spectrum of GSNO in Blood Plasma

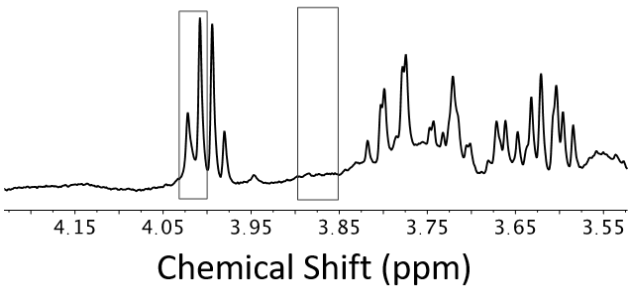

Figure S3.2. ^{1}H–NMR spectrum of bovine plasma. Boxed regions show the ppm region where resonances unique to GSNO are expected (4.00–4.03, 3.85–3.89).

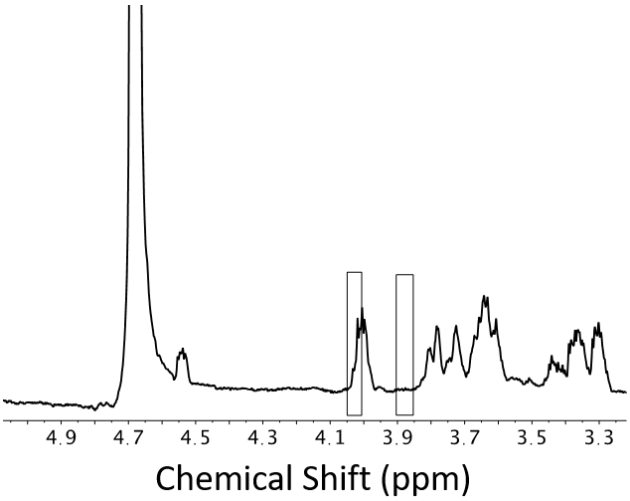

Figure S3.3. ^{1}H–NMR spectrum of 0.5mM GSNO in blood plasma. The two expected broad signals for GSNO (4.00–4.03, 3.85–3.89) were not observed. GSNO is not readily quantifiable in blood plasma by ^{1}H–NMR.

Detecting GSSG in Blood Plasma by ^{1}H NMR

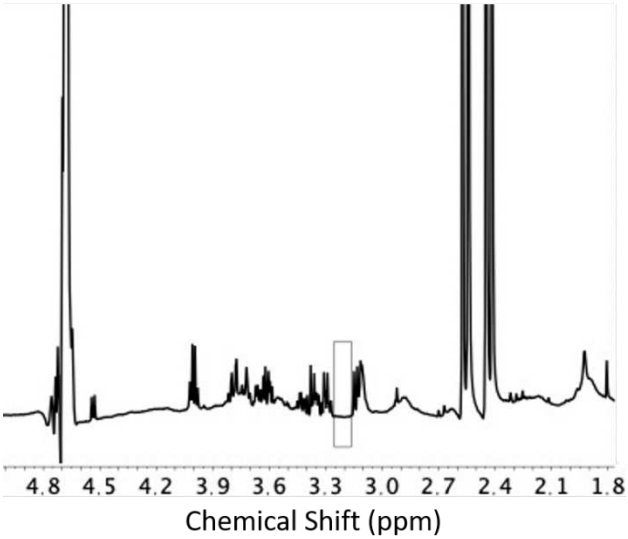

Figure S3.4. ^{1}H–NMR spectrum of bovine blood plasma. The boxed region of the spectrum shows that there are no interfering signals present in the ppm range where the diagnostic signals for GSSG are present.

UV-VIS Spectrum of Blood Plasma

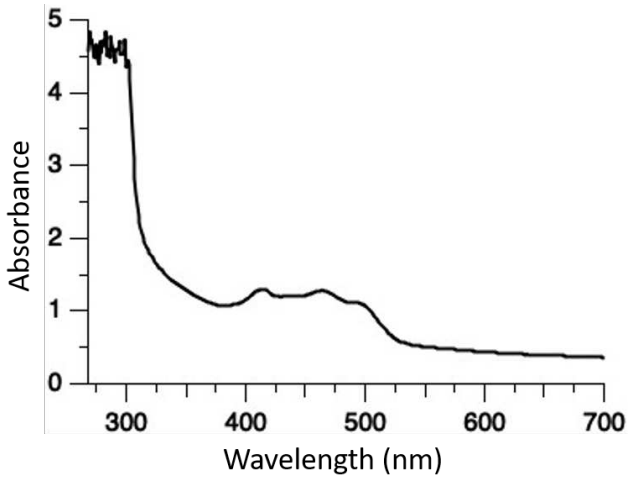

Figure S3.5. UV-VIS absorbance spectrum for bovine plasma from 275 to 700 nm.

^{1}H NMR Spectra of GSH in Plasma

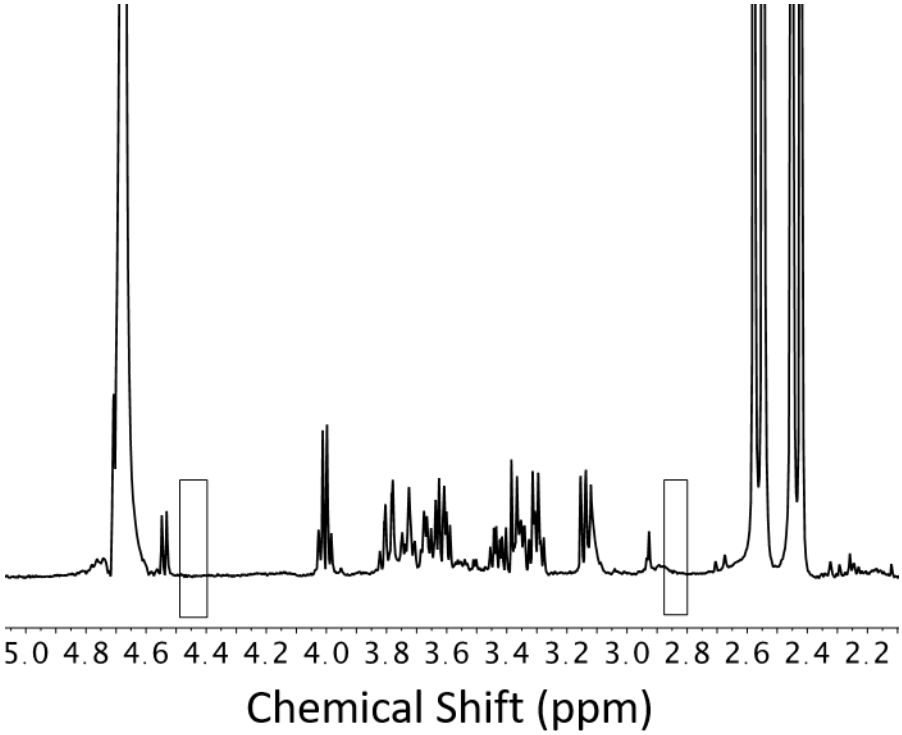

Figure S3.6. ^{1}H–NMR spectrum of 0.5mM GSH in plasma. The signals expected for GSH, (multiplets at 4.40–4.48 and 2.80–2.88 ppm) were not observed.

UV-VIS Absorbance Data Showing Loss of GSNO Over 16h of Reaction

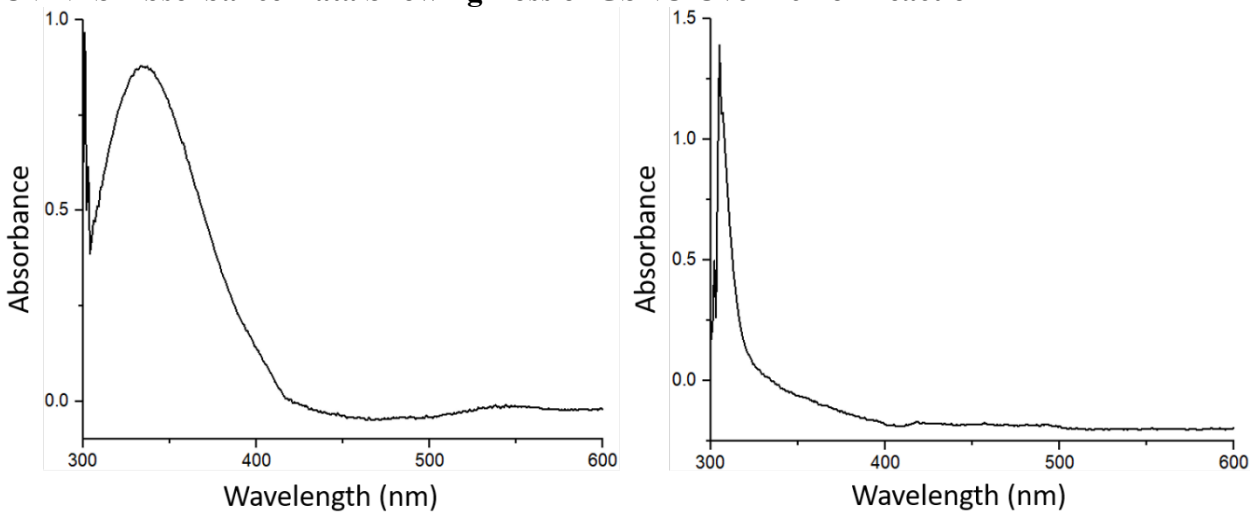

Figure S3.7. UV–VIS absorbance spectrum of the initial GSNO solution in bovine plasma where [GSNO] = 1 mM (Left). UV–VIS absorbance spectrum of the reaction supernatant after 16h, corresponding to [GSNO] = 0 mM (Right).

^{1}H NMR Data to Quantify [$GSSG_{(plasma)}$] After 16h of Reaction

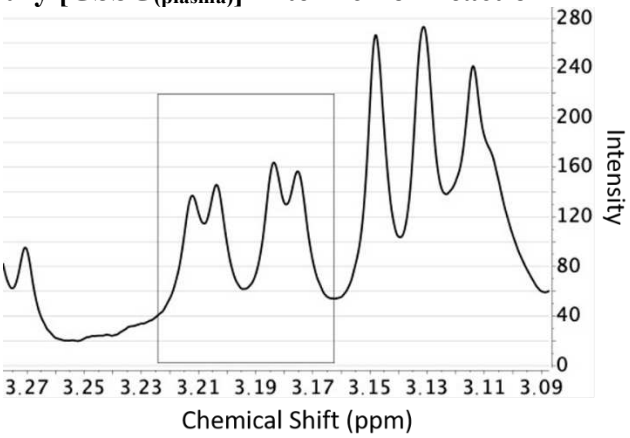

Figure S3.8. ^{1}H–NMR spectrum of reaction supernatant after 16h. The average of three trials corresponds to [$GSSG_{(plasma)}$] = 1.1 ± 0.1 mM. [$GSSG_{(plasma)}$] was calculated by measuring signal intensity at 3.2 ppm and then using the calibration curve presented in Chapter III (Figure 4B).

Determining the Amount of GSSG Present After 16 h and 20 min of Reaction

Table S3.1. [$GSSG_{(plasma)}$] in reaction supernatant for 20 minute and 16 hour experiments. The peak intensity was measured and [$GSSG_{(plasma)}$] was then determined using Figure 3.4B in Chapter III. The catalytic rate [+d[GSSG]/dt] was calculated using equation 3.1 in Chapter III.

Sample:	Time (h):	GSSG Intensity at Peak 3:	Average [GSSG] (mM):
Cell 1	16	137.44	1.122 ± 0.142
Cell 2	16	92.99	
Cell 3	16	115.23	
A	0.33	24.61	1.1 ± 0.1
B	0.33	33.98	
C	0.33	28.30	

CuBTTri Characterization by Powder X-Ray Diffraction

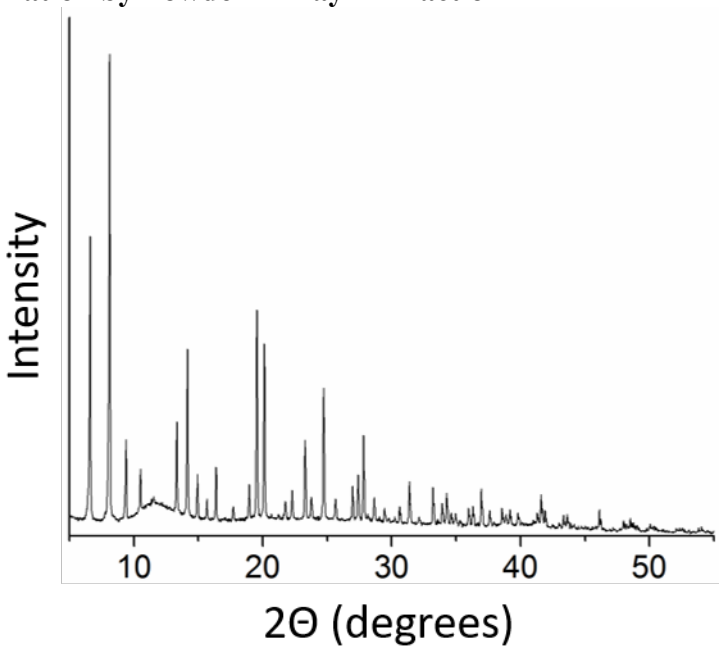

Figure S3.9. Diffraction pattern for CuBTTri as synthesized. The diffraction pattern matches a literature standard.[1] This is the same diffraction pattern used in a previous publication,[2]as the MOF used in this work is from the same batch of MOF synthesized for that work, copyright Elsevier 2019.

REFERENCES

1. Demessence, A., D'Alessandro, D. M., Foo, M. L. & Long, J. R. Strong CO2 Binding in a Water-Stable, Triazolate-Bridged Metal−Organic Framework Functionalized with Ethylenediamine. *Journal of the American Chemical Society* **131**, 8784–8786 (2009).

2. Tuttle, R. R., Rubin, H. N., Rithner, C. D., Finke, R. G. & Reynolds, M. M. Copper ion vs copper metal–organic framework catalyzed NO release from bioavailable S-Nitrosoglutathione en route to biomedical applications: Direct 1H NMR monitoring in water allowing identification of the distinct, true reaction stoichiometries and thio. *Journal of Inorganic Biochemistry* **199**, 110760 (2019).

APPENDIX III. SUPPORTING INFORMATION FOR CHAPTER IV.

Additional Characterization Methods

UV–VIS data were acquired using a Thermo Scientific Evolution 300 UV–Vis Spectrophotometer. Samples were prepared using millipore water in quartz cuvettes. FT–IR data were acquired using a Thermo Scientific Nicolet 6700 FTIR Spectrophotometer with MCT detector and ATR accessory. Powder X–Ray diffraction (PXRD) patterns were obtained using a Bruker D8 Discover DaVinci Powder X–ray Diffractometer with CuKα radiation operated at 40 kV and 40 mA. A typical scan rate was 0.3 sec/step with a step size of 0.02 deg. Ligand characterization ^{1}H NMR spectra was acquired using an Agilent (Inova) 400 MHz spectrometer. SEM micrographs were aquired using a JEOL JSM–6500F field emission scanning electron microscope with samples mounted on carbon tape. Dynamic light scattering (DLS) data were collected using a Malvern zetasizer nano zs. All data were processed and figures were prepared using either OriginPro 2019 64 bit software or Microsoft Excel.

GSNO Purity Assay

Table S4.1. Average absorbance values and concentration data of synthesized GSNO that was used in all of the reported studies.

Trial	[GSNO] (mM)	Absorbance at 335 nm
1	1.11	0.992
2	1.11	0.992
3	1.11	0.990
4	0.75	0.68
5	0.75	0.67
6	0.75	0.69
7	0.50	0.453
8	0.50	0.453
9	0.50	0.453
10	0.25	0.225
11	0.25	0.225
12	0.25	0.225
13	0.10	0.088
14	0.10	0.088
15	0.10	0.089

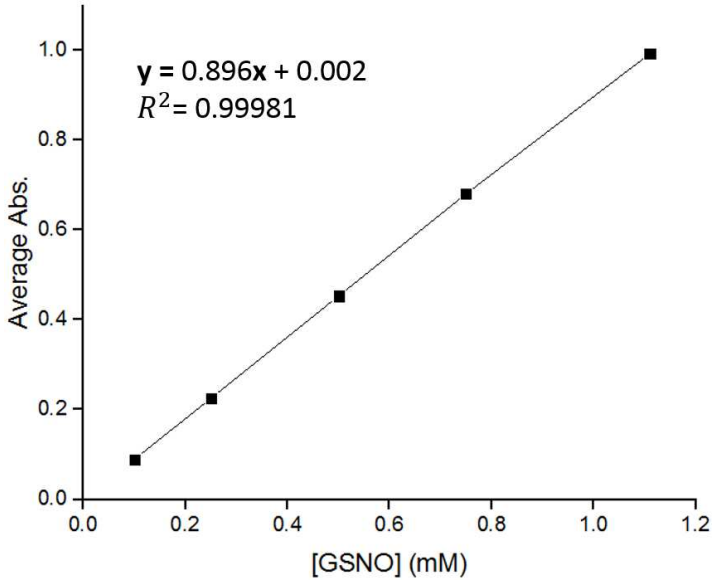

Figure S4.1. Average absorbance vs [GSNO] from which the molar extinction coefficient (ε) was determined to be 896 mM^{-1} cm^{-1}. The purity of GSNO was assessed by comparison of observed ε versus literature value (922 mM^{-1} cm^{-1}).[1,2] The resulting purity was determined to be 97 ± 2%.

CuBTTri Synthesis Characterization

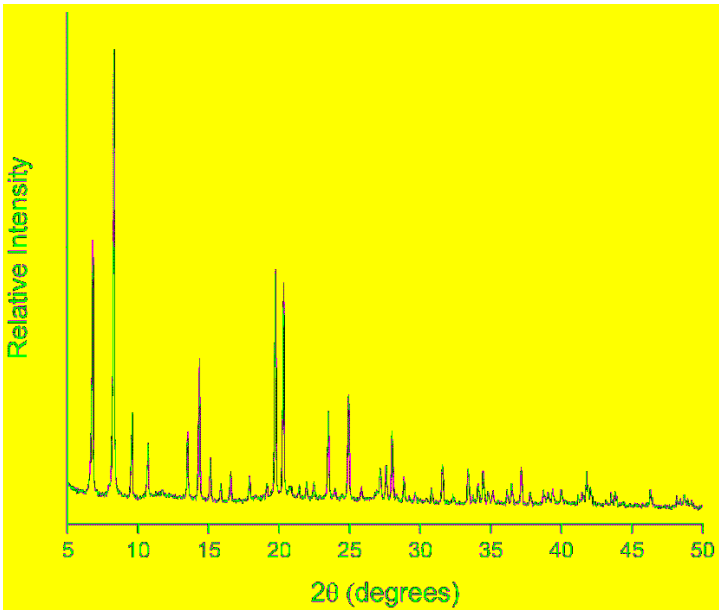

Figure S4.2. P–XRD of hand–ground CuBTTri. The observed diffraction pattern matches the pattern reported in the first synthesis of CuBTTri.[3,4]

Particle Filtration Analysis by DLS

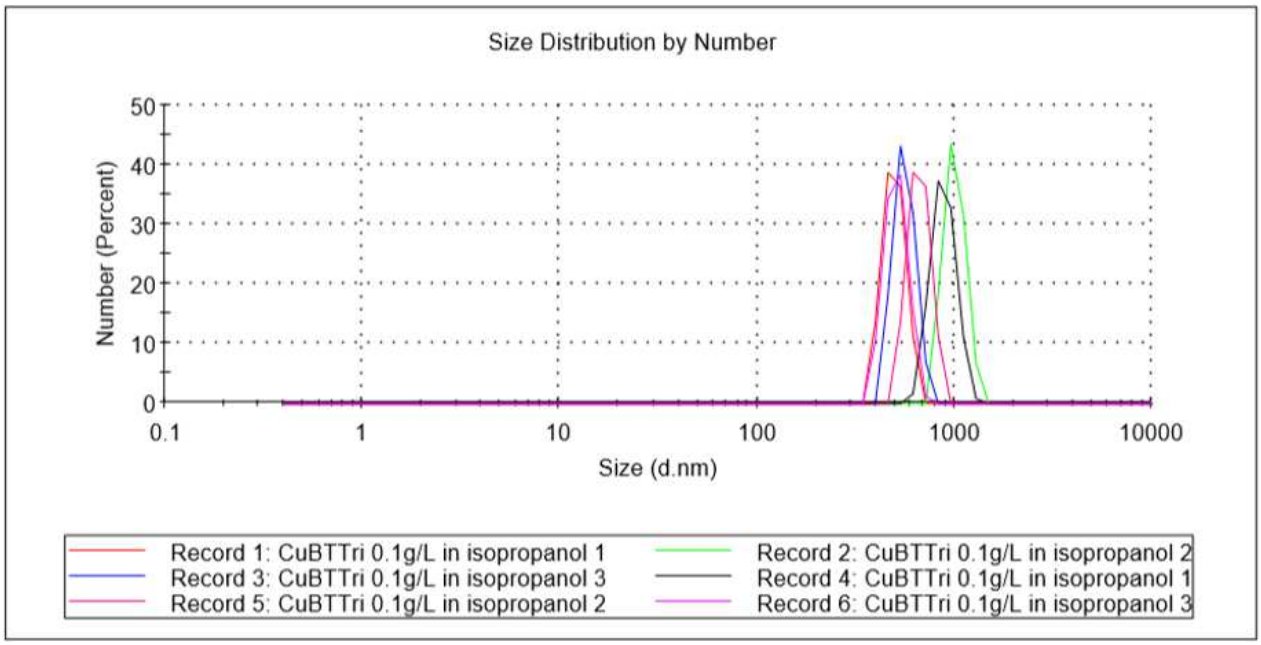

Figure S4.3. DLS results demonstrate that the cell strainers are reasonably effective for filtering out particles of size larger than 1 μm. The particle size distribution of $MOF_{Filtered}$ samples is too wide to allow for average particle size determination by DLS. DLS only confirms that particles greater than or equal to 1 μm are not present in large quantities in $MOF_{Filtered}$ samples.

^{1}H NMR Results of Particle Size vs. $[-d[GSNO]/dt]_i$

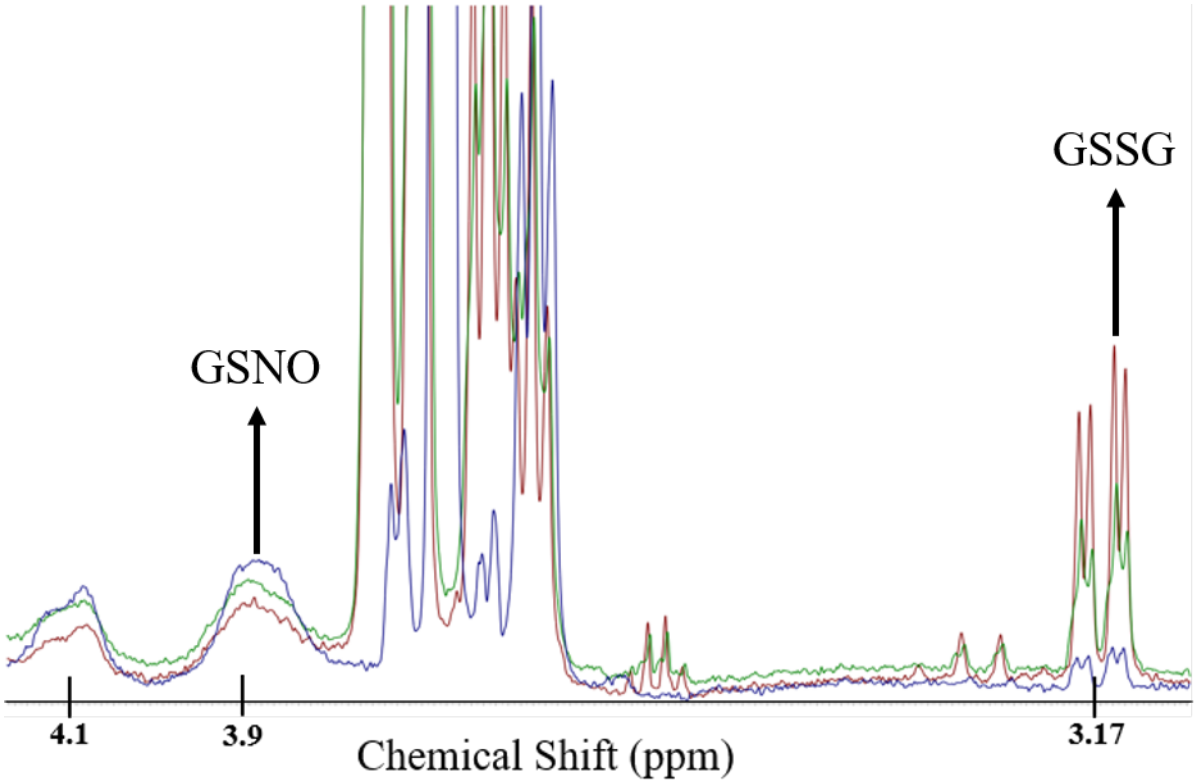

Figure S4.4. ^{1}H NMR results from MOF_{Large} (blue), MOF_{Ground} (green), and $MOF_{Filtered}$ (red) experiments at 20 min. Values for [GSNO] at 20 min were calculated using previously generated calibration curves[3] relating the intensity of the peak at 3.9 ppm to [GSNO]. The value of [GSNO] at 20 min was compared to the initial [GSNO] to calculate an average observed initial catalytic rate at 20 min. The initial [GSNO] for all experiments reported herein was 1 mM. No loss of GSNO was observed for MOF_{Large} reactions, $[-d[GSNO]/dt]_i = 0$ mM s^{-1} over 20 min. The small amount of glutathione disulfide (GSSG) present in MOF_{Large} samples (3.17 ppm) is attributed to the impurity generated from the synthesis of GSNO. Loss of GSNO for MOF_{Ground} experiments at 20 min yields $[-d[GSNO]/dt]_i = 1.6 \pm 0.25 \times 10^{-4}$ mM s^{-1}. Loss of GSNO for $MOF_{Filtered}$ experiments at 20 min yields $[-d[GSNO]/dt]_i = 2.9 \pm 0.3 \times 10^{-4}$ mM s^{-1}.

[GSNO] vs. Time

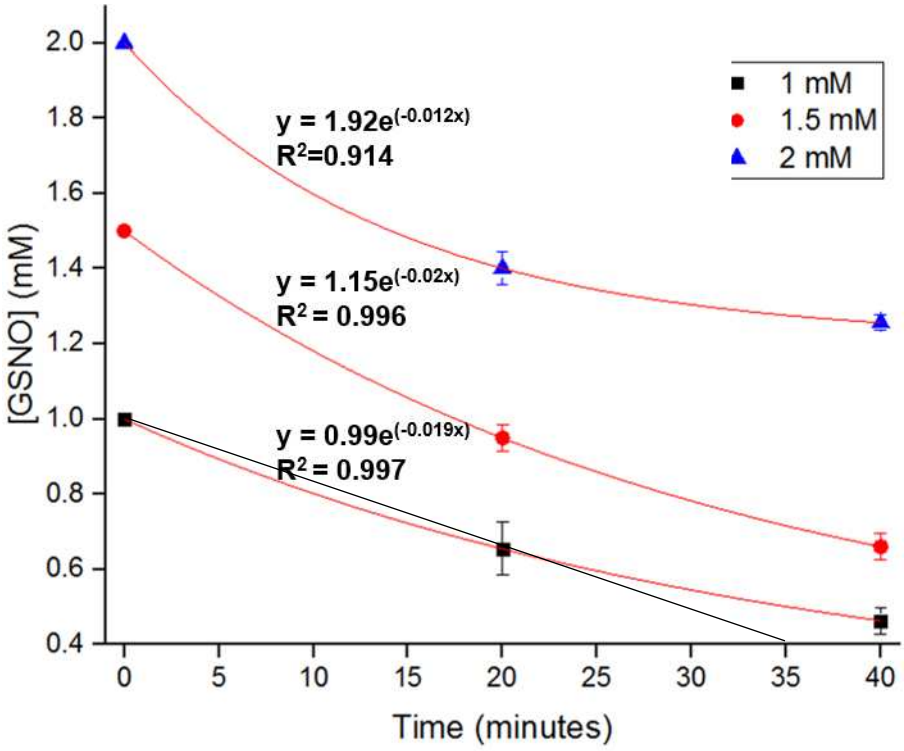

Figure S4.5. Observed loss of GSNO over time for MOF_{Ground} samples at $[GSNO]_i$ = 1 (square, black), 1.5 (circle, red), and 2 mM (triangle, blue). The slope of the solid black line (1.6 x 10^{-4} mM s^{-1}) represents the average observed initial catalytic rate at 20 min for experiments with $[GSNO]_i$ = 1 mM. The slope of the black line is determined by dividing the difference in [GSNO] at two points by the time difference between those points. Red lines represent the fit of concentration data over time to an exponential function.

Additional SEM Micrographs of MOF_{Ground} and $MOF_{Filtered}$ Samples

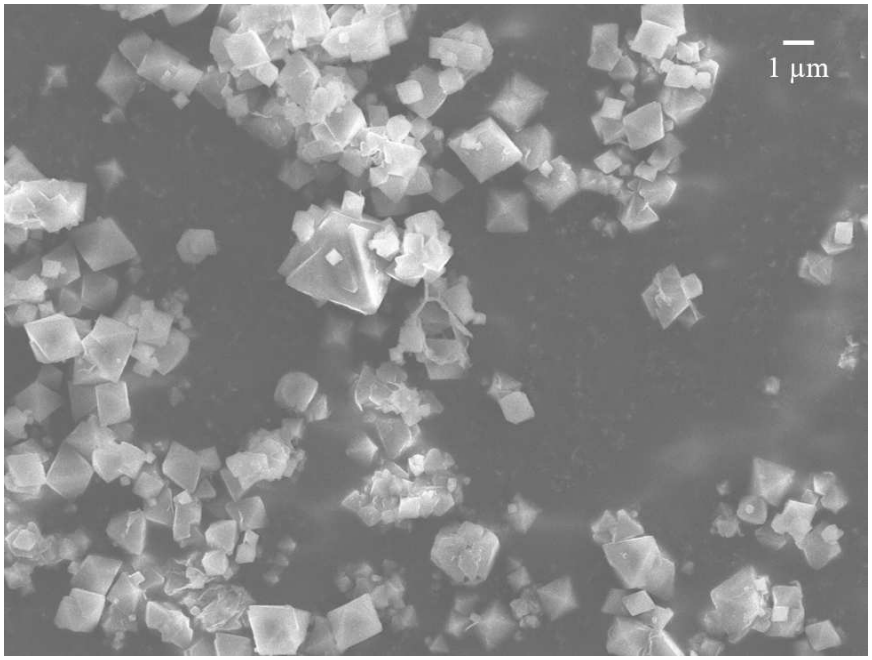

Figure S4.6. Additional SEM micrograph of a MOF_{Ground} used for average particle size determination. Particle sizes were determined by visual comparison to the scale bar. Either the total length of the octahedra or the square pyramid side length (which can be calculated into total length) were measured to determine particle size. In total, the length of 40 particles were measured in this micrograph. Reproduced with permission from the supporting information of reference 5. Copyright 2019 Elsevier.[5]

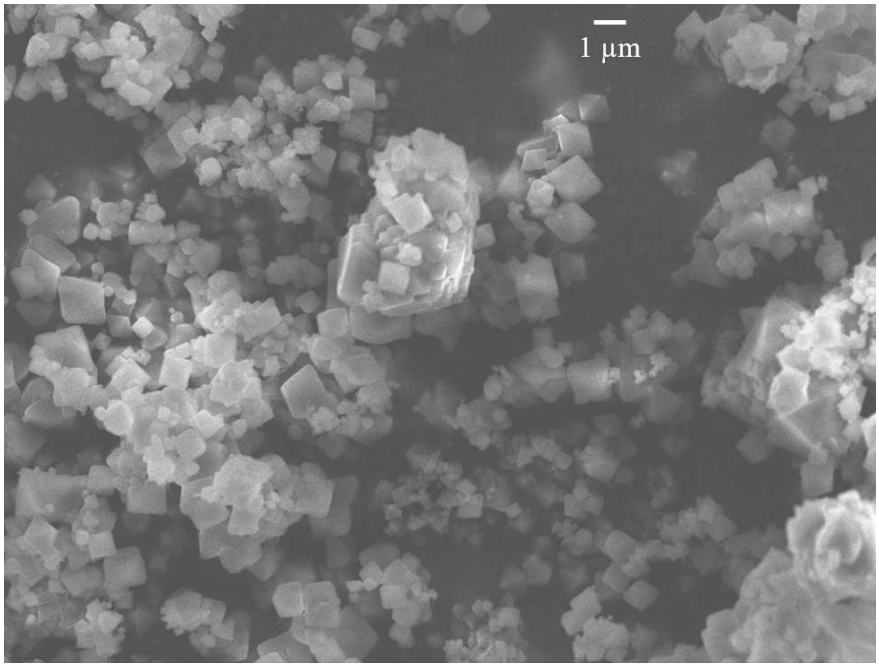

Figure S4.7. Additional SEM micrograph of a MOF_{Ground} used for average particle size determination. Particle sizes were determined by visual comparison to the scale bar. In total, the length of 60 particles were measured in this micrograph.

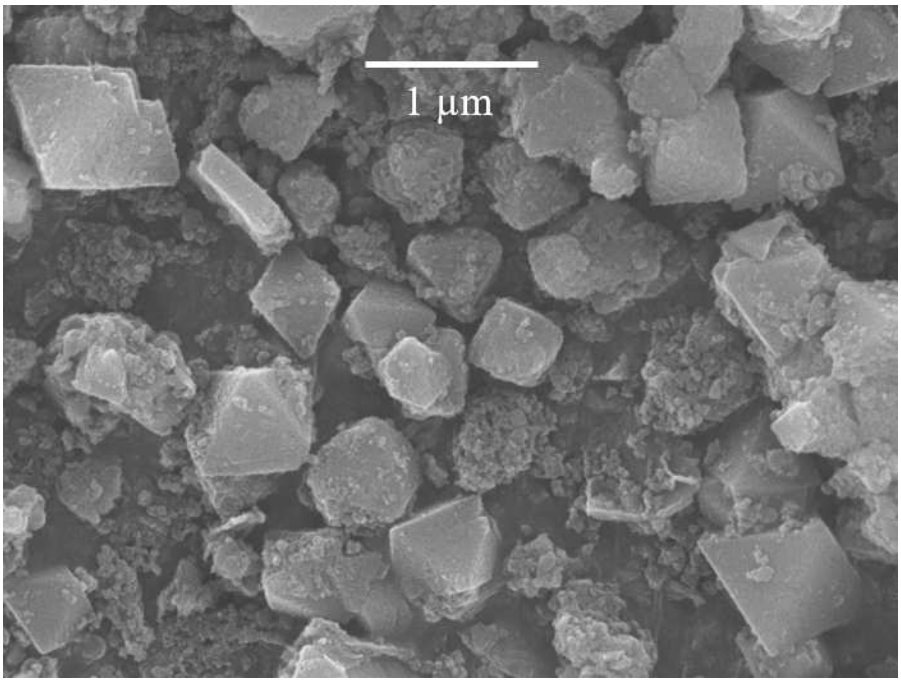

Figure S4.8. Additional SEM micrograph of a $MOF_{Filtered}$ sample used for average particle size determination. Particle sizes were determined by visual comparison to the scale bar. In total, the length of 12 particles were measured in this micrograph.

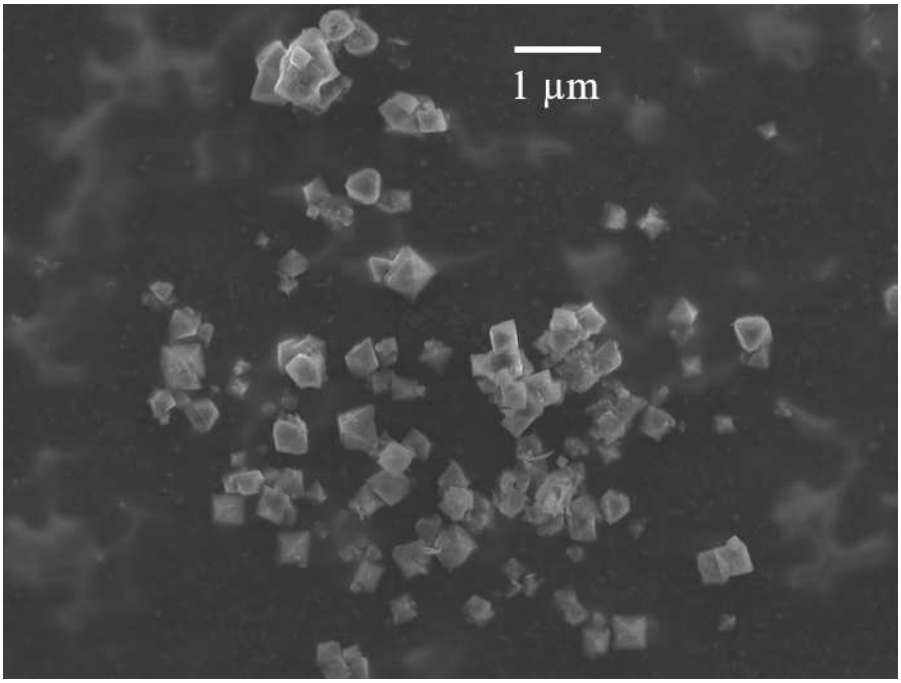

Figure S4.9. Additional SEM micrograph of a $MOF_{Filtered}$ sample used for average particle size determination. Particle sizes were determined by visual comparison to the scale bar. In total, the length of 30 particles were measured in this micrograph.

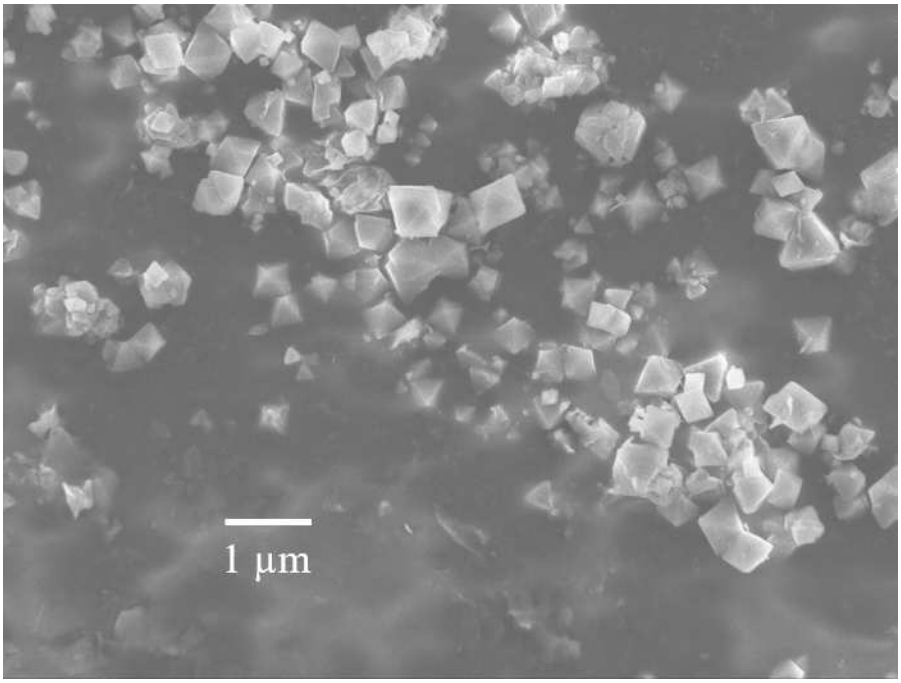

Figure S4.10. Additional SEM micrograph of a $MOF_{Filtered}$ sample used for average particle size determination. Particle sizes were determined by visual comparison to the scale bar. In total, the length of 30 particles were measured in this micrograph.

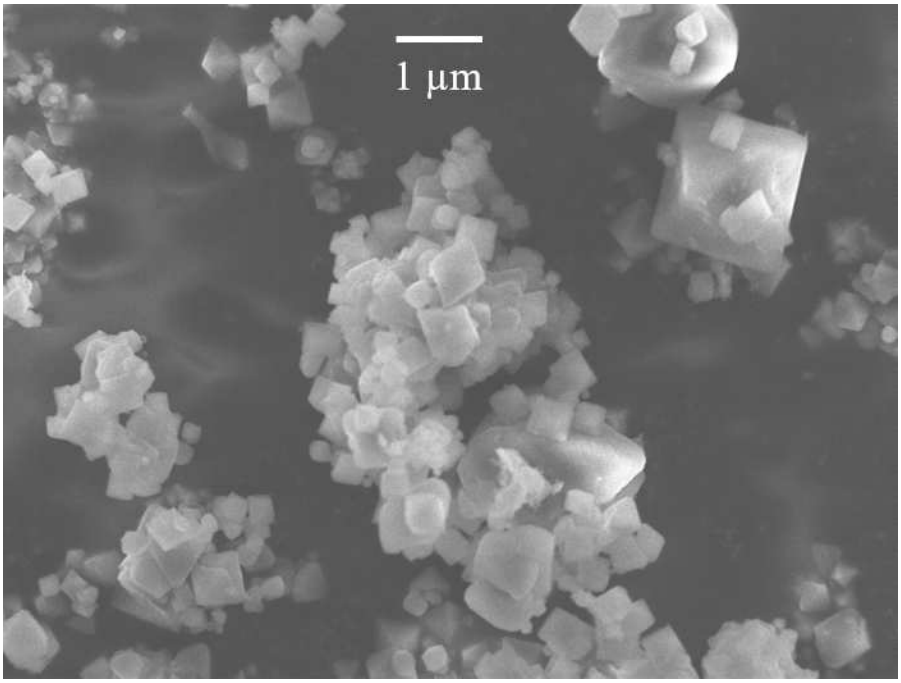

Figure S4.11. Additional SEM micrograph of a $MOF_{Filtered}$ sample used for average particle size determination. Particle sizes were determined by visual comparison to the scale bar. In total, the length of 28 particles were measured in this micrograph. This micrograph shows that while the cell strainers employed are effective at filtering out particles greater than 1 μm in size, some larger particles remain present, consistent with the DLS data presented in Figure S3.

^{1}H NMR Results for KCN Poisoning

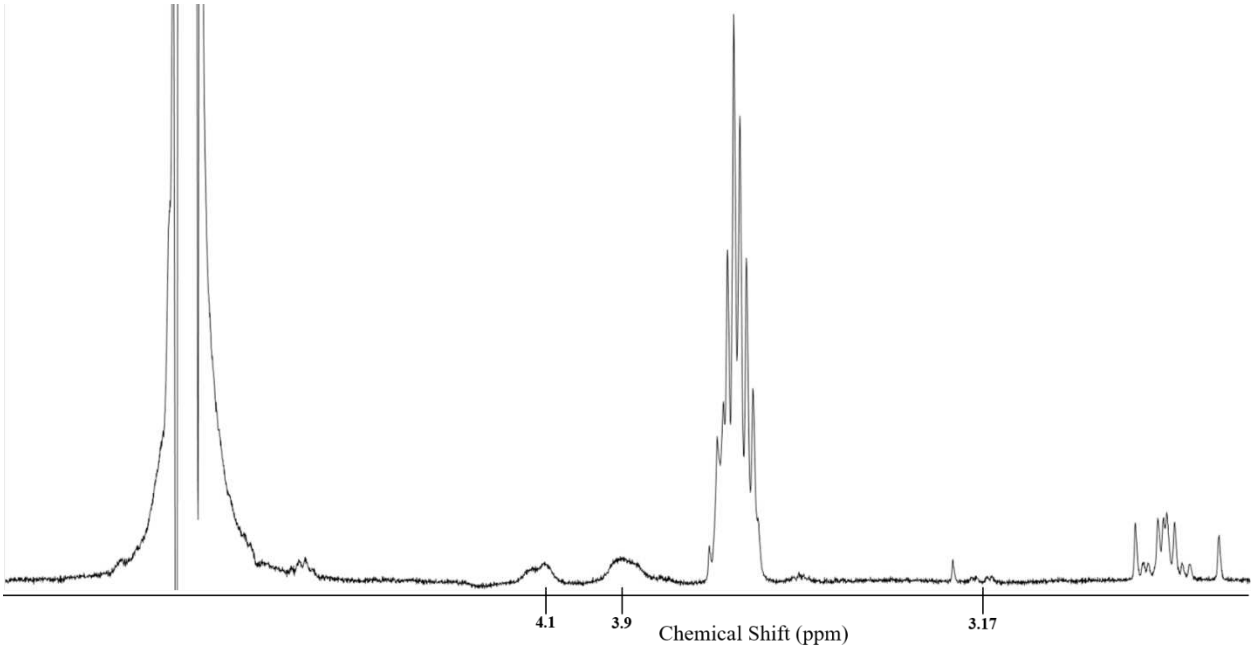

Figure S4.12. ^{1}H NMR results from MOF_{Ground} experiments with 2:1 CN^-:Cu at 20 min. No loss of GSNO (3.9 ppm) is observed from $[GSNO]_i$ (1 mM) and no generation of GSSG product (3.17 ppm) is observed at 20 min. The value of [GSNO] at 20 min was determined was calculated using previously generated calibration curves[3] relating the intensity of the peak at 3.9 ppm to [GSNO]. The small amount of GSSG (3.17 ppm) present is attributed to the impurity generated in the GSNO synthesis.

^{1}H NMR Results for TPPTS Poisoning Experiments

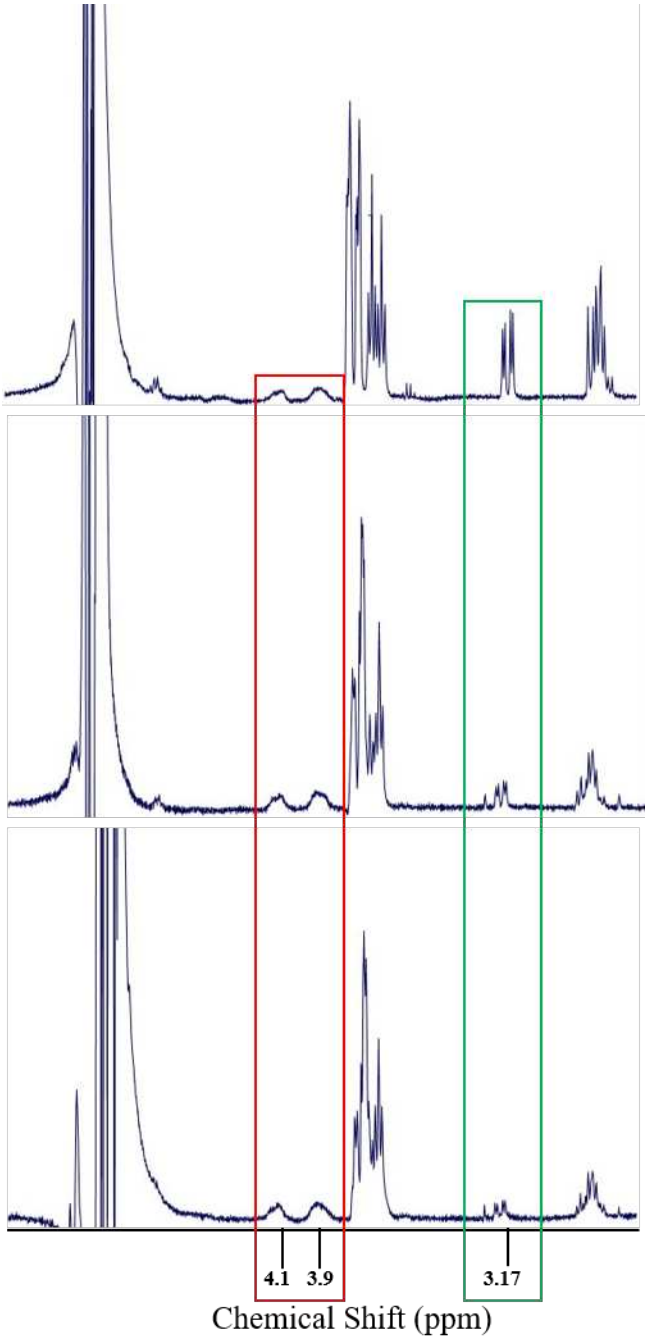

Figure S4.13. ^{1}H NMR results from $MOF_{Filtered}$ experiments at 20 min with 0.5 (top), 0.8 (middle), and 1.2 (bottom) % TPPTS of total mols Cu. Increasing levels of TPPTS lead to a decrease in [GSSG] product formation (3.17 ppm) at 20 min (green box). Increasing levels of TPPTS lead to an increase in [GSNO] starting material retention (3.9 ppm) at 20 min (red box). Rates from TPPTS poisoning experiments were calculated as described in the caption of Figure S4.

UV–VIS Results for TPPTS Poisoning Experiments

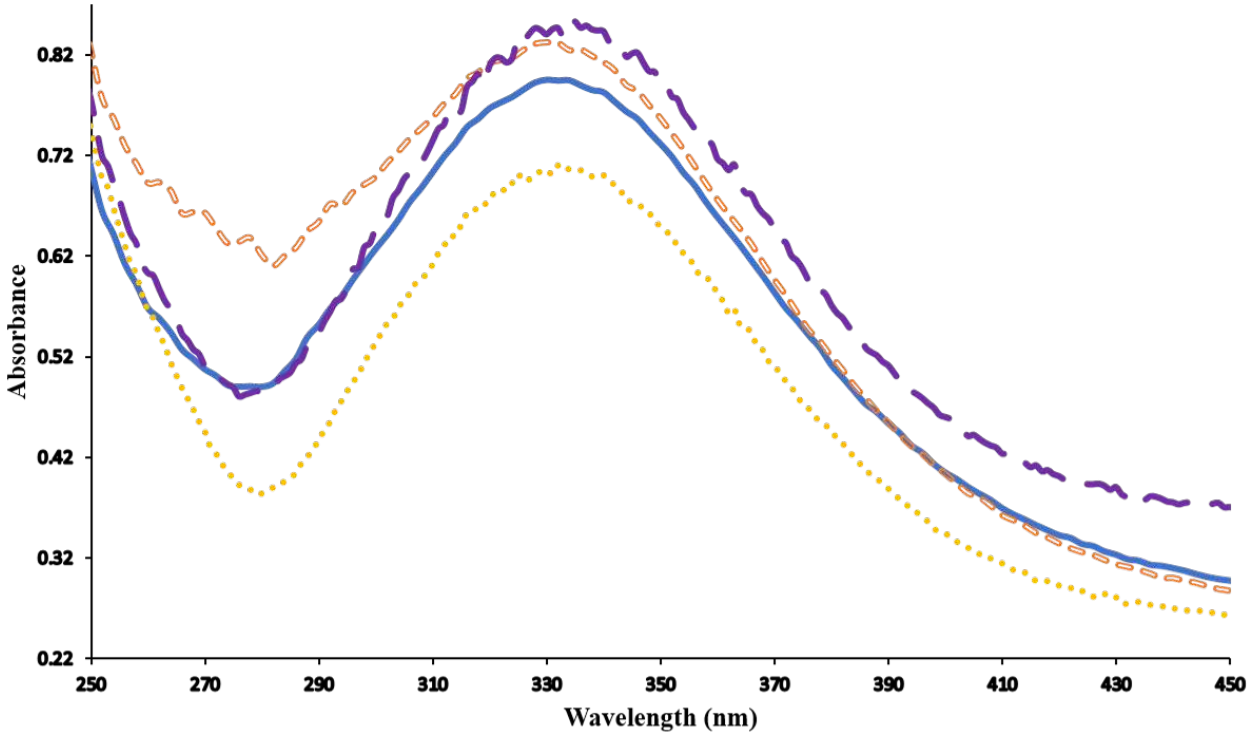

Figure S4.14. UV–VIS spectra from the supernatant of $MOF_{Filtered}$ reactions taken at 20 min with 10% TPPTS of total Cu (purple, solid dashes), 1% TPPTS of total Cu (blue, solid line), 0.1% TPPTS of total Cu (yellow, circles), and a 1mM GSNO in H_2O control (orange, hollow dashes). All reactions were carried out under identical conditions to the TPPTS poisoning experiments outlined in the experimental, with the only difference being that UV–VIS spectroscopy was used to analyze the supernatant as a secondary technique to results obtained using ^{1}H NMR. Values for [GSNO] were calculated using the known molar extinction coefficient for the electronic transition at 335 nm.[1,2] These data show that when TPPTS is present at 1% of total Cu in a given reaction, CuBTTri is very nearly completely poisoned for GSNO to NO conversion catalysis at 20 min, which is consistent with findings from ^{1}H NMR given in Chapter IV (where (1.3 ± 0.4)% TPPTS of total Cu corresponds to the x–intercept of the TPPTS poisoning curve). No loss of GSNO is observed by UV–VIS at 20 min when TPPTS is present at 10% of total Cu, as expected based upon the ^{1}H NMR poisoning results. Appreciable loss of GSNO is observed by UV–VIS at 20 min when TPPTS is present at 0.1% of total Cu, as expected.

FT–IR Analysis of MOF_{Large}, MOF_{Ground}, and $MOF_{Filtered}$ Particles

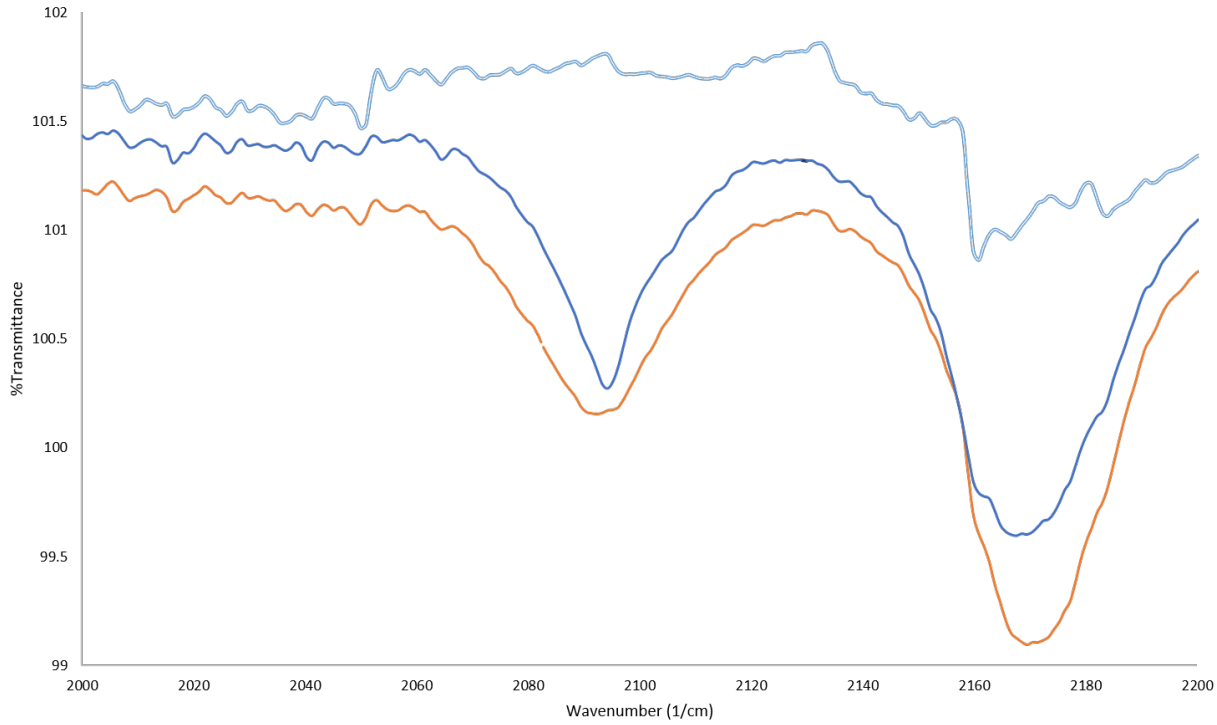

Figure S4.15. FT–IR spectra for MOF_{Large} (pale blue, top), MOF_{Ground} (dark blue, middle), and $MOF_{Filtered}$ particles poisoned with CN^- from 2000 to 2200 cm^{-1}. The Cu(CN) stretch (2170 cm^{-1}) and the $Cu(CN)_3$ stretch (2094 cm^{-1}) are both observed for MOF_{Ground} and $MOF_{Filtered}$ particles. As expected, the absorbance of the $Cu(CN)_3$ stretch is greater for $MOF_{Filtered}$ particles than MOF_{Ground} particles because the smallest $MOF_{Filtered}$ particles contain more $Cu_{surface}$ sites than the larger MOF_{Ground} particles. Only the Cu(CN) stretch is observed for MOF_{Large} particles. The lack of an observable $Cu(CN)_3$ stretch for MOF_{Large} particles is explained by the fact that the 3–coordinate $Cu_{surface}$ sites are present at such a low level in MOF_{Large} particles that upon poisoning of CuBTTri by CN^-, there are simply not enough $Cu(CN)_3$ sites generated to yield an observable stretch. However, MOF_{Large} particles *do* contain catalytically active, exterior surface Cu sites as demonstrated by the loss of GSNO over a longer time period shown in Figure S16. The relative intensities of the observed bands make sense because the smallest particles ($MOF_{Filtered}$) contain the highest number of CN^- accessible Cu sites (on the exterior surface and inside pores by diffusion), and should therefore exhibit the most absorbance, as seen in the figure. MOF_{Ground} particles contain fewer CN^- accessible sites than $MOF_{Filtered}$ particles but more than MOF_{Large} particles, so the absorbance for MOF_{Ground} particles poisoned by CN^- should fall in between the absorbance for the other two samples, as observed. Finally, with the lowest number of CN^- accessible Cu sites, MOF_{Large} particles poisoned with CN^- exhibit almost no observable absorbance of IR radiation.

Measuring the Loss of GSNO by UV–VIS using MOF_{Large} Particles

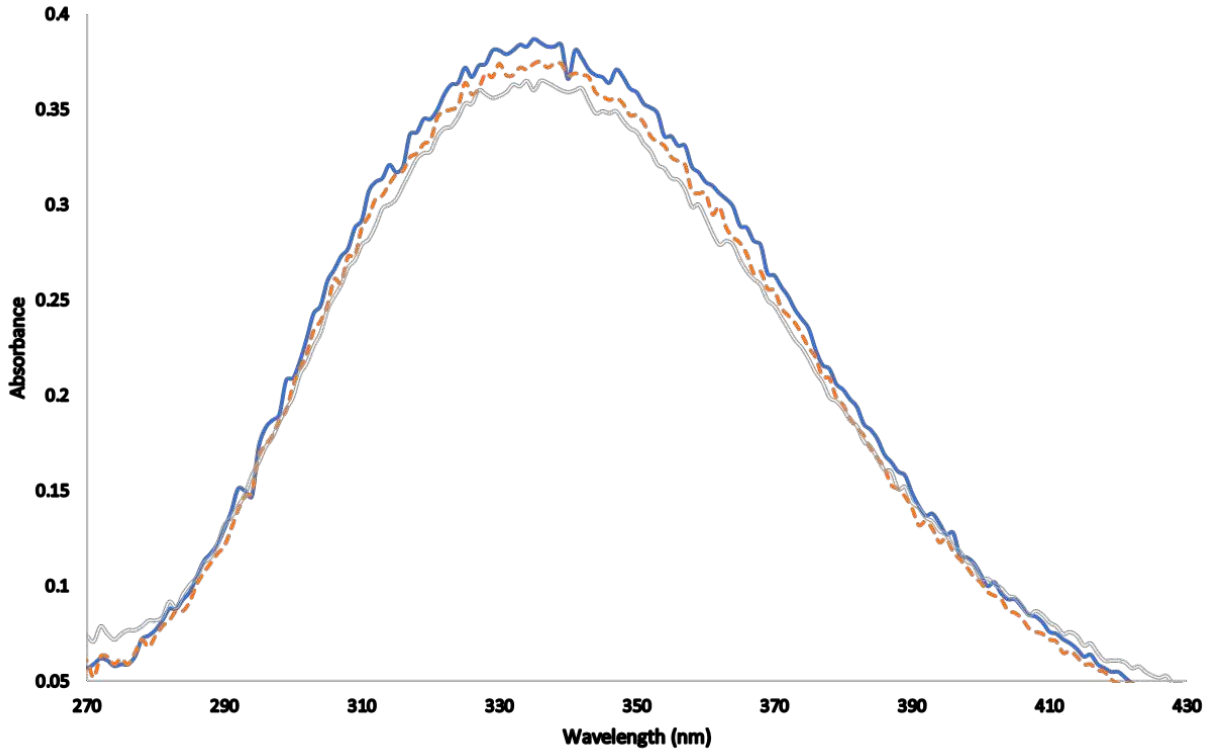

Figure S4.16. Experiments showing the loss of GSNO (0.50 mM standard, dark blue, top) at 2 h (orange dashes, middle) and 3 h (gray, bottom) when using MOF_{Large} particles for catalysis and $[GSNO]_i$ = 0.5 mM. Values for [GSNO] were calculated using the known molar extinction coefficient for the electronic transition at 335 nm.[1,2] [GSNO] at 2 and 3 h was determined to be 0.46 mM and 0.43 mM, respectively. These values correspond to 8% and 14% loss of GSNO in 2 and 3 h when using MOF_{Large} particles, much less than the ~30% loss of GSNO observed in 20 min when using the smaller $MOF_{Filtered}$ particles. The loss of GSNO is observed when using MOF_{Large} particles for catalysis, but on a much longer timescale than for MOF_{Ground} or $MOF_{Filtered}$ samples. These results show that MOF_{Large} particles contain catalytically active Cu sites, but at a very low level. This explains why no loss of GSNO is observed in 20 min when using MOF_{Large} particles, as detailed in Chapter IV.

TOF Calculation

Calculation S4.1. The normalized turnover frequency (TOF_{norm}) for a heterogeneous catalyst is defined as the mols of product generated in a given amount of time per the total number of active sites present, as defined below:

$$\mathrm{TOF_{norm}} = \frac{\text{mols product generated}}{(\text{mols acitve sites})\cdot(\text{time})} \text{ (eq. S4.1)}$$

The time of all reactions reported herein is 20 min, which is equal to 1200 s. The mols of product (nitric oxide, NO) generated can be determined by using the previously established reaction stoichiometry,[3] which shows that the loss of one mol of GSNO corresponds to the generation of one mol of NO. The ^{1}H NMR method utilized herein measures the concentration of GSNO over time, and hence yields the amount of NO generated at a given time:

$$\text{mols NO} = \text{mols GSNO lost} = ([\mathrm{GSNO}]_i - [\mathrm{GSNO}]_{20\,\mathrm{min}}) \cdot (\text{solution volume}) \text{ (eq. S4.2)}$$

The total number of active sites present in CuBTTri were determined experimentally herein by size–selective, quantitative kinetic poisoning studies. TPPTS poisoning shows that for $MOF_{Filtered}$ samples, 1.3 ± 0.4 % of Cu sites are active for GSNO to NO conversion catalysis. All experiments reported were carried out with a 2:1 ratio of GSNO molecules to total Cu atoms. Therefore, the number of active sites present in a reaction using $MOF_{Filtered}$ samples of CuBTTri can be calculated:

$$\text{mols active sites} = \left(\frac{1.3\pm0.4}{100}\right) \cdot \text{total mols Cu} \text{ (eq. S4.3)}$$

$$\text{total mols Cu} = \frac{\text{initial mols GSNO}}{2} = \frac{([\mathrm{GSNO}]_i \cdot (\text{solution volume}))}{2} \text{ (eq. S4.3)}$$

Hence, combining equations S4.2 and S4.3 yields the necessary components to solve for the TOF_{norm} value defined in equation S4.1.

Calculation of the Exterior Surface Area to Interior Volume Ratio for an Octahedron

Calculation S4.2. The external surface area (ESA) of an octahedron is defined by equation S4.4:

$$\mathrm{ESA} = 2 \cdot \sqrt{3} \cdot \mathrm{a}^2 \text{ (eq. S4.4)}$$

Where "a" is defined as the edge length of the octahedron shown below in Figure S4.17.

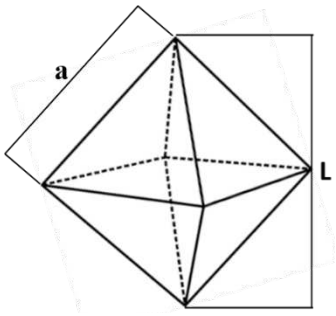

Figure S4.17. A regular octahedron showing edge length (a) and total particle length (L).

The interior volume (IntVol) of a regular octahedron is defined by equation S4.5:

$$\mathrm{IntVol} = \frac{\sqrt{2}}{3}\mathrm{a}^3 \text{ (eq. S4.5)}$$

Where "a" is defined as the edge length of the octahedron shown above in Figure S4.17.

Finally, the ratio between ESA and IntVol can be defined according to equation S4.6 which combines equations S4.4 and S4.5:

$$\frac{\mathrm{ESA}}{\mathrm{IntVol}} = \frac{2 \cdot \sqrt{3} \cdot \mathrm{a}^2}{\frac{\sqrt{2}}{3}\mathrm{a}^3} = \frac{3 \cdot \sqrt{6}}{\mathrm{a}} \text{ (eq. S4.6)}$$

Therefore, the ratio between exterior surface area and interior volume for differently sized sets of MOF particles can be calculated using equation S4.6. Measuring the total length (L) or edge length (a) of particles in SEM images allows for the generation of a size distribution for a set of particles. Equation S4.6 can then be used to calculate the exterior surface area to interior volume ratio for that size distribution. Total length (L) and edge length (a) can be interconverted by equation S4.7:

$$\mathrm{a} = \frac{\sqrt{2} \cdot \mathrm{L}}{2} \text{ (eq. S4.7)}$$

REFERENCES

1. Broniowska, K. A., Diers, A. R. & Hogg, N. S-nitrosoglutathione. *Biochimica et biophysica acta* **1830**, 3173–3181 (2013).

2. Hart, T. W. Some Observations Concerning the S-Nitroso and S-Phenylsulphonyl Derivatives of L-Cysteine and G. *Tetrahedron Letters* **26**, 2013–2016 (1985).

3. Demessence, A., D'Alessandro, D. M., Foo, M. L. & Long, J. R. Strong CO2 Binding in a Water-Stable, Triazolate-Bridged Metal−Organic Framework Functionalized with Ethylenediamine. *Journal of the American Chemical Society* **131**, 8784–8786 (2009).

4. Dincă, M. & Long, J. R. High-Enthalpy Hydrogen Adsorption in Cation-Exchanged Variants of the Microporous Metal−Organic Framework Mn3[(Mn4Cl)3(BTT)8(CH3OH)10]2. *Journal of the American Chemical Society* **129**, 11172–11176 (2007).

5. Tuttle, R. R., Rubin, H. N., Rithner, C. D., Finke, R. G. & Reynolds, M. M. Copper ion vs copper metal–organic framework catalyzed NO release from bioavailable S-Nitrosoglutathione en route to biomedical applications: Direct 1H NMR monitoring in water allowing identification of the distinct, true reaction stoichiometries and thio. *Journal of Inorganic Biochemistry* **199**, 110760 (2019).

APPENDIX IV: SUPPORTING INFORMATION FOR CHAPTER V

CuBTTri Characterization by Powder X-Ray Diffraction

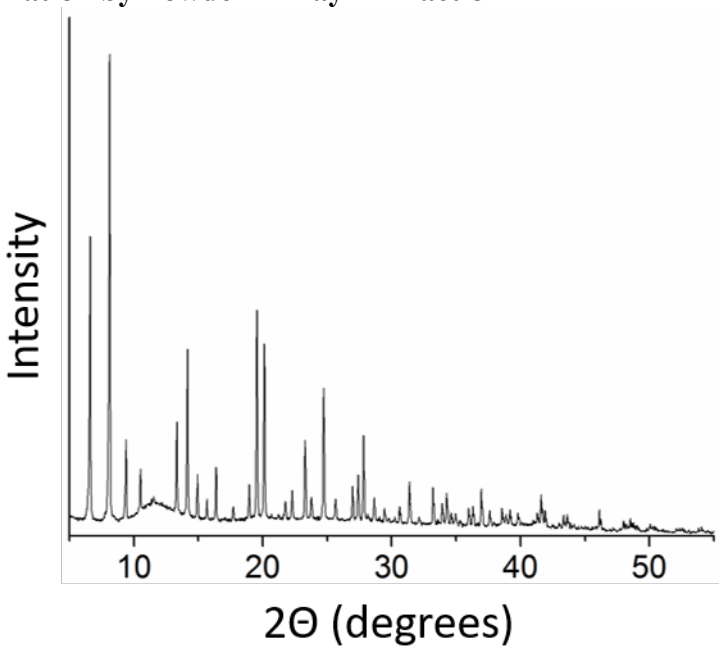

Figure S5.1. Diffraction pattern for CuBTTri as synthesized. The diffraction pattern matches a literature standard.[1–3] The MOF used in this work is from the same batch of MOF synthesized from two previous publications,[4] copyright Elsevier 2019.

Examining -d[GSNO]/dt versus $[GSNO]_i$ at Two Concentrations

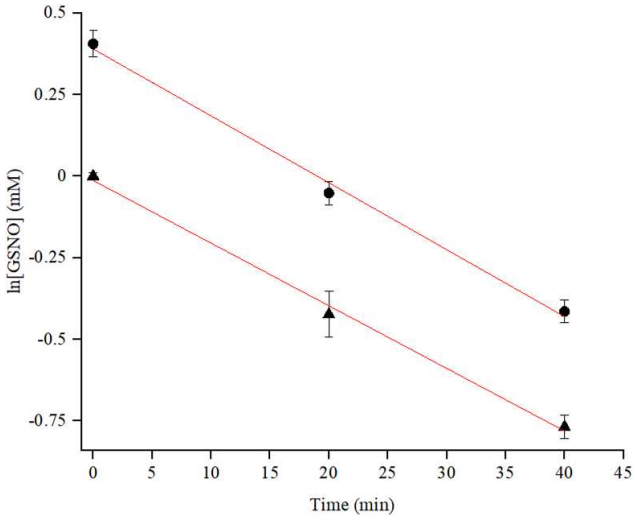

Figure S5.2. First-order plot of $\ln[GSNO]_t$ versus reaction time for experiments where $[GSNO]_i$ = 1 mM (triangles) and $[GSNO]_I$ =. 1.5 mM(circles). The linear trend line for the $[GSNO]_i$ = 1 mM data is fit by the equation $y = ((-1.92 \pm 0.11) \times 10^{-2})\boldsymbol{x} - ((1.32 \pm 2.94) \times 10^{-2})$, $R^2 = 0.99$. The linear trend line for the $[GSNO]_i$ = 1.5 mM data is fit by the equation $y = ((-2.05 \pm 0.13) \times 10^{-2})\boldsymbol{x} + (0.39 \pm 0.04)$, $R^2 = 0.99$. The fact that both plots are linear with identical slopes within experimental error is consistent with the reaction being first order in GSNO in the range of 1 to 1.5 mM and at 20 min (the standard reaction conditions employed in the present studies).

Evidence Against Dissociated Copper from the Framework as the Active Catalyst

The following evidence argues strongly *against* the hypothesis that leached Cu-ions from CuBTTri are the active NO release catalyst and even though that hypothesis is reasonable given: (i) (0.8 ± 0.3)% of the total Cu in CuBTTri samples is lost over a 16 h catalysis experiment;[4,5] and (ii) (1.3 ± 0.4)% of the total Cu in the CuBTTri samples used for catalysis are active.[5] In short, even though these two numbers overlap within 1 sigma error bars, the following list argues compellingly against the hypothesis that solvated Cu^{2+} ions "leached"[1] from the CuBTTri framework) being the active catalyst.[2]

1) The supernatant isolated from a CuBTTri catalyzed NO release experiment is not catalytically active for further NO release. Therefore, a homogeneous Cu containing species, generated during catalysis, that remains present in the reaction supernatant post reaction cannot be the kinetically dominant Cu species for NO-release catalysis.[4,6,7]

[1] An interesting point here is that very rough, back-of-the-envelope thermochemical calculations (described below) argue that the dissociation constant ($K_{eq,diss}$) for even the weakest bound, nominally 3-coordinate Cu surface sites with two Cu-N dative bonds and one Cu-Cl dative bond should be on the order of ~10^{-33} at room temperature. This implies but does not prove that the ~0.8% of "leached" Cu ions observed might well be adventitious Cu ions attached to the Cu-MOF surface. The details of this crude calculation are that: $K_{eq,diss}$ was calculated using the equation $K_{eq,diss}$ = e^(–ΔG/RT), where T is the temperature of the reaction (298.15K), R is the constant 8.314 J mol^{-1} K^{-1}, and ΔG is the Gibbs free energy change of the Cu site dissociation. The ΔG value was calculated under the assumption that dissociation of the Cu site from CuBTTri involves breaking two Cu-N bonds (estimated B.D.E. 35 kcal mol^{-1} each), breaking one Cu-Cl bond (estimated B.D.E. 55 kcal mol^{-1}), and gaining four net Cu-OH_2 bonds (estimated B.D.E. 20 kcal mol^{-1}) because of the dissociation.[15] Entropy has been neglected in this crude, back-of-the-envelope calculation.

[2] When no GSH beyond the impurity present in GSNO (from the synthesis) is added to the reaction, 10% loss of GSNO is observed over 16 h. It is conceivable that this loss of GSNO in the absence of added GSH could be the result of" leached"[1] Cu ion catalyzed NO generation. However, given the evidence discussed above (and the fact that the stoichiometry and rate law were measured under conditions where [GSH] is in 10^2 excess of any leached Cu), solvated Cu ion catalysis as the kinetically dominant mechanistic pathway cannot be the kinetically dominant catalyst in the present work, at least not under the conditions where the primary kinetics and other main evidence was obtained.

2) The level of [GSH] (0.5 to 1 mM) present in experiments where the stoichiometry was measured *does not* poison GSNO to NO conversion catalysis by CuBTTri. However, if leached Cu^{2+} ions (present at ~0.8% of total Cu) were the solve active catalyst, the literature indicates that this ~10^2 ratio of [GSH]/[leached Cu^{2+}] would have completely poisoned catalysis because even a 1:1 ratio of [GSH]/[Cu^{2+}] has been observed to poison GSNO to NO conversion catalysis.[4] It follows that leached Cu^{2+} ions cannot be the basis for the observed catalysis.

3) If leached Cu ions (present at ~1% of total Cu) were the *sole catalyst*, then previously reported poisoning by TPPTS to form, for example, at most a hypothetical "$Cu(TPPTS)_{2\text{-}3}^{2+}$" species, then the [TPPTS]/Cu_{total} ratio given by the x-intercept of that kinetic poisoning plot would be ~0.02-0.03, not the observed value of 0.013.[5] In short, the TPPTS selective poisoning results match the expected results nearly exactly for external surface Cu sites in CuBTTri as the active sites, but are not in quantitative agreement with the hypothesis of leached Cu ions as the sole, kinetically dominant catalyst.

4) Were Cu^{2+} ions the *sole catalyst*, then FT-IR analysis of the CuBTTri particles poisoned by KCN would be expected to show Cu to CN binding ratios other than the 1Cu:1CN and 1Cu:3CN ratios observed experimentally. Hypothetically, a "$Cu(CN)_4^{2-}$" or "$Cu(CN)_2$" species would be expected in the IR spectrum. However, the experimental data are that the *only* vibrational modes observed are $Cu(CN)_3$ at 2093 cm^{-1} and $Cu(CN)_1$ at 2190 cm^{-1},[8–10] precisely those binding ratios and vibrational modes predicted by the idealized, metal-terminated CuBTTri crystal structure.

Derivation S5.1: the Rate Law for the Proposed Cu^{II} to Cu^{III} Mechanism

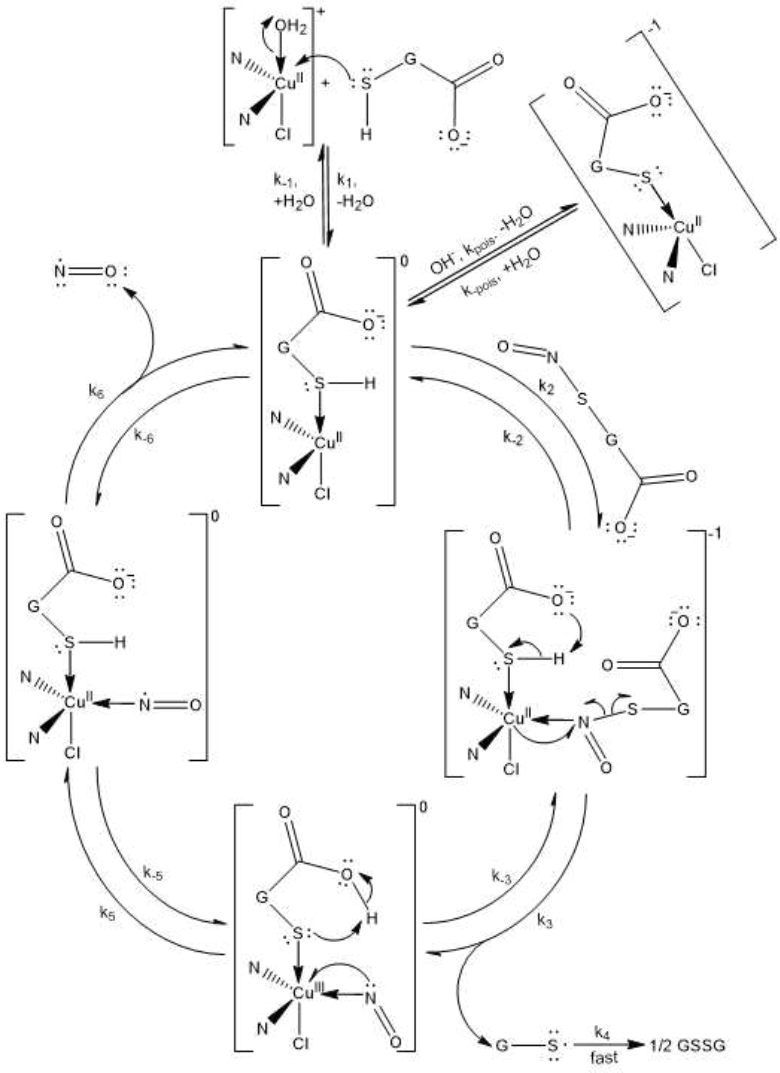

Figure 5.3. Proposed catalytic cycle for GSNO to NO conversion catalyzed by CuBTTri in water reproduced from the main text in Chapter V. The elementary steps, associated rate constants, and equilibrium constants shown in this mechanism will be used to derive the associated rate law, as shown in the derivation below.

$$2GSNO_{(aq)} + 0.3GSH_{(aq)} + CuBTTri_{(s)} \longrightarrow GSSG_{(aq)} + 2NO_{(g)} + [(0.3GSH)\text{-}CuBTTri]_{(s)}$$

Step 1: The experimentally observed rate law at pH = 4.5 is given below in equation S5.1. The derived rate law at pH = 4.5 will match equation S5.1.

$$\frac{-d[GSNO]}{dt} = k'_{obs}[GSNO]\left[Cu_{surface}\right][GSH]^{1\rightarrow 0} \quad (eq.S5.1)$$

Step 2: The experimentally observed rate law at pH > 4.5 when the reaction is saturated in [GSH(COO$^-$)] is given below in equation S5.2. The derived rate law at pH = 9 will match equation S5.2.

$$\frac{-d[GSNO]}{dt} = k_{obs}\frac{[GSNO][Cu_{surface}][GSH(COO^-)]^0}{[OH^-]^{1\rightarrow 0}} \ (eq.S5.2)$$

Step 3: First, deriving the rate law at pH = 4.5 requires that one write the necessary expression for total Cu ([Cu]$_T$). The turnover limiting step (t.l.s.) is proposed to be step 3 in Figure 5.2 above, therefore any Cu species which appear after step 3 will not appear in the expression for [Cu]$_T$, as shown below in equation S5.3. In equation S5.3 the terms for each Cu containing species are defined as follows: Cu^{II}(OH)$_2$ represents the pre-active Cu site before GSH coordination, Cu^{II}(GSH(COO$^-$)) represents the Cu site formed in step 1 of Figure 5.2, Cu^{II}(GS$^-$) represents the poisoned site in Figure 5.2 formed upon deprotonation of the thiol proton in GSH bound to Cu^{II} by hydroxide, and [A] represents the key reaction intermediate formed in step 2 of Figure 5.2 which then undergoes PCET in the t.l.s. (step 3 of Figure 5.2) to form Cu^{III} and release NO.

$$[Cu]_T = [Cu^{II}(OH_2)] + [Cu^{II}(GSH(COO^-)] + [Cu^{II}(GS^-)] + [A] \ (eq.S5.3)$$

Step 4: When the reaction is run at pH = 4.5, the expression for [Cu]$_T$ simplifies to equation S5.4 shown below. The concentration of the poisoned Cu^{II} site at pH = 4.5 is negligible in comparison to Cu^{II}(OH$_2$) and Cu^{II}(GSH(COO$^-$)). Additionally, the term for [A] in equation S5.4 can be discounted because no saturation kinetics are observed for [GSNO], which indicates that A (the intermediate formed in step 2 of Figure 5.2) does not build up after GSNO coordinates to Cu^{II}(GSH(COO$^-$)).

$$[Cu]_{T,pH=4.5} = [Cu^{II}(OH_2)] + [Cu^{II}(GSH(COO^-))] \ (eq.S5.4)$$

Step 5: The relevant equilibrium constants for the Cu containing species in equation S4 are given below in equations S5.5 and S5.6.

$$K_{eq,1} = \frac{[Cu^{II}(GSH(COO^-))]}{[Cu^{II}(OH_2)][GSH(COO^-)]} \rightarrow [Cu^{II}(OH_2)] = \frac{[Cu^{II}(GSH(COO^-))]}{K_{eq,1}[GSH(COO^-)]} \ (eq.S5.5)$$

$$K_{eq,2} = \frac{[A]}{[Cu^{II}(GSH(COO^-))][GSNO]} \rightarrow [Cu^{II}(GSH(COO^-))] = \frac{[A]}{K_{eq,2}[GSNO]} \ (eq.S5.6)$$

Step 6: Using the t.l.s. one can express the rate law for Figure 5.2 using equation S5.7 below.

$$-\frac{d[GSNO]}{dt} = k_3[A] \ (eq.S5.7)$$

Step 7: The concentration of $Cu^{II}(OH_2)$ can be expressed in terms of [A] inequation S5.8 below using equations S5.5 and S5.6.

$$[Cu^{II}(OH_2)] = \frac{[A]}{K_{eq,1}K_{eq,2}[GSH(COO^-)][GSNO]} \ (eq.S5.8)$$

Step 8: The expression for $[Cu]_T$ in equation S5.3 can be written in terms of [A] using equations S5.6 and S5.8, as shown below in equation S5.9. Equation S5.9 can then be simplified to equation S5.10, and then one can solve for [A] as shown in equation S5.11.

$$[Cu]_{T,pH=4.5} = \frac{[A]}{K_{eq,1}K_{eq,2}[GSH(COO^-)][GSNO]} + \frac{[A]}{K_{eq,2}[GSNO]} \ (eq.S5.9)$$

$$[Cu]_{T,pH=4.5} = \frac{[A]}{K_{eq,2}[GSNO]}\left(\frac{1}{K_{eq,1}[GSH(COO^-)]} + 1\right) \ (eq.S5.10)$$

$$[A] = \frac{K_{eq,2}[Cu]_T[GSNO]}{\left(\frac{1}{K_{eq,1}[GSH(COO^-)]} + 1\right)} \ (eq.S11)$$

Step 9: The expression for [A] given in equation S11 can be substituted into equation S5.7 to give the rate law shown below in equation S5.12.

$$-\frac{d[GSNO]}{dt} = \frac{k_3K_{eq,2}[Cu]_T[GSNO]}{\left(\frac{1}{K_{eq,1}[GSH(COO^-)]} + 1\right)} \ (eq.S5.12)$$

Step 10: When the value of [GSH(COO$^-$)] is low, then $1/K_{eq,1}$[GSH(COO$^-$)] >> 1, and the denominator of equation S5.12 simplifies to $1/K_{eq,1}$[GSH(COO$^-$)]. Therefore, when [GSH(COO$^-$)] is low, the derived rate law simplifies to the expression shown below in equation S5.13.

$$-\frac{d[GSNO]}{dt}_{pH=4.5} = k_3 K_{eq,1} K_{eq,2} [Cu]_T [GSNO][GSH(COO)^-] \ (eq.S5.13)$$

Step 11: When the value of [GSH(COO$^-$)] is increased, then $1/K_{eq,1}$[GSH(COO$^-$)] << 1, and the denominator of equation S5.12 simplifies to 1. Therefore, when [GSH(COO$^-$)] is increased, the derived rate law simplifies to the expression shown below in equation S5.14.

$$-\frac{d[GSNO]}{dt}_{pH=4.5} = k_3 K_{eq,2} [Cu]_T [GSNO] \ (eq.S5.14)$$

Step 12: Combining the rate laws derived in equations S5.13 and S5.14 results in the experimentally observed rate law at pH = 4.5 (shown in equation S5.1). First order dependence in [GSH(COO$^-$)] observed experimentally is confirmed by equation S5.13, while the saturation observed experimentally in [GSH(COO$^-$)] is confirmed by equation S5.14. Additionally, the k_{obs}' given in equation S5.1 is shown to be a composite of k_3, $K_{eq,1}$, and $K_{eq,2}$.

Step 13: When the reaction is run at pH > 4.5 and where saturation in [GSH(COO$^-$)] is observed (as was done experimentally), the expression for $[Cu]_T$ simplifies to equation S5.15 as shown below. When the reaction is saturated in [GSH(COO$^-$)], the amount of $Cu^{II}(OH_2)$ present can be ignored because the equilibrium of step 1 in Figure 5.2 is dominated by the reaction products. As the pH of the reaction is increased, the proportion of the poisoned Cu^{II} site must be accounted for. However, [A] can still be discounted at alkaline pH for the same reason as discussed above.

$$[Cu]_{T,pH>4.5} = [Cu^{II}(GSH(COO^-))] + [Cu^{II}(GS^-)] \ (eq.S5.15)$$

Step 14: The relevant equilibrium constants for $Cu^{II}(OH_2)$ and $Cu^{II}(GSH(COO^-))$ are given above in equations S5.5 and S5.6. The relevant equilibrium constant for $Cu^{II}(GS^-)$ is given below in equation S5.16.

$$K_{eq,pois} = \frac{[Cu^{II}(GS^-)]}{[Cu^{II}(GSH(COO^-))][OH^-]} \rightarrow [Cu^{II}(GS^-)]$$

$$= K_{eq,pois}[Cu^{II}(GSH(COO^-))][OH^-] \; (eq.S5.16)$$

Step 15: The concentration of $Cu^{II}(GS^-)$ can be expressed in terms of [A] using equations S5.16 and S5.6, as shown below in equation S5.17.

$$[Cu^{II}(GS^-)] = \frac{[A]K_{eq,pois}[OH^-]}{K_{eq,2}[GSNO]} \; (eq.S5.17)$$

Step 16: Combining equations S5.15, S5.16, and S5.6, one can express $[Cu]_T$ at pH > 4.5 in terms of [A] as shown in equation S5.18 below. Equation S5.18 can be simplified to give equation S5.19, and then [A] can be solved for at pH > 4.5 (as shown in equation S5.20).

$$[Cu]_{T,pH>4.5} = \frac{[A]}{K_{eq,2}[GSNO]} + \frac{[A]K_{eq,pois}[OH^-]}{K_{eq,2}[GSNO]} \; (eq.S5.18)$$

$$[Cu]_{T,pH>4.5} = \frac{[A]}{K_{eq,2}[GSNO]}\left(1 + K_{eq,pois}[OH^-]\right) \; (eq.S5.19)$$

$$[A] = \frac{K_{eq,2}[Cu]_T[GSNO]}{\left(1 + K_{eq,pois}[OH^-]\right)} \; (eq.S5.20)$$

Step 17: Substituting the term for [A] in equation S5.20 into equation S5.7 yields the derived rate law below in equation S5.21 for pH > 4.5.

$$\frac{-d[GSNO]}{dt}_{pH>4.5} = \frac{k_3K_{eq,2}[Cu]_T[GSNO]}{\left(1 + K_{eq,pois}[OH^-]\right)} \; (eq.S5.21)$$

Step 18: When $K_{eq,pois}[OH^-] << 1$, the expression in equation S5.21 simplifies to the derived rate law shown below in equation S5.22.

$$\frac{-d[GSNO]}{dt}_{pH>4.5} = \frac{k_3 K_{eq,2}[Cu]_T[GSNO]}{(1)} \quad (eq.S5.22)$$

Step 18: When $K_{eq,pois}[OH^-] >> 1$ as reaction pH increases, the expression in equation S5.21 simplifies to the derived rate law shown below in equation S5.23.

$$\frac{-d[GSNO]}{dt}_{pH>4.5} = \frac{k_3 K_{eq,2}[Cu]_T[GSNO]}{\left(K_{eq,pois}[OH^-]\right)} \quad (eq.S5.23)$$

Step 19: Combining the rate laws derived in equations S5.22 and S5.23 results in the experimentally observed rate law at pH > 4.5 (shown in equation S5.2). The inverse dependence in $[OH^-]$ (observed experimentally as $\log[OH^-]$) is confirmed by equation S5.23, while the saturation observed experimentally in $\log[OH^-]$ is confirmed by equation S5.22. Additionally, the k_{obs} given in equation S5.2 is shown to be a composite of k_3, $K_{eq,2}$, and $K_{eq,pois}$. Along with the analysis given in step 12 of this derivation, it has been demonstrated that the derived rate law for the mechanism shown in Figure 5.2 matches exactly the experimentally observed rate law at pH = 4.5 and pH > 4.5.

Estimation of Thermodynamic/Kinetic Parameters for Figure 5.2 in Chapter V

Based on the rate law derivation presented above in this Supporting Information and the data below in Figures S5.3 and S5.4, one can estimate both the value of $K_{eq,1}$ and $k_3*K_{eq,2}$ for Figure 5.2.

Step 1: When the rate law is 1st order in [GSH] at pH = 4.5 (Figure S5.4) the corresponding rate law is equation S5.13 in the derivation above and reproduced below.

$$-\frac{d[GSNO]}{dt}_{pH=4.5} = k_3 K_{eq,1} K_{eq,2} [Cu]_T [GSNO][GSH(COO)^-] \ (eq.S5.13)$$

According to equation S5.13, when the reaction is 1st order in [GSH], the slope of the line in Figure S5.4 should be equal to $k_3*K_{eq,1}*K_{eq,2}*[Cu]_T*[GSNO]$. Therefore, the value for $k_3*K_{eq,1}*K_{eq,2}*[Cu]_T*[GSNO]$ in Figure S5.4 is equal to $(1.76 \pm 0.1) \times 10^{-3}$.

Step 2: When the rate law is 0th order in [GSH] at pH = 4.5 (Figure S5.3) the corresponding rate law is equation S5.14 in the derivation above and reproduced below.

$$-\frac{d[GSNO]}{dt}_{pH=4.5} = k_3 K_{eq,2} [Cu]_T [GSNO] \ (eq.S5.14)$$

According to equation S5.14, when the reaction is 0th order in [GSH], -d[GSNO]/dt is a constant value equal to $k_3*K_{eq,2}*[Cu]_T*[GSNO]$. Therefore, the value for $k_3*K_{eq,2}*[Cu]_T*[GSNO]$ in Figure S5.3 is $(2.80 \pm 0.8) \times 10^{-4}$ (which is equal to the maximum rate observed in Figure S5.3).

Step 3: One can solve for the apparent value of $K_{eq,1}$ using the values for $k_3*K_{eq,1}*K_{eq,2}*[Cu]_T*[GSNO]$ and $k_3*K_{eq,2}*[Cu]_T*[GSNO]$ determined above from Figures S5.3 and S5.4 (shown below in equation S5.24).

$$\frac{k_3 * K_{eq,1} * K_{eq,2} * [Cu]_T * [GSNO]}{k_3 * K_{eq,2} * [Cu]_T * [GSNO]} = \frac{1.76 \times 10^{-3}}{2.8 \times 10^{-4}} \approx 6.1 \ (eq.S5.24)$$

Equation S5.24 shows that the apparent value for $K_{eq,1}$ calculated from the data in Figures S5.3 and S5.4 is equal to approximately 6.1 (summarized in Table 5.2 of Chapter V).

Step 4: One can solve for the apparent value of $k_3*K_{eq,2}$ using the fact that the experiments which generated the data in Figures S5.3 and S5.4 were carried out at $[Cu]_T$ = 0.5 mM and [GSNO] = 1 mM. Equations S5.25 and S5.26 below shows how the value for $k_3*K_{eq,2}*[Cu]_T*[GSNO]$ determined from Figure S5.3 can be used to determine $k_3*K_{eq,2}$.

$$k_3 * K_{eq,2} * [Cu]_T * [GSNO] = (2.80 \pm 0.8) \times 10^{-4} \; (eq.S5.25)$$

$$k_3 * K_{eq,2} = \frac{(2.80 \pm 0.08) \times 10^{-4}}{(0.5) * 1} \approx (5.6 \pm 1.6) \times 10^{-4} \; (eq.S5.26)$$

Therefore, the value for $k_3*K_{eq,2}$ is equal to approximately (5.6 ± 1.6) x 10^{-4} (summarized in Table 5.2 of Chapter V). The estimate for $k*K_{eq,2}$ given in equation S5.26 is reasonable given the fact that k_3 is expected to be small, as step 3 is hypothesized to be the t.l.s. in Figure 5.2.

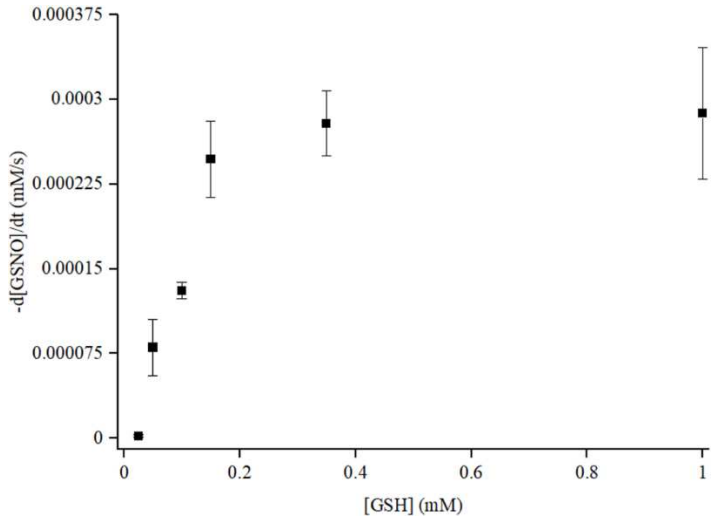

Figure S5.4. A reproduction of Figure 5.4 from Chapter V. The portion of the plot where the reaction is 1st order in [GSH] (shown in greater detail below in Figure S4) can be used to estimate $k_3*K_{eq,1}*K_{eq,2}$. The portion of the plot where the reaction is 0th order in [GSH] can be used to estimate $k_3*K_{eq,1}$. Together, these estimates yield an apparent value for the reaction parameters $K_{eq,1}$ and $k_3*K_{eq,2}$.

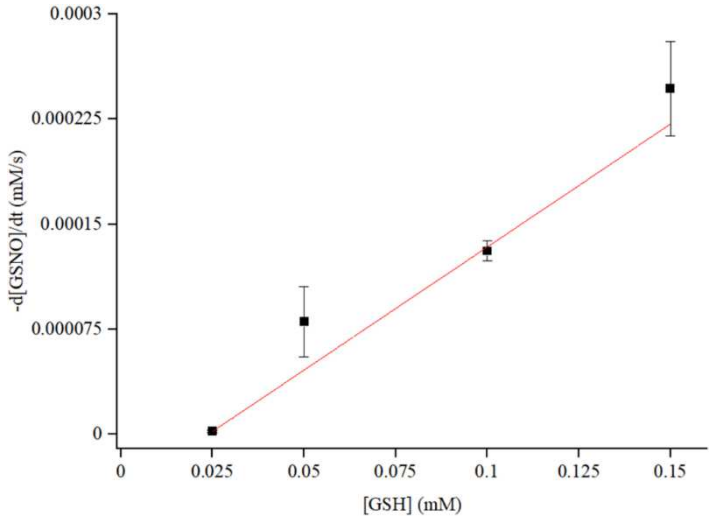

Figure S5.5. A reproduction of Figure 5.5 from Chapter V. The line is fit by the equation y = $((1.76 \pm 0.1) \times 10^{-3})\boldsymbol{x} - ((4.17 \pm 0.29) \times 10^{-5})$, $R^2 = 0.99$. The data in this plot can be used to calculate an estimate for $k_3 * K_{eq,1} * K_{eq,2}$.

Based on the rate law derivation presented above in this Supporting Information and the data below in Figures S5.5 and S5.6, one can generate a second estimate for $k_3 * K_{eq,2}$ and an estimate for $K_{eq,pois}$ for Figure 5.2.

Step 1: Based on the derivation given earlier in this Supporting Information, the derived rate law when pH > 4.5 (up to pH = 9) and the reaction is saturated in [GSH] (the conditions under which the data in Figures S5.5-S5.6 were collected) is given by equation S5.21 (which is reproduced below for the convenience of the reader).

$$\left.\frac{-d[GSNO]}{dt}\right|_{pH>4.5} = \frac{k_3 K_{eq,2}[Cu]_T[GSNO]}{\left(1 + K_{eq,pois}[OH^-]\right)} \quad (eq.S5.21)$$

Step 2: Equation S5.21 can be written in the more general form below (equation S5.27).

$$y = \frac{A}{(1 + Bx)} \quad (eq.S5.27)$$

Step 3: Using non-linear least squares to fit the data in Figures S5.5 and S5.6 using equation S5.27, one can generate estimates for A and B. It is important to note here that the data plotted in Figures S5.5 and S5.6 are identical and the *only* difference between Figures S5.5 versus S5.6 is that the x-

axis in Figure S5.5 is presented on a $\log_{10}$ scale while the x-axis in Figure S5.6 is presented on a traditional numerical scale. The data was presented in the two separate ways because: (i) presenting the x-axis on a $\log_{10}$ scale in Figure S5.5 is a clearer visual representation of the data, (ii) to check the fit of one data set using two different graphing methods, and (iii) Figure S5.5 illustrates the wide range (~4.5 orders of magnitude) over which $[OH^-]$ was varied experimentally.

Step 4: Fits of the data in Figures S5.5-S5.6 yield estimates of A = (2.5 ± 0.1) x 10^{-4} s^{-1} and B = (2.34 ± 0.01) x 10^8 (which is unitless because the parameter B represents an equilibrium constant). Therefore, the data suggest that $k_3*K_{eq,2}*[Cu]_T*[GSNO]$ = (2.51 ± 0.1) x 10^{-4} s^{-1} and $K_{eq,pois}$ = (2.34 ± 0.01) x 10^8.

There are two key conclusions one can draw from the second set of estimates for A and B. First, values for $k_3*K_{eq,2}*[Cu]_T*[GSNO]$ determined from two separate data sets (Figures S5.3-S5.4 and Figures S5.5-S5.6) overlap within 1 sigma. Therefore, the estimate for $k_3*K_{eq,2}$ given in equation S5.26 above is supported by the data in Figures S5.5-S5.6. Second, the value obtained for $K_{eq,pois}$ ((2.34 ± 0.01) x 10^8) is reasonable given the fact that the deprotonation shown in the poisoning step in Figure 5.2 is expected to be thermodynamically favorable.

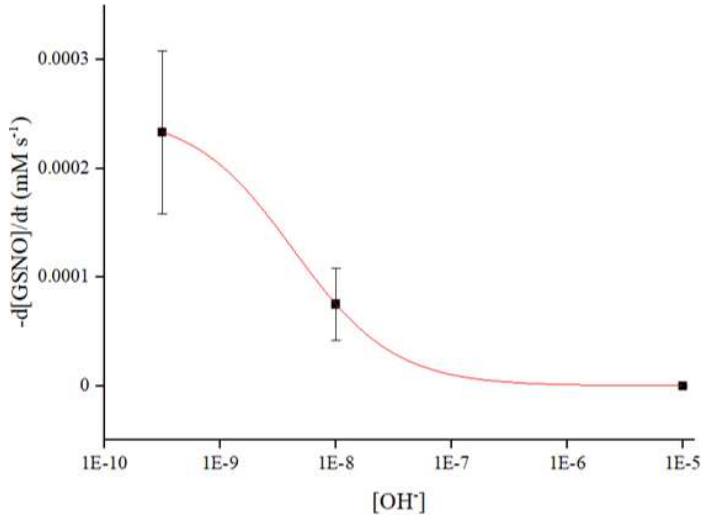

Figure S5.6. A reproduction of Figure 5.7 in Chapter V with a non-linear least-squares curve fit included. The x-axis in this plot has been presented on a $\log_{10}$ scale to reflect that $[OH^-]$ was varied over several orders of magnitude and for visual clarity. The $[OH^-]$ values for each data point are

the true [OH^-] levels used experimentally and are *not* log[OH^-]. The data has been fit using non-linear least squares to the equation y=A/(1+Bx) and using a Levenberg-Marquardt iteration algorithm. Values for A and B are estimated to be: A = (2.51 ± 0.1) x 10^{-4} s^{-1} and B = (2.34 ± 0.01) x 10^8. The estimates for A and B did not change significantly if the data points were weighted equally or weighted based upon their relative values and standard deviations. The values for A and B were not constrained when fitting the data.

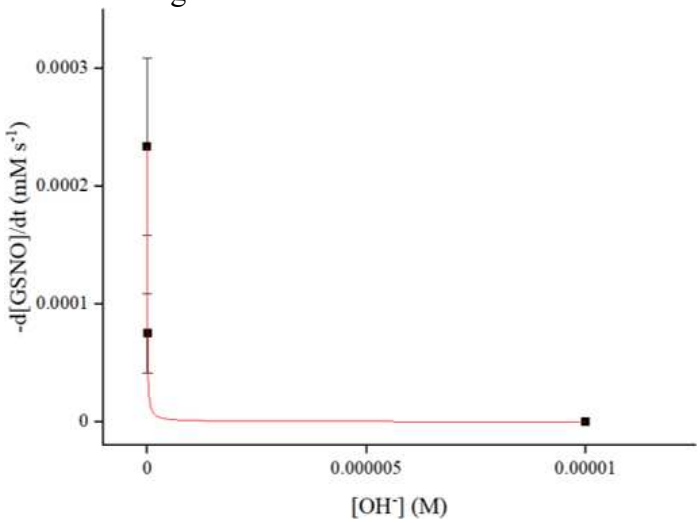

Figure S5.7. Plotting the same data as presented in Figure S5.5, but instead in this case the x-axis is presented on a traditional numerical rather than a log scale. The data in this plot was fit using the identical non-linear least squares method as for the data in Figure S5.6, while fitting to the equation y=A/(1+Bx). The values for A and B are estimated to be: A = (2.50 ± 0.1) x 10^{-4} s^{-1} and B = (2.34 ± 0.01) x 10^8.

Plausible, Alternative Cu^{I} Mechanistic Hypothesis

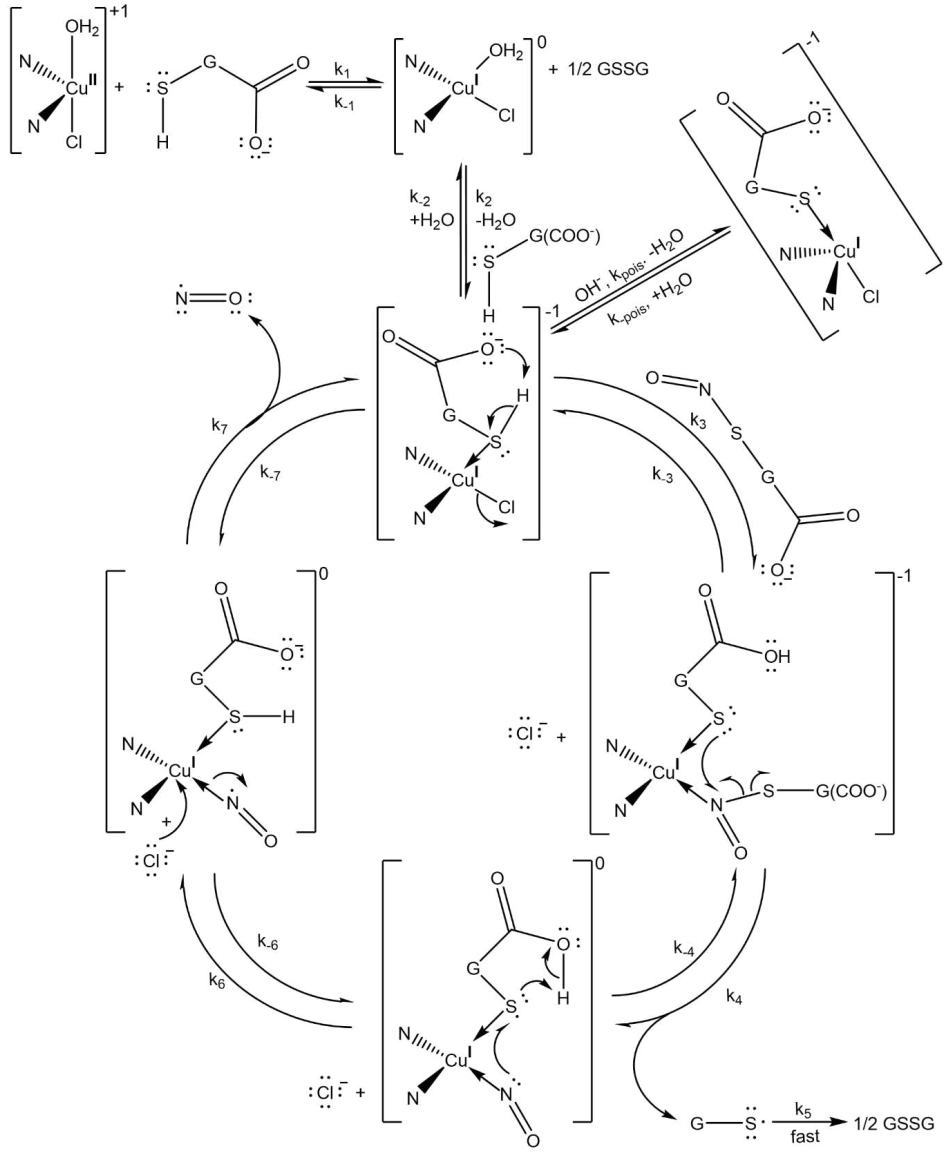

Figure S5.8. A PCET, "limiting" Cu^{I} hypothesis where the active Cu site remains formally +1 throughout the catalytic cycle. The mechanistic hypothesis below is the Cu^{I} analogue to Figure 5.3 in Chapter V, where S-N bond homolysis is driven by electron transfer between ligand-based orbitals with Cu^{I} acting as a conduit for electron transfer. Resonance structures of Figure S5.1 can be drawn with inner-sphere electron transfer between Cu^{I} and GSNO/GSH, but the "limiting", all Cu^{I} case is presented below. Future computational studies will address the question of, "where are the electrons during the catalytic cycle?" The oxidation of GSH to GSSG in step 1 to generate Cu^{I} in this mechanistic hypothesis does not violate the observed reaction stoichiometry.[4] The Cu active sites are present at ~1.3% of $[Cu]_T$ while $[GSH]_i$ and $[Cu]_T$ in kinetics experiments were set equal.[5] Therefore, the small amount of GSSG generated from oxidized GSH in Figure S5.1 is not detectable via the analytical techniques used data collection (UV-VIS and ^{1}H NMR spectroscopies). Figure S5.1 is the only Cu^{I}-based hypothesis where the derived and experimental rate laws match.

Disproven Mechanistic Hypotheses and Analysis

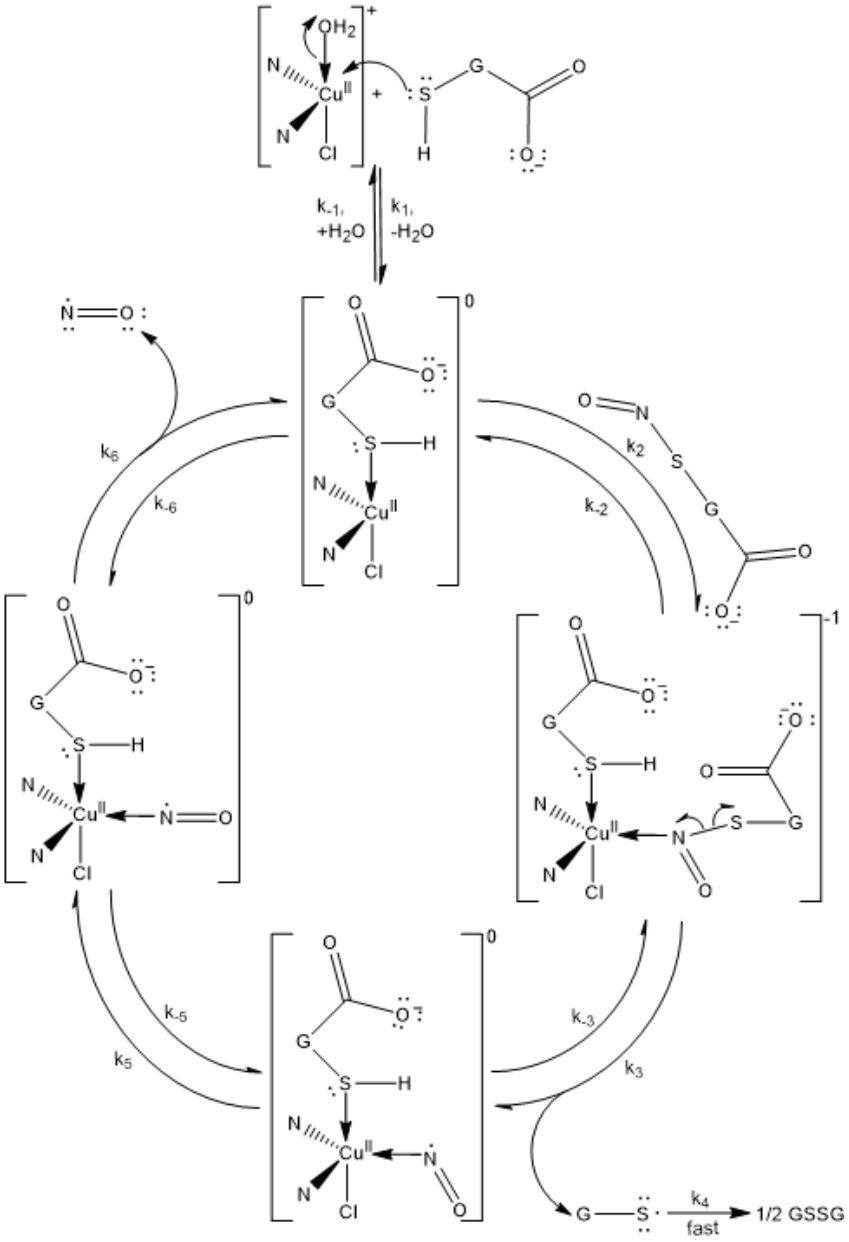

Figure S5.9. One alternative mechanistic hypothesis is Cu^{II} Lewis acid catalyzed GSNO to NO conversion as shown in the following mechanism. However, this mechanism is inconsistent with the data (as summarized in Table 5.1 of Chapter V). Specifically: (i) first, the derived rate law for Figure S5.2 does not match the experimentally observed rate law in that it predicts *no dependence* on pH while a strong dependence on pH is observed experimentally (Figure 5.7 of Chapter V); second (ii) GSH is a mere spectator in the reaction—and by its coordination would make the Cu^{II} a worse Lewis acid, so should slow not accelerate the reaction; and (iii) this mechanism doesn't provide a convincing driving force for S-N bond homolysis, through-bond, inductive effects being the explanation for S-N bond homolysis in GSNO in this conceivable mechanism. In short, the hypothesis that Figure S5.2 is the kinetically dominant mechanism is not consistent with the experimental observations and, hence, is considered disproved.

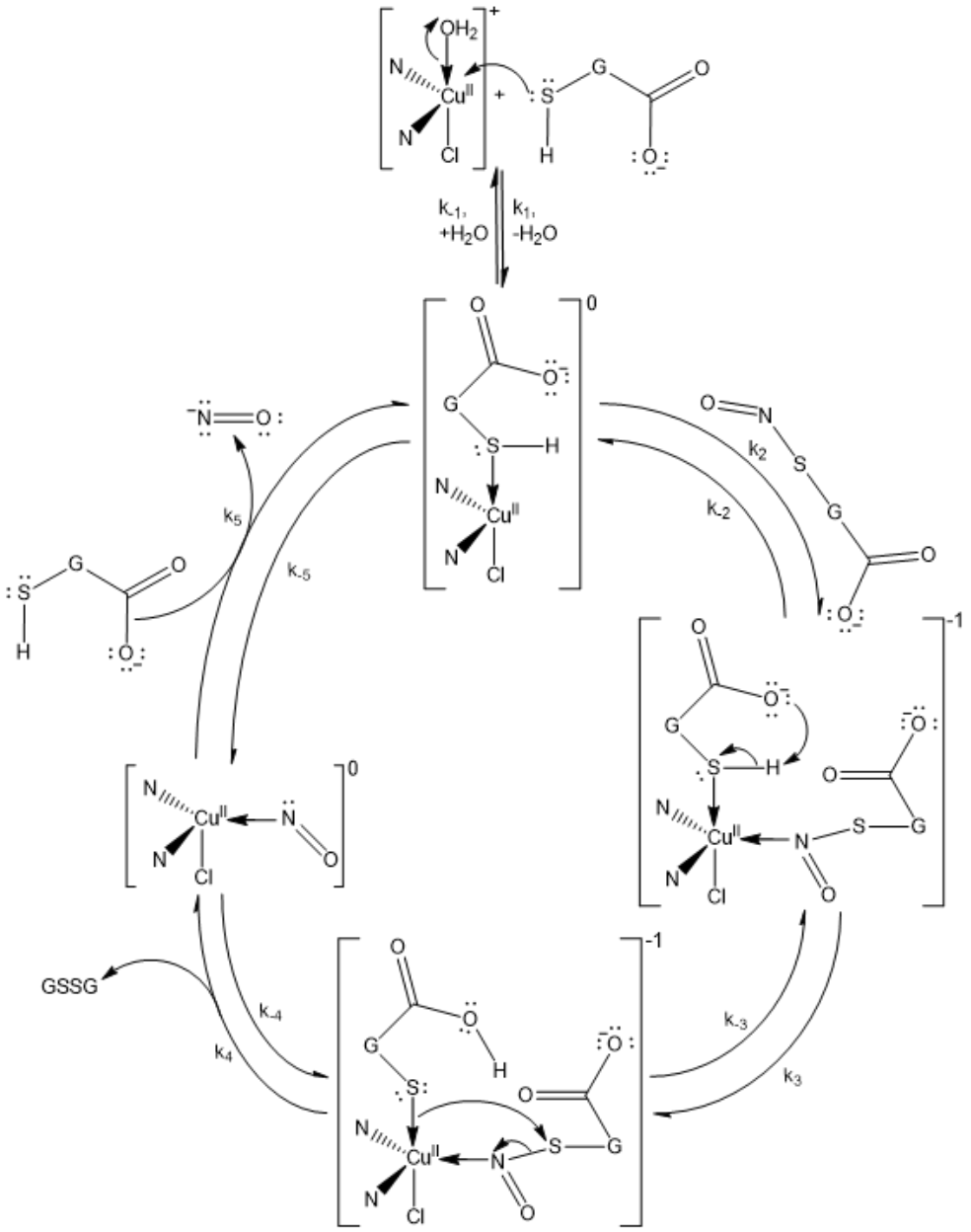

Figure S5.10. A second alternative mechanistic hypothesis is Cu^{II} Lewis acid catalyzed GSNO to NO conversion via thiol coupling and employing an intramolecular deprotonation analogous to Figure 5.2 of Chapter V. However, this mechanistic hypothesis is disproven by: (i) it predicts that GSSG is formed from both GSH and GSNO while the experimentally determined balanced reaction shows that GSSG is formed from just GSNO;[4] and (ii) this mechanism yields $[NO]^-$ as a reaction product while the observed product is •NO.

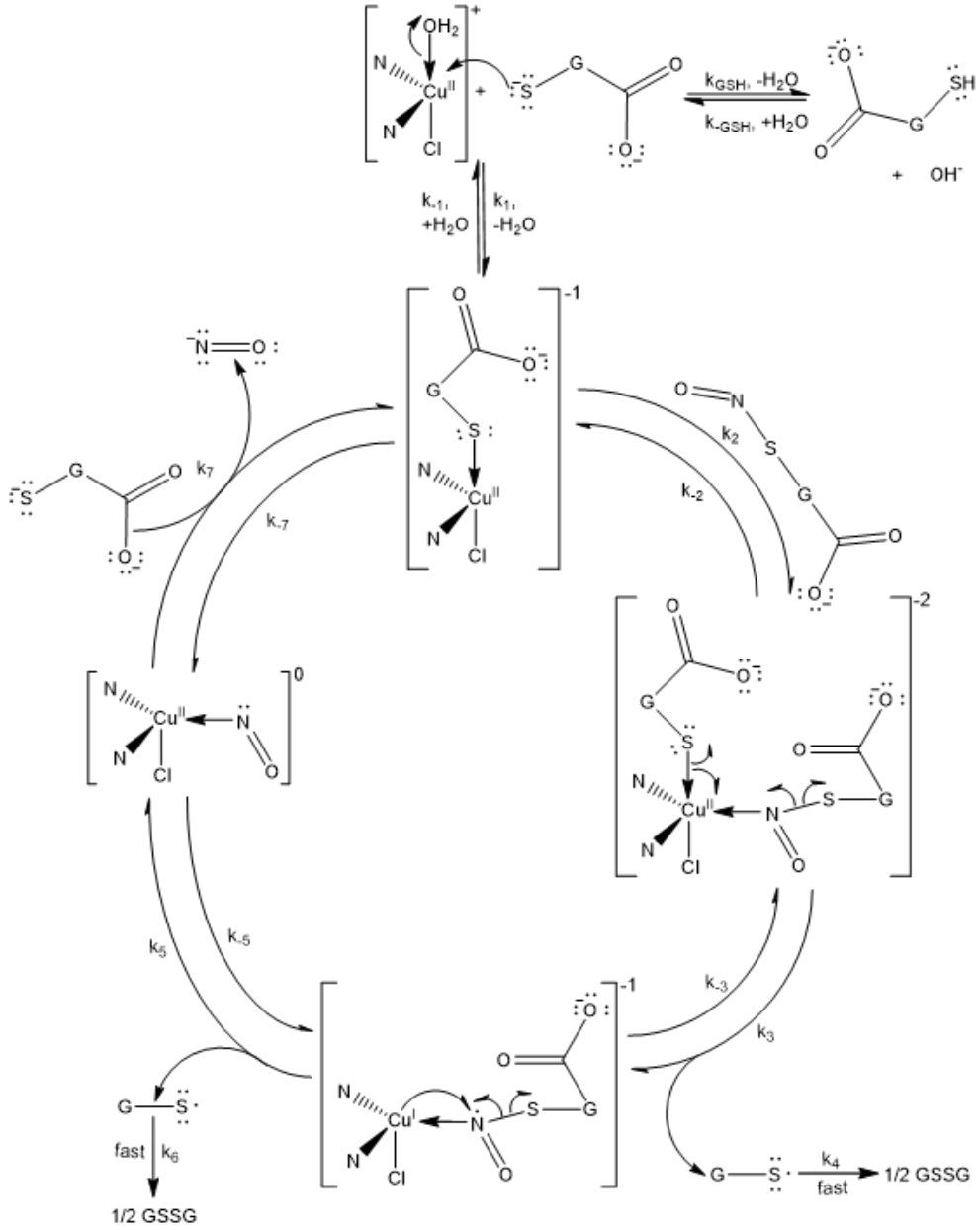

Figure S5.11. A third alternative mechanistic hypothesis is Cu^{II} *to* Cu^{I} redox catalysis where GS^- is the reductant. This mechanism is disproven by two observations: (i) Figure S5.4 involves significant formation of GSSG from GSH, which does not match the experimental stoichiometry (as discussed in Figure S5.3 above)[4] and, (ii) the expected rate law for Figure S5.4 is first order in $[OH^-]$, the opposite of the inverse first-order dependence observed experimentally, $[OH^-]^{-1}$ (Figure 5.7, Chapter V).

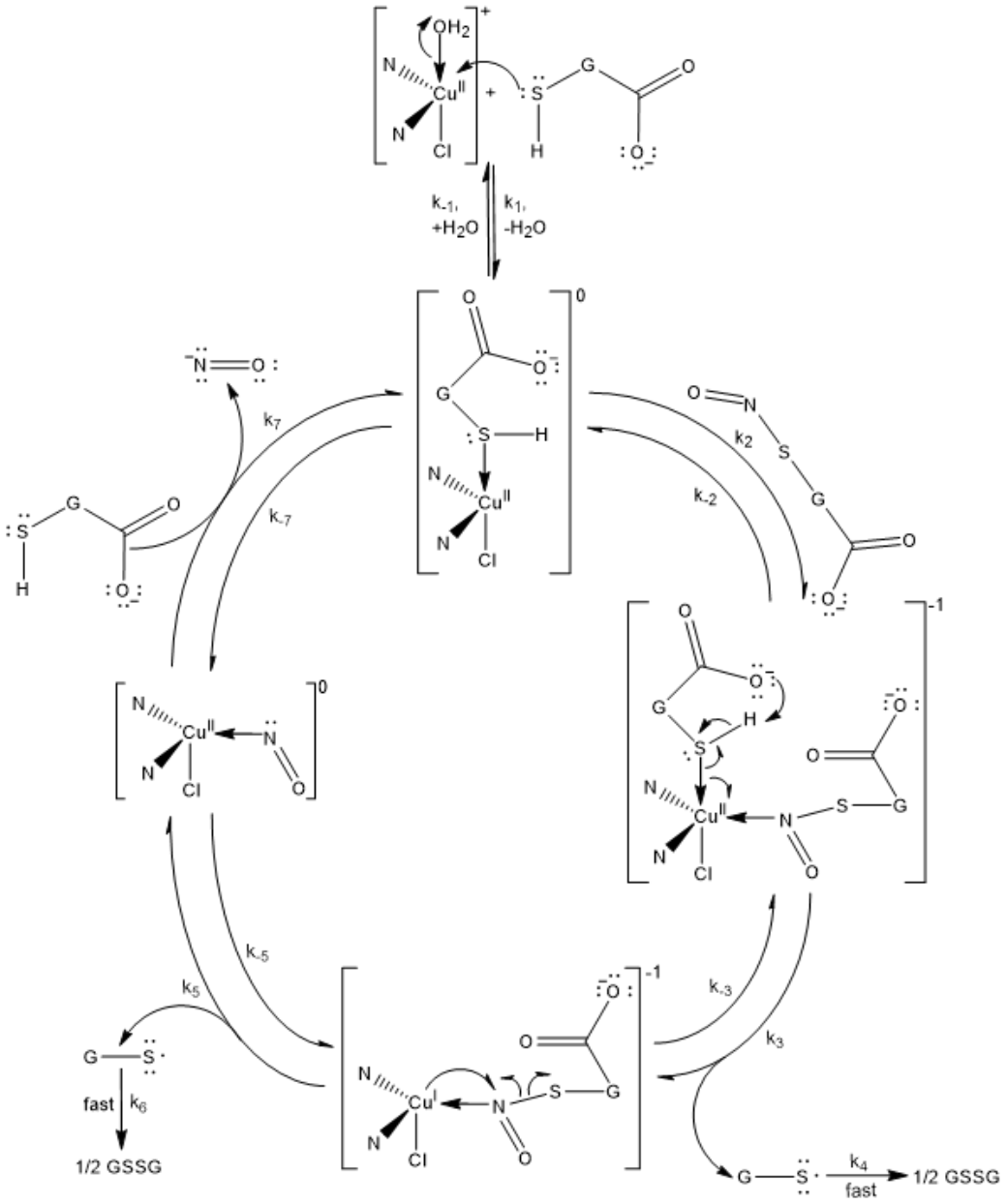

Figure S5.12. One can also write a hypothetical Cu^{II} to Cu^{I} redox catalysis mechanism, but now with an intramolecular deprotonation analogous to Figure 5.2 in Chapter V. Again, this possible mechanism is disproven by two lines of evidence: (i) significant formation of GSSG from GSH is predicted in opposition to the experimentally observed reaction stoichiometry; and (ii) $[NO]^{-}$ formation is predicted, inconsistent with the observed formation of •NO.

Calculation S5.1: the Ratio Between Thiolate and $Cu^{II}_{surface}$ at Varying Reaction pH

The pK_a of the unbound thiol proton in GSH is known to be 9.12 in water.[11] Therefore, one can calculate the relative amounts of thiolate (GS^-) versus $Cu^{II}_{surface}$ sites at different reaction pH values if one uses the Henderson-Hasselbalch equation (equations S5.28-S5.29) and knows the total amount of GSH added to each experiment.

$$pH = pK_a + \log\left(\frac{[GS^-]}{[GSH]}\right) (eq.S5.28)$$

$$\left(\frac{[GS^-]}{[GSH]}\right) = 10^{(pH-pK_a)} (eq.S5.29)$$

In each of the kinetic experiments reported in Chapter V, the total concentration of added GSH was 0.5 mM. Therefore, $[GS^-]$ and the ratio between GS^- and $Cu^{II}_{surface}$ can be calculated (equations S5.30-S5.31) and is reported below in Table S1.

$$[GSH]_T = [GSH] + [GS^-] (eq.S5.30)$$

$$[GSH] = [GSH]_T - [GS^-] (eq.S5.31)$$

Substituting the value for [GSH] in equation S5.31 into equation S5.29 yields equation S5.32 shown below.

$$\left(\frac{[GS^-]}{[GSH]_T - [GS^-]}\right) = 10^{(pH-pK_a)} (eq.S5.32)$$

Equation S5.32 can be set equal to zero, which yields equation S5.33.

$$0 = \left(\left[GSH\right]_T * 10^{(pH-pK_a)}\right) - \left([GS^-] * 10^{(pH-pK_a)}\right) - [GS^-] (eq.S5.33)$$

Solving for $[GS^-]$ from equation S5.33 yields equation S5.34.

$$[GS^-] = \frac{\left(\left[GSH\right]_T * 10^{(pH-pK_a)}\right)}{\left([10^{(pH-pK_a)} + 1\right)} (eq.S5.34)$$

The calculated value for $[GS^-]$ in equation S5.34 can then be used to calculate the ratio between $[GS^-]$ and the number of $Cu^{II}_{surface}$ sites in each experiment.

Based on the data in Table S1, there is only enough GS^- present in the reaction at pH = 6 to poison approximately 12% of the $Cu^{II}_{surface}$ sites for catalysis (assuming GS^- is a strong-binding poison and one GS^- binds to one $Cu^{II}_{surface}$ site). However, ~67% poisoning is observed at pH = 6 (Figure 5.7 of Chapter V), which disproves the hypothesis that GS^- is the kinetically dominant catalyst poison. The proton being abstracted by hydroxide in the reaction rate versus pH experiments must have a pK_a several orders of magnitude lower than the pK_a of the thiol proton in unbound GSH. Per the discussion in Chapter V, and analysis of the protons available in GSH/GSNO, one is naturally led to conclude that hydroxide is abstracting the thiol proton in GSH bound to Cu^{II} (i.e., $Cu^{II} \rightarrow S(\mathbf{H})G$).

Table S5.1. The ratio between $[GS^-]$ and amount of $Cu^{II}_{surface}$ sites at different reaction pH levels. The pH levels studied and reported in Chapter V are in bold.

pH	$\frac{[GS^-]}{[Cu^{II}_{surface}]}$
0	1.17×10^{-7}
1	1.17×10^{-6}
2	1.17×10^{-5}
3	1.17×10^{-4}
4	1.17×10^{-3}
4.5	$\mathbf{3.69 \times 10^{-3}}$
5	1.17×10^{-2}
6	**0.117**
7	1.16
9	**66.4**

Calculation S5.2: the Apparent pK_a of the Thiol Proton in GSH Bound to $Cu^{II}_{surface}$

The Henderson-Hasselbalch equation shows that when the pH of a solution equals the pK_a of a weak acid, the concentration of weak acid and its conjugate base will be equal. For this system, the weak acid is $Cu^{II}\rightarrow S(\mathbf{H})G$ and the conjugate base is $Cu^{II}\rightarrow SG$ (equation S5.35, Figure 5.2 in Chapter V).

$$pH = pK_a + \left(\frac{[Cu^{II} \rightarrow (SG)]}{[Cu^{II} \rightarrow (S(H)G)]}\right) (eq.S5.35)$$

If ~100% of available $Cu^{II}_{surface}$ active sites are active for catalysis at pH = 4.5 (where the maximum rate is observed, (2.3 ± 0.8) x 10^{-4} mM s^{-1}), then the pK_a of $Cu^{II}\rightarrow S(\mathbf{H})G$ should equal the reaction pH where 50% of the maximum catalytic activity (1.15 x 10^{-4} mM s^{-1}) is predicted by the linear fit in Figure 5.7 of Chapter V (y = (-0.21)$\boldsymbol{x}$ + 2.4 x 10^{-4}). In the linear fit of Figure 5.7, y represents -d[GSNO]/dt and $\boldsymbol{x}$ is reaction pH. The apparent pK_a of $Cu^{II}\rightarrow S(\mathbf{H})G$ is then calculated to be 5.6 (equations S5.36-S5.37). This pK_a estimate is supported by precedent that upon binding to Cu^{II}, the pK_a of thiol protons can drop 2-4 orders of magnitude.[12] Given that the pK_a of the thiol proton in unbound GSH is 9.12, a pK_a for $Cu^{II}\rightarrow S(\mathbf{H})G$ of ~5-7 is consistent with the observed pK_a ~5.6.

$$\frac{-d[GSNO]}{dt} = (-0.21) * (pH) + 2.4 \times 10^{-4} (mM\ s^{-1})\ (eq.S5.36)$$

$$pH = \frac{\left(\frac{-d[GSNO]}{dt} - 2.4 \times 10^{-4} (mM\ s^{-1}\right)}{-0.21}$$

$$= pK_a\ if\ \frac{-d[GSNO]}{dt}\ is\ 1.5 \times 10^{-4}\ mM\ s^{-1}\ (eq.S5.37)$$

This analysis operates under the assumption that 50% of the maximum catalytic activity corresponds to 50% of the $Cu^{II}\rightarrow S(\mathbf{H})G$ species having been deprotonated. All the -d[GSNO]/dt versus pH studies were carried out under conditions where the reaction was saturated in [GSH].

Therefore, the maximum number of $Cu^{II}_{surface}$ sites available were coordinated with GSH for all the data points reported in Figure 5.7 in Chapter V.

Possible Future Experiments and Computational Studies Based on Predications from the Proposed Mechanism in Figure 5.2 in Chapter V

Several predictions follow based upon Figure 5.2 in Chapter V and the proposed Cu^{II} to Cu^{III} redox, PCET mechanism.[13,14]

A. Saturation kinetics are predicted in [GSNO] (equations S8-S9) but will likely require another monitoring method to be verified experimentally. The range at which [GSNO] can be reliably monitored by ^{1}H NMR spectroscopy in water is approximately 0.5 to 1.5 mM, which is currently not wide enough to observe saturation in [GSNO]. Monitoring the reaction at [GSNO] below 0.5 mM requires massing out sub-milligram quantities of CuBTTri powder.

B. Running the reaction at pH = 9, where the thiol proton in Cu^{II}←(S(**H**)G) is irreversibly deprotonated (i.e., at pH ≥ 2 orders of magnitude higher than 5.6, the estimated pK_a for Cu^{II}←(S(**H**)G)), and *without GSNO* is predicted to trap the catalytically active surface sites in a Cu^{II} state. On the other hand, running the reaction at pH = 9 *but with GSNO* may trap the catalytically active surface sites in a Cu^{III} state (i.e., at the intermediate at "six o'clock" in Figure 5.2 in Chapter V). In principle, the Cu^{III} site could then be detected *ex situ* using a technique sensitive to Cu oxidation state such as X-ray photoelectron spectroscopy (XPS), the caveat there being the issue of just detecting the low level of ~1.3% surface active sites that are, then, also poisoned.[5]

C. The PCET steps of Figure 5.2 suggest that testing the rate of the reaction for deuterium substituted GSH (GSD), by carrying out the reaction in D_2O instead of H_2O, should affect the observed rate if the PCET steps as written in Figure 5.2 are part of the catalytic cycle. Additionally, computational studies proposed below (F) should yield a prediction of the kinetic isotope effect(s) for the proposed mechanism in Figure 5.2.

D. RSNO/RSH pairs with simpler structures than GSNO/GSH are predicted to react by, ultimately, different mechanisms under catalysis by CuBTTri. A good example is the previously studied pair of *S*-Nitrosocysteamine/Cysteamine (Cysam-SNO/Cysam-SH).[7] Cysam-SNO/ Cysam-SH do not contain the tripeptide backbone of GSNO/GSH. Addition of stoichiometric Cysam-SH *is not required* to completely catalyze NO release from Cysam-SNO with CuBTTri.[7] The Cysam-SNO/Cysam-SH pair looks to exhibit a different rate law—and therefore a different mechanism—for CuBTTri catalyzed NO release.

E. The PCET steps of Figure 5.2, poisoning observed at pH ~6.7, and a k_H/k_D isotope effect at pH = 4.5 are predictions that will be interesting to test computationally. The present system has the advantage of being a Cu-MOF system so atomic make-up and positions of the active sites are as well-known as for pretty much any solid-based catalyst. There are other details around the proposed mechanism in Figure 5.2 that computational studies could ideally probe. One example being the Marcus-type reorganization energy barrier in the computationally preferred mechanism that accompanies any Cu redox steps.

REFERENCES

1. Dincă, M. & Long, J. R. High-Enthalpy Hydrogen Adsorption in Cation-Exchanged Variants of the Microporous Metal−Organic Framework Mn3[(Mn4Cl)3(BTT)8(CH3OH)10]2. *Journal of the American Chemical Society* **129**, 11172–11176 (2007).

2. Demessence, A., D'Alessandro, D. M., Foo, M. L. & Long, J. R. Strong CO2 Binding in a Water-Stable, Triazolate-Bridged Metal−Organic Framework Functionalized with Ethylenediamine. *Journal of the American Chemical Society* **131**, 8784–8786 (2009).

3. Dincă, M. *et al.* Observation of Cu2+–H2 Interactions in a Fully Desolvated Sodalite-Type Metal–Organic Framework. *Angewandte Chemie International Edition* **46**, 1419–1422 (2007).

4. Tuttle, R. R., Rubin, H. N., Rithner, C. D., Finke, R. G. & Reynolds, M. M. Copper ion vs copper metal–organic framework catalyzed NO release from bioavailable S-Nitrosoglutathione en route to biomedical applications: Direct 1H NMR monitoring in water allowing identification of the distinct, true reaction stoichiometries and thio. *Journal of Inorganic Biochemistry* **199**, 110760 (2019).

5. R Tuttle, R., J Folkman, S., N Rubin, H., G. Finke, R. & M. Reynolds, M. Copper Metal–Organic Framework Surface Catalysis: Catalyst Poisoning, IR Spectroscopic, and Kinetic Evidence Addressing the Nature and Number of the Catalytically Active Sites En Route to Improved Applications. *ACS Applied Materials & Interfaces* **0**, (2020).

6. Harding, J. L. & Reynolds, M. M. Metal Organic Frameworks as Nitric Oxide Catalysts. *Journal of the American Chemical Society* **134**, 3330–3333 (2012).

7. Harding, J. L., Metz, J. M. & Reynolds, M. M. A Tunable, Stable, and Bioactive MOF Catalyst for Generating a Localized Therapeutic from Endogenous Sources. *Advanced Functional Materials* **24**, 7503–7509 (2014).

8. Chantry, G. W. & Plane, R. A. CN Stretching Bands in the Raman Spectra of Some Group Ib and Group IIb Compex Cyanides. *The Journal of Chemical Physics1* **33**, 736–739 (1960).

9. Penneman, R. A. & Jones, L. H. Infrared Absorption Studies of Aqueous Complex Ions. II. Cyanide Complexes of Cu(I) in Aqueous Solution. *The Journal of Chemical Physics* **24**, 293–296 (1956).

10. Jones, L. H. Vibrational Spectrum and Structure of Metal-Cyanide Complexes in the Solid State. IV. K3Cu(CN)4. *The Journal of Chemical Physics* **29**, 463–466 (1958).

11. Tummanapelli, A. K. & Vasudevan, S. Ab Initio MD Simulations of the Brønsted Acidity of Glutathione in Aqueous Solutions: Predicting pKa Shifts of the Cysteine Residue. *The Journal of Physical Chemistry B* **119**, 15353–15358 (2015).

12. Graminski, G. F., Kubo, Y. & Armstrong, R. N. Spectroscopic and kinetic evidence for the thiolate anion of glutathione at the active site of glutathione S-transferase. *Biochemistry* **28**, 3562–3568 (1989).

13. Hammes-Schiffer, S. Theoretical Perspectives on Proton-Coupled Electron Transfer Reactions. *Accounts of Chemical Research* **34**, 273–281 (2001).

14. Hammes-Schiffer, S. & Stuchebrukhov, A. A. Theory of Coupled Electron and Proton Transfer Reactions. *Chemical Reviews* **110**, 6939–6960 (2010).

15. Collman, J. ; H. L. ; N. J. ; F. R. *Principles and Applications of Organotransition Metal Chemistry*. (1987).